INVESTIGATION OF SURFACE DISCHARGE ALONG INTERFACE BETWEEN LIQUID AND NANOCOMPOSITE

Thesis presented for the degree of

Doctor of Philosophy

in the

Department of Electronic & Electrical Engineering

University of Strathclyde

2015

Yiming Gao, BEng (Hons), MSc

Department of Electronic & Electrical Engineering University

of Strathclyde

Glasgow, U.K.

DECLARATION OF AUTHENTICITY AND AUTHOR'S RIGHTS

This thesis is the result of the author's original research. It has been composed by the author and has not been previously submitted for examination which has led to the award of a degree.

The copyright of this thesis belongs to the author under the terms of the United Kingdom Copyright Acts as qualified by University of Strathclyde Regulation 3.50. Due acknowledgement must always be made of the use of any material contained in, or derived from, this thesis.

Signed:

Date:

Acknowledgement

Firstly, most sincere gratitude to my supervisor: Dr. Martin J Given. Thanking him for giving me this opportunity and continues support, guidance and encourage throughout this project both technically and mentally.

I would also like to thank my parents for their unconditional love, encourage and support.

There are also thanks to a special person and her family, thanks for her two and half years' accompany and support.

Special thanks to Mark Wilson and Michelle Maclean for their help during this project, and best wishes for their baby Murray.

Thanks to State Grid Tian Ji Electric Power Research Institute for their technical support.

Abstract

Surface discharge happened along the interface of liquid and solid insulation material can be considered the weakest link in an insulation system due to the lower breakdown voltage level than any individual insulating material. In recent years, solid nanocomposites have been discovered to possess improved dielectric properties, such as PD and aging resistance, breakdown strength and low dielectric losses. It is therefore important to investigate if the changes in the properties of a nanocomposite can change the behaviour of surface discharge along its surface.

The objectives of this project are to develop a suitable method for making nanocomposite (composite materials which contain nanoscale fillers) in the laboratory, to produce samples and test their dielectric properties, then investigate the surface discharge behaviour of these samples.

The matrix material used was HY5052/LY5052 epoxy resin. Two nanofiller materials were used in this project: ZnO and Al_2O_3 at concentrations between 0.1 wt%, and 5 wt%. Over 100 samples were made (diameter: 8.5 cm, thickness: 1 cm). Dielectric properties were tested for some sample types over the frequency range of 10^{-2} to 5×10^{6} Hz.

Over 50 samples were tested for surface discharges and the behaviors were characterized by: calculated the fractal dimension of the discharge pattern; measuring the maximum length and total light emission of the discharge. Current pulses occurring during the discharge were also measured. For the samples examined no significant changes were observed in the fractal dimension or maximum length of the discharges for differing nanofillers and concentration of nanofiller. However changes did occur in the light emission and current pulse activity when nanocomposites were compared with the pure epoxy.

LIST OF ACRONYMS

AC	Alternating Current
DC	Direct Current
PD	Partial Discharge
EHD	Electro-Hydrodynamic Motion
PTFE	Polytetrafluoroethylene

LDPE	Low-density polyethylene
3D	3-Dimensional
EPN	Phenolic epoxy resin
ECN	Phenolic epoxy resin (Cresol)
SEM	Scanning Electron Microscope
LCR	Inductance, Capacitance, Resistance
HV	High Voltage
PVC	Polyvinyl chloride
PMMA	Poly(methyl methacrylate)
HFCT	High Frequency Current Transformer
DF	Fractal Dimension
TLE	Total Light Emission
FL	Final Length (Maximum Length)
R_2	Pearson Correlation

OP	Offset Point
HFN	Hypothetic Frames Number
CCD	Charge-Coupled Device

CONTENTS

1. INTRODUCTION

Surface breakdown along the interface of two insulating materials can be the weakest link of a combined insulation system. The breakdown voltage level of surface breakdown is usually lower than each individual insulating material. The initial stage of surface breakdown is surface discharge, even though these discharges do not always necessarily generate complete breakdowns, the surface tracking, carbonisation and aging effect caused by surface discharge would slowly erode the insulating performance of the materials.

The surface discharge along the solid and gas interface has been investigated more than for liquid solid interfaces. The reasons for this situation are probably due to that large portion of insulation condition in power industry involves solid/gas insulation.

In power industry, liquid and solid combine insulation is commonly used in transformer, switches, cable, capacitors and equipment that involve long operating time and generating large quantity of heat, since insulating liquid is not just used as insulator but also a cooling and sealing agent. Most commonly used liquid/solid insulation type is oil/paper or pressboard insulation. To judge whether the liquid and solid are a suitable combination for insulation， the combination should fit for the following requirements[1]:

1. Under operating voltage level, there are not any harmful partial discharge;
2. Under AC condition test, there isn't severe partial discharge, breakdown and flashover
3. Under lightening impulse, there isn't any breakdown or flashover.

Under DC condition, the breakdown strength of the combination insulation is normally higher than AC condition; this is because the partial discharge, aging and flashover events are less severe in DC condition than AC condition.

Previous studies of surface discharge and creeping discharge over the interface of combine insulation have discovered several parameters which can influence the behaviors of discharges, for example, the thickness of solid insulation[2], the permittivity of both materials[3].

Composite materials where fillers such as mica are added to a polymer matrix have been used for many years in insulation systems. In recent years due to the advances in nanoparticle science there has been increasing interest in the development and properties of nanocomposites. A nanocomposite is one where the size of the filler particles has at least one dimension in the sub-micron range. Due to the small size of the filler particles significant behaviour changes are expected , it has been discovered that the nanocomposite could possess a better PD and aging resistance, a higher breakdown strength and a lower dielectric loss under same frequency level. There are also some researches done regarding the surface degradation resistance of nanocomposite[4][5], the thermal conductivity and electrical conductivity of the materials[6][7], permittivity and dielectric loss of the materials[8][9]. It is interesting to see how the nanocomposite behaves when the surface discharges occur.

1.1 Objectives and Achievements

The main objectives of this project can be summarized into the following:

1. Explore and develop the possible method of making nanocomposite in the lab
2. Discover dielectric properties of the nanocomposite.
3. Investigate the surface discharge and flashover behavior under AC condition over the surface of nanocomposite immersed in mineral oil.

Several nanocomposites were produced and investigated in this project regarding surface discharge behavior along the surface; there were two nanoparticles involved: ZnO and Al_2O_3. Seven concentrations for each type of nanoparticles were investigated: 0.1 wt%, 0.5 wt%, 1 wt%, 2 wt%, 3 wt%, 4 wt% and 5 wt%. The Matrix material used was Hy5052/LY5052. Techniques were developed to allow suitable samples to be manufactured for surface discharge tests (diameter 8.5 cm and thickness 1 cm).

Changes in the dielectric properties of the nanocomposites have been measured in the frequency range of 10^{-2} to 5×10^{6} Hz.

The behaviors of surface discharges have been examined for over one thousand individual tests on 50 different samples over a range of 50 Hz AC voltages. The optical behavior of surface discharges were characterised by: calculating their fractal

dimension; measuring the maximum length and measuring the total light emission from the active areas of the discharge. Relationships between the nature of the solid material and these measurements were examined. Current pulse measurements have also been performed and changes in the pulse activity as a function of voltage and sample material have been examined.

The dielectric properties of the nanocomposite material were different to those of the pure matrix material but the relationship with filler concentration is complex.

No significant changes were seen in the fractal dimension or the maximum length of discharges between pure epoxy resin and nanocomposite samples. Changes were observed in both light emission and current pulse activity.

1.2 Thesis structure

The subsequent chapters of this thesis are as follow:

Chapter 2 is the literature review chapter.

- Section 2.1 covers the knowledge of insulating properties about liquid, solid and combine insulation of solid and liquid.
- Section 2.2 introduced the knowledge of nanocomposite material.
- Section 2.3 was used to describe the general idea of fractal dimension.

Chapter 3 described the sample manufacture of nanocomposite in this project:

- Section 3.1 will introduce the basic knowledge of epoxy resin that includes the identification of epoxy resin; basic categories of different resins and the properties associated with them, especially their electrical properties which are most relevant to this project.
- Section 3.2 describes the specific materials that were actually used in this project. The reason for choosing these materials will be stated. Molecular formula and the chemical reaction mechanism of the matrix materials will be described. The additive nanoparticles will also be described.

- Section 3.3 describes in detail the procedures developed for processing and manufacturing samples.

Chapter 4 describes the observed dielectric properties of newly made nanocomposite:

- Section 4.1 introduced the major properties and the common test methods.
- Section 4.2 introduced the test method actually used in this project.
- Section 4.3 is presenting the test results from Section 4.2.
- Section 4.4 is the discussion of the test results.

Chapter 5 gives a detailed description of the setup of the surface discharge observation experiment.

- Section 5.1 is introducing Power supply
- Section 5.2 described the design and manufacture of the test cell and the insulating liquid were used.
- Section 5.3 introduce the waveform collecting equipment, there is also the details of the image analysis methods used in this project.
- Section 5.4 introduce the equipment and operating procedures for image acquisition
- Section 5.5 described the image processing and analysis method used on the raw data

Chapter 6 was presenting and discussed the optical data.

- In Section 6.1, the results for fractal dimension, light emission and final length will be listed and described;
- In Section 6.2, there are the discussions of the permittivity changes affected on the optical results and other possible meanings that indicate;
- In Section 6.3, the usage of fractal dimension is discussed and the advantage and disadvantage of this method are discussed.

Chapter 7 focuses on the electrical data for discharge pattern.

- In Section 7.1, the detail of processing the electrical pulse data of surface discharge for each nanocomposite under different applied voltage level will be

described and data for the behavior of the discharge pulse pattern with phase angle and any changes occurring per cycle during the tests will be presented.

- In Section 7.2, the optical discharge images was matched with the sensed electrical pulse in 2 seconds period to reveal more information of the surface discharge for each different nanocomposite.

Chapter 8 is the conclusion and future work chapter which gives the detail of the achievement of this project and the possible directions for further research on this topic.

References

[1] X. Liang, *High Voltage Engineering (Chinese Edition)*, 1st Editio. BEIJING: Qing Hua university, 2003.

[2] A. Beroual, L. Kebbabi, E. A. Al-Ammar, and M. I. Qureshi, "Analysis of creeping discharges activity at solid/liquid interfaces subjected to ac voltage," *IET Gener. Transm. Distrib.*, vol. 5, no. 9, p. 973, 2011.

[3] R. J. Taylor, "Effect of permittivity matching on the flashover of solid/liquid interfaces," *Proc. Inst. Electr. Eng.*, vol. 124, no. 10, p. 899, 1977.

[4] P. H. F. Morshuis, "Degradation of solid dielectrics due to internal partial discharge: some thoughts on progress made and where to go now," *IEEE Trans. Dielectr. Electr. Insul.*, vol. 12, no. 5, pp. 905–913, Oct. 2005.

[5] P. Maity, S. Basu, V. Parameswaran, and N. Gupta, "Degradation of polymer dielectrics with nanometric metal-oxide fillers due to surface discharges," *IEEE Trans. Dielectr. Electr. Insul.*, vol. 15, no. 1, pp. 52–62, 2008.

[6] R. Kochetov, T. Andritsch, P. H. F. Morshuis, J. J. Smit, and A. Materials, "Dielectric Response and Thermal Conductivity of Epoxy Resin Filled with Nanoalumina Particles of Different Size in α , γ and δ Phase," in *Annual Report Conference on Electrical Insulation and Dielectric Phenomena*, 2010, pp. 3–6.

[7] P. Preetha and M. Thomas, "AC breakdown characteristics of epoxy nanocomposites," *IEEE Trans. Dielectr. Electr. Insul.*, vol. 18, no. 5, pp. 1526–1534, Oct. 2011.

[8] S. Singha and M. Thomas, "Dielectric properties of epoxy nanocomposites," *IEEE Trans. Dielectr. Electr. Insul.*, vol. 15, no. 1, pp. 12–23, 2008.

[9] A. R. Conference, E. Insulation, D. Phenomena, J. K. Nelson, M. Ful, and U.

Kingdom, “Dielectric Properties of Epoxy Nanocomposites containing TiOz, Ab03 and ZnO fillers,” no. type 1255, pp. 406–409, 2004.

2. LITERATURE REVIEW

This project involved the knowledge of engineering, mathematics and chemistry. This chapter will introduce some of the background knowledge used in this project. More detailed information on the methods used and the results obtained is given in Chapters 3 to 7.

In Section 2.1, The basic dielectric and breakdown properties of liquid, solid and combine insulation systems are reviewed.

In Section 2.2, Ideas related to nanoparticles, nanodielectrics, and nanocomposite materials are introduced. The background to the methods of manufacturing a nanocomposite is discussed. Possible future applications for nanodieletrics are considered.

In Section 2.3, the ideas associated with fractal dimension and its applications are introduced. The basis of calculating the fractal dimension of self-similar and irregular objects is described.

2.1 Insulation system

The performance of Electrical component working in high voltage environment is strongly depending on the insulation system. Therefore, the design and the usage of insulation system have to follow the technical requirement for the specific environment.

An insulation system is a combination of insulating material under certain condition and rules. The reason of using combining insulating system is to cover the shortage of properties of each material. Many practical insulating systems have already been used in industry, like paper-oil insulation in transformer[1]–[3].

This project is aim to research the combined insulation system of solid and liquid concentrating on breakdown along the surface of the solid insulation. Section 2.1.1, 2.1.2 and 2.1.3 will be introducing the basic knowledge of these two kinds of materials as insulator.

2.1.1 Solid Insulation

Solid insulation system has been a main type of insulation in the power industry for the beginning [4]. It has been applied as insulation in many different electrical components. Solid insulation materials are not used only because of their electrical insulation performances, but also their mechanical properties, like ceramic insulators in power distribution systems. The solid insulation, up to a limit, can effectively protect the component from the chemical and mechanical damages. This section will focus of introducing its dielectric insulation properties.

2.1.1.1 Dielectric properties of solid

Unlike gases and liquids insulation, solid insulating material does not have a selfhealing ability; if a breakdown occurred, the solid insulation cannot restore its dielectric properties. Solid dielectrics that can be used as high voltage insulation materials will normally presenting suitable dielectric properties under circumstances, these properties are[5]:

- Breakdown strength
- Bulk and surface conductivity
- Relative permittivity
- Dielectric loss

Between these properties, relative permittivity is related to the electrical field distribution and the capacitance of the solid insulation; conductivity and dielectric loss have effect on power losses during operation; breakdown strength is the key factor to determine the application area of solid system.

2.1.1.2 Breakdown Mechanism of solid

There are several different breakdown mechanisms for solid material. Broadly speaking, they can be categories into three kinds [6]:

- Electro-mechanical (Intrinsic) Breakdown
- Thermal Breakdown
- Electro-chemical Breakdown

The mechanism of breakdown can be identified by the operating time of solid under high voltage field; the difference is showing in Figure 2.1. With the time increased, the mechanism and the breakdown strength changed. Electrical breakdown take the shortest application time and highest breakdown strength to occur; electro-chemical breakdown takes the longest application time and the lowest breakdown strength to develop.

Second and third mechanisms are more related to dielectric aging and degradation of the dielectric properties; the application time of mechanism is also not applied in this project, electro-chemical breakdown can take years to initiate. This project will be more focused on the first mechanism.

In the solid dielectric, there are usually free charged carriers; under the electrical filed, the carriers will accelerate and collide with atoms or ions; when the energy that acquired from the electrical field can not be counteract by the energy of the collide, ionization occurs, the number of free charged carrier increased dramatically and electron avalanche initiated[7][8]; this process will damage the lattice structure of the dielectric and increase the conductance which can lead to breakdown. If there are no charged carriers in the dielectrics, breakdown can be caused by the injected charged carrier from electrode[9].

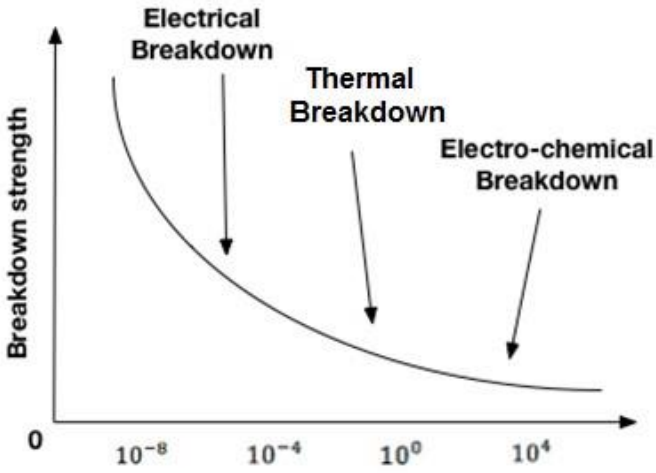

Figure 2.1 Relationship between breakdown strength (kV/cm) of solid and time (s)

The character of intrinsic breakdown can be state as follow[10]:

1. Breakdown strength is not effected by the temperature of the dielectric, heat dispersion of the dielectric and the frequency of applied power supply;
2. Uniformity of the electrical field have a strong effect on the breakdown strength;
3. The bubble and impurities in the dielectric will have impact on the electrical field and bring down the breakdown strength of dielectric.

The mechanism of Thermal breakdown can be described as this: because the existence of the dielectric loss and conductance loss, when the dielectric is under electrical field, it will generate heat and if the heat cannot be fully dissipated, the resistance of dielectric will decrease and current will increase which makes the heat even higher till reach the breakdown point. Thermal breakdown is strongly depended on the temperature, the dielectric loss and conductance of the dielectric[11].

Electro-chemical breakdown (aging) is caused by the irreversible degradation of the physical or chemical properties of dielectric. Under AC condition, electro-chemical breakdown can be divided into two kinds: partial discharge[12] and water treeing[13]. Under DC condition, electro-chemical breakdown can take long time, moisture and contamination can accelerate this process. There is another electro-chemical breakdown happening on the surface of organic dielectric, also known as tracking, it will cause the carbonization of the surface and create breakdown channels[15][16].

2.1.1.3 Influence Factors of breakdown

For solid insulation materials, If consider all mechanisms, dielectric breakdown strength can be affected by the following factor:

1. **Application time of the electrical field:** although intrinsic breakdown is not affect by the application time; thermal and electro-chemical breakdown is strongly affect by the application time [6].
2. **Temperature:** temperature of the environment have strong impact on the thermal breakdown; normally, with temperature increase, the breakdown strength decrease[16] increased temperature will also cause ageing processes to occur more rapidly;
3. **Moisture:** the moisture on or in the dielectric can decrease the breakdown strength significantly[17];

4. **Uniformity of the electrical field and the thickness of dielectric:** under uniform electrical field, the breakdown strength should increase linearly with thickness increase. Under a non-uniform electrical field the behavior is more complex depending on the field distribution in the system.

2.1.2 Liquid insulation

Liquid insulation is widely used in electrical industry. Most commonly used liquids are nature mineral oil and synthetic insulating oil. Different to the solid insulation material, liquid insulation materials have a capability of self-healing. When the breakdown is over, the dielectric properties recover to values close to their original values. The liquid dielectric is not just providing the insulation, it is used as a cooling agent.

2.1.2.1 Breakdown Mechanism of liquid

The breakdown mechanism of liquid is not as well established as gas and solid. The mechanisms are not completely defined. The breakdown process is also affected by contamination of the liquid. In pure liquid dielectric, there are two theories[18]:

1. Because of thermionic emission, free discharge carriers is injected and accelerated in the liquid; the carrier cause the ionization in the liquid and the number of the carrier increased, eventually a path will formed in the liquid and the liquid breakdown
2. Under the electrical field, there will be bubbles form inside the liquid dielectric; the bubbles and liquid electrode is like connecting in series. For two dielectrics connecting in series, the electrical field distribution is in inversely proportional of relative permittivity of the dielectric. The gas will take most of the electric strength and ionized, with ionization proceed, the bubble will expand and inner temperature will increase, the heat will generate more bubbles and the process goes on in cycles till the liquid breakdown.

Because the density of the liquid dielectric is much higher than the density of gas, the mean free path of electron in liquid is shorter than in gas; it is harder for the electron in liquid to generate enough kinetic energy for ionization, so in general, pure liquid dielectric have higher breakdown strength than pure gas.

Most of the liquid dielectric used in industry cannot be kept totally pure. There are many possible ways to bring in impurities. The particle or moisture could be brought in during the manufacture procedure; aging and mechanical damage can also bring in impurities. If there are impurities present, the breakdown mechanism can rely on the impurities. One example is that under electrical field, the impurities are more likely to be polarized and form a "bridge" between anode and cathode; because the existence of this "bridge", the leakage current in the dielectric will increase and the heat generated from leakage current will vaporize the moisture to form more bubbles. This bubble bridge becomes the breakdown path[18].

2.1.2.2 Influence factor of Breakdown

Based on the breakdown theories, several factors can have influence on the breakdown strength and they are listed below:

1. **Impurities:** Impurities is key factor on influencing the breakdown strength and the hardest one to eliminate[18], such as solid particles, carbon, fibre generated from aging and discharge.
2. **Application time of the electrical field:** if the application time is short, the breakdown behaviour is more likely follow the first two theories; if the application time is long, the breakdown behaviour is more likely to follow an impurity based breakdown theory[19].
3. **Temperature:** with the temperature increase, the breakdown strength decrease[20].
4. **Uniformity of the electrical field**: if the electrical field is uniform, the breakdown would occur when the field strength in the whole region is exceed the breakdown strength of the liquid; if the electrical field is non-uniform, there could be a unexpected high field region which induce the breakdown. The propagation of the streamer is also different in the two field polarities; a streamer is a gathering of the free electrons moving in electrical field, in nonuniform fields, streamer propagation mechanism and behaviour is in part depending on polarity [21]
5. **Pressure**: with pressure increasing, it is more difficult to form gas bubbles, this make the breakdown strength increase[22].

2.1.3 Combine solid-liquid Insulation

Combine insulation is used mostly in transformer and switches in power industry. Under this regime, the dielectrics properties of the composite insulation are entirely depend on the dielectric property of each material. In this section, the properties of combine insulation will be discussed.

2.1.3.1 Breakdown mechanism of combine insulation

With a insulating system made up of two different insulating materials, the breakdown of the system does not always happen inside either of the insulating materials, it can initiate and propagate on the interface of the materials and the breakdown initiating voltage level is much lower than the breakdown voltage level of the individual materials[11].

For a solid liquid insulating interface as investigated in this project it has been suggested that a discharge is initiated on the surface due to a high local field or presence of impurities. Once the discharge initiates there is a possibility that it will continually grow and become a flashover or treeing event, eventually damage the insulating materials by leaving tracks and carbonized the materials[23]. In the long term, discharge events occurring with high frequency will generated heat which will accelerate degradation of dielectric properties and the aging states of the materials[24].

In the initiating stage a proposed mechanism is the emission of the electrons in the triple junction of an electrode or a metallic impurity and two dielectrics (liquid/solid). Due to the differences in permittivity of the three different materials at the triple junction high electric fields can be produced. This increases the probability of electron injection and discharge initiation. The mechanism for a surface discharge propagating and developing into a breakdown reminds undetermined[25].

2.1.3.2 Influence Factors of surface discharge

Based on the knowledge gather from the literatures, the influence factors of surface discharge occurring on the interface of solid and liquid can be listed as follow:

1. **Impurity states in the liquid:** the impurity could be generated by the aging process of the dielectrics, could be brought in by manufacture process; with impurity, surface discharge is more likely to occur[26], [27].
2. **Relative permittivity match/mismatch of two dielectric:** under combine insulation**,** the electrical field distribution of each dielectrics is determined by their relative permittivity; if the differences between permittivity are large, the initiating voltage level of surface discharge will be low[26], [27]
3. **Surface roughness:** in certain experiments[28], surface roughness can impact on the final length of the surface discharge branches. If the surface is smooth, the final length will be shorter.
4. **The thickness of the solid dielectric:** under extremely non-uniform electric field, if the thickness of the solid dielectric is large, the initiating voltage of discharge voltage will be higher[29].
5. **Electro-hydrodynamic motion of liquid:** EHD motion is another factor which need to be considered for surface discharge; when the discharge occurred, the liquid start to flow and the electric field of both dielectric will be influenced, so the discharge will be influenced[30], [31].

2.2 Nanodielectric Material

Before the discussion of nanodielectric materials, it is better to spend some time on nanocomposite materials, nanodielectric materials are a subset of nanocomposite materials. Composite materials have a long history; mud and straw for instance, has been used for building material for a very long time. With technological evolution, composites have becomes more and more advanced and functional materials. Polymer composites started to be investigated since the 1900s to improve the properties of the base polymer materials[32].

With the introduction of nanoparticles, the first polymer nanocomposite material was developed by a Toyota research group in 1990[33]. This material was aimed at improved mechanical and thermal properties for timing belt covers. In 1994, T.J Lewis first introduced the concept nanometric dielectrics in general[34]; following the initial work, Lewis present two more paper[35], [36] on this topic and suggest that the unique properties of this kind of materials is related to the interface effects. These effects

become more significant when the size of a dielectric layer is reduced or in a composite material when the size of particles is reduced. The definition of nanodielectric first appeared in 2001, this definition defines the essence of nanodielectrics and still applies today:

"In the contest, a nanodielectric would consist of a multi component dielectric possessing nanostructures, the presence of which lead to changes of one or several of its dielectric properties." [37]

Also In 2001, it was shown that nanofiller, (well dispersed organically modified layered silicate) could enhance the thermal and mechanical properties of epoxy with a small weight percentage[38]. Changes in the temperature dependence of both permittivity (ε_r) and tanδ were also observed. In the same year, J.K Nelson investigated the dielectric properties of epoxy with TiO_2 nanofiller [39] and found permittivity and dielectric loss changes in the dielectric spectra. Since these two papers, the research on nanodielectrics has been motivated and fruitful, many facts about the nanocomposite has been discovered, Section 2.2.1 will present a general view of the productive.

2.2.1 Productivity of Nanodielectric Research

Experiment results of the nanodielectric have begun to emerge since 2001 and the results are very encouraging with evidence of the electrical, mechanical and thermal properties of materials being enhanced. As of July 2015 a search on the keyword nanocomposite and dielectric on the IEEE explore website produced 930 conference papers and 270 journal and magazine articles.

The research on nanodielectrics can be categorised into the following directions:

- Modelling or simulating nanodielectric material to predict their properties and to determine the underlying reasons for these changes, compared to the properties of unmodified materials
- Different manufacture methods for manufacturing nanodielectrics and how these methods can affect the properties of the material.
- Experimental work to find the changes in material properties that are possible with nanodielectrics.

In the first category, many models have been generated [40]–[47]. Multi core model for instance, is a model for explaining the bonding between the polymer materials and inorganic nanofillers. It proposed that there are multiple layers around the nanofiller whose properties are different from that of the polymer material. The size of these layers are influenced by the size and type of nanofiller. The changes of properties depend on the interface between matrix material and the nanofiller. There is also an influence of the surface treatments which are applied to nanoparticles to prevent agglomeration and to make mixing easier. Based on these models, research has been done to try to explain or predict the property changes of nanodielectrics for example changes in permittivity [48]–[50], but the modelling techniques and underlying theories require more effort to be sufficient and accurate.

The manufacture methods of the nanodielectric have to consider the properties of the matrix material and the filler. The research on manufacture is trying to explore impact of the manufacturing techniques on the properties of nanocomposite and the possible improvement on manufacture methods which can improve these properties. For example, in [51], the good dispersion of the nanofiller has been identified as an important factor in terms of enhancing the insulating behaviour of the nanocomposites, a uneven dispersion can reduce the insulating properties significantly.

Most of the dielectric research has been done in the final category to verify the property changes through experiments. The properties which have been investigated included: partial-discharge resistance and treeing[52]–[54], breakdown strength[54]– [56], space charge accumulation [53]–[55], tracking resistance [57] [58], permittivity and dielectric loss[62]–[64] and DC conductivity[65] . For example, Al_2O_3 and ZnO nanofiller have been added into LDPE materials and the treeing resitance has been examined. It was shown that the tree inception voltage, tree growth resistance and PD resistance were improved by adding Al_2O_3 nanofiller[52]. At concentrations above 10 wt% ZnO nanofiller was shown to decrease the conduction current, lower concentrations of ZnO nanofiller enhanced the breakdown strength of the material[55]. Other examples include modifications to space charge development as a result of using nanofillers [68]. Changes in permittivity have also been reported, however the behaviour is complicated and it is not possible to predict the changes[69]–[71].

Determined by their usage in industry now, the most popular matrix materials used in these researches for property test are epoxy resins, polyethylene, XLPE, polypropylene, and ethylene vinyl acetate. Existing applications in industry have also led to research concentrating on the nanofillers: layered silicate, SiO_2, TiO_2, Al_2O_3 and MgO[72] as these fillers have already been used in micron size in industry.

2.2.2 Matrix Materials

The matrix materials used for making nanodielectrics are usually thermoplastic material or thermosetting polymer material. As mentioned above the first nanocomposite was using thermoplastic material as matrix material in Toyota group.

Thermoplastic is the kind of polymer or plastic material which can become liquid in certain temperature and back to solid upon cooling. Thermosetting polymer or plastic involves chemical bonding between polymer chains and the curing or setting process is irreversible.

Both kinds of plastic are widely used in industry; most of the plastic things in people's life a thermoplastic, like nylon, PTFE, polyethylene; epoxy resin is used in transformer, insulating the circuit board of electronic devices. They both have good dielectric properties, which is why there are widely used as insulating materials. Thermoplastics can be taken into a liquid state by heating; thermosetting plastics have a liquid form before the curing reactions. This liquid state allows the mixing of fillers or nanofillers into the polymer before cooling or a curing reaction takes it into its solid state.

2.2.3 Nanofiller

The electric properties of polymers can be modified by adding in nanoparticles. The changes in properties are complex and depend on the material of the nanoparticles the presence and type of surface coating and the shape of the nanoparticle. Nanoparticles can be categorized into three types based on their shapes [73]:

- Spherical particles
- Whiskers and rod particles
- Platelet particles

The most common nanofillers used for forming electrical insulating nanocomposite are[74]:

- Metal and Silicon oxides
- Nanoclays
- Carbon nanotubes

Metal and silicon oxides are the most commonly reported nanofiller in research at present. This is because with appropriate surface treatment they can be easily dispersed in polymer and changes in the dielectric properties of the matrix have been observed. Among the available metal oxide nanoparticles, the four most commonly reported are:

- Titanium dioxide: the most common nano-additive for epoxy resins, also known as titanium oxide. It has been shown to be able to influence the dielectric properties of epoxy resin[70][75], [76], the electrical tree effect[77] and surface or creeping discharge[78]
- Magnesium oxide: most used for low-density polyethylene (LDPE), also been investigated for the filler of epoxy resin and show a strong ability to decrease the permittivity[58]
- Aluminium oxide: also refer to as alumina, can be used in electrical insulation to improve thermal conductivity of epoxy resin[79]–[81]. The permittivity and loss tangent would also be influenced by Al_2O_3 nanofiller[63].
- Zinc oxide: it has a semiconductor behaviour, recent investigation show that by increase the volume of the addition, it can increase the conductivity when they are coupled with LDPE[59]. It can also change the permittivity value and loss tangent when coupling with epoxy resin[76].

The changes in properties of nanodielectrics as results of adding nanoparticles have been widely reported. However the reasons for the observed changes in properties are not clear. One assumption is that because of the small size of a nanoparticle for a given weight concentration they have a large specific surface area compared to micron scale particles. This means that more molecules in the filler are exposed to the surface of the nanoparticle increasing the effective surface activity[82]. The physical properties of the nanoparticle itself may be different from those observed in larger particles. However it is not clear what these differences, if they exist, are. Nanoparticles have

also been shown to add or modify trapping levels for electrons in the material close to the particle[83].

The high surface activity of nanoparticles tends to cause them to bond together and agglomerate into larger clusters. The surface energy also can make it difficult to mix these materials with a uniform dispersion. Nanoparticles are therefore modified with coatings to prevent agglomeration and to make them easier to disperse. The surface coating can also provide functional groups that bond chemically to the matrix surrounding them [84][85]

2.2.4 Manufacture of Nanodielectric

The unique properties that nanodielectric present relies on the addition of nanoparticles to a material. There is one common problem amongst all the steps for manufacture of the nanodielectric this is aggregation of the nanoparticles during their manufacture, during storage and transportation during their mixing with the matrix while it is a liquid and finally during cooling or curing when the matrix becomes a solid. This problem can be solved by several different methods

The process of aggregation is very complicated but it can be described by Equation 2.1 [86]. Assuming the force needed to stop a particle from aggregation is F_A, F_A can be described using Equation 2.1:

$$F_A = F_V + F_R + F_S \tag{2.1}$$

Where F_V stands for attractive van der Waal's force between particles caused by induced instantaneous polarizations in the particles and F_R stands for electrostatic repulsion force between the particles. The force F_S arises from large molecules adsorbed onto the surface of the nanoparticles. To move the nanoparticles together requires the movement of the molecules. This movement will result in a change of potential energy of the molecule and nanoparticle. The change in potential energy causes a force to act when the relative position of two nanoparticles is changed. In Equation 2.1, the van der Waal's force F_V is always negative, the electrostatic force F_R is always positive and the sign of F_S can be either negative or positive. A net negative

value of F_A indicates that an attractive force exists between two particles and aggregation is likely to occur. The van der Waal's force depends on the material making up the particles, the size of the particles and the dielectric properties of the matrix material; the electrostatic repulsion can be adjusted by the varying the pH value or temperature; the direction and value of F_S is determined by the properties and volume percentage of the adsorbed molecules.

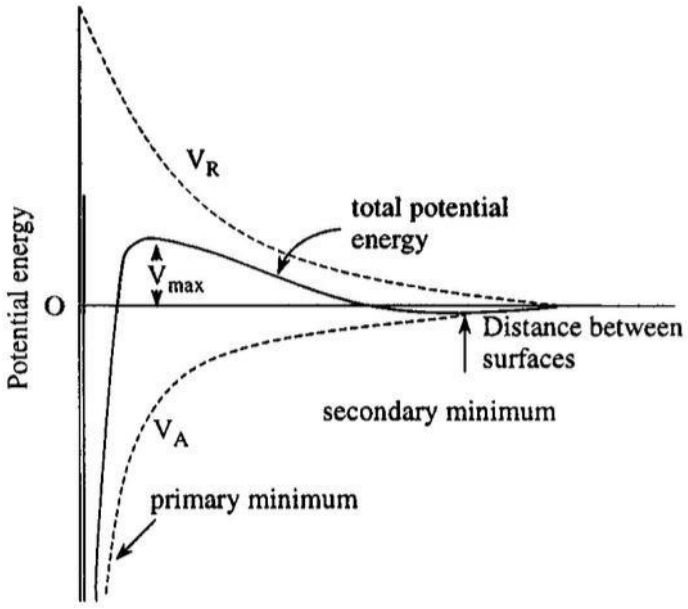

Figure 2.2 Plot of Potential Energy and Separation distance (nm)[87]

Figure 2.2 shows the potential energy curve for two nanoparticles as a function of separation, where V_R stands for the repulsive electrostatic potential and V_A stands for the attractive potential (van der Waal's). There is a maximum in the potential. Particles whose separation is greater than the position of the maximum undergo a repulsive force. At the point of the maximum energy the net force will be zero, particles separated by a smaller distance than this will undergo an attractive force which can cause aggregation. The motion of nanoparticles in a liquid follows Brownian motion. This random movement can cause the separation of two particles to reduce to the point where the attractive forces are larger than the repulsive forces.

2.2.4.1 Methods for overcome aggregation

Aggregation of nanoparticles in matrix materials is a dynamic and reversible process and can be overcome by several methods:

1. Select a filler with low van der Waal's force
2. Sol-gel Method
3. Ultrasonic treatment in Mixture with matrix
4. Surface modification/ Surface treatment

The first method is to reduce the F_V (van der Waal's force). This force increases as particle size decreases, however there are limits to the maximum size of a nanoparticle. For a given size of nanoparticle the force is decreased as the molecular weight (M.W.) of the material making up the particle is decreased. [88]. So all other things being equal the van der Waal's force between ZnO nanoparticles (M.W. 81) would be less than that between Al_2O_3 (M.W. 102)

Sol-gel is a method for generating nanoparticles, but it also can be used to create the matrix too. Therefore it can be used to generate the matrix and nanoparticles together avoiding the requirements of mixing. This method will be introduced in Section 2.2.4.2.

Third method is using the energy from the cavitation of ultrasonic wave, like mentioned before, aggregation of the nanoparticles is a reversible process. The range where the van der Waal's force is greater than the electrostatic force is small of the order of 5 nm, If sufficient energy is introduced to separate the particles by more than this distance the aggregation bond is broken. Details on how ultrasonic treatment was used in this projected will be reported in Chapter 3.

The last method is through changing the properties of nanoparticles through surface modification where molecules are bonded to the nanoparticle. Such treatments can be used to increase the value of F_R through the use of polar molecules. It can also be used to insure that F_S is positive and to increase its value. In [89], magnetite nanoparticles were treated with oleic acid forming a polar layer preventing the nanoparticles from approaching each other sufficiently closely to aggregate. This also increased its lipophilicity, since compared to nanoparticles, the oleic acid can attach to the oil molecule much easier. This method is normally done in two ways:

- **Physical treatment**: the molecules and nanoparticles are linked by van der Waal's force and electrostatic attractions;

- **Chemical reaction**: molecules and nanoparticles are linked by chemical reaction with the formation of bonds between the particle and the molecules.

2.2.4.2 Manufacture Methods for Nanodielectric

A requirement for polymer nanodielectrics is that the nanofillers are well dispersed and combine with the polymer surround them. In addition to the techniques to overcome the aggregation, techniques to disperse the nanoparticles in the polymer are required.

Based on the summary in [72] and [90], the dispersion methods can be categorised into three kinds: Intercalation method, Sol-gel method and Direct mixing method.

Intercalation Method

This method is the original method for making nanocomposite. It is used for nanoclays where the filler material has a layered silicate structure. Although the individual silicate layers are nanostructures they are ionically bound into stacks through the presence of ions between the layers. To form a nanocomposite it is necessary to introduce polymer between these layers, intercalation or to completely separate these layers exfoliation. At first, the clay particles are treated with an Alkylamine which replaces the ions between the layers of silicate. This increases the separation between the silicate layers. If polymer chains can be formed or penetrate between the layers without completely separating them an intercalated nanocomposite is formed. If the formation of the polymer results in complete separation of the layers an exfoliated nanocomposite is formed[91]. Detail shows in Figure 2.3.

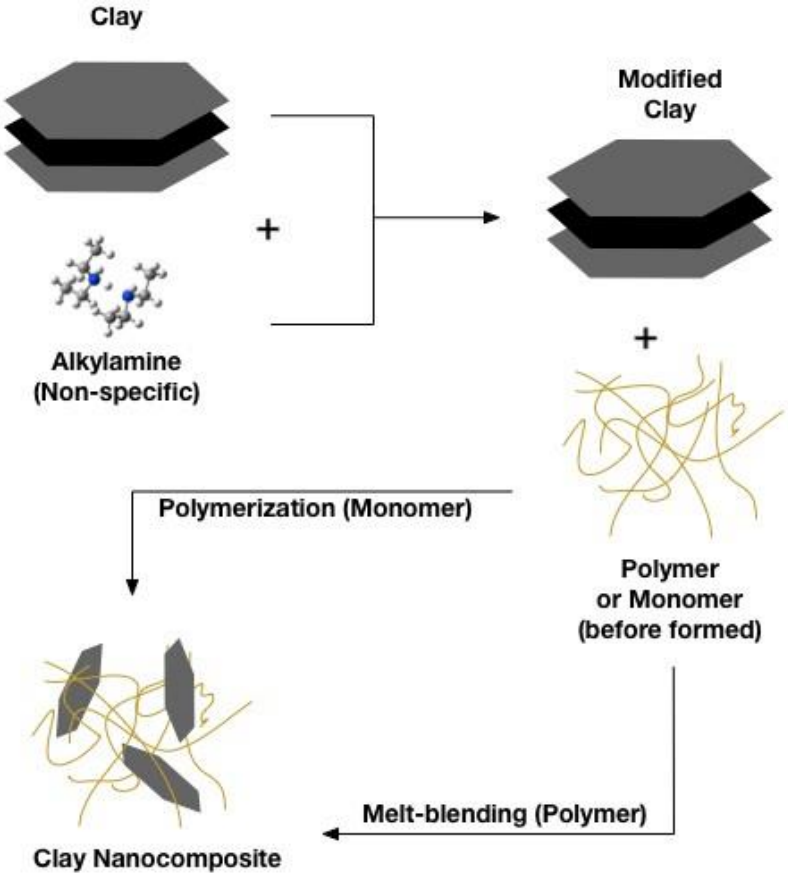

Figure 2.3 Intercalation Method

Sol-gel Method

This method contains three basic steps: hydrolysis, poly-condensation and drying. At first, the Alkoxide metal salt, solvent, water and catalyser are mixed, forming the Sol solution; under the effect of catalyser, the salt goes through hydrolysis and polycondensation reaction, which forms the gel state. The gel then goes through drying processes to form either the nanoparticles or a nanocomposite.

In the literature this process has been used to manufacture nanoparticles and composite materials made up of two phases of nanoscaled domains[92]. This material was referred to as a nanocomposite but the use is different from this area of work where a nanocomposite is regarded as nanoparticles distributed in a bulk polymer matrix. This method has also been used to generate a polymer based nanodielectric by manufacturing nanoparticles and polymer together through two parallel reactions. An example of this is reported in [68] where a silicone polymer Polydimethylsiloxane was

formed round various metal oxide nanoparticles. This combined process avoids the problems of aggregation in the nanocomposite

Direct Mixing Method

Direct mixing method is an easy method for manufacturing nanocomposite and is commonly used in epoxy and metal/silicon oxide nanocomposite research [56][65][93][94]. The problem with this method is that it is difficult to generate a well-dispersed and acceptable nanodielectric because the mixing process usually causes aggregation. The problems observed in early composites produced by mixing were avoided by the introduction of surface modification of the nanoparticles as described in Section 2.2.1.

This method usually contains two steps: stirring and ultrasonic treatment [95]–[97]. Stirring is used to ensure an acceptable dispersion of nanoparticles in the polymer although these particles may have become aggregated. The ultrasonic treatment is then used to break the aggregation and further disperse the particles. In the mixing step, Solvent may also be used to reduce the viscosity of the system to making the dispersion of particles easier[94][98]. This method seems to be effective and was adopted in this project by using acetone as solvent or media, since acetone can solve both materials and can be easily removed during degas process.

A degassing procedure is also generally required as the ultrasonic treatment and mechanical stirring can generate large amount of bubbles. This has also been observed by researchers using the intercalation and Sol-Gel methods. In dielectric materials for electrical insulation the presence of gas filled voids is generally to be avoided as they are a source of partial discharges and can trigger premature breakdown of the material. This makes degassing important, and it is a common process applied to the manufacture of epoxy resin insulators.

So the process of direct mixing method is a suitable combination of these steps for the matrix material. Figure 2.4 shows a direct mixing method with general process steps.

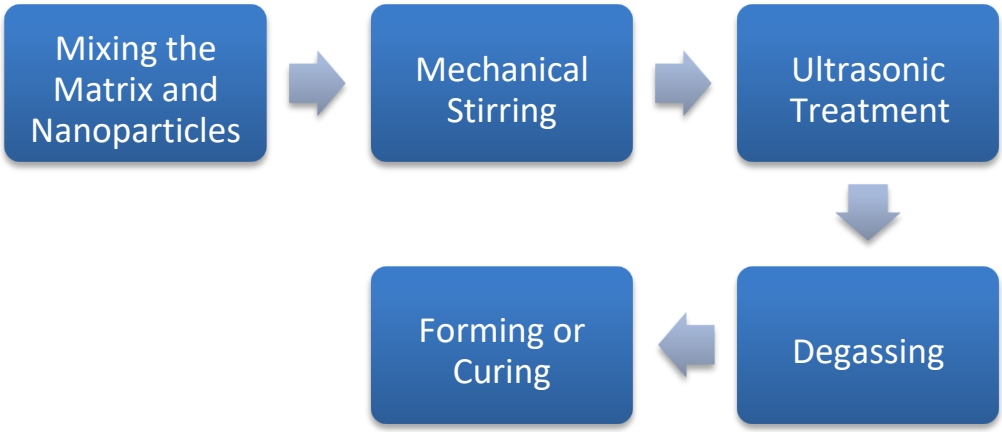

Figure 2.4 Direct Mixing Method

Comparison of these manufacture methods

These three methods are all used to produce nanocomposite. It is hard to compare these three methods, they all have advantages and disadvantages and the correct method will depend on material and application.

For nanoclay based composites the intercalation method seems to remain the most appropriate approach. The Sol-Gel method was used to generate nanocomposite films or sheets, it seems suitable for thermoplastic materials with inorganic salt nanofillers, but has these problems:

1. After the condensation stage of the process, a drying stage is required to remove the water and gas generated from the reactions. This will leave bubbles in the nanocomposite, which can impact the quality of the material.
2. Currently, the chemicals used in the sol-gel reactions are expensive. There can also be safety issues due to some of the organic material used in this method.
3. Producing a nanocomposite using the sol-gel method is slow and may take weeks.

Direct mixing is the least complicated method in terms of chemical processes. However the precise combination of the steps shown in Figure 2.4 needs to be established and depends on the matrix material the nanoparticle and the surface treatments.

To avoid the chemical processing required in the first two methods this project used the direct mixing. The matrix this project used is epoxy resin, the nanofillers were metal oxide nanoparticles which were assumed to be spherical by the manufacturer. The details of the epoxy resin and the nanoparticles used together with the mixing and curing processes developed will be discussed in Chapter 3.

2.2.5 Summary of Nanodielectrics

As an insulating material, nanodielectric can be widely used in power and electronic industry to replace the materials currently used. Since it has been proved that the dielectric properties of original used materials can be improved by adding nanofillers. In power industry, the thermoplastic materials are currently used as the cable insulating materials, wire and winding insulating material, bushings and as dielectrics in capacitors; thermosetting materials, for example epoxy resin is used as the insulating material of transformer, bushing and the circuit breakers in substations. For technical or economic reasons, thermoplastic and thermosetting materials were limited to these applications. But with the property modification that may be possible through the nanofillers, these materials can fulfil current applications better and find new applications extending their use.

However, there are still more research needed to be done on this area to complete the theoretical bases of the property changes, to discover more properties that can be modified and to identify optimal manufacturing techniques of nanodielectrics.

Section 2.3 will be introducing the basic knowledge of the Fractal dimension which is one of the optical properties calculated from the optical data for further analysis.

2.3 Fractal Dimension

Fractal is rather a new word that was first seen in 1975, Created by the Prof. Benoit B. Mandelbrot from Mathematic department of Harvard. In 1977 and 1982, two of his publications was widely regarded as the first introduction of the idea of fractal[99][100] . After these, the fractal theory was developed.

Although the word came late, the discussing about fractured dimension was appeared in Mandelbrot's paper published at 1967 about self-similarity of British coastline[101]. This case also became a good demonstration of idea about fractal dimension. Since it was introduced, the research and usage of Fractal dimension was expanded tremendously.

2.3.1 Application of Fractal Dimension

Since this idea was invented, Fractal dimension was quickly adopted by the mathematics, physicists and engineers to study and analyse complex geometry problems which they were trying to explain in Euclid terms before. It has been used in the areas of Brownian Motion[102], electrical treeing[103], electrical breakdown[104], the arrangement of array in phased array antenna[105] and many other areas.

The usage of fractal dimension theory currently can be summarized into four directions:

1. Using fractal theory to calculate the fractal dimension of real objects to analyze their properties and gather the information for direction 2. For example, calculating the fractal dimension of electrical trees [106], Lightening and discharging Modelling[107];
2. Using fractal theory for simulating or predicting the future development of a physical phenomenon, like the Brownian Motion [102]or electric tree growth and breakdown[99][97];
3. Using fractal theory to design a device which can improve the properties of the device; for example, the Sierpinski carpet antenna [105] and Fractal capacitor[108], these fractal designs can change the performance of these two components significantly [7][8][109]
4. Mathematic method to solve some problem (High impedance fault detection[110], load curve[111])

Fractal dimension is relevant to this project as surface discharge pattern are similar to fractal patterns. The shape of the surface discharge pattern under an extremely nonuniform electrical field of a combined insulating system is a Lichtenberg figure, also known as the lightening tree. Figure 2.5 shows the appearance of Lichtenberg

figure. Lichtenberg figures have referred to both surface discharges and breakdown inside solid insulating material. Researchers have calculated the fractal dimension of both surface and bulk discharges and used it as a parameter to describe the appearance of the discharge [112][113].

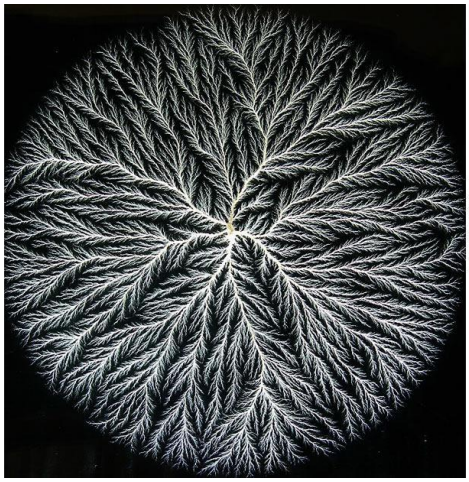

Figure 2.5 Lichtenberg figure [114]

2.3.2 Definition of Fractal Dimension

There is no uniform definition for fractal dimension; a general description is that it is a statistic which describes the scale of a fractal filling a space. For the definition of a fractal, in Euclidean geometry, the world people are living in is a three-dimension world. The dimension count was based on first one of Euclid's postulated: "To draw a straight line from any point to any point".

- One-dimension is a straight line, the length of the straight line is L;
- Two-dimension is a surface, measurement of the surface is area, kL^2, any point in this surface is give in two variables;
- Three-dimension is a bulk, the measure of the bulk is volume, kL^3, any point in this bulk is given in three variables;
- n- dimension object can be measure by kL^n

In Physics, higher dimensional geometries are considered; for example time has been added as a dimension, leading to a four dimensional system. Modern physics uses

much higher dimensions. In these geometries the number of dimensions is equal to the number of variables required to describe the geometry objects in the space. This means the number of dimension is an integer.

In 1890, Giuseppe Peano created a space-filling curve: Peano curve[115]. The curve is a self-similar shape and at its limit covers the area of an entire surface. Figure 2.6 shows three examples of a Peano curve covering more of the surface. At the limit any 2 dimensional point on this surface can be located using only one variable the distance along the curve from its origin. This curve causes a contradiction with the previous ideas of spatial dimension, as a surface is two-dimensional, that it should be described by two variables, but now it can be described by one variable.

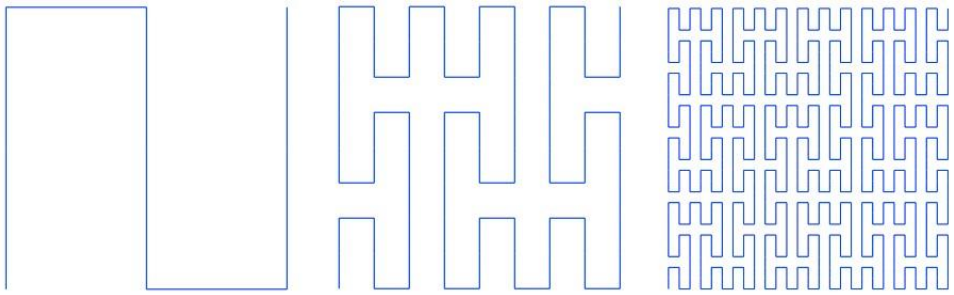

Figure 2.6 Peano Curve

To avoid this contradiction, a system called the similarity dimension is introduced. Under this system, the definition for the dimension of a line, a square, a cube and other high dimensional figures is a little different.

If a line is divided in half it becomes 2 self-similar lines. If the sides of a square are divided in half it becomes 4 self-similar squares. Dividing the sides of a cube in half leads to cube becomes 8 self-similar cubes, as shown in Figure 2.7. The number of self-similar objects produced is always a power of 2 for this halving operation. The index that 2 is raised 2 is 1 for a line, 2 for a square and 3 for a cube. These correspond to the expected Euclidean dimension. Under this system, the halving operation on a Peano curve filling a surface produces 4 self-similar Peano curves due to its fractal nature. Therefore the similarity dimension of the Peano curve is 2. The contradiction has disappeared. Halving is not inherent to the similarity dimension the same indices would be observed if a line a square and a Peano curve were divided into thirds.

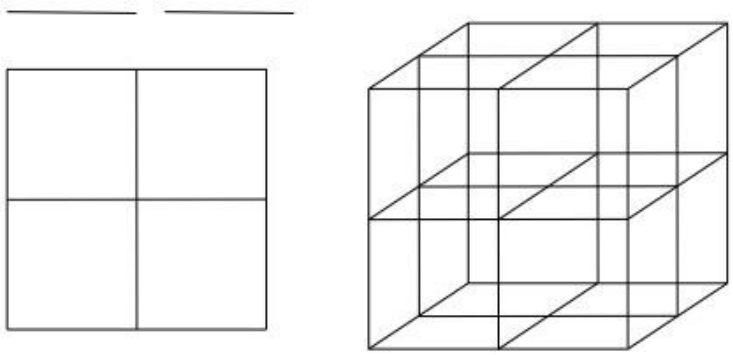

Figure 2.7 Divide objects of different dimension by halving the side.

From the description in last paragraph, in the similarity dimension system, for any figure that can be divided into self-similar figures, the dimension number can be written in Equation 2.2:

$$b = a^{D_s} \rightarrow D_s = \frac{\ln b}{\ln a} \tag{2.2}$$

Where b is the number of the smaller figures that can be divided from the original figure; a is the divisor of the variables, for example the unit length can be divided into 1/ a self-similar lengths; D_s is the resulting similarity dimension.

From this new system of dimension, the dimension number is not necessarily an integer. For example there is the Koch curve, shown in Figure 2.8. First described in [116]. By its generating rules, the Koch curve can be generated by repeatedly adding equilateral triangles of 1/3 the current dimension to a straight line. Applying the rules of similar dimension to a Koch curve results in its dimension being:

$$D = \frac{\ln 4}{\ln 3} \approx 1.2618$$

These non-integer similarity dimensions are referred to as fractal dimensions as fractal patterns such as the Mandlebrot set are self-similar.

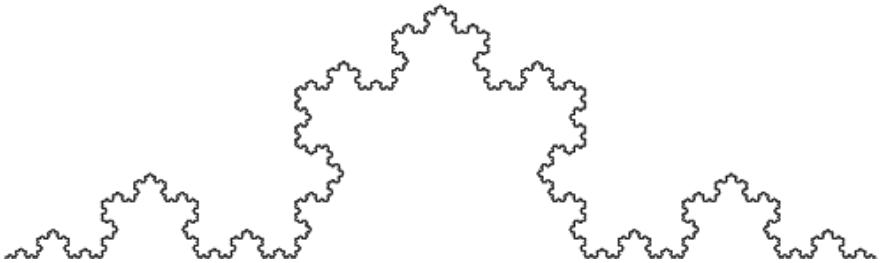

Figure 2.8 Koch Curve (adapted from [117])

Although the similar dimension has created a new way of defining the dimension of an object, there is a limitation. It can only be used to define a figure with strictly selfsimilar properties. It is not suitable for a random figure, which most of the figures or objects in nature are.

Many new systems have been developed based on the idea of similar dimension. One of them is Hausdorff dimension which calculates fractal dimension for self-similar objects but also allows a fractal dimension to be calculated for objects that are not self-similar. A line, figure or 3D object in nature under Euclid dimension can be considered as a set of points with Euclidean coordinates. Using the Hausdorff dimension, a line, figure and 3D object can also be consider as a set of points [118].

Assuming there is a line with the length of L, if a ruler of length r was used to measure it, the results would be according to Equation 2.3:

$$N(r) = \frac{L}{r} \tag{2.3}$$

The value of $N(r)$ was also shown to depend on r and the fractal dimension of selfsimilar objects as $r \to 0$ (Equation 2.4).

$$N(r) = r^{-D_H} \tag{2.4}$$

Applying natural logarithms to both sides, an approximation to the fractal dimension can be calculated using Equation 2.5:

$$D_H = \frac{\ln N(r)}{\ln(r^{-1})} \tag{2.5}$$

As r becomes smaller, the calculated value of Hausdorff dimension D_H comes closer to the actual fractal value. As displayed in Equation 2.6, the mathematic description of Hausdorff Dimension can be derived from the Equation 2.5:

$$D_H = \lim_{r \to 0} \frac{\ln N(r)}{\ln(r^{-1})} \tag{2.6}$$

The Hausdorff dimension was used by Mandelbrot in his definition of fractal behaviour [100]: In Euclidean space, if the Hausdorff dimension of a set defining an object is larger than its Euclidean dimension, the object is Fractal in nature. There is however no strict academic definition of a fractal. In[119], several classic properties was given for fractal:

1. Extremely Irregular that it is not easily described in traditional Euclidean geometric language
2. Usually with detailed structure, even in tiny scale.
3. Self-similarity

It is important to point out that fractal dimension alone is not enough to give the full information of a set of Euclidean points. If the fractal dimension of a set is 1.7, there is not enough information to determine whether this is a set of scattered points or an irregular line or solid.

2.3.3 Calculation of fractal dimension in practice

Based on the idea of the variable ruler used for the Hausdorff Dimension, the common practical method to calculate fractal dimension is box counting on box dimension. It is generally applied to two dimensional images so the boxes used are squares. The image is covered with a set of boxes of known dimension, and the number of boxes required is counted. The box side is then reduced, the image is covered in boxes again and a new box count value is determined. The dimension of the image is determined using Equation 2.7:

$$D(\delta) = \lim_{\delta \to 0} \frac{\log N(\delta)}{-\log \delta} \tag{2.7}$$

Where δ is the side length of each box, and $N(\delta)$ is the number of boxes with side δ required to cover the image.

Figure 2.9 shows how it works. The original image of this figure was a surface discharge event captured in this project. In (a), the discharge pattern was fully covered with boxes with side length of δ_1. Any area of the image where light was being emitted was covered with a box. The number of boxes N_1 (seven) and the side length of the box δ_1 was recorded for further calculation. In (b), the side length of the boxes δ_2 is $\delta_1/2$, and the image can be covered with N_2 (eighteen) boxes. In (c), the side length δ_3 is $\delta_1/4$, and the number of the boxes required to cover the discharge pattern N_3 is again found. The process of halving the box side goes on until it reaches the pre-set limit based on the size of a pixel in the image.

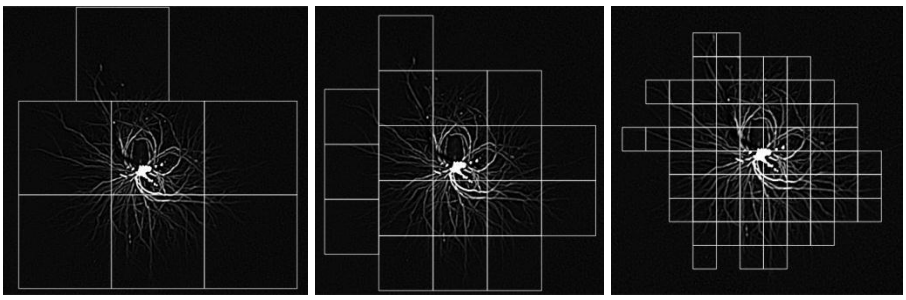

(a) (b) (c)

Figure 2.9 Box – Counting Method

From this box counting process, the relationship of N as a function of the box side length □ can be determined. The fractal dimension can be calculated from this data using Equation 2.7. As the box size does not reach the limit of $\delta \to 0$, in practice the gradient of a plot of $\frac{\log N(\delta)}{-\log \delta}$ is used to give an approximation of the fractal dimension.

Details of the calculation and programing method will be introduced in Chapter 5. In this project, the fractal dimension of surface discharge patterns was calculated in an

attempt to define the optical properties of the patterns. The results of this are reported in Chapter 6.

2.3.4 Concerns of Fractal Dimension

Although the fractal dimension has been used to describe various electric phenomena there can be problems with using fractal dimension to characterise breakdown. The first problem is using the fractal dimension of a 2D image to describe a 3D structure, the second is the technical limitation imposed by the image and the calculation method.

Misusage of Fractal dimension

In electrical tree or breakdown phenomenon, the tree branch is a three dimensional structure, all of the analysis reported used two dimensional images captured from a side direction of the event[119]. Strictly speaking the fractal dimension of a 3 dimensional figure would have values between 2 and 3. However as the researchers are limited to a 2 dimensional image the fractal dimensions quoted are always in the range of 1 to 2. There will be a relationship between the actual fractal dimension of the discharge and the measured, 2 dimensional value calculated from the image. It is expected that the 2D fractal dimension will increase as the 3D fractal dimension increases the precise relationship will depend on the shape of the discharge.

Attempts have been made to relate changes in fractal dimension to changes in the experimental system[120], [121]. However without knowledge of the relationship between the 2D and 3D fractal dimensions it is uncertain how useful these comparisons are.

Technical limitation

The fractal dimension value calculated is the slope of $\log N_\delta(P)/-log\delta$based on box counting which is the only practical method which can be easily used. Mathematically this will produce an accurate value of the fractal dimension of a true fractal figure, where the size of the measuring box can always be decreased and new features observed within the boxes. This leads to a straight line on the $\log N_\delta(P)/-log\delta$ plot with the theoretical fractal dimension being between 1 and 2.

In a discharge pattern, the image obtained is not truly fractal. This is because of the limit in the pixel size and also because the individual branches of the pattern are of finite size, that is there will be a minimum propagation length for the discharge on the surface. Therefore fractal values for images of discharge patterns based on box counting will always be an estimate. This means that the values of $\log N_\delta(P)/-log\delta$ do not lie on a straight line. Several methods can be used to get a value of fractal dimension: one is use the least square method to determine the best linear fit to the data and use the slope of the trend line as the fractal dimension; another method is to calculate the slope between adjacent data points and calculate their mean value which can be considered as the fractal dimension value, the second method is used in this project.

Figure 2.10 shows the $\log N_\delta(P)/-log\delta$ plot for one of the discharge measured in this project. The red dotted line shows a fractal dimension of 2 when the whole surface is covered, the blue points show the box-count result and the green line shows the slope associated with the calculated fractal dimension.

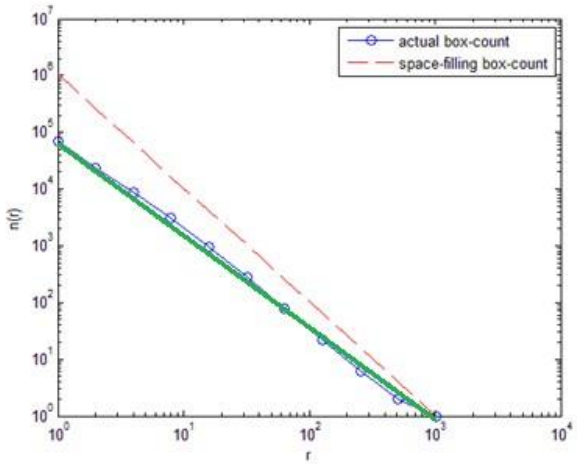

Figure 2.10 Box-count results plot

To test the validity of calculated values of fractal dimension a series of test figures based on a 1024 by 1024 array of pixels were created in Matlab. These test figures were larger than the images recorded in this project (648x 494)but the dimension was better suited for computation. A box counting algorithm was used to calculate fractal dimension. Figure 2.11 (a) is a straight line 1 pixel wide and 420 pixels long, the

calculated fractal dimension of this straight line was 0.9455 where the true value should be 1.

Figure 2.11 shows a series of patterns which are becoming more fractal and have an increasing number of branches. Fractal dimension was calculated using the box counting method for these patterns each branch was 1 pixel wide and the width of the pattern was fixed at 420 pixels. It can be seen that the derived fractal dimension increases as the figures become more branched.

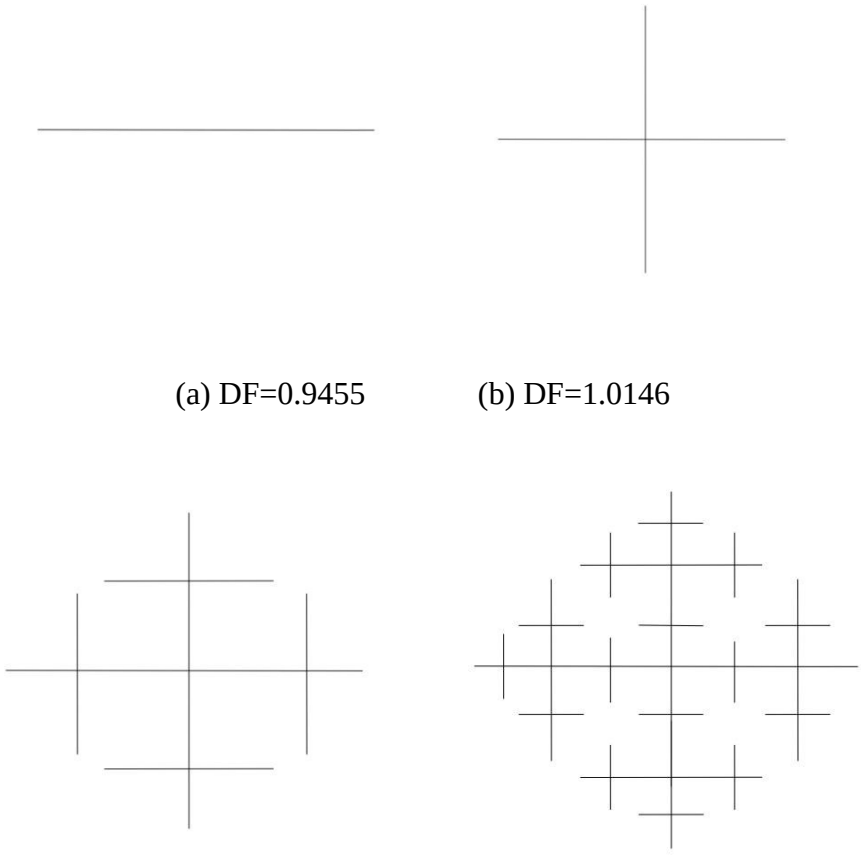

(a) DF=0.9455 (b) DF=1.0146

(c) DF= 1.1302 (d) DF= 1.2776

Figure 2.11 Demonstration of fractal dimension pixel dependency

This appears helpful as the changes in the complexity of the pattern leads to changes in the fractal dimension. However in these figures as the size of the image is fixed as the number of branches is increasing the number of pixels in the pattern is also

increasing. The changes in the fractal dimension are coming from the changes in the number of pixels. This leads to the situation in Figure 2.12 where two very different patterns give the same fractal dimension as they have the same number of pixels. Therefore the fractal dimension obtained by box counting does not necessarily describe the degree of branching in an image.

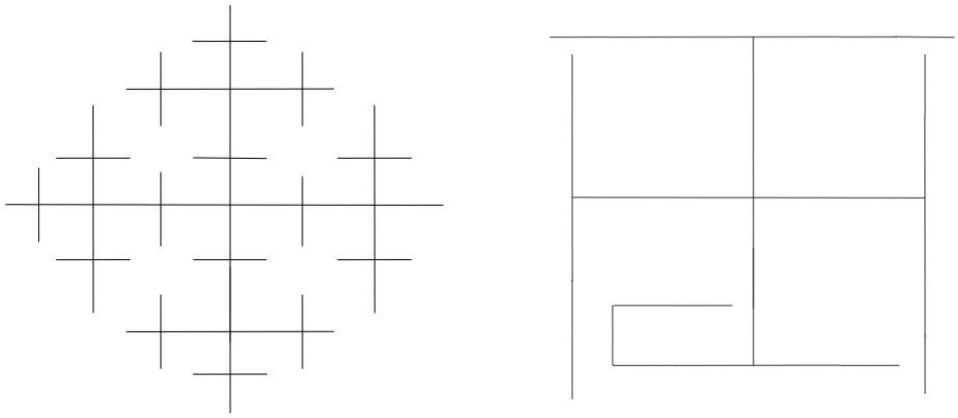

(a) DF=1.2776±0.2 (b) DF= 1.2776±0.39

Figure 2.12 Different discharge pattern with same pixel numbers

In addition, if the pattern in Figure 2.12 (a) was reduced in width while the total image size remained the same, although the fractal dimension of the image itself should not change, box counting resulted in a calculated fractal dimension of 1.17±0.19 for the smaller pattern compared with the value of 1.2776±0.2 obtained for the image in Figure 2.12 (a)

Using box counting methods on an image leads to a value of fractal dimension which describes: **How many pixels does a discharge pattern occupy in the whole image area.** The fractal dimension obtained by box counting is therefore proportional to:

$$Ratio(\%) = \frac{N_{dp}}{N_{total}} \times 100\%$$

Where $N_{dp}$is the pixel number that a discharge pattern took; N_{total} is the total pixel number of one image (pixel resolution).

The limitation of this method is obvious: the fractal dimension calculated strongly depends on the image resolution. Compared with this ratio method, fractal dimension should have clear advantages. As for a true fractal pattern the fractal dimension is only related to the shape of the pattern, the size of the image should no effect on the final result. But in reality, calculated fractal dimension for a non-fractal discharge pattern is strongly affected by the pixel resolution (in a sense, equal to the pixel size). Since the pixel size cannot be infinitely small, this advantage no longer applies.

This makes comparisons of the values obtained by different research groups difficult without an accurate definition of image sizes and pixel sizes. These problems could become more serious when reports are made of the fractal dimension of a 3 dimensional pattern based on a 2 dimensional image.

In this project as the surface discharge pattern could be assumed to be 2 dimensional rather than 3 dimensional the problems the first difficulty is not relevant. Despite the concerns about how the fractal dimension represents the shape of a discharge pattern, it does provide a method to quantify the discharge pattern with a number which can be used with a fixed and defined measurement system to investigate the optical behaviour of discharge patterns within this project. The values of fractal dimension calculated are specific to the test equipment used at Strathclyde.

2.4 Summary

In this chapter, the basic mechanisms of breakdown in liquid, solid and across liquid/solid interface have been reviewed; the factors that can influence the breakdown mechanisms were also discussed. Although the mechanisms yet need to be complete by further research, they have been adapted on modern insulation technics.

Nanoparticles bring new opportunities to the insulation technical research by influencing the properties of existing insulating materials, the newly formed nanocomposite have been proved to possess better properties which lead to more options for application of these insulations. The basic knowledge of the nanocomposites have been discussed in this chapter along with the possible manufacturing methods.

Fractal dimension which is used as an analysis technique has been discussed and methods of calculating the fractal dimension have been described. It has been used as a method of characterizing discharge patterns. The problems with calculating fractal dimension from an image have been discussed. It has been shown that using the accepted box counting methods radically different images will produce the same value of fractal dimension. It has also been shown that box counting will give different values of fractal dimension for self-similar patterns of different size. Within the limits of box counting the fractal dimension is strongly influenced by the pixel resolution. However changes in fractal dimension calculated will reflect in some way changes in the discharge pattern.

In Chapter 3, the methods developed in this project to produce nanocomposites will be described with detailed information on the epoxy resins chosen in the project, the nanoparticles employed and all the stages of the manufacturing processes.

References

[1] J. B. Whitehead and W. H. Macwilliams, “Temperature and electric stress in impregnated-paper insulation,” *Electr. Eng.*, vol. 61, no. 1, pp. 10–13, Jan. 1942.

[2] E. Asenjo and G. Eidelstein, “Paper - Oil Insulation - New Definition of Damage,” *IEEE Trans. Electr. Insul.*, vol. EI-13, no. 3, pp. 179–183, Jun. 1978.

[3] Y. Wang, J. Li, Y. Wang, and S. Grzybowski, “Electrical breakdown properties of oil-paper insulation under AC-DC combined voltages,” in *2010 IEEE International Power Modulator and High Voltage Conference*, 2010, pp. 115–118.

[4] J. S. T. Looms, *Insulators for High Voltages*, 1st Editio. The Institution of Engineering and Technology, 2006.

[5] M. P. Wilson, “IMPULSE BREAKDOWN OF LIQUID-SOLID,” 2011.

[6] X. Liang, *High Voltage Engineering (Chinese Edition)*, 1st Editio. BEIJING: Qing Hua university, 2003.

[7] A. Von Hippel, “Electric Breakdown of Solid and Liquid Insulators,” *J. Appl. Phys.*, vol. 8, no. 12, p. 815, Apr. 1937.

[8] M. Sparks, D. L. Mills, R. Warren, T. Holstein, A. A. Maradudin, L. J. Sham, E. Loh, and D. F. King, “Theory of electron-avalanche breakdown in solids,” *Phys. Rev. B*, vol. 24, no. 6, pp. 3519–3536, Sep. 1981.

[9] D. L. Pulfrey, “The electrical breakdown of solid dielectrics in non-uniform fields,” *J. Phys. D. Appl. Phys.*, vol. 5, no. 3, pp. 647–655, Mar. 1972.

[10] Z. Yan and D. Zhu, *High Voltage Insulation Technology (2)*. 2007.

[11] J. Kuffel and P. Kuffel, *High Voltage Engineering Fundamentals*. Newnes, 2000.

[12] P. H. F. Morshuis, “Degradation of solid dielectrics due to internal partial discharge: some thoughts on progress made and where to go now,” *IEEE Trans. Dielectr. Electr. Insul.*, vol. 12, no. 5, pp. 905–913, Oct. 2005.

[13] J.-P. Crine, “Electrical, chemical and mechanical processes in water treeing,” *IEEE Trans. Dielectr. Electr. Insul.*, vol. 5, no. 5, pp. 681–694, 1998.

[14] G. M. L. Sommerman, “Electrical Tracking Resistance of Polymers,” *Trans. Am. Inst. Electr. Eng. Part III Power Appar. Syst.*, vol. 79, no. 3, pp. 969–974, Apr. 1960.

[15] R. Sarathi, R. K. Sahu, and P. Rajeshkumar, “Understanding the thermal, mechanical and electrical properties of epoxy nanocomposites,” *Mater. Sci. Eng. A*, vol. 445–446, pp. 567–578, Feb. 2007.

[16] G. Raju, A. Katebian, and S. Z. Jafri, “Breakdown voltages of polymers in the temperature range 23°-250°C,” *IEEE Trans. Dielectr. Electr. Insul.*, vol. 10, no. 1, pp. 117–127, Feb. 2003.

[17] C. S. Richards, C. L. Benner, K. L. Butler-Purry, and B. D. Russell, “Electrical behavior of contaminated distribution insulators exposed to natural wetting,” *IEEE Trans. Power Deliv.*, vol. 18, no. 2, pp. 551–558, Apr. 2003.

[18] M. S. Naidu, *High Voltage Engineering*. Tata McGraw-Hill Education, 2009.

[19] K. C. Kao and J. H. Calderwood, “Effects of hydrostatic pressure, temperature and impurity on electric conduction in liquid dielectrics,” *Proc. Inst. Electr. Eng.*, vol. 112, no. 3, p. 597, 1965.

[20] J. J. Leckbee, R. D. Curry, K. F. McDonald, W. R. Cravey, G. Anderson, and S. Heidger, “Design, Modeling, and Verification of a High-Pressure Liquid Dielectric Switch for Directed Energy Applications,” *IEEE Trans. Plasma Sci.*, vol. 32, no. 5, pp. 1790–1798, Oct. 2004.

[21] P. Wedin, “Electrical breakdown in dielectric liquids-a short overview,” *IEEE Electr. Insul. Mag.*, vol. 30, no. 6, pp. 20–25, Nov. 2014.

[22] K. Yoshino, “Electrical Conduction and Dielectric Breakdown in Liquid Dielectrics,” *IEEE Trans. Electr. Insul.*, vol. EI-21, no. 6, pp. 847–853, Dec. 1986.

[23] J. Mason, “Disharges,” *IEEE Trans. Electr. Insul.*, vol. EI-13, no. 4, pp. 211–238, Aug. 1978.

[24] P. Maity, S. Basu, V. Parameswaran, and N. Gupta, “Degradation of polymer dielectrics with nanometric metal-oxide fillers due to surface discharges,” *IEEE Trans. Dielectr. Electr. Insul.*, vol. 15, no. 1, pp. 52–62, 2008.

[25] H. C. Miller, “Surface flashover of insulators,” *IEEE Trans. Electr. Insul.*, vol. 24, no. 5, pp. 765–786, 1989.

[26] R. J. Taylor, “Effect of permittivity matching on the flashover of solid/liquid interfaces,” *Proc. Inst. Electr. Eng.*, vol. 124, no. 10, p. 899, 1977.

[27] M. Anker, “Effect Of Test Geometry, Permittivity Matching And Metal Particles On The Flashover Voltage Of Oil/Solid Interfaces,” *IEEE Trans. Power Appar. Syst.*, vol. PAS-102, no. 12, pp. 3796–3802, Dec. 1983.

[28] X. Yi and Z. Wang, “The influences of solid surface on the propagation of creepage discharge in insulating liquids,” *IEEE Trans. Dielectr. Electr. Insul.*, vol. 22, no. 1, pp. 303–312, Feb. 2015.

[29] a. Beroual, L. Kebbabi, E. a. Al-Ammar, and M. I. Qureshi, “Analysis of creeping discharges activity at solid/liquid interfaces subjected to ac voltage,” *IET Gener. Transm. Distrib.*, vol. 5, no. 9, p. 973, 2011.

[30] E. Cherney and J. Cross, “Electric-Field Distortions at Solid-Liquid Dielectric Interfaces,” *IEEE Trans. Electr. Insul.*, vol. EI-9, no. 2, pp. 37–42, Jun. 1974.

[31] E. Kelley and R. Hebner, “Electrical Breakdown in Composite Insulating Systems: Liquid-Solid Interface Parallel to the Field,” *IEEE Trans. Electr. Insul.*, vol. EI-16, no. 4, pp. 297–303, Aug. 1981.

[32] R. . Seymour and R. D. Deanin, *History of Polymeric Composites*. VSP, 1987.

[33] Y. Kojima, A. Usuki, M. Kawasumi, A. Okada, T. Kurauchi, and O. Kamigaito, “One-pot synthesis of nylon 6–clay hybrid,” *J. Polym. Sci. Part A Polym. Chem.*, vol. 31, no. 7, pp. 1755–1758, Jun. 1993.

[34] T. J. Lewis, “Nanometric Dielectrics,” *IEEE Trans. Dielectr. Electr. Insul.*, vol. 1, no. 5, pp. 812–825, 1994.

[35] T. J. Lewis, “Interfaces and nanodielectries are synonymous,” in *Proceedings of the 2004 IEEE International Conference on Solid Dielectrics, 2004. ICSD 2004.*, 2004, vol. 2, pp. 792–795.

[36] T. J. Lewis, “Interfaces are the dominant feature of dielectrics at the nanometric level,” *IEEE Trans. Dielectr. Electr. Insul.*, vol. 11, no. 5, pp. 739–753, Oct. 2004.

[37] M. F. Frechette, M. Trudeau, H. D. Alamdari, and S. Boily, “Introductory remarks on nanodielectrics,” in *2001 Annual Report Conference on Electrical Insulation and Dielectric Phenomena (Cat. No.01CH37225)*, 2001, pp. 92–99.

[38] T. Imai, Y. Hirano, H. Hirai, S. Kojima, and T. Shimizu, “Preparation and properties of epoxy-organically modified layered silicate nanocomposites,” in *Conference Record of the the 2002 IEEE International Symposium on Electrical Insulation (Cat. No.02CH37316)*, 2002, pp. 379–383.

[39] J. K. Nelsons, J. C. Fothergill, L. A. Dissado, and W. Peasgood, “Towards an understanding of nanometric dielectrics,” in *Annual Report Conference on Electrical Insulation and Dielectric Phenomena*, 2002, pp. 295–298.

[40] T. Tanaka, M. Kozako, N. Fuse, and Y. Ohki, “Proposal of a multi-core model for polymer nanocomposite dielectrics,” *IEEE Trans. Dielectr. Electr. Insul.*, vol. 12, no. 4, pp. 669–681, Aug. 2005.

[41] T. J. Lewis, “Interfaces: nanometric dielectrics,” *J. Phys. D. Appl. Phys.*, vol. 38, no. 2, pp. 202–212, Jan. 2005.

[42] T. Tanaka, “Multi-core model for nanodielectrics as fine structures of interaction zones,” in *CEIDP ’05. 2005 Annual Report Conference on Electrical Insulation and Dielectric Phenomena, 2005.*, 2005, pp. 713–716.

[43] S. Raetzke and J. Kindersberger, “The Effect of Interphase Structures in Nanodielectrics,” *IEEJ Trans. Fundam. Mater.*, vol. 126, no. 11, pp. 1044–1049, Feb. 2006.

[44] S. Li, G. Yin, S. Bai, and J. Li, “A new potential barrier model in epoxy resin nanodielectrics,” *IEEE Trans. Dielectr. Electr. Insul.*, vol. 18, no. 5, pp. 1535–1543, Oct. 2011.

[45] T. Andritsch, R. Kochetov, P. H. F. Morshuis, and J. J. Smit, “Proposal of the polymer chain alignment model,” in *2011 Annual Report Conference on Electrical Insulation and Dielectric Phenomena*, 2011, pp. 624–627.

[46] Y. Huang, T. M. Krentz, J. K. Nelson, L. S. Schadler, Y. Li, H. Zhao, L. C. Brinson, M. Bell, B. Benicewicz, K. Wu, and C. M. Breneman, “Prediction of interface dielectric relaxations in bimodal brush functionalized epoxy nanodielectrics by finite element analysis method,” in *2014 IEEE Conference on Electrical Insulation and Dielectric Phenomena (CEIDP)*, 2014, pp. 748–751.

[47] M. Kuhn and H. Kliem, “A numerical method for the calculation of dielectric nanocomposites,” *IEEE Trans. Dielectr. Electr. Insul.*, vol. 17, no. 5, pp. 1499–1508, Oct. 2010.

[48] D. Pitsa and M. G. Danikas, “Modeling relative permittivity and electrical treeing in polymer nanocomposites,” *2013 IEEE Int. Conf. Solid Dielectr.*, pp. 832–835, Jun. 2013.

[49] T. Andritsch, R. Kochetov, P. H. F. Morshuis, J. J. Smit, and A. S. Vaughan, “Modeling of the permittivity of epoxy nanocomposites,” in *2013 Annual Report Conference on Electrical Insulation and Dielectric Phenomena*, 2013, pp. 722–725.

[50] D. Min, W. Wang, and S. Li, “Numerical analysis of space charge accumulation and conduction properties in LDPE nanodielectrics,” *IEEE Trans. Dielectr. Electr. Insul.*, vol. 22, no. 3, pp. 1483–1491, Jun. 2015.

[51] C. Calebrese, L. Hui, L. Schadler, and J. Nelson, “A review on the importance of nanocomposite processing to enhance electrical insulation,” *IEEE Trans. Dielectr. Electr. Insul.*, vol. 18, no. 4, pp. 938–945, Aug. 2011.

[52] S. Alapati and M. J. Thomas, “Electrical treeing and the associated PD characteristics in LDPE nanocomposites,” *IEEE Trans. Dielectr. Electr. Insul.*, vol. 19, no. 2, pp. 697–704, Apr. 2012.

[53] S. Raetzke, Y. Ohki, T. Imai, T. Tanaka, and J. Kindersberger, “Tree initiation characteristics of epoxy resin and epoxy/clay nanocomoposite,” *IEEE Trans. Dielectr. Electr. Insul.*, vol. 16, no. 5, pp. 1473–1480, Oct. 2009.

[54] M. Danikas and T. Tanaka, “Nanocomposites-a review of electrical treeing and breakdown,” *IEEE Electr. Insul. Mag.*, vol. 25, no. 4, pp. 19–25, Jul. 2009.

[55] Fuqiang Tian, Qingquan Lei, Xuan Wang, and Yi Wang, “Investigation of electrical properties of LDPE/ZnO nanocomposite dielectrics,” *IEEE Trans. Dielectr. Electr. Insul.*, vol. 19, no. 3, pp. 763–769, Jun. 2012.

[56] P. Preetha and M. Thomas, “AC breakdown characteristics of epoxy nanocomposites,” *IEEE Trans. Dielectr. Electr. Insul.*, vol. 18, no. 5, pp. 1526–1534, Oct. 2011.

[57] E. Belgaroui and a Kallel, “Space charge characterization in nano-dielectrics by the Thermal Step Method,” *2010 Annu. Rep. Conf. Electr. Insul. Dielectic Phenom.*, pp. 1–6, Oct. 2010.

[58] T. Andritsch, R. Kochetov, P. H. F. Morshuis, and J. J. Smit, “Dielectric Properties and Space Charge Behavior of MgO-Epoxy Nanocomposites,” in *International Conference On Solid Dielectrics*, 2010, pp. 5–8.

[59] R. J. Fleming, C. Manufacturing, and M. Technology, “Conductivity and Space Charge in LDPE Containing Nano- and Micro-sized ZnO Particles,” pp. 118–126, 2008.

[60] T. Tanaka, G. C. Montanari, and R. Mulhaupt, “Polymer nanocomposites as dielectrics and electrical insulation-perspectives for processing technologies, material characterization and future applications,” *IEEE Trans. Dielectr. Electr. Insul.*, vol. 11, no. 5, pp. 763–784, Oct. 2004.

[61] G. Iyer, R. Gorur, R. Richert, a. Krivda, and L. Schmidt, “Dielectric properties of epoxy based nanocomposites for high voltage insulation,” *IEEE Trans. Dielectr. Electr. Insul.*, vol. 18, no. 3, pp. 659–666, Jun. 2011.

[62] Q. Wang, G. Chen, and A. S. Alghamdi, “Influence of nanofillers on electrical characteristics of epoxy resins insulation,” *2010 10th IEEE Int. Conf. Solid Dielectr.*, vol. 9, pp. 1–4, Jul. 2010.

[63] J. Katayama, Y. Ohki, N. Fuse, M. Kozako, and T. Tanaka, “Effects of nanofiller materials on the dielectric properties of epoxy nanocomposites,” *IEEE Trans. Dielectr. Electr. Insul.*, vol. 20, no. 1, pp. 157–165, Feb. 2013.

[64] J. C. Fothergill, J. K. Nelson, and M. Fu, “Dielectric properties of epoxy nanocomposites containing TiO/sub 2/, Al/sub 2/O/sub 3/ and ZnO fillers,” in *The 17th Annual Meeting of the IEEE Lasers and Electro-Optics Society, 2004. LEOS 2004.*, 2004, pp. 406–409.

[65] S. Singha and M. Thomas, “Dielectric properties of epoxy nanocomposites,” *IEEE Trans. Dielectr. Electr. Insul.*, vol. 15, no. 1, pp. 12–23, 2008.

[66] N. Chalashkanov, S. Dodd, L. Dissado, and J. Fothergill, “Re-examination of the dielectric spectra of epoxy resins: bulk charge transport and interfacial polarization peaks,” *IEEE Trans. Dielectr. Electr. Insul.*, vol. 21, no. 3, pp. 1330–1341, Jun. 2014.

[67] J. Katayama, Y. Ohki, N. Fuse, M. Kozako, and T. Tanaka, “Effects of nanofiller materials on the dielectric properties of epoxy nanocomposites,” *IEEE Trans. Dielectr. Electr. Insul.*, vol. 20, no. 1, pp. 157–165, Feb. 2013.

[68] L. Banet, G. Camino, J. Castellon, H. Couderc, O. Dellea, N. Dreuilles, H. Eggenschwiler, M. F. Frechette, P. Fugier, F. Gao, G. Malucelli, R. Nigmatullin, T. Plyhm, I. Preda, M. D. Reading, S. Savoie, C. Schubert, H. Simon, S. Thompson, A.-F. Vaessen, C. V. Bouanga, and A. S. Vaughan, “Nano-structured hybrid sheets for electrotechnical high-power insulating applications: The sol-gel route,” in *2012 Annual Report Conference on Electrical Insulation and Dielectric Phenomena*, 2012, pp. 919–923.

[69] T. Andritsch, R. Kochetov, P. H. F. Morshuis, and J. J. Smit, “The complex permittivity of epoxy based nanocomposites with alumina and magnesium oxide fillers at very low temperatures,” in *2011 Annual Report Conference on Electrical Insulation and Dielectric Phenomena*, 2011, pp. 306–309.

[70] S. Li and G. Yin, “Investigation on the dielectric properties of nano- titanium dioxide - low density polyethylene composites,” in *International Conference On Solid Dielectrics*, 2010, no. 50625721, pp. 5–8.

[71] R. Kochetov, T. Andritsch, P. H. F. Morshuis, and J. J. Smit, “Anomalous behaviour of the dielectric spectroscopy response of nanocomposites,” *IEEE Trans. Dielectr. Electr. Insul.*, vol. 19, no. 1, pp. 107–117, Feb. 2012.

[72] T. Tanaka and T. Imai, “Advances in nanodielectric materials over the past 50 years,” *IEEE Electr. Insul. Mag.*, vol. 29, no. 1, pp. 10–23, Jan. 2013.

[73] J. K. Nelson, *Dielectric Polymer Nanocomposites*, 1st ed. Springer, 2010.

[74] C. Reed, “Polymer Nanodielectrics-Basic Concepts,” *IEEE Electr. Insul. Mag.*, vol. 29, no. 6, pp. 12–15, Nov. 2013.

[75] A. R. Conference, E. Insulation, D. Phenomena, J. K. Nelson, M. Ful, and U. Kingdom, “Dielectric Properties of Epoxy Nanocomposites containing TiOz, Ab03 and ZnO fillers,” no. type 1255, pp. 406–409, 2004.

[76] S. Singha and M. Thomas, “Dielectric properties of epoxy nanocomposites,” *IEEE Trans. Dielectr. Electr. Insul.*, vol. 15, no. 1, pp. 12–23, 2008.

[77] M. Musa, Y. Z. Arief, Z. Abdul-Malek, M. H. Ahmad, and A. A. A. Jamil, “Influence of nano-titanium dioxide (TiO_2) on electrical tree characteristics in silicone rubber based nanocomposite,” in *2013 Annual Report Conference on Electrical Insulation and Dielectric Phenomena*, 2013, pp. 498–501.

[78] Y. Lv, Y. Zhou, C. Li, K. Ma, Q. Wang, W. Wang, S. Zhang, and Z. Jin, “Nanoparticle effects on creeping flashover characteristics of oil/pressboard interface,” *IEEE Trans. Dielectr. Electr. Insul.*, vol. 21, no. 2, pp. 556–562, Apr. 2014.

[79] M. Kurirnoto, H. Watanabe, N. Hayakawa, M. Hanae, Y. Hoshina, and M. Takee, “Dielectric Properties of Epoxy/Alumina Nanocomposite Influenced by Particle Dispersibility and Filler Content,” in *The 9th International Conference on Properties and Applications of Dielectric Materials*, 2009, pp. 749–752.

[80] R. Kochetov, T. Andritsch, P. H. F. Morshuis, J. J. Smit, and A. Materials, “Dielectric Response and Thermal Conductivity of Epoxy Resin Filled with Nanoalumina Particles of Different Size in α , γ and δ Phase,” in *Annual Report Conference on Electrical Insulation and Dielectric Phenomena*, 2010, pp. 3–6.

[81] N. Jäverberg, H. Edin, P. Nordell, H. Hillborg, B. Azhdar, U. W. Gedde, and A. Materials, “Dielectric Properties of Alumina-filled poly (ethylene- co-butyl acrylate) Nanocomposites,” in *Annual Report Conference on Electrical Insulation and Dielectric Phenomena*, 2010, pp. 2–5.

[82] C. Green and A. Vaughan, “Nanodielectrics – How Much Do We Really Understand ?,” *IEEE Electr. Insul. Mag.*, vol. 24, no. 4, pp. 6–16, 2008.

[83] C. Mu-tian, D. Yue-fan, L. Yu-zhen, Z. Jian-quan, L. Xiao-xin, and L. Chengrong, “Effect of nanoparticles on the dielectric strength of aged transformer oil,” in *2011 Annual Report Conference on Electrical Insulation and Dielectric Phenomena*, 2011, pp. 664–667.

[84] O. Moscoso-Londono, D. Muraca, L. A. S. de Oliveira, K. R. Pirota, and L. M. Socolovsky, “The Effect of Coated Fe_3O_4Nanoparticles on Magnetic

Properties of Ferrogels Produced by Diffusion Route," *IEEE Trans. Magn.*, vol. 49, no. 8, pp. 4551–4554, Aug. 2013.

[85] X. Huang, L. Xie, K. Yang, C. Wu, P. Jiang, S. Li, S. Wu, K. Tatsumi, and T. Tanaka, "Role of interface in highly filled epoxy/$BaTiO_3$ nanocomposites. Part I-correlation between nanoparticle surface chemistry and nanocomposite dielectric property," *IEEE Trans. Dielectr. Electr. Insul.*, vol. 21, no. 2, pp. 467–479, Apr. 2014.

[86] Q. Li, *Nano Materials(Chinese Edition)*, 1st Editio. BEIJING: Chemistry and Application Technology Industry Pres, 2008.

[87] G. Cao and Y. Wang, *Nanostructures and Nanomaterials: Synthesis, Properties, and Applications*, 2nd editio. World Scientific, 2011.

[88] L. Pauling, *General Chemistry*, vol. 24. Courier Corporation, 2014.

[89] C. Rodriguez, M. Banobre-Lopez, Y. V. Kolen'ko, B. Rodriguez, P. Freitas, and J. Rivas, "Magnetization Drop at High Temperature in Oleic Acid-Coated Magnetite Nanoparticles," *IEEE Trans. Magn.*, vol. 48, no. 11, pp. 3307–3310, Nov. 2012.

[90] J. K. Nelson, *Dielectric Polymer Nanocomposites*. Boston, MA: Springer US, 2010.

[91] V. Mittal, "Polymer Layered Silicate Nanocomposites: A Review," *Materials (Basel).*, vol. 2, no. 3, pp. 992–1057, Aug. 2009.

[92] M. Tyagi, M. Kumari, R. Chatterjee, A.-C. Sun, and P. Sharma, "Electrical and Magnetic Properties of Multiferroic (1-x)$BiFeO_3$-x$CoFe_2O_4$ Nanocomposite Thin Films Derived by Sol-gel Proc," *IEEE Trans. Magn.*, vol. 50, no. 1, pp. 1–4, Jan. 2014.

[93] S. Zhao, H. Hillborg, E. Mårtensson, and G. Paulsson, "Evaluation of Epoxy Nanocomposites for Electrical Insulation Systems," in *Annual Report Conference on Electrical Insulation and Dielectric Phenomena*, 2010, pp. 2–4.

[94] P. Maity, S. Basu, V. Parameswaran, and N. Gupta, "Degradation of polymer dielectrics with nanometric metal-oxide fillers due to surface discharges," *IEEE Trans. Dielectr. Electr. Insul.*, vol. 15, no. 1, pp. 52–62, 2008.

[95] M. Kurimoto, H. Watanabe, K. Kato, M. Hanai, Y. Hoshina, M. Takei, and H. Okubo, "Dielectric Properties of Epoxy/Alumina Nanocomposite Influenced by Particle Dispersibility," *2008 Annu. Rep. Conf. Electr. Insul. Dielectr. Phenom.*, pp. 706–709, Oct. 2008.

[96] F. Hussain, “Review article: Polymer-matrix Nanocomposites, Processing, Manufacturing, and Application: An Overview,” *J. Compos. Mater.*, vol. 40, no. 17, pp. 1511–1575, Jan. 2006.

[97] Z. Li, K. Okamoto, Y. Ohki, and T. Tanaka, “The role of nano and micro particles on partial discharge and breakdown strength in epoxy composites,” *IEEE Trans. Dielectr. Electr. Insul.*, vol. 18, no. 3, pp. 675–681, Jun. 2011.

[98] W. Yan, B. T. Phung, Z. J. Han, and O. K, “Surface insulation performance of epoxy resin□silica nanocomposite material,” in *Electrical Insulation Conference*, 2011, pp. 235–239.

[99] P. Campbell and S. Abhyankar, “Fractals, form, chance and dimension,” *Math. Intell.*, vol. 1, no. 1, pp. 35–37, Mar. 1978.

[100] B. B. Mandelbrot, *The Fractal Geometry of Nature*. Henry Holt and Company, 1983.

[101] B. Mandelbrot, “How long is the coast of britain? Statistical self-similarity and fractional dimension.,” *Science*, vol. 156, no. 3775, pp. 636–8, May 1967.

[102] P. Zhang, H. Barad, and A. Martinez, “Fractal dimension estimation of fractional Brownian motion,” in *IEEE Proceedings on Southeastcon*, 1990, pp. 934–939.

[103] K. Kudo, “Fractal analysis of electrical trees,” *IEEE Trans. Dielectr. Electr. Insul.*, vol. 5, no. 5, pp. 713–727, 1998.

[104] S. Fujimori, “Fractal properties of breakdowns,” *Proceedings., Second Int. Conf. Prop. Appl. Dielectr. Mater.*, pp. 519–522, 1988.

[105] M. F. A. Kadir, A. S. Ja’afar, and M. Z. A. A. Aziz, “Sierpinski carpet fractal antenna,” in *2007 Asia-Pacific Conference on Applied Electromagnetics*, 2007, pp. 1–4.

[106] K. Kudo, “Fractal analysis of electrical trees,” *IEEE Trans. Dielectr. Electr. Insul.*, vol. 5, no. 5, pp. 713–727, 1998.

[107] J. Li, Q. Yang, W. Sima, C. Sun, T. Yuan, and M. Zahn, “A new estimation model of the lightning shielding performance of transmission lines using a fractal approach,” *IEEE Trans. Dielectr. Electr. Insul.*, vol. 18, no. 5, pp. 1712–1723, Oct. 2011.

[108] H. Samavati, A. Hajimiri, A. R. Shahani, G. N. Nasserbakht, and T. H. Lee, “Fractal capacitors,” *IEEE J. Solid-State Circuits*, vol. 33, no. 12, pp. 2035–2041, 1998.

[109] D. H. Wqrner and S. Ganguly, “An overview of fractal antenna engineering research,” *IEEE Antennas Propag. Mag.*, vol. 45, no. 1, pp. 38–57, Feb. 2003.

[110] A. V. Mamishev, B. D. Russell, and C. L. Benner, “Analysis of high impedance faults using fractal techniques,” *IEEE Trans. Power Syst.*, vol. 11, no. 1, pp. 435–440, 1996.

[111] C. Liu and D. Li, “The Chaos and Fractal Characteristics and Predication of Shearer Load Power,” in *2010 International Conference on Electrical and Control Engineering*, 2010, pp. 5696–5699.

[112] a. Beroual, V. H. Dang, M. L. Coulibaly, and C. Perrier, “Investigation on creeping discharges propagating over pressboard immersed in mineral and vegetable oils under AC, DC and lightning impulse voltages,” *IEEE Trans. Dielectr. Electr. Insul.*, vol. 20, no. 5, pp. 1635–1640, 2013.

[113] H. Ding and B. R. Varlow, “Electrical treeing studies on the Araldite LYMY 5052 epoxy resin over a wide range of stressing voltage,” pp. 306–309, 2004.

[114] B. Hickman, “Captured Lightning: fractal-like Lichtenberg figures frozen in acrylic blocks,” *The Telegraph*, 2009.

[115] G. Peano, “Sur une courbe, qui remplit toute une aire plane,” *Math. Ann.*, vol. 36, no. 1, pp. 157–160, Mar. 1890.

[116] H. Von Koch, “Sur une courbe continue sans tangente obtenue par une construction geometrique elementaire,” *Ark. för Mat.*, vol. 1, Jan. 1904.

[117] Fibonacci, “Koch curve. svg,” *Wikipedia*, 2007. [Online]. Available: https://commons.wikimedia.org/wiki/File:Koch_curve.svg. [Accessed: 01-Jan2015].

[118] L. Dong, “Fractal Theroy and Applications.” Liaoning ke xue ji shu chu ban she, Shenyang Shi :, 1991.

[119] K. Falconer, *Fractal Geometry: Mathematical Foundations and Applications*. John Wiley & Sons, Ltd., 2003.

[120] L. Kebbabi and a Beroual, “Fractal analysis of creeping discharge patterns propagating at solid/liquid interfaces: influence of the nature and geometry of solid insulators,” *J. Phys. D. Appl. Phys.*, vol. 39, no. 1, pp. 177–183, Jan. 2006.

[121] a. Beroual, “Fractal analysis of lightning impulse surface discharges propagating over pressboard immersed in mineral and vegetable oils,” *IEEE Trans. Dielectr. Electr. Insul.*, vol. 20, no. 4, pp. 1402–1408, Aug. 2013.

[122] L. Niemeyer, L. Pietronero, and H. J. Wiesmann, “Fractal Dimension of Dielectric Breakdown,” *Phys. Rev. Lett.*, vol. 52, no. 12, pp. 1033–1036, Mar. 1984.

3. SAMPLE MANUFACTURE

As epoxy based nanocomposites are fairly new materials; therefore commercial samples cannot be purchased. In order to run this project, the nanocomposites will have to be made in the lab. This chapter will introduce the detail of relevant material and the development of the methods used to manufacture epoxy resin based nanocomposites.

Section 3.1 will introduce the basic knowledge of epoxy resin that includes the identification of epoxy resin; basic categories of different resins and the properties associated with them, especially their electrical properties which are most relevant to this project.

Section 3.2 describes the specific materials that were actually used in this project. The reason for choosing these materials will be stated. Molecular formula and the chemical reaction mechanism of the matrix materials will be described. The additive nanoparticles will also be described.

Section 3.3 describes in detail the procedures developed for processing and manufacturing samples.

3.1 Introduction of Epoxy Resin

3.1.1 What are Epoxy Resins?

Epoxy resin is a name derived from epoxide, which stands for a three-part oxide ring structure in chemistry; it contains one oxygen atom and two carbon atoms linked in triangle structure[1]. The most simply epoxide compound is ethylene oxide, Figure 3.1 shows its molecular structure.

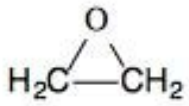

Figure 3.1 Ethylene Oxide

The actual definition of epoxy resin is a type of compound that has at least two epoxide group per molecule and will form a 3D cross-linked network solid by reaction with certain compounds[2], [3], generally referred to as hardeners.

3.1.2 Types of Epoxy Resin

Because the definition of epoxy resin is relatively broad, there are many organic compounds that fall into this category; therefore, it is hard to classify epoxy resins. Base on the operating complexity, there are three widely accepted standards:

1. Chemical Structure
2. Chemical State
3. Chemical reaction for manufacturing

Glycerol triglycidyl ether Epoxy Resin

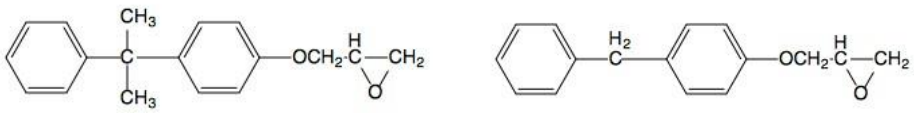

(a) Bisphenol A (b) Bisphenol F

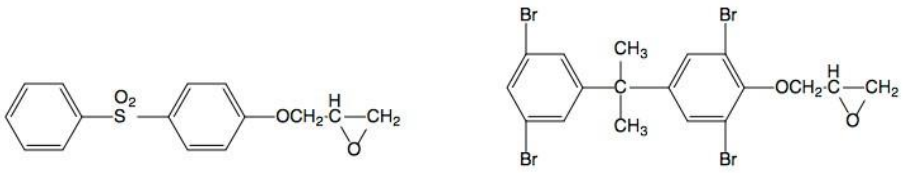

(c) Bisphenol S (d) Brominated Epoxy Resin

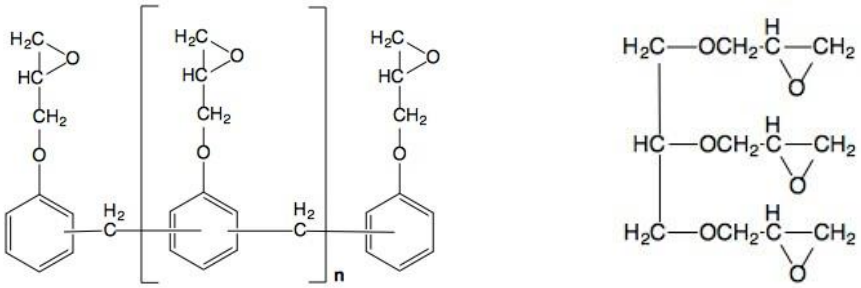

(e) Phenolic Epoxy Resin (f) Aliphatic Epoxy Resin

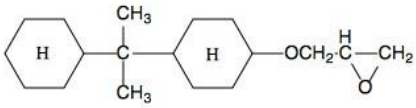

(g) Hydrogenated Bisphenol

Cycloaliphatic Epoxy Resin

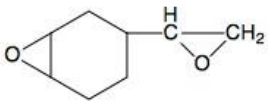

Figure 3.2 Structure of Epoxy Resin

Chemical structure is the most convenient standard for predicting the chemical and mechanical properties of epoxy resins; it is also the most diverse standard, because there are so many types. Base on chemical structure, epoxy resin compounds can be separated to six types. Among these, two types are most commonly used as electrical insulators. These are: Glycerol triglycidyl ether Epoxy Resin and Cycloaliphatic Epoxy Resin. The chemical structures of these two types of resin are shown in Figure 3.2.

In first type, Bisphenol-A is widely researched for insulation system [4]–[8]. Later research and practice show that Bisphenol-A and F can be mixed with phenolic epoxy resin (ENP) and (ECN) and that the mixture showed better mechanical properties while maintaining the same electrical and dielectric properties[2]. In recent year, cycloaliphatic epoxy resin have been shown to have useful properties as an insulator material[9][10], but the viscosity of cycloaliphatic epoxy is usually high, therefore it is not appropriate to use as a matrix material for new polymer composite.

3.1.3 Properties of Epoxy resin system

Epoxy resin is normally in liquid state with respect to the viscosity. By adding in Amine or Anhydride type compounds, it will go through a curing process and become a solid material. The details of the curing reaction for the resin and hardener used in this project are given in Section 3.2.1. The cured compound that results will usually show good mechanical, electrical, and thermal properties. For selecting the material that will be using in this project, the electrical and thermal properties were considered to be most important.

There are also some other properties regarding the epoxy resin and hardener before curing has taken place that need consideration: the molecular weight; the viscosity the gel point were the resin can no longer flow and the related pot lifetime. In the manufacture of nanocomposite samples viscosity and pot lifetime are important factors.

- **Viscosity**: viscosity is an important property for handling epoxy, especially for making composites. The majority of nanoparticle fillers are not readily miscible; higher viscosity will make the mixing process even harder. In addition with nanocomposites, because the aggregation of nanoparticles may occur, again a low viscosity is useful. The viscosity can be reduced by heating the epoxy, but since heating the epoxy resin system will also accelerate the curing process, this method has to be used carefully.

- **Pot lifetime:** is the time for which the epoxy resin system remains in a liquid state after the hardener has been added. To achieve a good dispersion of the nanoparticles in the epoxy several procedures have to be followed, mixing,

degassing and sample moulding. The pot life is therefore important and needs to be relatively long (at least 5 hours).

The selection of the epoxy resin therefore was based on the following:

- Good electrical and thermal properties
- Low viscosity
- Relatively long pot life

3.2 Experiment Materials

The material chosen as the matrix the nanocomposites is LY/HY5052 (Huntsman co.). From the data sheet the epoxy and hardener are mixed in a ratio of 100:47 by volume. The dielectric and electrical properties of this Epoxy Resin/ Hardener system have been established by several research groups. In addition it has been used in investigations of electrical treeing and surface flashover [11][12][13][14], [15]. Besides the data available on this system, there are some other factors for using these compounds:

1. The viscosity of this system is lower than most of the epoxy resins (viscosity of resin/hardener mixture: 500-700 Pa□s, typical value for epoxy resin: 100065000 Pa□s)[16], [17], which makes the mixing process easier and as was mentioned before, the viscosity can have a strong effect on the dispersion of the nanofiller.
2. The curing period of LY5052/HY5052 Epoxy Resin system is relatively long, it remains liquid for about five and half hours after curing has started, which provides enough time to do all the necessary processes to ensure a well dispersed nanocomposite sample without gas bubbles or other flaws.

Although there are resin systems with lower viscosities than LY/HY5052 they have much shorter pot lifes which makes them unsuitable.

3.2.1 Molecular Formula and Chemical reaction Mechanism of Matrix

LY5052 contains two chemical compounds:

a) Epoxy phenol novalok resin (32-45% composition)
b) Butanedioldiglycidyl ether (55-68% composition).

HY5052 consist of three compounds:

c) 2,4,6-tris (dimethylaminomethyl) phenol,
d) 3-(Aminomethyl)-3,5,5-trimethylcyclohexanamine also known as Isophorone diamine
e) 2,2-dimethyl-4,4-methylnebis (cyclohexylamine).

The molecular formula of LY/HY5052 is shown in Figure 3.3: [18]:

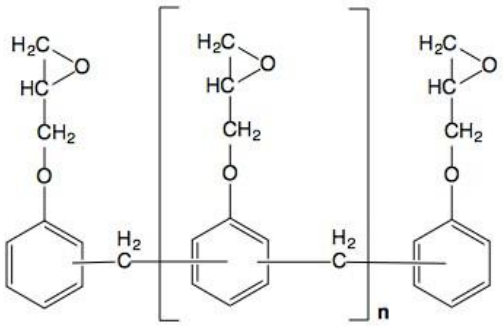

(a) Epoxy phenol novalok resin

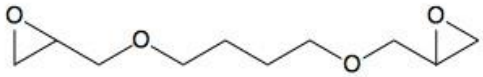

(b) Butanedioldiglycidyl ether

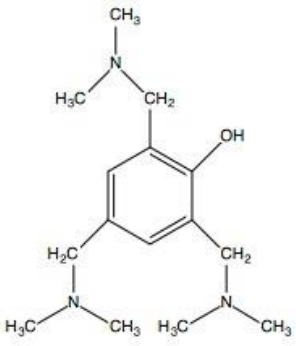

(c) 2,4,6-tris (dimethylaminomethyl) phenol

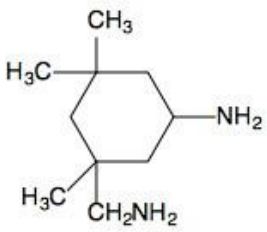

(d) Isophorone diamine

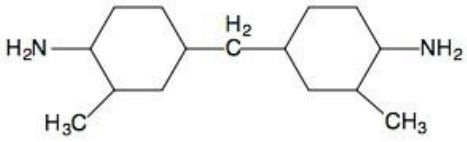

(e) 2, 2-dimethyl-4,4-methylnebis (cyclohexylamine)

Figure 3.3 Chemical structure of LY/HY5052 Epoxy Set

The principle of the chemical reactions is ring-opening reaction between amidogen and epoxide group in each molecules. The chemical equation displayed in Figure 3.4 demonstrates this reaction:

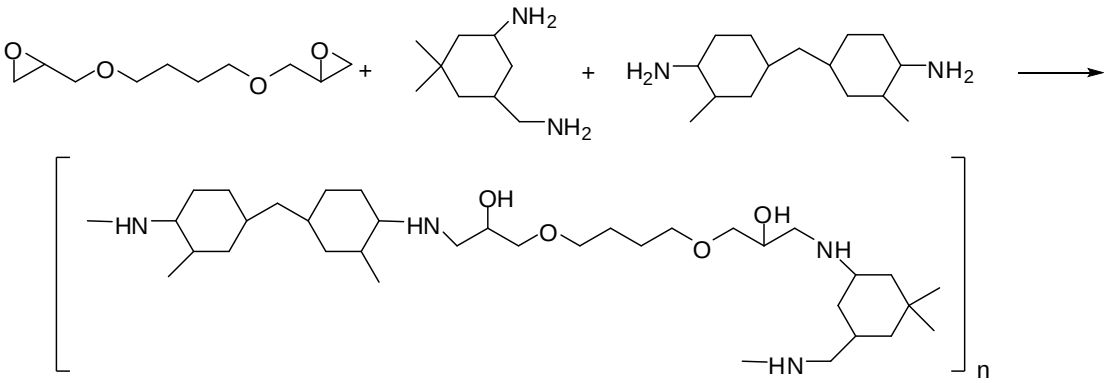

Figure 3.4 Basic Chemical reaction of Curing Process of Epoxy Resin

Here it can be seen that the epoxide rings at the end of Butanedioldiglycidyl molecule have reacted with the NH_2 groups associated with an Isophorone diamine and a cyclohexylamine molecules. The reactions between the epoxide rings and the amidogen groups leads to the formation of a crosslinked three dimensional network resulting in a solid material.

3.2.2 Nanoparticles

As mentioned in the introduction, the nanoparticles chosen for use in this project were ZnO and Al_2O_3. As described in Section 2.2, the influence of these nanoparticles on properties such as thermal conductivity, permittivity and loss tangent have been reported extensively for different matrix materials [19]–[25]. These previous experiments have established a base line for the effects of the nanoparticles on basic

properties of the insulator. However no work had been reported at the start of this project on their influence on surface breakdown behaviour.
This was the main reason for choosing these two nanoparticles.

In previous experiments, nanoparticles have mostly been introduced into the polymer matrix in powder form[26]. But in this project it was decided to see if it was possible to start with nanoparticles that were already dispersed in a solution. There are advantages in choosing solutions over powders:

1. The nanoparticles start in a dispersed state which may not be the case for nanoparticles in powder form.
2. The solutions used, provided by Sigma Aldrich contained particles that had been surface modified to prevent aggregation. This should also minimize or prevent aggregation of the particles once mixed with epoxy resin
3. It has been reported that it is easier to add the nanoparticles to an epoxy resin when a nanopowder was added to a hardener/ acetone mixture [27].

Three solutions of nanoparticles were used in this work:

ZnO solution (50 wt% in water) is a Sigma-Aldrich Product (721077-100G), average particle size is less than 35 nm, surface modification type: cationic - 3Aminopropyl triethoxysilane; (this solution was used in the early stages of the manufacturing process, but the number of successfully-produced samples was too low. This is probably due to the fact that water cannot mix well with resins. Even with the acetone involved, there is still a high chance that the nanoparticles will aggregate).

ZnO solution (40 wt% in ethanol) is a Sigma-Aldrich Product (721085-100G), average particle size is less than 35 nm, surface modification type: polymericalkyl ammonium salt of a polymer.

Al_2O_3 solution (20 wt% in isopropanol) is also Sigma-Aldrich Product (702129100G), average particle size is less than 50 nm, particles are not surface modified, the good dispersion is maintained by adding a dispersant (proprietary).

3.3 Sample Preparation

For surface breakdown measurements a relatively thick sample with thickness of 10 mm was required. The area of the samples also had to be relatively large; diameter of the sample is 85 mm. These requirements meant that the material had to be made in the lab. This sections will introduce the development of a method to manufacture epoxy resin based nanocomposite samples.

3.3.1 Principle of treatment

For epoxy resin based nanocomposite, the conventional way of manufacture methods are Sol-Gel [28]–[30]and direct mixture[24], [31]–[33]. These two methods represent two different ideas:

- **Sol-Gel** method: This method manufactures the nanoparticles and nanocomposite at same time. It generated the nanoparticles inside the matrix material, so good dispersion is easily achieved.
- **Direct mixture** method: Using manufactured nanoparticle directly, nanoparticles will be added into the matrix material through solvent or a high shear mixer.

Although the Sol-Gel method can generate nanocomposite in a reliable dispersion, it is not suitable for this project. The reasons are following[34]:

1. The chemical processes require long reaction times. It normally last several days, even weeks. It is hard to keep the epoxy resin in liquid state for that long.
2. This method requires chemical processing out with the skills of the research group. In addition the chemical components requires are expensive and in several cases toxic.

In this project, direct mixture is more suitable. Figure 3.5 shows the step in conventional method. Because the nanoparticles do not need to be made, the manufacture period depends on the curing time of epoxy resin, which is no longer than 30 hours. The disadvantage of this method comparing to Sol-Gel is achieving good dispersion. In order to achieve a relatively good dispersion, there are two problem needed to be solved: van der Waal's Forces (described in Section 2.2) and Viscosity.

- The role of van der Waal's forces on aggregation has been discussed in Section 2.2
- The higher the viscosity the harder it becomes to ensure a good distribution of the nanoparticles, as it becomes more difficult for the particles to move in the resin and achieve separation.

Ultrasonic treatment has the ability to overcome the effect of van der Waal's force[36], it can be introduced into the mixture process. Viscosity is a mechanical property of epoxy resin. The LY/HY 5052 system is a low viscosity epoxy resin system. The viscosity can also be reduced by several methods, like heating the resin, adding in solvent (alcohol, acetone, etc.).

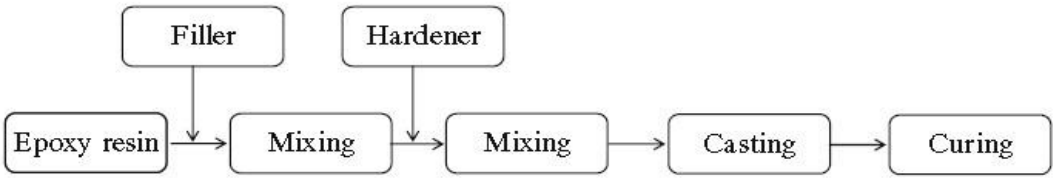

Figure 3.5 Conventional procedures for direct mix filler with epoxy resin

3.3.2 Mould Design

Both resin and hardener is in liquid state; after the mixture, a suitable container is needed to hold the resin in the desired shape while it went through degassing and the curing reaction. The requirement for a suitable mould is following:

1. The sample geometry required is a disc, the sizes are: 1 cm thickness; 8.5 cm as diameter.
2. Epoxy resin is strongly adhesive; the mould must allow the sample to be easily removed after the curing process is finished.
3. The curing processing of epoxy is an exothermic reaction in addition elevated temperatures can be used during curing to increase the curing rate. The mould will need to stay rigid under these conditions of temperature.

4. Good surface condition of the sample is also required; one of the parameters which has influence on surface discharge behaviour is surface condition.

3.3.2.1 Initial Mould Design

The first mould designed was a horizontal one, main material is Nylon; the basic geometry is showing in Figure 3.6 and Figure 3.7.

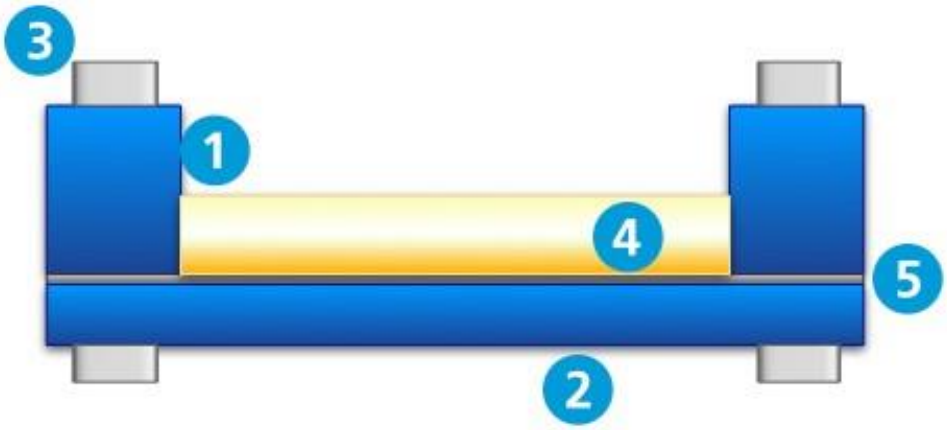

Figure 3.6 First mould

- Component.1 is the side wall of the mould, made of nylon
- Component. 2 is the bottom of the mould, also made of nylon. Three sections of nylon studding labelled 3 in the diagram were mounted on this component to allow the sections of the mould to be held together
- Component 4 is the space to be occupied by the epoxy sample
- Component 5 is a thin acetate sheet, as a separator between sample and the bottom of the mould.

The acetate sheet was used in this mould to prevent adhesion between the sample and the mould base and also to achieve a good surface finish on the sample. It was found that the epoxy used did not bind to the acetate sheet. There is also a layer of vacuum greace between sample and the sidewall to prevent adhesion.

The procedure of using this mould was as follows:

- Component 1 which forms the side wall of the mould was turned upside down.
- A thin layer of vacuum grease was applied to inner surface of the side wall to prevent adhesion between the sample and the mould.

- Vacuum grease was also applied to the surface of component 1 which would be in contact with the acetate sheet. This was done to ensure a good seal between this component and the acetate sheet.
- A circular piece of acetate sheet with a diameter of 90 mm was then placed on top of this layer of vacuum grease and lightly pressed into place
- The Sidewall and acetate sheet, were then turned over and placed on top of the mould base using the studding to align the components. Nuts were used on the studding to compress the components and to ensure a good seal.
- A pre-calculated volume of epoxy hardener mixture with nanoparticles as required was poured into the central well of the mould.
- The mold and epoxy was then placed in a vacuum chamber (0.2 bar absolute). The samples were left under this vacuum for one hour to remove any gasses or volatile liquids that had been introduced into the resin during mixing with nanoparticles.
- Once the vacuum treatment had been completed the sample was left to cure for a period of 24 hours under room temperature (20 °C).

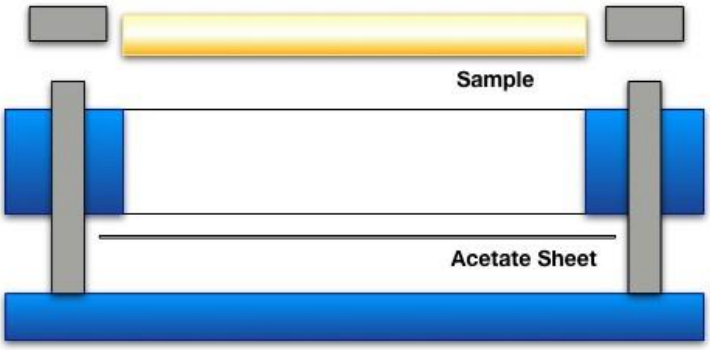

Figure 3.7 Assembled First Mould

The thickness of the sample is pre-calculated by Equation 3.1, where *V* is the volume of the mixed epoxy liquid; *A* is the area of the experimental surface; *d* is the thickness of the sample.

$$V = A \cdot d \tag{3.1}$$

This mould was found to be unsuitable for several reasons:

The surface condition of the samples was generally poor. Although the open design should have allowed easy degassing of the sample and it was assumed that surface tension and gravity would produce a smooth upper surface[37]. After the vacuum treatment: pitting was observed on the surface of the samples where bubbles had burst and frequently intact gas bubbles were found close to the sample surface.

Because of the open nature of the mould, the samples were easily contaminated with dust and other foreign bodies during the curing process even with an acetate sheet cover during the curing.

There were problems in achieving uniform thickness between samples due to difficulties in transferring the entirety of the measured volume of epoxy into the mould.

The nylon studding and nuts used to clamp the samples together tended to soften at the elevated temperatures (100 °C) during curing.

3.3.2.2 Vertical mould design

Based on the experience of first design, second mould was designed as a vertical one, where the diameter of the disc being modelled was vertically orientated.

Figure 3.8 and Figure 3.9 show the basic geometry of this mould: This was not designed to create a disc shaped sample but rather to produce a blank from which a disc shaped sample could be cut. The detailed final design of this mould are shown in Appendix A.

The advantages of this design were that:

1. The surfaces where surface tracking will occur are in contact with acetate sheets, surface condition should therefore be good and contamination avoided;

2. Because of the orientation of the mould during degassing, gas bubbles will tend to move towards the edge of the sample rather than the surfaces were surface tracking will occur. Even if the bubbles are not completed removed they will be in a region of the epoxy that would be cut away from the sample region.
3. The sample thickness is fixed by the dimensions of a spacer.

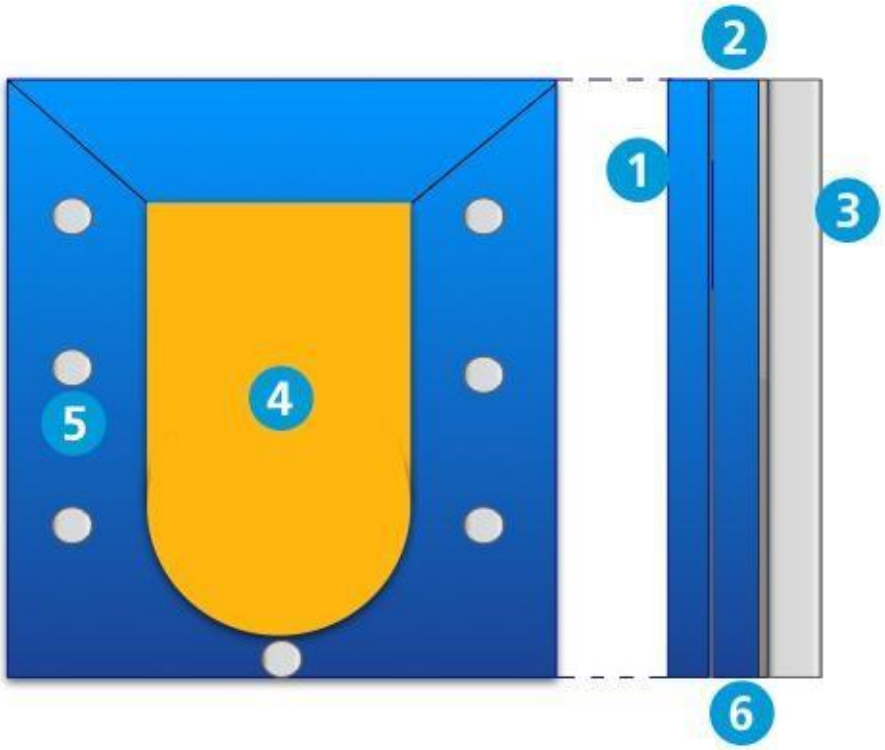

Figure 3.8 Second Mould

- Component.1 is the back of the mould, made of nylon
- Component.2 is the spacer (thickness ~1 cm), made of nylon
- Component.3 is the front part of the mould, made of polycarbonate, since it is a transparent material and it act like a window for observing the curing state.
- Component.4 is the epoxy sample
- Component.5 are metal nut and bolts which avoid the problems observed with the nylon nuts used in the first design.
- Component.6 are the acetate sheets between the back of the mould and spacer and also between the front part of the mould and spacer.

- Again there is a layer of vacuum grease applied to the inside surface of the spacer to prevent adhesion to the sample.

The procedures of using this mould are as follow:

- Wipe vacuum grease at inner side of the spacer where the sample would make contact with the mould, the grease is not likely to enter the sample, even if this happens, the contaminated part would be cut out after curing.
- Insert the bolts into their holes in Component 1 and assemble the mould by placing first an acetate sheet, then the spacer, then the second acetate sheet and finally the front of the mould (Component3).
- Use the nuts to tighten the mould components together and make a seal between the acetate sheets and the spacer.
- The epoxy hardener mixture with nanoparticles as required is then added to the mould. The mixture is poured slowly along one side of the space as this avoids the air originally present within the mould from becoming trapped within the sample.
- Once the mould has been filled to a suitable level it is placed in a vacuum chamber for a period of 1 hour at a pressure of 0.2 bar absolute.
- The sample is then removed from the vacuum chamber and allowed to cure for 30 hours.

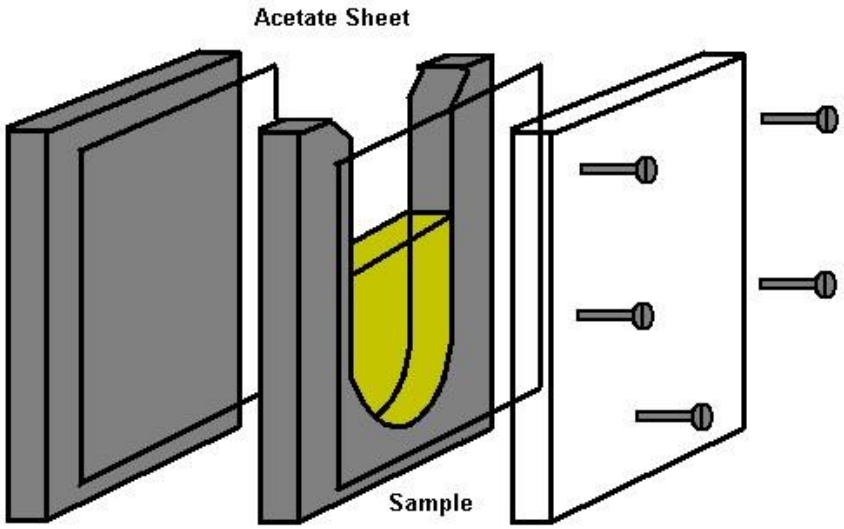

Figure 3.9 Second Mould Assembled

It is more difficult to remove gas bubbles from the sample by vacuum treatment using this design compared to the first mould. However even with the first mould it was not possible to remove all of the bubbles. This mould has the advantage that although a larger number of bubbles remain they are located in a non-critical region of the sample

and no bubbles are observed on the surface regions where surface discharge measurements are to be made.

Figure 3.10 Real Sample

As these surfaces are also in contact with clean smooth acetate sheet during the moulding process the surface of the sample is smooth and is not contaminated. However a certain amount of the epoxy nanoparticle mixture is wasted, due to the requirement for a non-critical region where bubbles can migrate.

Originally the spacer was designed with a simple profile. Problems occurred both in adding the resin to the mould and during vacuum degassing where there was insufficient room for the foam that formed initially in the upper regions of the mould. These problems were addressed by modifying the spacer design by adding shoulders to the top of the spacer as shown in Figure 3.10. It was also found that some bubbles remained trapped in the region of the epoxy close to the spacer.

Although these bubbles would have been in a relatively low field region during testing there were concerns about their presence. The interior dimensions of the spacer were therefore increased from 85 mm to 90 mm to allow a disk shaped sample with diameter 85 mm to be cut from the sample avoiding the inclusion of these bubbles.

3.3.3 Creating Epoxy Nanocomposite

One of the most difficult challenges in this research was developing methods of mixing the nanoparticles with the epoxy resin. The methods used can be divided into two types: mixing the nanoparticles with the base resin before adding the hardener and mixing the nanoparticles with the hardener before adding this mixture to the epoxy resin. In general terms, four main processes were tried in the development of the final method. Two of these processes involved adding nanoparticles to epoxy. When these processes proved to be unsatisfactory; two further processes were developed where the nanoparticles were added to the hardener. In all of the processes described in this section the epoxy and hardener were mixed in a ratio of 100:47 by volume.

In all of the methods, some additional processes to those in Figure 3.5 were used including mechanical stirring, ultrasonic treatment, vacuum treatment and modifications to the curing processes. Each one of them is necessary for making a well dispersed and gas free sample.

- **Mechanical stirring:** this procedure is a common method for mixing different liquid and for dispersing solids into a liquid. A rotary magnetic stirrer was used for the mechanical mixing processes.
- **Ultrasonic treatment**: ultrasonic wave can induce cavitation effect in liquid; the energy generated from bubble bursting will keep nanoparticles from aggregating. It can also break the existing aggregation caused by van der Waal's forces.
- **Vacuum treatment:** mixing of the nanocomposite can introduce gas bubbles into the mixture. Solvents as described later were also used to assist in the dispersion of the nanocomposite. Vacuum treatment was used to remove the gas bubbles and the solvent from the sample
- **Curing Process:** this process can be accelerated or a higher degree of cure

  can be made by heating the sample. But this method was not used in this project.

As mentioned in Section 3.3.1, good dispersion is critical for a nanocomposite. The first two procedures above are used for overcoming the forces that jeopardizes the good

dispersion of nanoparticles. The following sections show the full procedures for each of the 4 methods developed and the experience gained from it.

3.3.3.1 Initial trials of nanoparticle dispersion in a resin

At the beginning of the project, the nanoparticle solution available was ZnO in water by 50 wt%. Initial trials of dispersing the particles were carried out using a clear polyester casting resin (Polylite 32032) for testing the manufacture procedures and the effect of ultrasonic bath. The test was carried out without using the mould discussed earlier. Initial results were unsatisfactory even with the use of mechanical stirring and ultrasonic treatment with the nanoparticles aggregating and forming visible clumps. Figure 3.11 shows an early polyester sample 3 cm in diameter and 2 mm thick were this clumping is clearly visible.

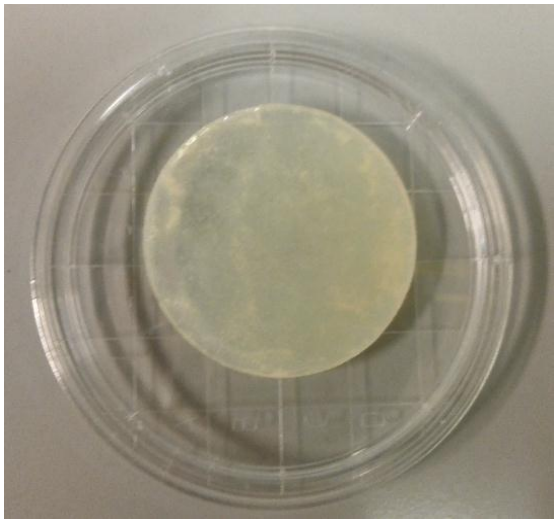

Figure 3.11 Polyester casting resin and Sample condition

The process was modified using different durations of both mechanical and ultrasonic treatment. The differences in behaviour when the nanoparticle solution was added to the resin and when the resin was added to the solution were also investigated. Ultrasonic pre-treatment of the nanoparticle solution to cause deaggregation was also tested. Finally a process was refined that resulted in well-dispersed samples. Having shown that it was possible to produce a well-dispersed nanoparticle composite in

polyester resin starting with a nanoparticle solution, the next step was to develop a method using epoxy resin.

3.3.3.2 Initial Sample manufacturing procedure using epoxy resin

The viscosity of the epoxy resin (1500 Pa□s) is approximately twice that of the polyester resin (about 700 Pa□s). To achieve good mixing the viscosity of the resin was reduced by heating.

The process for the first sample manufacturing attempts based on the experience with polyester samples was as follows:

1. Heat the epoxy resin to 60 °C to reduce the viscosity to approximately 800 Pa□s.
2. Add the nanoparticle solution while using mechanical stirring, continue stirring for 40 minutes while maintain the epoxy temperature.
3. Expose the nanoparticle /resin mixture from the previous step to ultrasound for 60 minutes. During this process the mixture was cooled to ambient temperatures.
4. The hardener was then added and the mixture stirred for 40 minutes at ambient temperature.
5. The resin/hardener/nanoparticle mixture was then exposed to ultrasound for 60 minutes.
6. The mixture was then placed in a vacuum chamber for 60 minutes at a pressure of 0.2 bar absolute to remove the air and water.
7. The mixture was then poured into a mould, and allowed to cure at ambient temperature for 24 hours.

The outcomes of this first method were not good. The problems with this method are:

1. Most of time, the nanoparticles aggregated soon after they were added into the epoxy resin, this indicates that the viscosity is still too high and two solution are not easily mixed. Although the ultrasonic treatment can break the bond between nanoparticles, it is not helpful when the particle is too large.

2. The curing process was working unpredictably. Based on the datasheet, significant curing should not start till five and half hours after the mixing of HY5052 and LY 5052. It was usually faster in the process described above. In some cases, significant curing had occurred during Step 4, less than one hour and forty minutes after the hardener was added. The possible reason for this outcome is that although it was assumed that the resin had cooled to ambient temperature before adding the hardener this may not have been the case. Long ultrasonic treatment times also lead to increases in temperature. The water present in the sample prior to vacuum treatment may also have influenced the curing process. After six trials of this method it was decided to abandon it.

3.3.3.3 Second sample manufacturing procedure

Because of the problems that exist in the method described in 3.3.3.2 it was decided to reduce the viscosity of the resin by adding acetone as a media. As acetone is miscible with both epoxy resin and water, it can also be used to assist the removal of the water from the mixture during outgassing under vacuum as acetone is a volatile liquid.

The processes for manufacturing samples using the second method are as follows:

1. The viscosity of the resin was reduced by adding acetone.
2. The ZnO nanoparticle suspension in water was then added to the thinned resin and mixed for 40 minutes
3. The mixture was treated with ultrasound for 60 minutes to attempt to ensure good dispersion
4. While Steps 2 and 3 was being carried out the harder was degassing under a vacuum of 0.2 bar absolute.
5. The hardener was then added to the resin nanoparticle mix and stirred for 40 minutes
6. The mixture was treated with ultrasound for 60 minutes.
7. The resin/hardener/nanoparticle mixture was then degassed in the vacuum chamber for at least one hour to remove the air water and acetone
8. The Mixture was poured into a mould, and allowed to cure for 24 hour under ambient temperature.

This method improved the quality of the sample making. The curing behaviour became more consistent and the pot life of the mixture was sufficiently long to allow samples to be moulded. However, the problem with aggregation was still occurring. The process was then modified by adding the acetone to the nanoparticle suspension rather than to the epoxy resin. It was hoped that the larger separation of the nanoparticles caused by this dilution would reduce the probability of aggregation. The presence of the acetone would still provide the benefit of reducing the viscosity of epoxy during mixing.

The modified process replaced Steps 1 and 2 with the following.

1. The ZnO nanoparticle suspension in water was mixed with acetone (initially 1:5 by volume）
2. This was then mixed with the base resin while stirring for 40 minutes

Steps 3 to 8 were identical to the method above.

The initial ratio for mixing the nanoparticle suspension and the acetone (one part to five by volume) lead to instability in the nanoparticle solution with aggregation occurring prior to mixing with the resin. Trials with a ratio of 1:1 rather than 1:5 were made. Here the nanoparticle suspension remained stable but the viscosity of the resin was too high to achieve good dispersion. Ten samples were made under the new ratio; only three of them seem acceptable (without visible clumps of nanofiller).

During these trials it was observed that no significant improvement in dispersion occurred after the first 10 minutes of stirring therefore the time associated with this step could be reduced. This had the benefit of reducing the loss of pot life in producing a gas free epoxy/ nanoparticle hardener mix.

3.3.3.4 Third and final sample manufacturing procedure

Following the last method, the success rate of sample making is still too low. In order to attempt to improve this, it was decided to mix the nanofiller into the hardener then combine this mixture to the epoxy. The reasons for this are: the viscosity of the hardener is much lower (200-300 Pa□s) than that of the epoxy; the amount of acetone

was also reduced due the low viscosity of the hardener. With several trails, the best ratio was found to be 4:1 nanoparticle suspension to acetone by weight.

The processes for manufacturing samples using the third method are as follows:

1. Hardener is mixed with acetone and nanoparticles which is in needed concentration, the ratio for nanoparticles and suspension acetone is 4:1 by weight
2. The mixture was treated with mechanical stirring for 10 minutes, then ultrasonic treatment for 30 minutes to disperse the nanoparticles into the hardener
3. The required quantity of resin was slowly introduced into the hardener using a syringe to allow accurate control of the volume of resin added. During this process the system was being stirred. The time taken to introduce the resin was ~60 seconds. This length of time minimized the introduction of gas bubbles into the mixture without causing premature curing reactions. Once all of the resin had been added the mixture was stirred for 10 minutes followed by 30 minutes in the ultrasonic bath.
4. The solution was then poured into the mould and the degassed under a vacuum of 0.2 bar absolute for one hour
5. Take the mould out of the vacuum chamber and let it cure in ambient temperature for about 30 hours.

Once initial problems had been addressed, this method is successful at providing good samples. The sample was then tested by a Scanning Electron Microscope (SEM), the test image shows in the Figure 3.12 reveal the distribution of nanofiller is good (the bright spots shown in the image represent the nanoparticles).

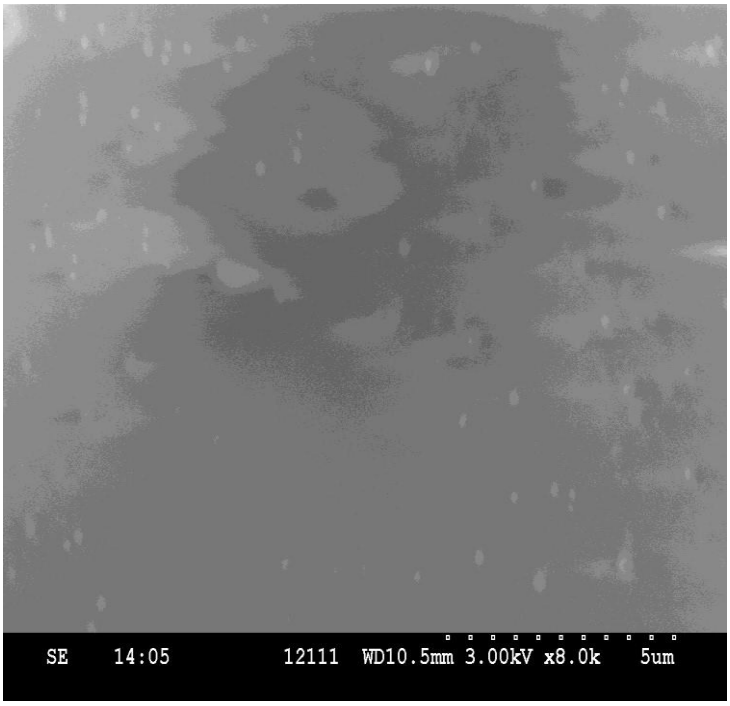

Figure 3.12 SEM image for one of the sample under last method

There were still some problems with this method, the time taken for a sample to cure completely was found to be longer than expected. Under first two methods, the curing times are both under 24 hours, but in this method, the curing time is nearly 30 hours. This condition may be resolved by using increased temperatures to accelerate the curing process. The data for temperature dependence of curing is given in the datasheet of epoxy resin system. Some trials with accelerated curing were attempted but the mould used was not stable at elevated temperatures.

It was also found that significant curing could occur during the second ultrasonic treatment. The reasons for this are not clear. The only difference between the methods is acetone and nanoparticle suspension was added to the hardener rather than the epoxy. The presence of acetone in the epoxy resin did not impact the curing time in the earlier methods and in this method a smaller quantity of acetone was being added. This problem was solved by reducing the duration for second ultrasonic treatment to 10 minutes. The dispersion of the nanoparticles was not affected by this change in processing.

The final method of making nanocomposite sample has been set to the following steps:

1. Harder is mixed with acetone and nanoparticles which is in needed concentration, the ratio for nanoparticles suspension acetone and is 4:1 by weight
2. The mixture was treated with mechanical stirring for 10 minutes, then ultrasonic treatment for 30 minutes to disperse the nanoparticles into the hardener
3. The required quantity of resin was slowly introduced into the hardener using a syringe to allow accurate control of the volume of resin added. During this process the system was being stirred. The time taken to introduce the resin was ~60 seconds. This length of time minimized the introduction of gas bubbles into the mixture without causing premature curing reactions. Once all of the resin had been added the mixture was stirred for 10 minutes followed by 10 minutes in the ultrasonic bath.
4. The solution was then poured into the mould and the degassed under a vacuum of 0.2 bar absolute for one hour
5. Take the mould out of the vacuum chamber and let it cure in ambient temperature for about 30 hours.

This final method has been used to make well dispersed nanocomposites using the following solutions: ZnO (50 wt% in water); ZnO solution (40 wt% in ethanol) and Al_2O_3 solution (20 wt% in isopropanol)

3.4 Conclusion

In this chapter, the processes investigated to successfully manufacture samples suitable for surface breakdown testing have been described. The investigation was drawn out and tedious and many different attempts were needed before developing the successful procedures which has been described in detail. The development of the moulding technique has been described and the geometries of the moulds are also given to ensure that this work can be repeated if needed in any further research.

After the successful making of the nanocomposites, the exploration of its dielectric properties becomes the next topic. In Chapter 4, the methods and equipment for testing the dielectric properties (mainly the dielectric constant or so called permittivity and the

loss tangent) of the manufactured nanocomposite will be described in detail. There will also be the description and analysis of the property results collected from different method.

References

[1] K. L. L. Henry and Neville, *Handbook of Epoxy Resins*. New York: Mcgraw Hill, 1967.

[2] C. PING and L. XING, *Epoxy resin and its application*, Chinese Ed. BEIJING: Chemical Industry Press, 2011.

[3] J.-P. P. R. J. J. Williams, *Epoxy Polymers: New Materials and Innovations*. Wiely VCH, 2010.

[4] J. Katayama, Y. Ohki, N. Fuse, M. Kozako, and T. Tanaka, "Effects of nanofiller materials on the dielectric properties of epoxy nanocomposites," *IEEE Trans. Dielectr. Electr. Insul.*, vol. 20, no. 1, pp. 157–165, Feb. 2013.

[5] T. Andritsch, R. Kochetov, P. H. F. Morshuis, and J. J. Smit, "The complex permittivity of epoxy based nanocomposites with alumina and magnesium oxide fillers at very low temperatures," in *2011 Annual Report Conference on Electrical Insulation and Dielectric Phenomena*, 2011, pp. 306–309.

[6] D. Pitsa and M. G. Danikas, "Modeling relative permittivity and electrical treeing in polymer nanocomposites," *2013 IEEE Int. Conf. Solid Dielectr.*, pp. 832–835, Jun. 2013.

[7] S. J. Dodd, N. M. Chalashkanov, J. C. Fothergill, and L. A. Dissado, "Influence of the temperature on the dielectric properties of epoxy resins," in *2010 10th IEEE International Conference on Solid Dielectrics*, 2010, pp. 1–4.

[8] J. K. Nelson, *Dielectric Polymer Nanocomposites*, 1st ed. Springer, 2010.

[9] J. Katayama, Y. Ohki, N. Fuse, M. Kozako, and T. Tanaka, "Effects of nanofiller materials on the dielectric properties of epoxy nanocomposites," *IEEE Trans. Dielectr. Electr. Insul.*, vol. 20, no. 1, pp. 157–165, Feb. 2013.

[10] W. Zhong-gang*, L. Wan-shuang, Z. Lin-ni, and C. Zhuo, “Progress on Molecular Design and Synthesis of High-Performance Cycloaliphatic Epoxy Resins,” *Polym. Bull.*, vol. 9, pp. 13–21, 2011.

[11] H. Ding and B. R. Varlow, “Electrical treeing studies on the Araldite LYMY 5052 epoxy resin over a wide range of stressing voltage,” pp. 306–309, 2004.

[12] B. Bolasodun, “Microwave effects on the curing , stucture properties and decomposition of epoxy,” University of Manchester, 2010.

[13] H. Ding and B. R. Varlow, “Effect of Nano-Fillers on Electrical Treeing in Epoxy Resin Subjected to AC Voltage Samples and experiments,” pp. 332– 335, 2004.

[14] S. Bahadoorsingh and S. Rowland, “Investigating the impact of harmonics on the breakdown of epoxy resin through electrical tree growth,” *IEEE Trans. Dielectr. Electr. Insul.*, vol. 17, no. 5, pp. 1576–1584, Oct. 2010.

[15] S. Bahadoorsingh and S. M. Rowland, “Investigating the influence of the lubricant coating on hypodermic needles on electrical tree characteristics in epoxy resin,” *IEEE Trans. Dielectr. Electr. Insul.*, vol. 17, no. 3, pp. 701–708, Jun. 2010.

[16] HUNTSMAN, “Araldite ® LY 5052 / Aradur ® 5052 *,” pp. 1–6, 2007.

[17] Huntsman, “Advanced Materials - Electrical Engineering,” 2012. [Online]. Available: http://www.huntsman.com/portal/page/portal/D47E6374FB79B294E040EBCD2C6B113A. [Accessed: 01-May-2015].

[18] S. Rao and R. Rao, “Cure studies on bifunctional epoxy matrices using a domestic microwave oven,” *Polym. Test.*, vol. 27, no. 5, pp. 645–652, Aug. 2008.

[19] R. J. Fleming, C. Manufacturing, and M. Technology, “Conductivity and Space Charge in LDPE Containing Nano- and Micro-sized ZnO Particles,” pp.

118–126, 2008.

[20] A. R. Conference, E. Insulation, D. Phenomena, J. K. Nelson, M. Ful, and U. Kingdom, “Dielectric Properties of Epoxy Nanocomposites containing TiOz, Ab03 and ZnO fillers,” no. type 1255, pp. 406–409, 2004.

[21] P. Maity, P. Poovamma, S. Basu, V. Parameswaran, and N. Gupta, “Dielectric spectroscopy of epoxy resin with and without nanometric alumina fillers,” *IEEE Trans. Dielectr. Electr. Insul.*, vol. 16, no. 5, pp. 1481–1488, Oct. 2009.

[22] S. Singha and M. Thomas, “Dielectric properties of epoxy nanocomposites,” *IEEE Trans. Dielectr. Electr. Insul.*, vol. 15, no. 1, pp. 12–23, 2008.

[23] R. R. Patel and N. Gupta, “Dielectric spectroscopy of epoxy-based nanodielectrics with metal oxide fillers,” *2010 Annu. Rep. Conf. Electr. Insul. Dielectic Phenom.*, pp. 1–4, Oct. 2010.

[24] P. Preetha and M. J. Thomas, “AC breakdown characteristics of epoxy alumina nanocomposites,” *2010 Annu. Rep. Conf. Electr. Insul. Dielectic Phenom.*, pp. 1–4, Oct. 2010.

[25] Y. Okazaki and M. Kozako, “Effects of addition of nano-scale alumina and silica fillers on thermal conductivity and dielectric strength of epoxy/alumina microcomposites,” *Solid Dielectr. (ICSD), …*, vol. 2010, pp. 4–7, 2010.

[26] C. Calebrese, L. Hui, L. Schadler, and J. Nelson, “A review on the importance of nanocomposite processing to enhance electrical insulation,” *IEEE Trans. Dielectr. Electr. Insul.*, vol. 18, no. 4, pp. 938–945, Aug. 2011.

[27] W. Yan, B. T. Phung, Z. J. Han, and O. K, “Surface insulation performance of epoxy resin□silica nanocomposite material,” in *Electrical Insulation Conference*, 2011, pp. 235–239.

[28] L. Banet, G. Camino, J. Castellon, H. Couderc, O. Dellea, N. Dreuilles, H. Eggenschwiler, M. F. Frechette, P. Fugier, F. Gao, G. Malucelli, R.

Nigmatullin, T. Plyhm, I. Preda, M. D. Reading, S. Savoie, C. Schubert, H. Simon, S. Thompson, A.-F. Vaessen, C. V. Bouanga, and A. S. Vaughan, "Nano-structured hybrid sheets for electrotechnical high-power insulating applications: The sol-gel route," in *2012 Annual Report Conference on Electrical Insulation and Dielectric Phenomena*, 2012, pp. 919–923.

[29] Y. V. Borodin, A. V. Polushina, and A. N. Sergeev, "The formation of nanocomposition structure of Al_2O_3 by the sol-gel method," in *2008 Third International Forum on Strategic Technologies*, 2008, pp. 177–178.

[30] S. Salehi and M. H. Fathi, "Preparation of sol-gel derived hydroxyapatite/yttria stabilized zirconia nanocomposite coatings on 316 L stainless steel," in *2010 17th Iranian Conference of Biomedical Engineering (ICBME)*, 2010, pp. 1–4.

[31] T. Rouyre, a. C. Taylor, M. Fu, F. Perrot, and I. James, "Nano-and micro-silica modification of epoxy polymers," *2010 10th IEEE Int. Conf. Solid Dielectr.*, pp. 1–4, Jul. 2010.

[32] M. Kurimoto, H. Watanabe, K. Kato, M. Hanai, Y. Hoshina, M. Takei, and H. Okubo, "Dielectric Properties of Epoxy/Alumina Nanocomposite Influenced by Particle Dispersibility," *2008 Annu. Rep. Conf. Electr. Insul. Dielectr. Phenom.*, pp. 706–709, Oct. 2008.

[33] E. Tuncer, C. Cantoni, K. L. More, D. R. James, G. Polizos, I. Sauers, and a R. Ellis, "Breakdown properties of epoxy nanodielectric," *2010 Annu. Rep. Conf. Electr. Insul. Dielectic Phenom.*, pp. 1–4, Oct. 2010.

[34] G. W. S. C. Jeffrey Brinker, *Sol-gel Science: The Physics and Chemistry of Sol-gel Processing*. Gulf Professional Publishing, 1990.

[35] L. H. Lee, *Fundamentals of Adhesion*. Springer Science & Business Media, 1991.

[36] C. Green and A. Vaughan, "Nanodielectrics – How Much Do We Really Understand ?," *IEEE Electr. Insul. Mag.*, vol. 24, no. 4, pp. 6–16, 2008.

[37] S. G. Sa'ad, "The effect of Gamma irradiation on the electrical properties of the epoxy resins," University of Strathclyde, 1988.

4. DIELECTRIC PROPERTY TESTS

The nanocomposites manufactured in this project are effectively unknown materials. Before the electrical tests, basic knowledge about their dielectric properties: Dielectric constant, loss tangent, conductivity etc. was required.

In this chapter, the dielectric properties of the materials under consideration will be reported. Initially the properties considered important for an insulating material will be introduced. Then the experiment procedures for measuring these properties will be described. Then the results obtained for the nanocomposites manufactured in this project will be reported.

The chapter will look at the following:

- The background to the dielectric properties considered and how the values can be measured and calculated.
- The instrumentation used, the sample manufacture techniques and the test geometries, Sample making and Electrode design;
- Results for the complex permittivity and tan delta found for the nanocomposites;
- A discussion of these results and possible explanations for their behaviour

4.1 Major properties and test methods

There are three major electrical properties under consideration for selecting an insulating material for insulation system[1]:

a) The electrical strength (Breakdown voltage)

b) The relative permittivity (Dielectric constant, ε)

c) The dielectric loss (represented by Loss tangent, tanδ)

In these three properties, electrical strength is widely considered the dominant one. But base on different application of insulating materials, the importance of these properties can change. For instance, in normal circumstances, insulating materials are required to have a small relative permittivity, except the material is for capacitor insulation, since high permittivity material can increase the capacitance.

In this project, because surface discharge is a pre breakdown state, the bulk breakdown of the material will not be investigated. The literature on surface breakdown suggests that the behaviour of the breakdown is effected by the mismatch in permittivities between the liquid and the solid. Therefore the property tests were focused on measuring relative permittivity and dielectric loss.

4.1.1 Complex permittivity ε_c

Complex permittivity ε_c is a derivate parameter of Maxwell's equations[2]. Using Maxwell's equations as shown in Equations 4.1 and 4.2:

$$J = \sigma E \tag{4.1}$$

$$\nabla \times H = J + j\omega\varepsilon E = (\sigma + j\omega\varepsilon)E = j\omega\left(\varepsilon - j\frac{}{\omega}\right)E_{\sigma} \tag{4.2}$$

Where J is the current density, E is the electric field strength, H is the magnetic field strength. So, complex permittivity can be written as Equation 4.3:

$$\varepsilon_c = \varepsilon - j\frac{\sigma}{\omega} \equiv \varepsilon' - j\varepsilon'' \tag{4.3}$$

ζ is the conductivity of the material; ω is the angular frequency of the electromagnetic wave. The imaginary part of the complex permittivity, ζ/ω can also be written as ε'' and is related to conduction and or losses in the material. The real part of the complex permittivity which is also known as ε' gives the relationship between the D (electric flux density) and E fields in a material and is a measure of polarization, as in Equation 4.4:

$$D = \varepsilon E = \varepsilon_0 \varepsilon' E \tag{4.4}$$

Where ε_0 is the absolute permittivity or vacuum permittivity, the permittivity for every material is the multiple of the value of $\varepsilon_0 = 8.854 \times 10^{-12}$ F/m. The meaning of complex permittivity is the quantization of different materials' polarization. Equation 4.4 can also be written as Equation 4.5:

$$D = \varepsilon_o \varepsilon' E = \varepsilon_o E + P \tag{4.5}$$

Where *P* is called polarization density, and can de defined as in Equation 4.6:

$$P(\omega) = \varepsilon_o \chi_e(\omega) E(\omega) \tag{4.6}$$

Where χ_e is called the electric susceptibility and is a measurement of how easily a dielectric material can be polarized. The relative permittivity ε_r also known as the real part of the complex permittivity ε' can be derived from Equations 4.5 and 4.6, as shown in Equation 4.7:

$$\varepsilon_r = \chi_e(\omega) + 1 \tag{4.7}$$

By Equations 4.6 and 4.7, the polarization is related to the applied electrical field *E* and the complex permittivity respect to the frequency.

When an electrical field is applied to dielectric material, the polarization does not respond instantaneously, the time for the material to response is described by a characteristic time. A simple model of this is the Debye relaxation [3]. This model assumes that the rate of change of polarization *P* is given by Equation 4.8:

$$\frac{dP}{d(t)} = -\frac{P(t)}{\tau} \tag{4.8}$$

Where is the characteristic time for the polarization process, for a step change in *E* Equation 4.8 leads to an exponential response in the polarization, characterised by Equation 4.9.

$$P(t) = P_0 \left(1 - e^{\frac{-t}{\tau}}\right) \tag{4.9}$$

Under AC conditions this delay in the development of the polarization introduces a component of current in phase with the applied voltage which can be modelled as

conductivity in the system although charge is not necessarily being transferred through the dielectric. In addition there can be elements of conventional conductivity in the dielectric with charge carriers being injected into the dielectric, moving across it under the influence of an applied field and being discharged at the opposite side of the material.

The characteristic time sometimes referred to as the dielectric relaxation time corresponds to a frequency (Equation 4.10):

$$f_r = \frac{1}{\tau} \quad (4.10)$$

In reality, polarization of a dielectric material can be categorized into three different models:

- **Electronic polarization model**: In the atom of the dielectric material, because of the applied electrical field, the movement locus of the electron is distorted. When the applied electrical field changed, the time for elements reaching a new equilibrium is call relaxation time. This polarization is very quick; the characteristic time is around 10^{-15} s.

- **Ionic Polarization model:** Most of non-organic solid compound contain ions. When a electrical field is applied, the ions move towards to the opposite polarity. This polarization is also quick, the characteristic time is around 10^{-13} s.

- **Dipolar polarization model:** For some molecules, the distance or locus for positive and negative element is fixed. Under applied electrical field, the molecules are simply rearrange the position, where positive part of the molecules is facing the negative electrode while negative part is facing positive electrode. The polarization time for this model is much longer than two previous models, for different material, the characteristic time is between 10^{-2} - 10^{-10} s.

Figure 4.1 shows the relationship between complex permittivity associated with polarization and the frequency. If the period of the applied ac field is much smaller than the characteristic time of the polarization mechanism, the resulting polarization density *P* is low and therefore the susceptibility is small. Based on Equation 4.7, the relative permittivity is close to one. At frequencies much lower than characteristic frequency the polarization develops fully and therefore the value of $_r$ is greater than one.

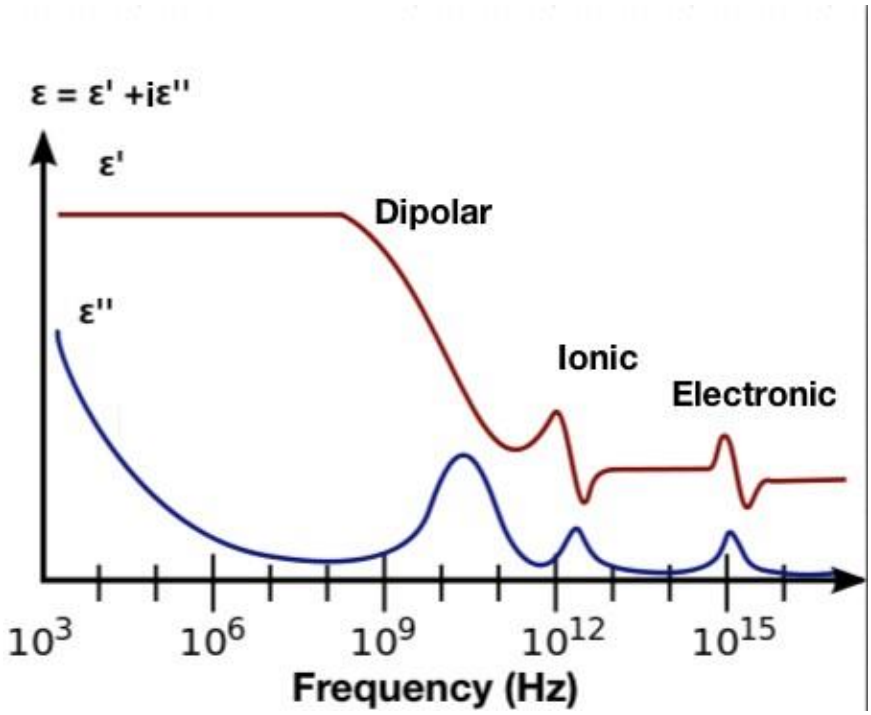

Figure 4.1 Complex permittivity spectrum. Based on [4]

4.1.2 Loss tangent tanδ

Any real dielectric will undergo energy losses under an applied electrical field; Lossless dielectric does not exist in practice. The loss is caused by polarization losses as discussed above or conduction losses. Under DC condition, degree of polarization is constant and the energy loss caused by polarization can be ignored, and so dielectric loss is due to conduction. The dielectric loss in DC condition can be reflected by bulk and surface conductivity.

Under AC conditions, the losses due to polarization and conduction can be combined and represented by a single resistance in parallel or series with capacitor, as shown in Figure 4.2:

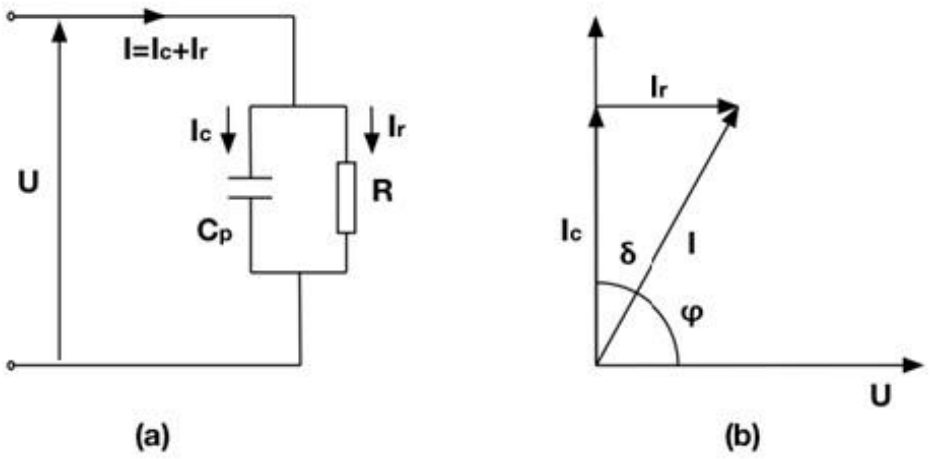

Figure 4.2 (a) Equivalent circuit of dielectric material (**b)** Phase diagram of the (a)

So the dielectric loss can be written as Equation 4.11:

$$\mathcal{P} = UI\cos\varphi = UI_R = UI_C\tan\delta = U^2\omega C_P\tan\delta \qquad (4.11)$$

Where $\mathcal{P}$ is the power dissipated in the material; U is the voltage on dielectric; ω is the angular frequency of the applied voltage; C_p is the equivalent of sample capacitance.

The power dissipated in a dielectric material is an important engineering parameter. However it is dependent on geometry, frequency and applied field. Loss tangent is more directly related to fundamental properties of the material; based on Figure 4.2(b), Equation 4.12 can be derived:

$$\tan\delta = \frac{I_r}{I_c} = \frac{1}{\omega C_p R} \qquad (4.12)$$

Where

$$C_p = \varepsilon' \frac{A}{d} \qquad (4.13)$$

$$R = \rho \frac{d}{A} \qquad (4.14)$$

With Equation 4.13 and Equation 4.14, Equation 4.12 can be written as Equation 4.15:

$$\tan\delta = \frac{1}{\omega \cdot \varepsilon' \frac{A}{d} \cdot \rho \frac{d}{A}} = \frac{\sigma}{\omega\varepsilon'} = \frac{\omega\varepsilon''}{\omega\varepsilon'} \quad (4.15)$$

Following from Equation 4.15, loss tangent can be written as Equation 4.16:

$$\tan\delta = \frac{\varepsilon''}{\varepsilon'} \quad (4.16)$$

Here the conductivity term associated with the parameter ε'' (Equation 4.3) describes both the polarization losses and conduction within the material.

Measurement systems such as bridges, frequently give the values for capacitance and tan for a sample or the equivalent series capacitance and resistance. From the measured value of capacitance, it is possible to derive value of ε' with this value and tan possible to get value ofε''.

4.1.3 Measurement of permittivity and tanδ

In a practical measurement system it is not possible to measure the capacitance of the dielectric material directly. Additional stray capacitances will be present and will contribute to the measured value. The effects of these stray capacitances need to be eliminated. For a sample of dielectric placed between two electrodes as in Figure 4.3

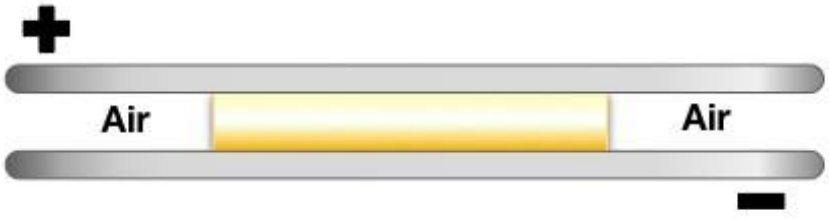

Figure 4.3 Geometry of parallel Electrode arrangement

The capacitance of the sample itself will be given by Equation 4.17:

$$C = \varepsilon_o \varepsilon_r \frac{A}{d} \quad (4.17)$$

Where ε_r is the relative permittivity of the testing material; A is the contact area between the sample and electrode; d is the distance between electrodes, it can also be described as the thickness of the sample. As can be seen in Figure 4.3, the area of the sample is smaller than the electrode. The capacitance between the electrodes is made up of two elements: The capacitance of the sample itself C_{sample} and the capacitance of the air between the electrodes surrounding the sample C_{air}. The capacitance C_{air} will contain a component due to the fringing field lines. As the sample is in the uniform field region of the electrodes it is not affected by these fringing effects. The electrode system is connected to the measuring equipment by cables there is also the possibility of capacitive coupling from the electrodes to ground points. This capacitance is represented by C_{stray}

4.1.3.1 Calculation of permittivity from measured values

The measured capacitance of plane-parallel electrodes is summation of three elements: C_{air}, C_{stray} and C_{sample}; Figure 4.4 is the simplified circuit diagram.

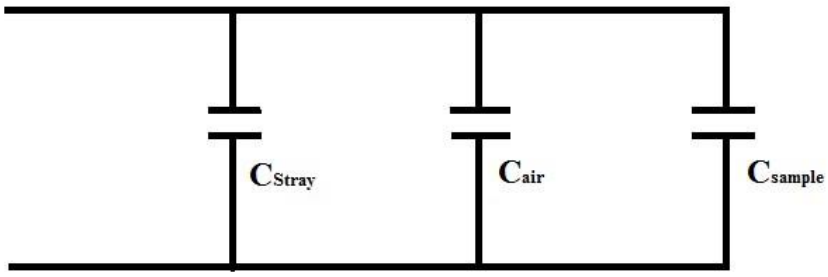

Figure4.4 Circuit diagram of test cell with sample

To calculate the permittivity, the capacitance between the electrodes is measured with the sample present C_{sm} and with the sample removed with the same electrode separation C_{am}.

Equation 4.18 is used for the measurement with the sample present:

$$C_{sm} = C_{sample} + C_{air} + C_{stray} \tag{4.18}$$

For the measurement without the sample present, Equation 4.19 is used:

$$C_{am} = C_{samplevolume-air} + C_{air} + C_{stray} \tag{4.19}$$

where $C_{samplevolume-air}$ is the capacitance for air in the same volume as that of the sample.

Based on Equation 4.17, Equation 4.18 and Equation 4.19 can be re-written as Equation 4.20 and Equation 4.21, respectively:

$$C_{sm} = \varepsilon_o \varepsilon_r \frac{A}{d} + C_{air} + C_{stray} \tag{4.20}$$

$$C_{am} = \varepsilon_o \frac{A}{d} + C_{air} + C_{stray} \tag{4.21}$$

By subtracting Equation 4.20 from Equation 4.21, C_{stray} and C_{air}.can be eliminated Equation 4.22:

$$C_{sm} - C_{am} = \varepsilon_o(\varepsilon_r - 1)\frac{A}{d} \tag{4.22}$$

Equation 4.22 allows the value of ε_r to be derived as Equation 4.23:

$$\varepsilon_r = \frac{(C_{sm} - C_{am})d}{A\varepsilon_o} + 1 \tag{4.23}$$

4.1.3.2 Calculation of tanδ from measured values

For similar reasons, the measured results for tanδ cannot be used directly; it includes the results from stray capacitance and resistances. For calculating tanδ, like calculation of permittivity, measurements need to be performed with sample present between the electrodes and with the corresponding air gap.

- *Air test for tanδ*

For air testing, there are two aliments recorded: air capacitance C_{am} and loss tangent of air tanδ_{am}. Figure 4.5 shows the circuit diagram.

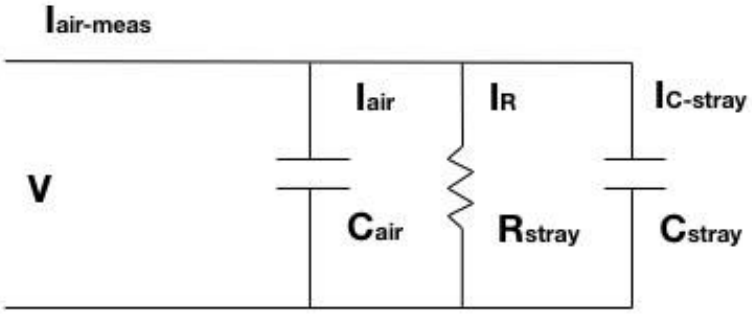

Figure 4.5 Circuit diagram of test cell with no sample

The total capacitance measured in air test is defined in Equation 4.24:

$$C_{am} = C_{air} + C_{stray} \tag{4.24}$$

Loss tangent, tanδ measured in this test is calculated using Equation 4.25:

$$\tan\delta_{am} = \frac{I_R}{I_{am} + I_{Cs}} \tag{4.25}$$

In Equation 4.25, the denominator can be written as Equation 4.26:

$$I_{am} + I_{Cs} = \frac{V}{X_{C-am}} = V\omega C_{am} \tag{4.26}$$

In Equation 4.25, the numerator can be described as Equation 4.27:

$$I_R = \frac{V}{R_{stray}} \tag{4.27}$$

Combining with Equations 4.26 and 4.27, Equation 4.25 can be rewritten as Equation 4.28:

$$\tan\delta_{am} = \frac{V/R_{stray}}{V\omega C_{am}} = \frac{1}{\omega\, C_{am} R_{stray}} \tag{4.28}$$

So the value of stray resistor, also the total resistance in this circuit is defined in Equation 4.29:

$$R_s = \frac{1}{\omega \tan\delta_{am} C_{am}} \tag{4.29}$$

Equation 4.29 can also be written in another form (Equation 4.30):

$$G_s = \omega \tan\delta_{am} C_{am} \tag{4.30}$$

- *Sample test for tanδ*

For sample test, there are also two elements recorded: sample capacitance C_{sm} and sample loss tangent $\tan\delta_{sm}$; the circuit diagram and equation is displayed in Figure 4.6 and Equation 4.31.

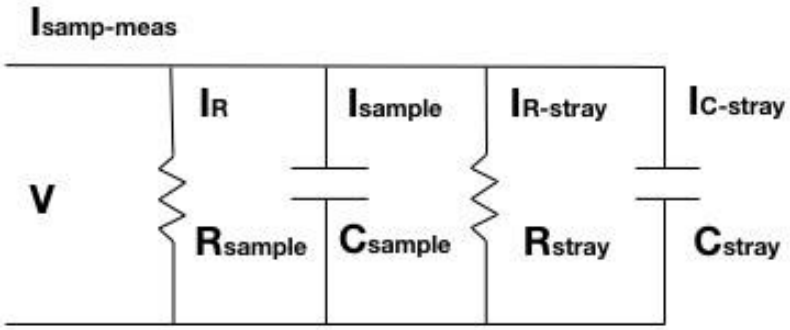

Figure 4.6 Circuit Diagram of test cell with sample and air

As the circuit deals with parallel resistive elements it is easier to work with conductance (Equation 4.31):

$$G_{sample} + G_s = \omega tan\delta_{sm} C_{sm} \tag{4.31}$$

Combining with Equations 4.30, Equation 4.31 can be rewritten as Equation 4.32:

$$G_{sample} = \omega(tan\delta_{sm} C_{sm} - tan\delta_{am} C_{am}) \tag{4.32}$$

And as the value of $tan\delta$ for the sample is given by Equation 4.33:

$$G_{sample} \tag{4.33}$$

$$\tan\delta = \frac{}{\omega C_{sample}}$$

Combining Equation 4.32 with Equation 4.33, the loss tangent of sample becomes Equation 4.34:

$$\tan\delta = \frac{\tan\delta_{sm} C_{sm} - \tan\delta_{am} C_{am}}{C_{sample}} \quad (4.34)$$

4.1.3.3 Measurement Procedure adopted

Therefore the Measurement process was conducted as follow:

1. Calibration of the equipment. The video bridge has a calibration function which helps to eliminate stray capacitive effects and check accuracy.

2. Put material sample between two electrodes in good contact a micrometer built into the electrode system was used to establish electrode separation.

3. Measure capacitance under a range of frequencies.

4. Remove the sample from between the electrodes and set electrode gap to value measured in Step 2.

5. Repeat Step 3

6. Calculate the permittivity and$\tan\delta$ of test material using the values measured in Steps 3 to 5 by using Equations 4.23 and 4.34, measured value and sample geometry.

4.2 Test Methods used in this project

A standard method for measuring capacitance and $\tan\delta$ is the Schering Bridge. Figure 4.7 is a basic circuit diagram of a Schering bridge. The idea is to adjust the low voltage components of the bridge so that points A and B have the same value of voltage magnitude and phase with respect to the ground at C and therefore the voltage between them is zero, then use the value of known components to calculate the capacitance and

the resistance of the sample, after these two values has been determined, the capacitance and loss tangent can be calculated by Equations 4.35 and 4.36:

$$C_X = \frac{R_4 C_N}{R_3(1 + \omega^2 C_4^2 R_4^2)} \tag{4.35}$$

$$\tan\delta = \frac{1}{\omega R_X C_X} = \omega R_4 C_4 \tag{4.36}$$

Schering Bridge is just a basic method for testing sample's dielectric properties. In practice, there are different equipments which derive on Schering Bridge can test the properties in much larger frequency range and achieve more accuracy. Video bridge and Broadband Dielectric Spectrometer were used in this project.

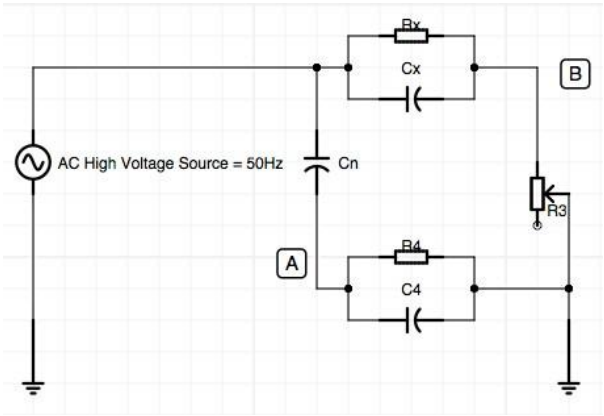

Figure 4.7 Circuit diagram of Schering bridge

4.2.1 ESI Video Bridge 2160

As a low voltage alternative to the Schering Bridge, tests were performed using the ESI (Electro Scientific Industries) Video Bridge 2160. It is an Auto LCR meter, although this was made in 1980s, it is still regarded as useful equipment to test the inductance, capacitance, resistance and the loss tangent of materials. The basic accuracy for video bridge is 0.02 %. The Video Bridge provides data on capacitance and tanδ or capacitance and Equivalent series resistance in this project capacitance and

tanδ were measured. The range for capacitance test is 0.1 pF-10 F under the frequency of 20 Hz-150 kHz. Video Bridge was shown in Figure 4.8(a)

(a) (b)

Figure 4.8 Video Bridge and test cells

The test cell shown in the image was a plane /plane electrode system covered in PVC, designed for use in high voltage tests with a Schering bridge, made by the group workshop. The diameter for the electrodes is 8 cm and the distance of the electrode can be varied from 0 cm to 2.5 cm. The test cell used with the Video Bridge is shown in Figure 4.8 (b). The diameter for electrodes is 5.5 cm, allowed sample thickness is from 0 cm to 4.5 cm the electrode position is controlled with a micro meter.

Tests were made on epoxy nanocomposite samples manufactured in the project. Two types of sample were tested. Figure 4.9 shows all of them and includes an intermediate sample type that was not used for measurements.

Type 1 sample is cut out directly from the original moulding, diameter is 8.5 cm and thickness is 1 cm, this sample geometry is used for discharge observation. It was used at first because the mechanical properties of the nanocomposite were not known and it was not certain whether it could be machined. The Results obtained using this type of sample were not satisfactory, because the capacitance (normally around 7 pF) of the samples were close to the voltage 0 testing limit of the Video Bridge so differences in the permittivity and loss tangent between samples were difficult to resolve. According

to Equation 4.17, increasing the diameter or reducing the thickness of the sample will increase the capacitance value of a sample. This leads to the development of the Type 3 sample through the intermediate Type 2 sample.

As the diameter of the electrodes was 5.5 cm there was no possibility of increasing the capacitance by increasing the area of the samples. Ideally the sample diameter should be smaller than the electrodes to avoid fringing effects. It was decided therefore to produce samples with a smaller thickness by lathe machining from Type 1 samples. Trials in the workshop showed that a sample diameter of 3 cm was best suited for this machining. This allowed samples with a thickness of 1 mm to be produced. The 3 cm diameter had the additional advantage that 4 or more Type 3 samples can be cut from a single Type 1 sample. The capacitance of a Type 3 sample was of the order of 50 pF. Type 2 samples had a diameter of 3 cm and a thickness of 1 cm and were produced as intermediate step.

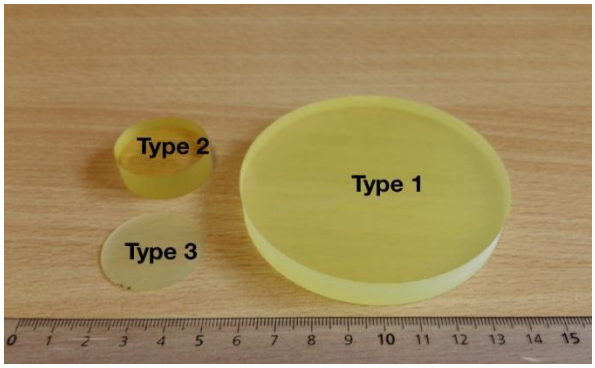

Figure 4.9 Samples for property test

The samples were measured at frequencies in the range of 500 Hz to 50 kHz, the reason for not using the full range of the Video bridge is that under 500 Hz, the results are shown as open circuit, over 5 kHz, there are only 5 frequency point to 150 kHz. working voltage level is 1 V and integrating time is 50ms, each results shown was the average value of 10 tests for each frequency. For each concentration of nanofiller, 5 samples were measured; the final results are the mean value of these test results. Figure 4.10 shows the behaviour of the results

4.2.1.1 Results

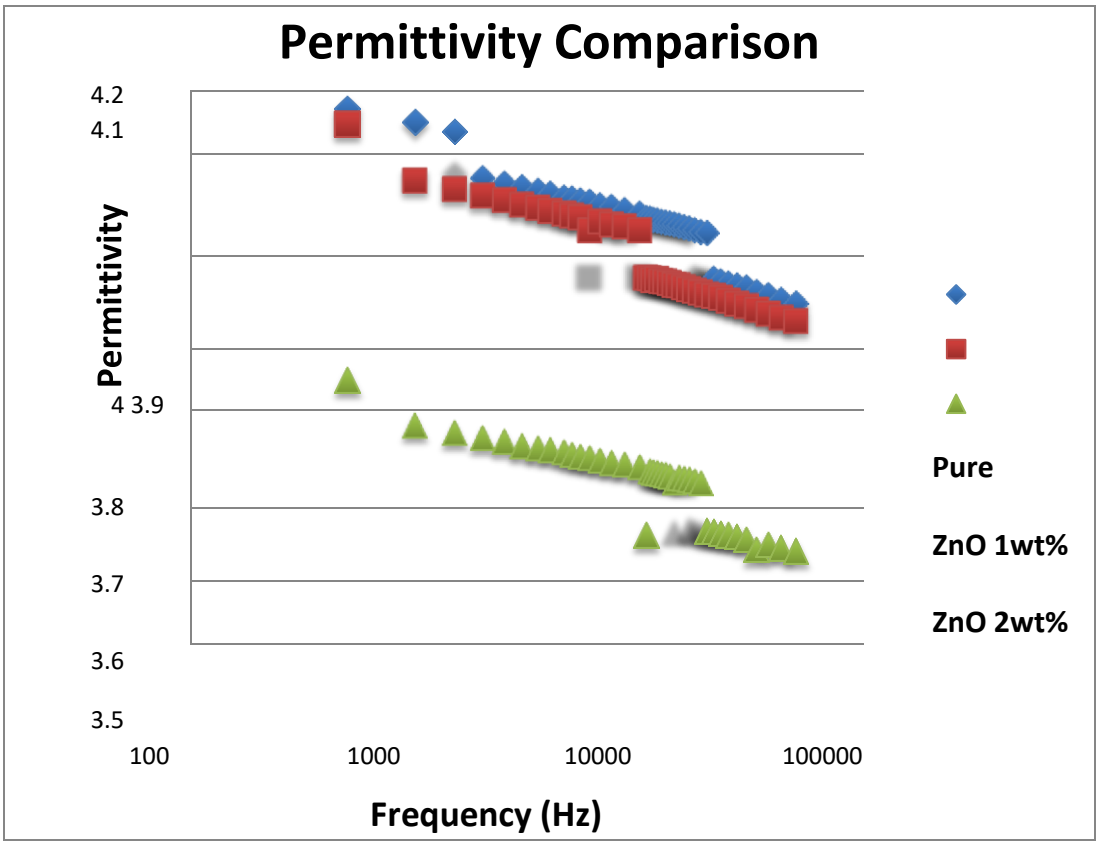

Figure 4.10 Permittivity comparison results from video bridge

Figure 4.10 show the results obtained for the permittivity of epoxy resin with ZnO nanofiller (in ethanol). The results show that for the three materials that permittivity is increasing as the frequency decreases. This behaviour has classified epoxy resin and the nanocomposite based on epoxy to dipolar polarization model. It can also be seen that the nanocomposite with 2 wt% ZnO nanoparticles has a smaller permittivity across this frequency range dropping by about 0.4. For the nanocomposite with 1 wt% ZnO nanoparticles the permittivity has decreased but by a much smaller amount.

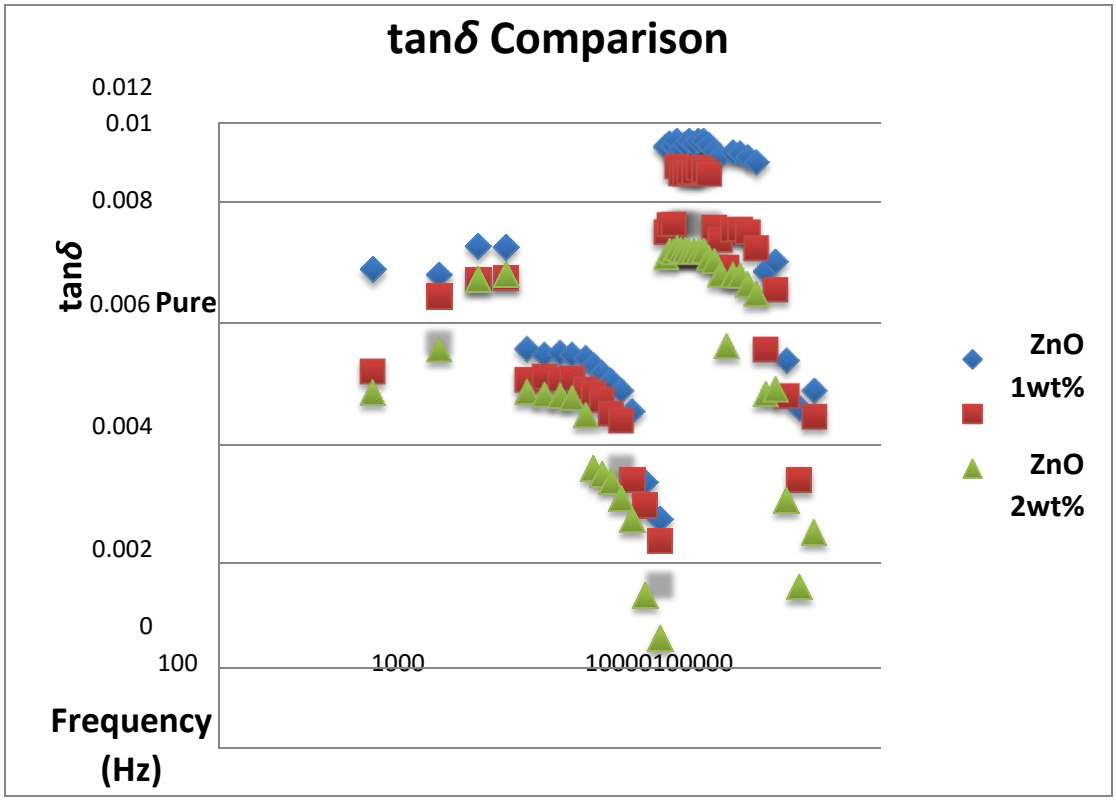

Figure 4.11 Tan delta comparison

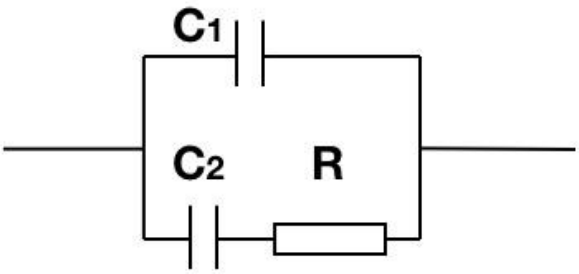

Figure 4.12 Debye Model Circuit

Figure 4.11 shows the results of tanδ with frequency. There is an apparent abrupt change in the value of tanδ at 2.5 kHz and 10 kHz. This behaviour in tan delta value measured is not usual. It was therefore decided to test the accuracy of this equipment using a Debye circuit model. The circuit is show in Figure 4.12.

Expressing in terms of measured capacitance is given in Equation 4.37:

$$C_{meas} = C_0\varepsilon = \left(C_1 + \frac{}{1+\omega^2\tau^2}\right) \quad , \quad C_2 \tag{4.37}$$

Real part of complex permittivity is given in Equation 4.38:

$$\omega C_0 \varepsilon' = \frac{\omega^2 \tau C_2}{(1+\omega^2\tau^2)} \Rightarrow \varepsilon' = \frac{\omega\tau C_2}{(1+\omega^2\tau^2)} \frac{1}{C_0} \tag{4.38}$$

From Figure 4.12, if $C_1 = C_2 = 100$ pF, $R = 6.8$ MΩ; then $\eta = 0.00068$, by setting the frequency range (1 Hz to 10 MHz), complex permittivity and loss tangent can be calculated, the results for ε' and ε'' is showing in Figure 4.13, the results for tanδ under this model is shown in Figure 4.14.

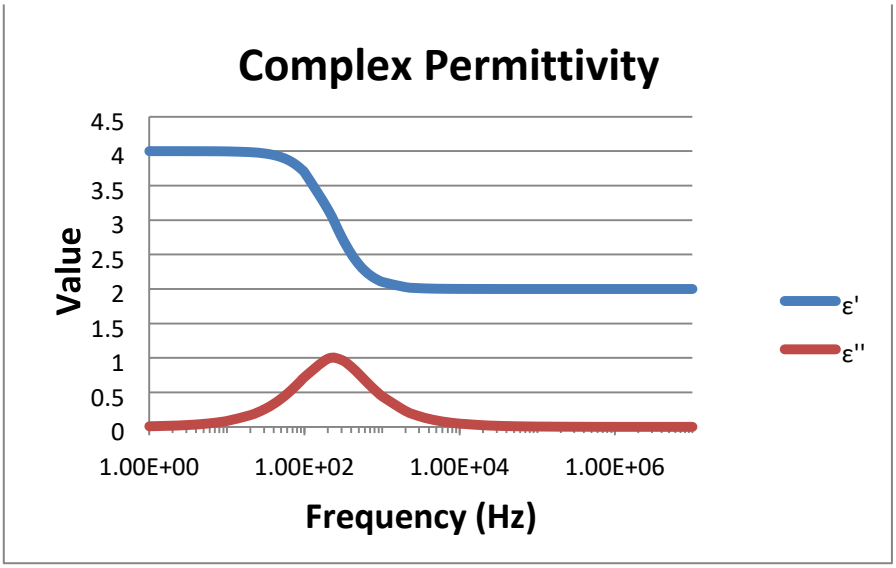

Figure 4.13 Complex permittivity of set Debye Model

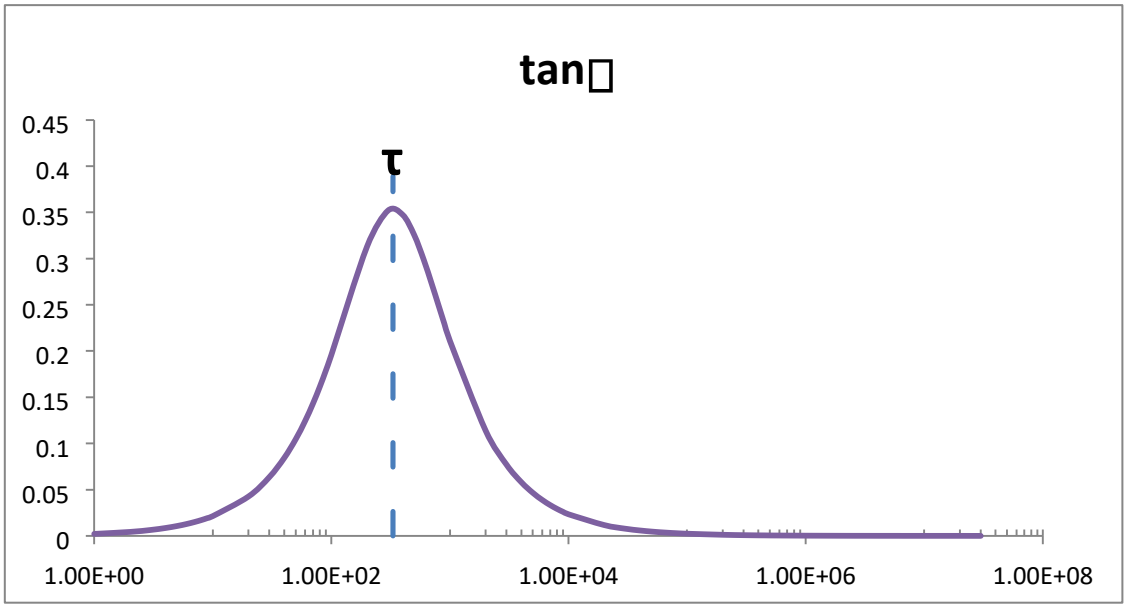

Figure 4.14 tanδ calculated from Debye model

A real circuit of Debye model was made using the same value of the resistor and capacitor. The comparison of the test results and theoretical results that calculated the model are shown in Figure 4.15 and 4.16.

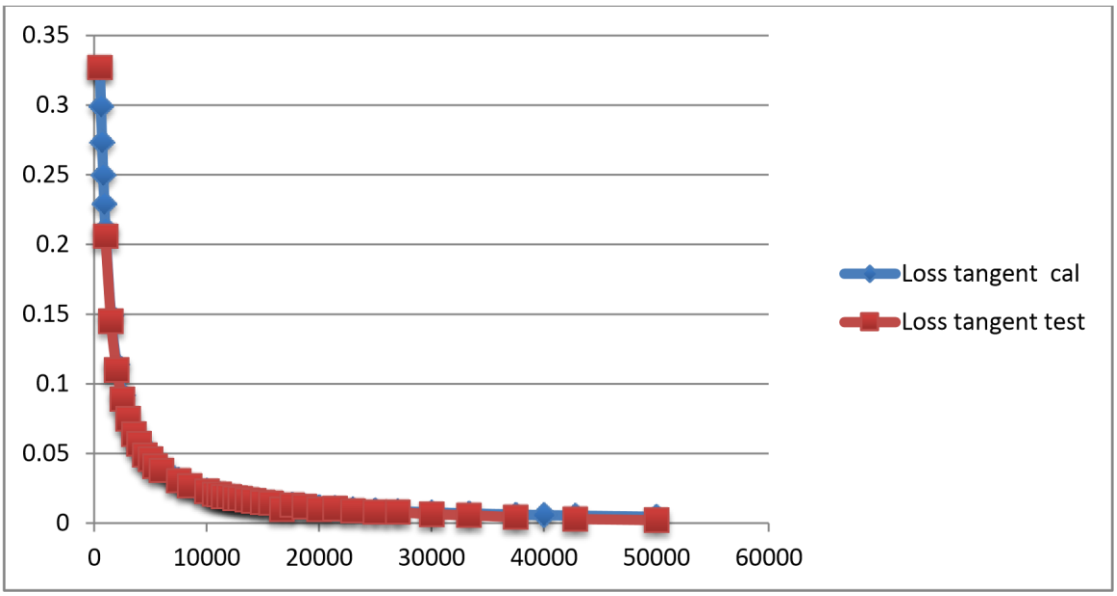

Figure 4.15 The results comparison for loss tangent

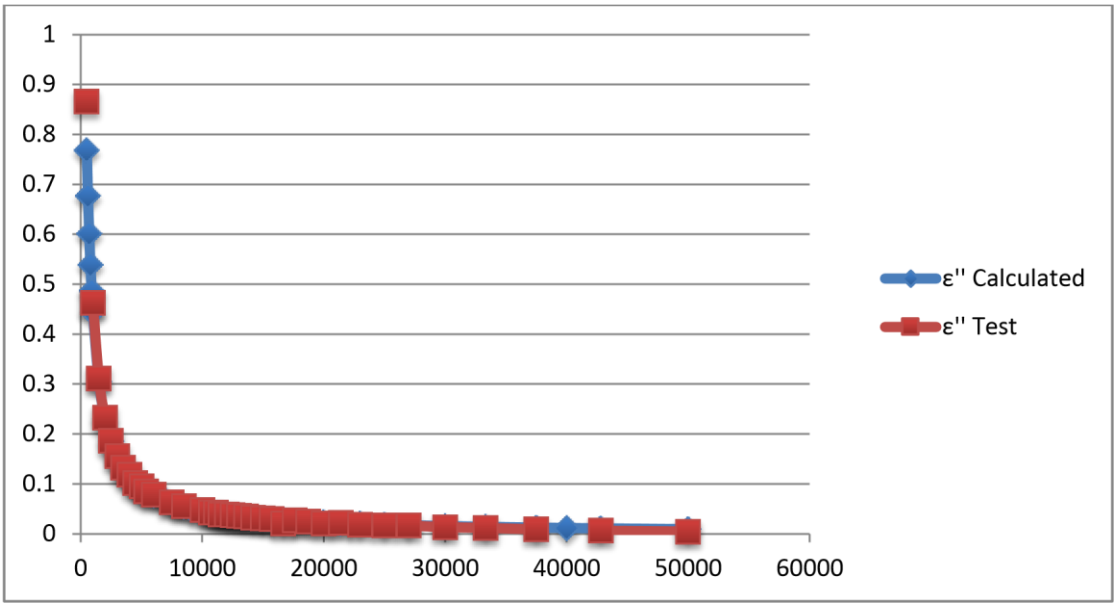

Figure 4.16 Results comparison for ε''

Based on the test results from the ideal Debye model circuit, the video bridge appears to be working fine for values of loss tangent in the range of 0.02 to 0.01. However it is

known that an internal range change occurs at 10 kHz and this has been observed to introduce discontinuities in the values of tanδ[5] There is also a slight difference between calculated results and measured ones; it is showing in Figure 4.17

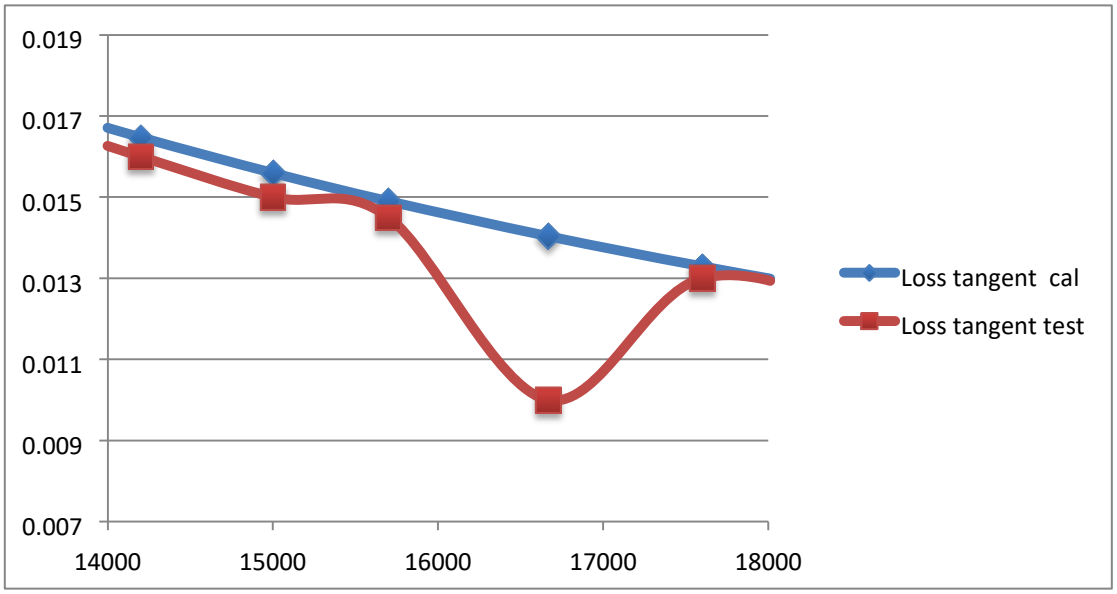

Figure 4.17 Slight difference for loss tangent results

However despite this certain trends can be observed in the data measured using the Video bridge and ZnO nanocomposites. If the discontinuity is attributed to the range change of the instrument, in general, the value of tanδ is increasing as the frequency decreases.

4.2.1.2 Discussion

The results from video bridge test and calculation provide a general picture of the dielectric properties of involved nanocomposite. But the results have some apparent flaws. The frequency range is narrow. Maximum from 20 Hz to 150 kHz, this project only chooses from 500 Hz to 50 kHz. Originally, the ideal frequency range should be from 0.01 Hz to 1000 kHz; this range will provide a better condition of permittivity.

After testing the accuracy by using Debye model, although the Debye testing results are fine, there is still concern about that suspicious gap at 10 kHz for testing tan delta. Normally tan delta value should not present that dramatic change. Even with the narrow frequency range, it should appear as the permittivity curve. There could be some sort of measurement range shifting inside of the video bridge. As it appears in

every result in every sample, there could be a problem. For these two reasons, the test equipment has been change to more advanced one, Broadband spectrometer.

4.2.2 Broadband dielectric spectrometer

From last section, the results for tanδ from video bridge show certain irregularity. Although it has been tested by Debye circuit, it is hard to determine what the problem is; it may be caused by the range shifting inside. Fortunately, there was an opportunity for getting the access to Broadband dielectric spectrometer (BDS) at State Grid Laboratories in Tianjin China. BDS is advanced testing equipment for testing the dielectric properties of insulating materials, manufactured by Novocontrol Technologies. Comparing to video bridge, it have certain advantages:

- BDS can test the dielectric properties of an insulating material under different temperature
- The frequency range of BDS is much wider than Video bridge
- The accuracy is also higher for BDS

BDS have several different models; in this project, Alpha-A Modular Measurement System was used, Figure 4.18 shows its main body. It contains three components:

- **Alpha-A Impedance analyser**:
  - Frequency range: 3×10^{-5} - 2×10^{7} Hz, for this project, the frequency range was selected to be 1×10^{-2} - 5×10^{6} Hz
  - Capacitance range: 10^{-15} - 1 F;
  - Accuracy: less than 3×10^{-5}
  - Voltage range: 100 μV – 3 Vrms(AC), ±40 VDC (70 mA max)
  - Control software: WINDETA
- **Sample test cell:** Alpha active cell
- **Temperature control chamber**

Before running the test the staff at the State Grid Laboratories recommended that the surfaces of the Type 3 sample should be coated with conductive silver paint because the silver paint can provide a better contact with the surface. The paint used was Electrolube ERSCP03B. After brushing the paint on, the sample was placed into an oven for drying for 30 mins at 50 □C. An example of a coated sample is shown in Figure 4.19.

Figure 4.18 Alpha-A Modular Measurement System

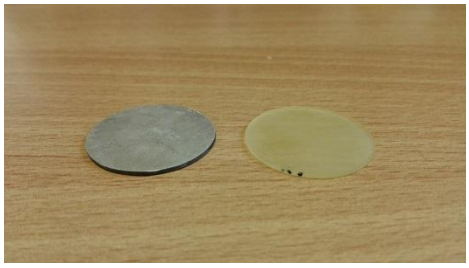

Figure 4.19 Coated sample

4.3 Results

The results obtained from the broadband dielectric spectroscopy experiments are reported in the following section:

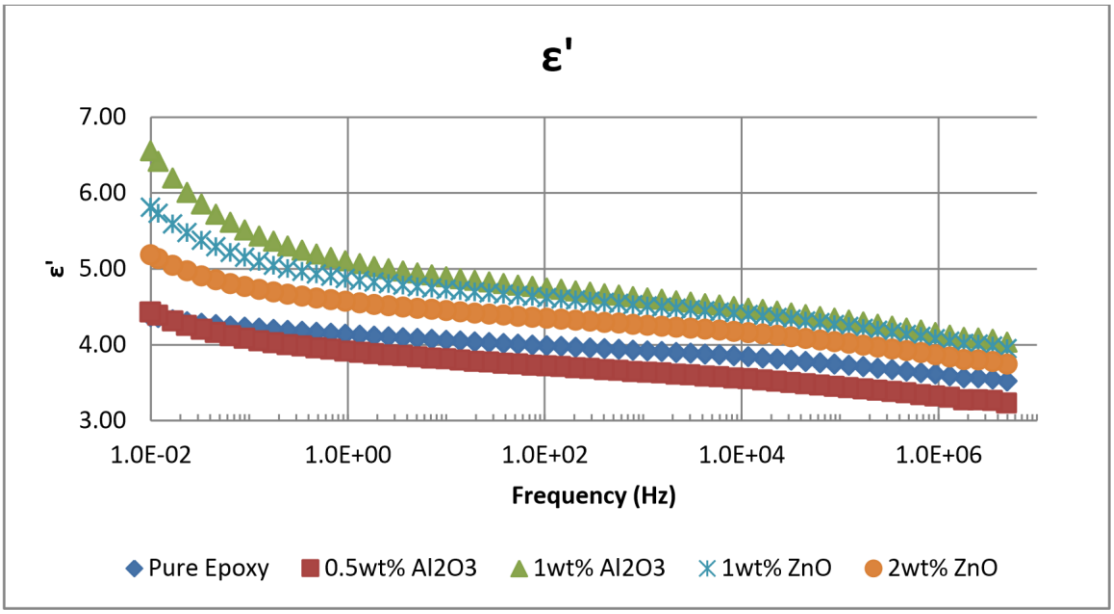

Figure 4.20 Permittivity comparison

Figure 4.20 shows the results for the real part of the permittivity for different types of test sample. Frequency range of these tests is from 0.01 Hz to 5×10^6 Hz. At least 3 samples were tested in each type; the plotted value is the average value of these test results. As it shows, epoxy with 1 wt% aluminium oxide addition has increase the permittivity the most; epoxy with 0.5 wt% aluminium oxide is the only tested sample that decreased the value of relative permittivity.

For clearer look, Figure 4.21 and Figure 4.22 show a comparison of results for ZnO nanocomposites and Al_2O_3 nanocomposite. It is very interesting to see that the relative permittivity value of 2 wt% ZnO is lower than 1 wt% ZnO, this may suggest that a peak in relative permittivity value for ZnO composite exists below the weight percentage of 2 wt%. For Al_2O_3, 0.5 wt% Al_2O_3 appears to decrease the permittivity of epoxy. The 1 wt% Al_2O_3 showed a significant increase in the permittivity larger than any value observed with ZnO. The behaviour for Al_2O_3 nanocomposites suggest that relative permittivity seems to change dramatically with different weight percentage of Al_2O_3 nanofiller.

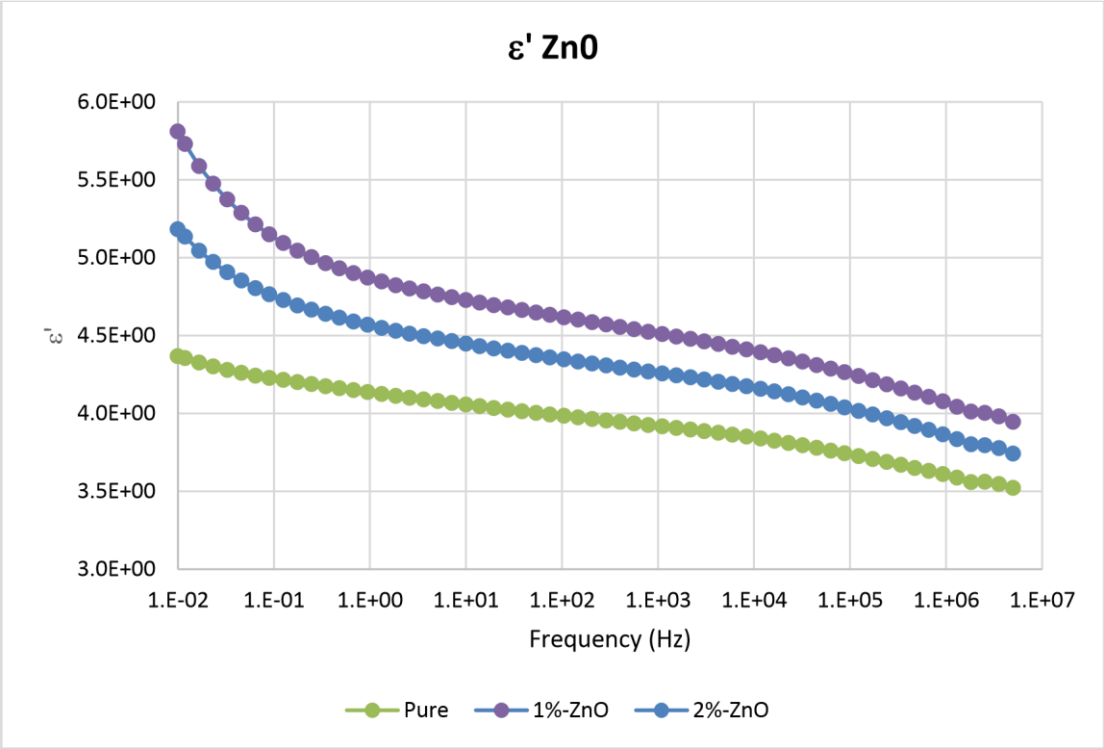

Figure 4.21 Relative permittivity comparison of ZnO composite

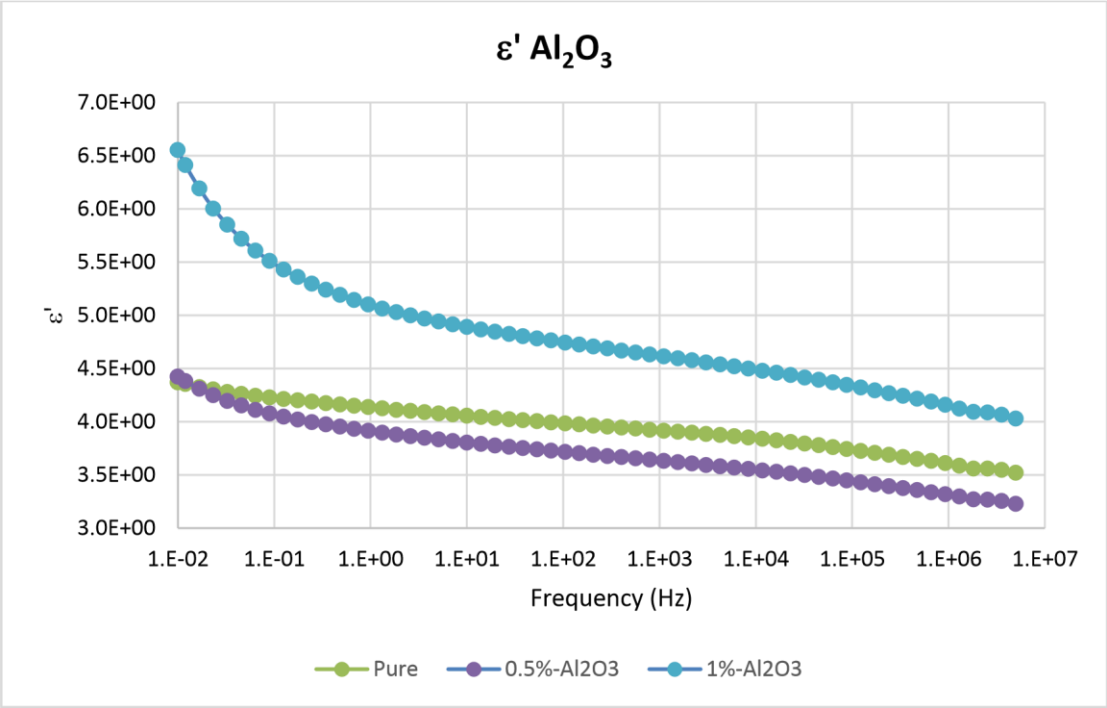

Figure 4.22 Relative permittivity comparison of Al_2O_3 composite

Figure 4.23 and Figure 4.24 show the imaginary part of the permittivity of the ZnO nanocomposite samples over the same frequency range the plots have been split into a

low frequency range (0.01 Hz to 10 Hz) and a high frequency range (10 Hz to 5 MHz). In the low frequency range the value of □'' can be seen to decrease as frequency increases. In the higher frequency range a peak is appearing as the frequency is increased. The increase in □'' observed at low frequencies can be attributed to bulk conduction processes in the nanocomposite and this will be discussed later.

Pure epoxy sample have the lowest value of □'' across both frequency ranges. The low frequency peak below 0.1 Hz has the largest value for the nanocomposite with 1 wt% ZnO. The values for 2 wt% ZnO fall between those for 1 wt% ZnO and the pure material. A similar behaviour was observed in the values of □' in this region.

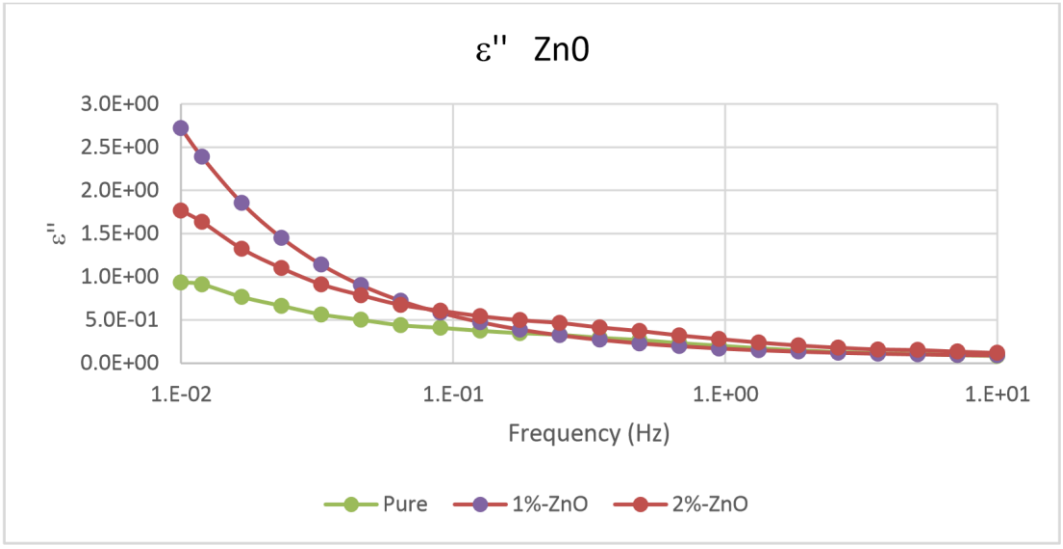

Figure 4.23 Low frequency range results of ZnO nanocomposite

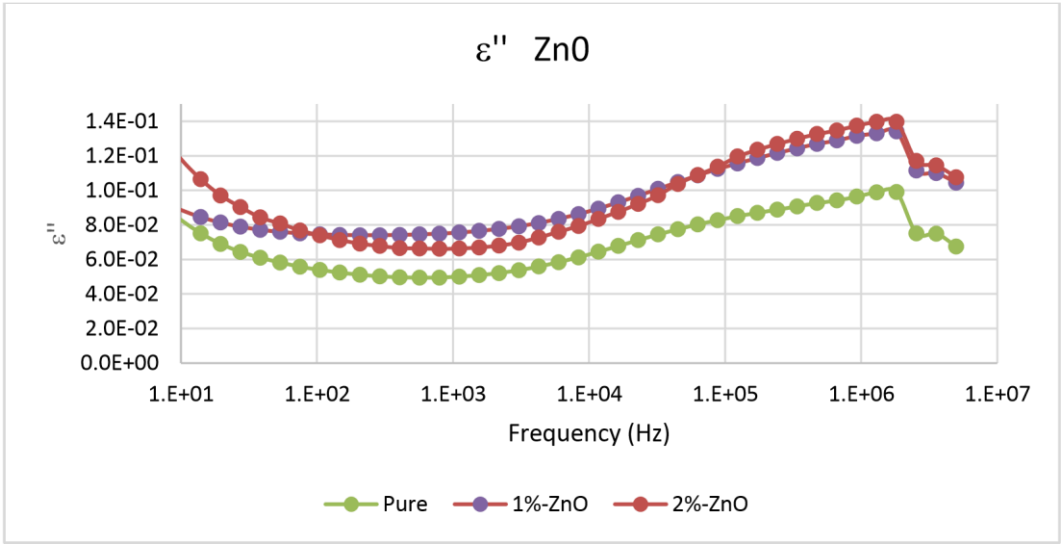

Figure 4.24 High frequency range results of ZnO nanocomposite

In the high frequency data all three plots show a sudden change in the value of □'' between 1.82 and 2.55 MHz. This is probably not real and caused by a range change within the instrument. The change can be seen in all the □'' results at the same position. Points above this shift seem however to be decreasing. This suggests that there may be a peak in the value of □'' in this region. If this is a peak its position is not changed by the presence of the ZnO nanofiller. There is however an increase in the size of the peak when nanofiller is present but there is little difference between the results at 1 wt% and 2 wt%

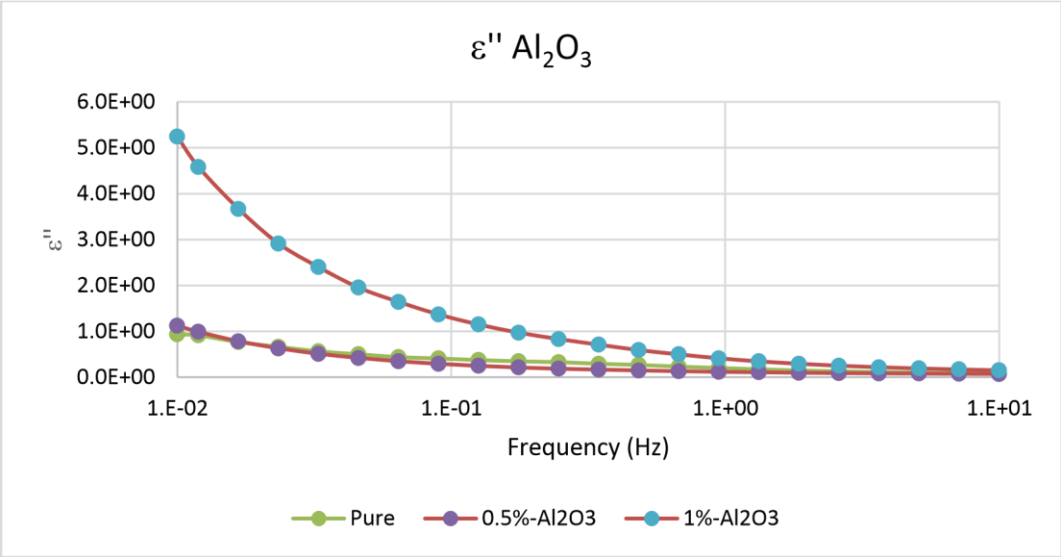

Figure 4.25 Low frequency range results of Al_2O_3 nanocomposite

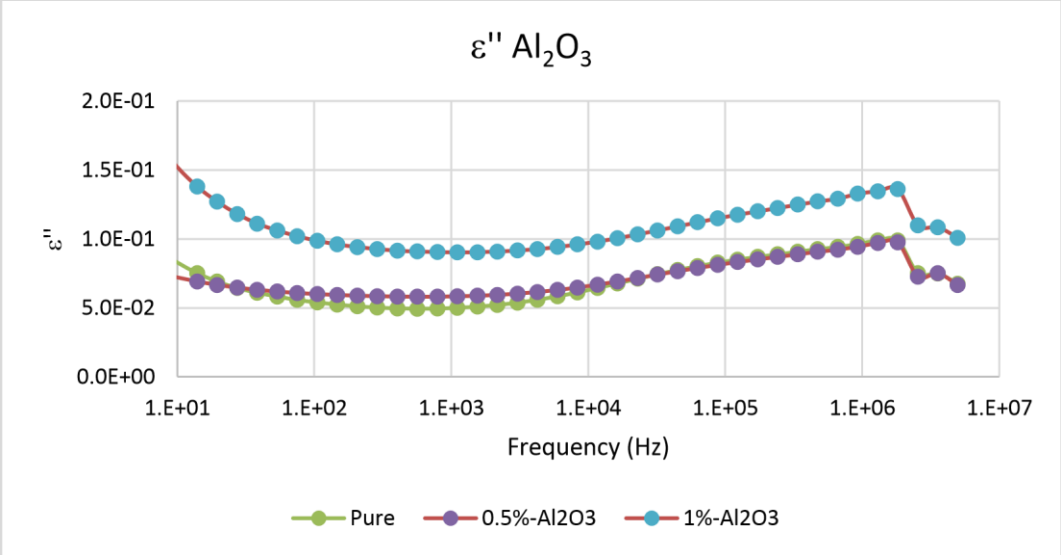

Figure 4.26 High frequency range results of Al_2O_3 nanocomposite

Figure 4.25 and Figure 4.26 shows □'' for the Al_2O_3 nanocomposites testing sample in different frequency range. There is little difference between the values of □'' for the pure and 0.5 wt% Al_2O_3 nanocomposite over the measured frequency range. The values for the 1 wt% Al_2O_3 are significantly higher across the entire frequency range. At low frequencies the value of □'' rises, and the difference of the behaviour of the 1 wt% Al_2O_3 is obvious. In the high frequency range, there is again evidence of a peak at 1.82 MHz. The position of the peak is unaffected by the presence of the Al_2O_3 nanofiller but the 1 wt% Al_2O_3 data is again significantly larger.

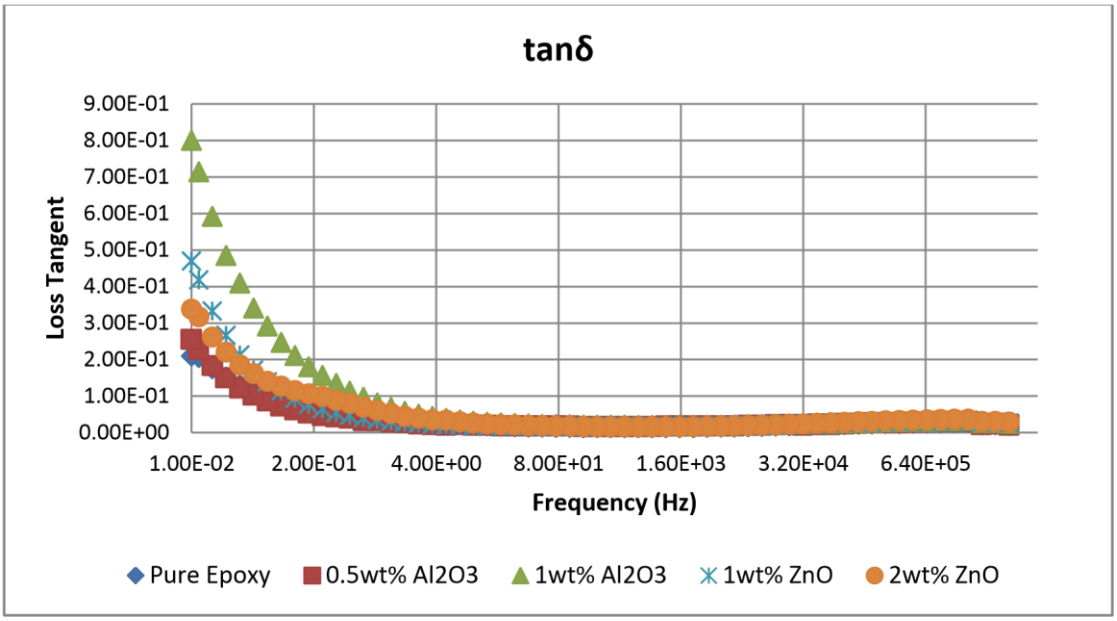

Figure 4.27 Loss tangent comparison

Figure 4.27 shows the comparison of the loss tangent of different testing samples. As expected the behaviour of tan□ is closely related to that of □''. However in the high frequency regime it shows the changes in behaviour slightly more clearly. Because of the high values at low frequency the behaviour has been split into the same low frequency and high frequency regions used with the □'' results

At frequencies between 0.1 and 10 Hz there is little difference between the pure, 1 wt% and 2 wt% ZnO nanocomposites. There is perhaps evidence of a shoulder around 0.24

Hz. Below 0.1 Hz there are significant differences. In all cases tan□ increases as the frequency falls but as was seen in the □'' results the value for tanδ is larger for the 1 wt% ZnO than the 2 wt% ZnO

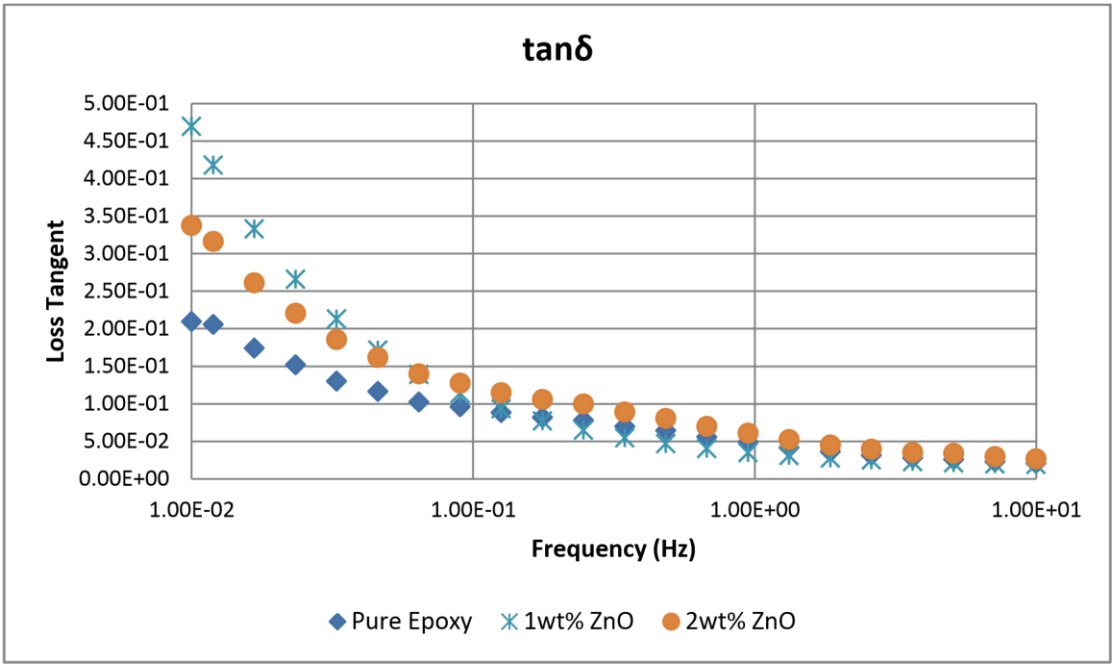

Figure 4.28 loss tangent comparison for ZnO nanocomposite in low frequency

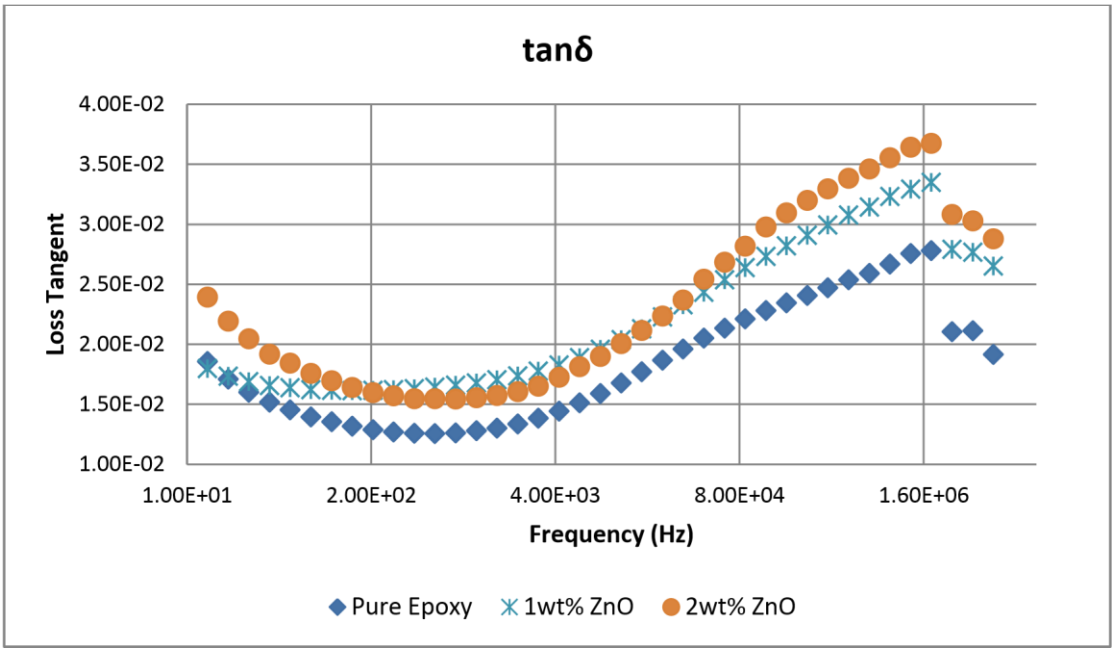

Figure 4.29 loss tangent comparison for ZnO nanocomposite in high frequency

Figure 4.28 and Figure 4.29 show the tanδ comparison results for ZnO nanocomposite. Again, in high frequency range, there is a sudden change around 1.82 MHz attributed to a change in range in the instrumentation. The appearance of the peak is clearer as compared to the □ ’’ data. The peak position does not appear to change with nanofiller concentration but the peak height increases with concentration. This behaviour appears to be coming from the differences in the value of □ ’ as a function of concentration.

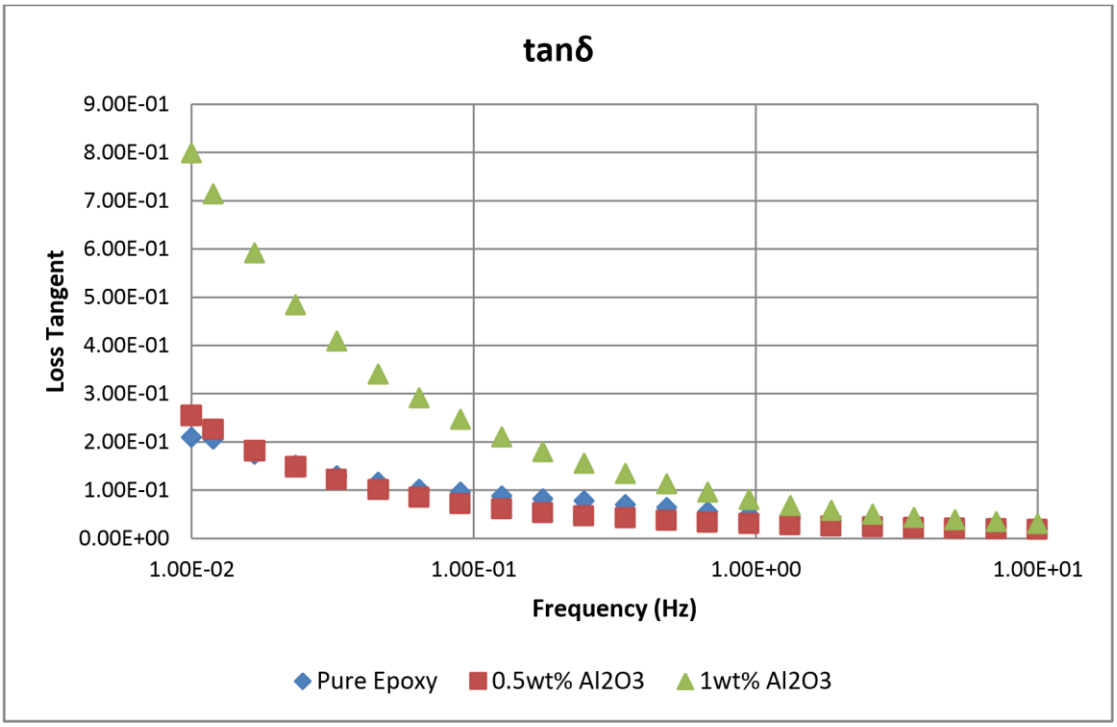

Figure 4.30 tanδ comparison for Al_2O_3 nanocomposite in low frequency

Figure 4.30 shows the tanδ comparison results in the low frequency range, for Al_2O_3 nanocomposites the behaviour of 1% nanocomposite diverges from the 0.5% and pure epoxy results at frequencies below 1 Hz. There is little apparent difference between the behaviours for the 0.5% and pure samples. In all cases the value of tan□ increases as the frequency decreases with this behaviour being very strong for the 1%wt sample.

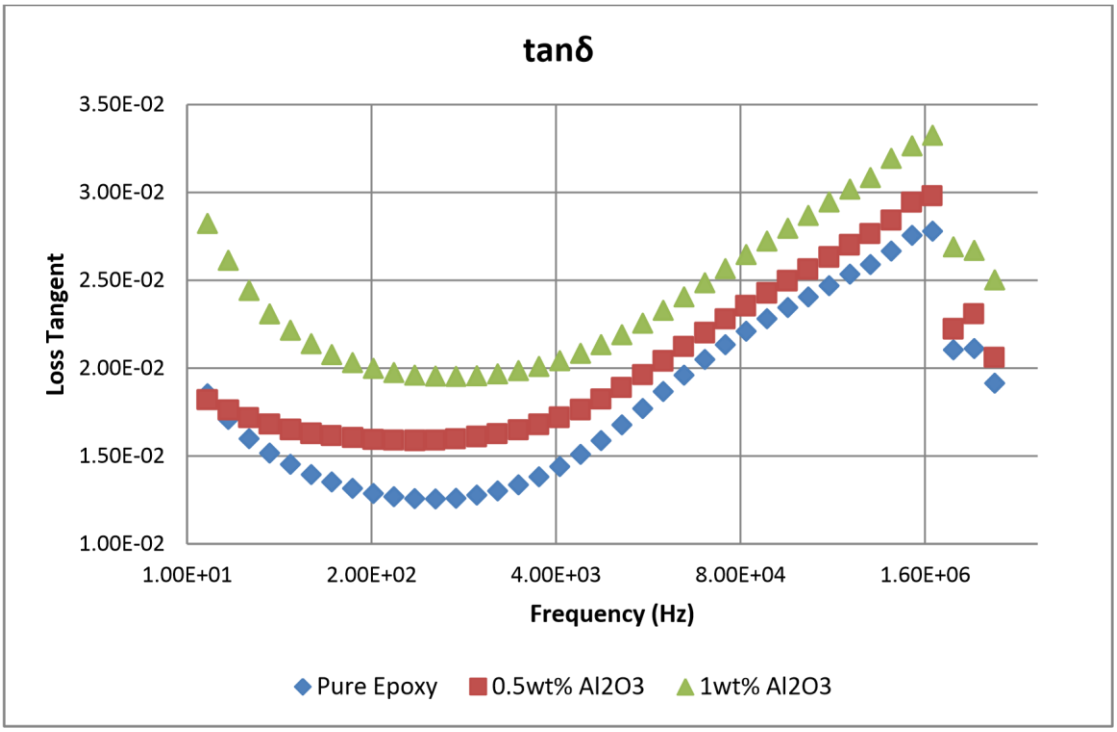

Figure 4.31 tanδ comparison for Al_2O_3 nanocomposite in high frequency

Figure 4.31 shows the tanδ comparison results in the high frequency range, the peak around 1.82 MHz can clearly be observed. The peak position is not effected by nanofiller concentration but as with the ZnO results the peak height varies with nanofiller concentration. Again this behaviour is coming in part from the dependency of the value of □’ on nanofiller concentration in this frequency regime.

4.4 Discussion

4.4.1 Positions of relaxation peaks.

Shifts in the location of relaxation peaks have been attributed to changes in the polymer structure as a result of interactions between the nanoparticle and any surface treatment it may have received and the polymer molecules. There is no evidence of such shifts in the position of the only peak observed in the region of 4 MHz. At low frequencies a shoulder which may be occurring between 0.1 and 1 Hz in the pure polymer appeared to be reduced with the addition of nanofiller but this may be due to it being hidden by the increased low frequency conduction which is discussed in

Section 4. 3

4.4.2 Relative permittivity for mixtures

In previous results, for relative permittivity, there is a value change between pure epoxy and nanocomposite. Various equations have been proposed to derive the effective permittivity, for example the Maxwell Garnatt Model displayed in Equation 4.39[6]:

$$\varepsilon_{eff} = \varepsilon_m * \frac{2\delta_i(\varepsilon_i - \varepsilon_m) + \varepsilon_i + 2\varepsilon_m}{2\varepsilon_m + \varepsilon_i - \delta_i(\varepsilon_i - \varepsilon_m)} \quad (4.39)$$

Where ε_m is the permittivity of the matrix material; ε_i is the permittivity of the inclusion, δ_i is the volume faction of the inclusion.

For ZnO the expected permittivity in the frequency range considered is 7.76 [7], Using the Maxwell Garnatt model the expected permittivities of our nanocomposites can be calculated. The results are shown in Table 4.1a. The actual measured permittivity results for ZnO nanocomposite is shown in Table 4.1b.

Table 4.1a Calculated Permittivity Value

Sample	Pure ZnO	ZnO 1 wt%	ZnO 2 wt%
Permittivity	7.76	4.36	4.38

Table 4.1b Measured Permittivity Value

Frequency	**Pure Epoxy**	**ZnO 1 wt%**	**ZnO 2 wt%**
0.01 Hz	4.35	5.73	5.13
0.1 Hz	4.21	5.09	4.73
1 Hz	4.12	4.85	4.55
10 Hz	4.05	4.71	4.43
100 Hz	3.97	4.6	4.33
1000 Hz	3.91	4.51	4.24
10000 Hz	3.84	4.39	4.16
100000 Hz	3.73	4.24	4.02

Figure 4.32 shows a plot of the differences between the measured experimental results and values predicted using Maxwell- Garnatt model.

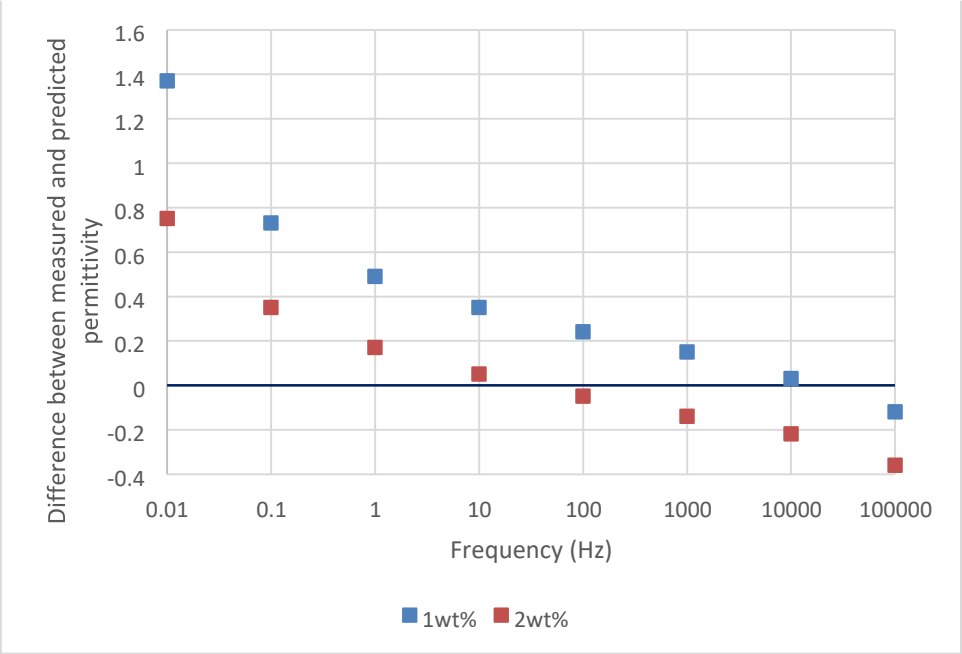

Figure 4.32 Difference between measured and predicted permittivity of ZnO nanocomposite

It can be seen that the behaviour of this difference is similar for both concentrations of nanofiller. It can also be seen that the values of difference are lower for the 2 wt% concentration of nanofiller. This behaviour may be explained in terms of two competing processes. It has been reported that nanocomposites have lower permittivities than the pure material as due to the reduction of polarizability in the polymer resulting from interactions between: the epoxy resin and the nanoparticles or the epoxy resin and the surface coating of the particles[1], [8]–[16]. This effect is stronger for the 2 wt% ZnO nanocomposite. Which would be expected to have reduced the polarizability in a larger volume of the polymer therefore causing a larger decrease in the permittivity differences. The competing processes causing the permittivity to increase are less clear. At low frequencies, see the discussion below, the conductivity of the polymer is increased due to the presence of nanoparticles. This may introduce a low frequency space charge based component in the polarization. In addition the permittivity of the zinc oxide has been assumed to be constant over the frequency range. This may be correct for bulk materials but the frequency dependence of the permittivity of nanoparticles may be different. In addition interactions between the surface coating of the nanoparticle and the nanoparticle itself may affect the dielectric response.

For Al_2O_3, the permittivity expected in the frequency range is 10.1 [17]. Again by using the Maxwel Garnatt model, the expected permittivities of Al_2O_3 nanocomposite can be calculated. The results are shown in Table 4.2a. The actual measured permittivity results for Al_2O_3 nanocomposite is shown in Table 4.2b.

Table 4.2a Calculated Permittivity Value

Sample	Pure Al_2O_3	Al_2O_3 0.5 wt%	Al_2O_3 1 wt%
Permittivity	10.1	4.355	4.36

Table 4.2b Measured Permittivity Value

Frequency	**Pure Epoxy**	**Al_2O_3 0.5 wt%**	**Al_2O_3 1 wt%**
0.01 Hz	4.35	4.36	6.41
0.1 Hz	4.21	4.05	5.43
1 Hz	4.12	3.9	5.06
10 Hz	4.05	3.8	4.87
100 Hz	3.97	3.7	4.72
1000 Hz	3.91	3.63	4.61
10000 Hz	3.84	3.54	4.48
100000 Hz	3.73	3.43	4.32

Figure 4.33 shows a plot of the differences between the measured experimental results for Al_2O_3 nanocomposite and values predicted using Maxwell- Garnatt model of Al_2O_3 nanocomposite.

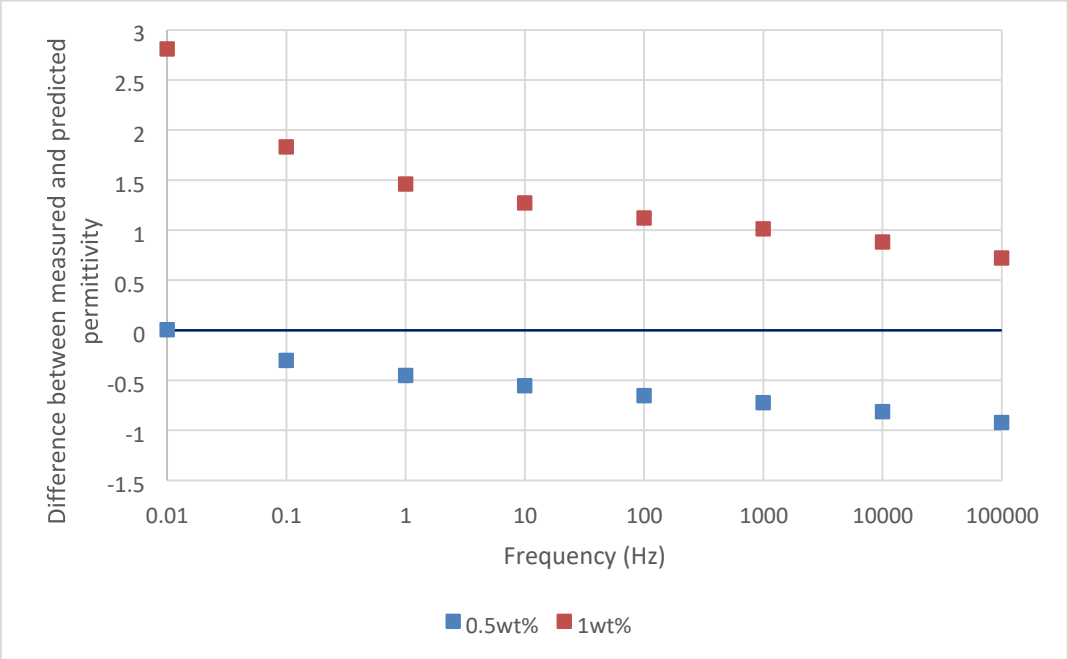

Figure 4.33 Difference between measured and predicted permittivity of Al_2O_3 nanocomposite

For the 0.5 wt% Al_2O_3 nanocomposite the permittivity is below that predicted by the Maxwell Garnatt model over the entire frequency range. This can be explained by the reduction in the polarizability of the polymer in the regions around the nanoparticles due to interactions with the particles.

The general form of the difference in permittivities is again similar for the two concentrations of nanofillers. The changes observed are larger for the higher concentration 1 wt% of filler. This suggests that the concentration of the filler is having an effect on the behavior of the permittivity. In general the permittivity for the 1 wt% filler is larger than that predicted by the Maxwell Garnett model. A possible explanation is that the increase in permittivity due to the presence of the nanoparticles is greater than the decrease caused by the reduced polarizability of the epoxy material in the regions close to the nanoparticles.

4.4.3 Conductivity at low frequencies

The increase in □'' observed at low frequencies is associated with DC conduction. Based on Equation 4.3, □'' can be calculated by Equation 4.40:

$$\varepsilon'' = \frac{\sigma}{\omega} \tag{4.3}$$

If the conductivity at low frequencies is constant a plot of □'' against *1/*□ should produce a straight line whose gradient gives the d.c conductivity of the nanocomposite.

As can be seen in Figure 4.34 and Figure 4.35, straight line plots were obtained. From the gradients of the lines it can be seen that the addition of nanofiller in general increases the conductivity. For ZnO nanocomposite, 1 wt% ZnO nanocomposite has a higher conductivity than those observed for 2% ZnO and pure epoxy resin. For Al_2O_3 nanocomposites there is no observable change in the conductivity for pure and for 0.5 wt% materials. However a much higher conductivity is observed for 1 wt% material. The conductivity of 1 wt% Al_2O_3 nanocomposite is larger than 1 wt% ZnO nanocomposite. As further describe in Chapter 5, it was not possible to perform surface breakdown tests on the 1 wt% Al_2O_3 materials due to rapid bulk breakdown.
This may be as a result of the high conductivity observed in these samples.

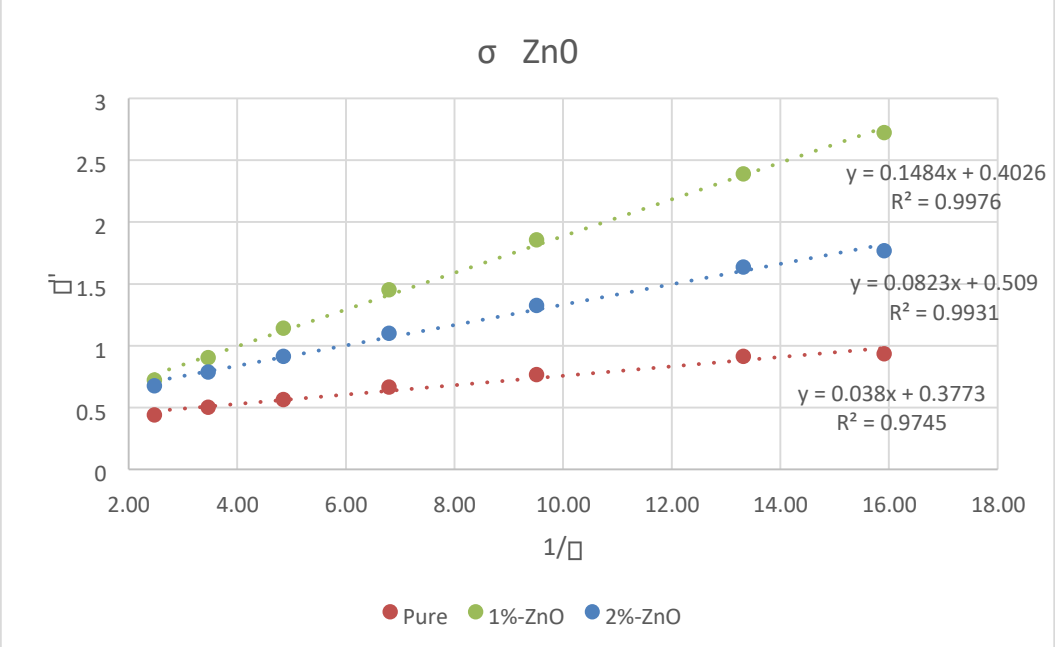

Figure 4.34 conductivity comparison of ZnO nanocomposite

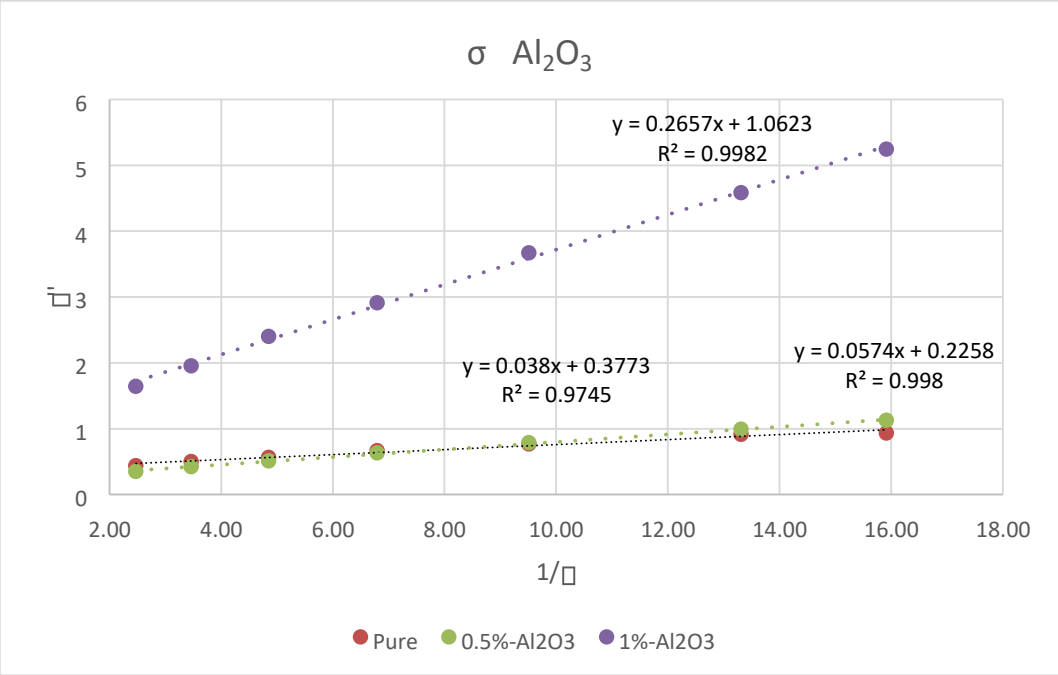

Figure 4.35 conductivity comparison of Al_2O_3 nanocomposite

It is not clear how the presence of nanoparticles would lead to these observed increases in conductivity. In the literature, it is generally assumed that nanoparticles will reduce conductivity due to the introduction of deeper trapping levels in the regions around the nanoparticles. Though increases in conductivity have also been reported [9] [18] [20]

At the concentrations of nanofiller used a continuous path through the material is unlikely based on percolation theory so agglomeration of the particles is not a reasonable suggestion.

It has been suggested that the presence of ionic contamination resulting from the manufacturing of the nanoparticles can lead to increases in conductivity[21]. The nanoparticles used in this work were supplied by Sigma-Aldrich and the product should be carefully examined before using .It may have been possible that contamination of the samples occurred during manufacture.

Some authors have explained differences in the space charge distributions observed in nanocomposites as having resulted from shallow traps being introduced into the polymer in the regions close to the nanoparticles. They also suggest that deeper traps are moved to shallower regions[19]. The presence of shallow traps would cause an

increase in conductivity. It has also been suggested that quasi conductive regions could be formed close to the nanoparticle [22]. These quasi conductive regions were assumed to exist for some 10nm around the particle. It should be noted that the results reported in [22] dealt with much higher nanofiller loads 10%wt.

Assuming that the nanoparticles are evenly distributed through the material it is possible to calculate the separation of the particles based on their concentration. For 1 wt% Al_2O_3 this separation was found to be of the order of 800 nm. This separation is considerably larger than those assumed for the quasi conducting regions or the trapping zones close to the particles of the order of 10 to 30 nm. This separation of the quasi conducting regions is sufficiently large that it is unlikely that charge carriers would be easily transferred between quasi conducting regions. The calculation of the separation of 800nm between particles was based on a uniform distribution of particles. Therefore it is a median value for the separation. It was suggested in [22] that if the particle distribution is random there will be regions rich in nanoparticles and regions poor in nanoparticles. Particle separation will be smaller in the rich regions and overlaps between the quasi conducting regions may occur. Leading to increases in polarisabilty and therefore an increase in both permittivity and conductivity.

4.5 Conclusion

In this chapter, the dielectric properties were introduced; the principle method and different practice methods of testing dielectric properties were discussed. By using these methods, some manufactured nanocomposite were tested to investigate the property changes among them. The permittivity and loss tangent of Both ZnO and 1 wt% Al_2O_3 nanocomposite were increased comparing to pure epoxy; the permittivity and loss tangent of 0.5 wt% Al_2O_3 nanocomposite has no significant changes comparing to pure epoxy. There are also increases on the conductivity of all the nanocomposite comparing to pure epoxy. At present it is not possible to fully explain the observed behaviour of the dielectric properties of the material.

In [23]–[25], the permittivity of epoxy based ZnO nanocomposite was investigated.
For 5 wt% ZnO nanocomposite, the permittivity increased compared with pure epoxy.
For 1 wt% ZnO nanocomposite, the permittivity decreased compared with pure epoxy.

In [20][23] [26], 0.5 wt% Al_2O_3 nanocomposite slightly decreased the permittivity value compared to pure epoxy and 1 wt% Al_2O_3 nanocomposite decreased further.

These results are contradiction with the results measured in this project. Where 1 wt% ZnO was found to increase the permittivity. This situation is probably caused by: the different manufacture methods of the nanoparticles with the possibility of introducing impurities; different surface modifications being made to the nanoparticles, different methods of mixing the nanoparticles into the polymer matrix which may affect the distribution of the nanoparticle after they had been added into the matrix material. There is also the effect of the matrix material; as the properties of nanocomposite can be impact by both materials. All of these make comparisons of the results obtained by different laboratories in this are very difficult.

Although the outputs of two projects are different, they could be explained by same theory: the balancing between increase effect in permittivity due to the presence of the nanoparticles and the decrease effect caused by the reduced polarizability of the epoxy material in the regions close to the nanoparticles.

Further research on the properties under carefully controlled conditions is needed.

Chapter 5 will introduce the experimental set up and measurement techniques used for electrical tests on the nanocomposites.

References

[1] J. K. Nelson, *Dielectric Polymer Nanocomposites*, 1st ed. Springer, 2010.

[2] F. T. Ulaby, *Electromagnetics for Engineers*, Illustrate. Pearson/Prentice Hall, 2005, 2005.

[3] A. K. Jonscher, "Dielectric relaxation in solids," *J. Phys. D. Appl. Phys.*, vol. 32, no. 14, pp. R57–R70, Jul. 1999.

[4] Wikipedia, "Permittivity." [Online]. Available: http://en.wikipedia.org/wiki/Permittivity. [Accessed: 03-Jun-2015].

[5] M. J. Given, "Private Communication." .

[6] O. Levy and D. Stroud, "Maxwell Garnett theory for mixtures of anisotropic inclusions: Application to conducting polymers," *Phys. Rev. B*, vol. 56, no. 13, pp. 8035–8046, Oct. 1997.

[7] A. Calzolari and M. B. Nardelli, "Dielectric properties and Raman spectra of ZnO from a first principles finite-differences/finite-fields approach.," *Sci. Rep.*, vol. 3, p. 2999, Jan. 2013.

[8] C. Calebrese, L. Hui, L. Schadler, and J. Nelson, "A review on the importance of nanocomposite processing to enhance electrical insulation," *IEEE Trans. Dielectr. Electr. Insul.*, vol. 18, no. 4, pp. 938–945, Aug. 2011.

[9] S. Singha and M. Thomas, "Dielectric properties of epoxy nanocomposites," *IEEE Trans. Dielectr. Electr. Insul.*, vol. 15, no. 1, pp. 12–23, 2008.

[10] P. Maity, P. Poovamma, S. Basu, V. Parameswaran, and N. Gupta, "Dielectric spectroscopy of epoxy resin with and without nanometric alumina fillers," *IEEE Trans. Dielectr. Electr. Insul.*, vol. 16, no. 5, pp. 1481–1488, Oct. 2009.

[11] R. R. Patel and N. Gupta, "Dielectric spectroscopy of epoxy-based nanodielectrics with metal oxide fillers," *2010 Annu. Rep. Conf. Electr. Insul. Dielectic Phenom.*, pp. 1–4, Oct. 2010.

[12] J. Katayama, Y. Ohki, N. Fuse, M. Kozako, and T. Tanaka, "Effects of nanofiller materials on the dielectric properties of epoxy nanocomposites," *IEEE Trans. Dielectr. Electr. Insul.*, vol. 20, no. 1, pp. 157–165, Feb. 2013.

[13] G. Iyer, R. Gorur, R. Richert, a. Krivda, and L. Schmidt, "Dielectric properties of epoxy based nanocomposites for high voltage insulation," *IEEE Trans. Dielectr. Electr. Insul.*, vol. 18, no. 3, pp. 659–666, Jun. 2011.

[14] M. Kurirnoto, H. Watanabe, N. Hayakawa, M. Hanae, Y. Hoshina, and M.

Takee, “Dielectric Properties of Epoxy/Alumina Nanocomposite Influenced by Particle Dispersibility and Filler Content,” in *The 9th International Conference on Properties and Applications of Dielectric Materials*, 2009, pp. 749–752.

[15] N. Jäverberg, H. Edin, P. Nordell, H. Hillborg, B. Azhdar, U. W. Gedde, and A. Materials, “Dielectric Properties of Alumina-filled poly (ethylene- co-butyl acrylate) Nanocomposites,” in *Annual Report Conference on Electrical Insulation and Dielectric Phenomena*, 2010, pp. 2–5.

[16] N. Hayakawa, M. Kurimoto, Y. Fujii, J. Shimomura, M. Hanai, Y. Hoshina, M. Takei, and H. Okubo, “Influence of dispersed nanoparticle content on dielectric property in epoxy/alumina nanocomposites,” *2010 Annu. Rep. Conf. Electr. Insul. Dielectic Phenom.*, pp. 1–4, Oct. 2010.

[17] *Metals, Alloys, Compounds, Ceramics, Polymers, Composites: Catalogue 1996/97*. Goodfellow, 1997.

[18] T. Tanaka, “Dielectric nanocomposites with insulating properties,” *IEEE Trans. Dielectr. Electr. Insul.*, vol. 12, no. 5, pp. 914–928, Oct. 2005.

[19] T. Tanaka, G. C. Montanari, and R. Mulhaupt, “Polymer nanocomposites as dielectrics and electrical insulation-perspectives for processing technologies, material characterization and future applications,” *IEEE Trans. Dielectr. Electr. Insul.*, vol. 11, no. 5, pp. 763–784, Oct. 2004.

[20] S. Singha and M. Thomas, “Dielectric properties of epoxy nanocomposites,” *IEEE Trans. Dielectr. Electr. Insul.*, vol. 15, no. 1, pp. 12–23, 2008.

[21] G. C. Montanari, D. Fabiani, F. Palmieri, D. Kaempfer, R. Thomann, and R. Mulhaupt, “Modification of electrical properties and performance of EVA and PP insulation through nanostructure by organophilic silicates,” *IEEE Trans. Dielectr. Electr. Insul.*, vol. 11, no. 5, pp. 754–762, Oct. 2004.

[22] J. K. Nelson and J. C. Fothergill, “Internal charge behaviour of nanocomposites,” *Nanotechnology*, vol. 15, no. 5, pp. 586–595, May 2004.

[23] A. R. Conference, E. Insulation, D. Phenomena, J. K. Nelson, M. Ful, and U. Kingdom, “Dielectric Properties of Epoxy Nanocomposites containing TiOz, Ab03 and ZnO fillers,” no. type 1255, pp. 406–409, 2004.

[24] M. Kuhn and H. Kliem, “A numerical method for the calculation of dielectric nanocomposites,” *IEEE Trans. Dielectr. Electr. Insul.*, vol. 17, no. 5, pp. 1499–1508, Oct. 2010.

[25] S. Singha and M. J. Thomas, “Influence of filler loading on dielectric properties of epoxy-ZnO nanocomposites,” *IEEE Trans. Dielectr. Electr. Insul.*, vol. 16, no. 2, pp. 531–542, Apr. 2009.

[26] Q. Wang, G. Chen, and A. S. Alghamdi, “Influence of nanofillers on electrical characteristics of epoxy resins insulation,” *2010 10th IEEE Int. Conf. Solid Dielectr.*, vol. 9, pp. 1–4, Jul. 2010.

5.SURFACE DISCHARGE EXPERIMENTAL METHODS

This chapter will describe the development of the experimental setup for causing and observing surface discharges on the epoxy and nanocomposite samples. The general view of experiment setup will be described along with the technical detail of equipment used. The reasons for selecting experimental equipment will be discussed along with the problems for linking them together and how these problems were solved. The data processing performed on images prior to analysis will also be described.

The general layout of the experimental setup is showing in Figure 5.1, there are four parts of the system for generating and measuring surface discharges:

- **Power Supply:** HV AC transformer described in Section 5.1
- **Test cell:** Self designed and manufactured by the group workshop described in Section 5.2
- **Waveform collection:** Oscilloscope and current sensor described in Section 5.3.
- **Image acquirement:** CCD industrial camera, the control software and the preprocessing of the image data is described in Section 5.4

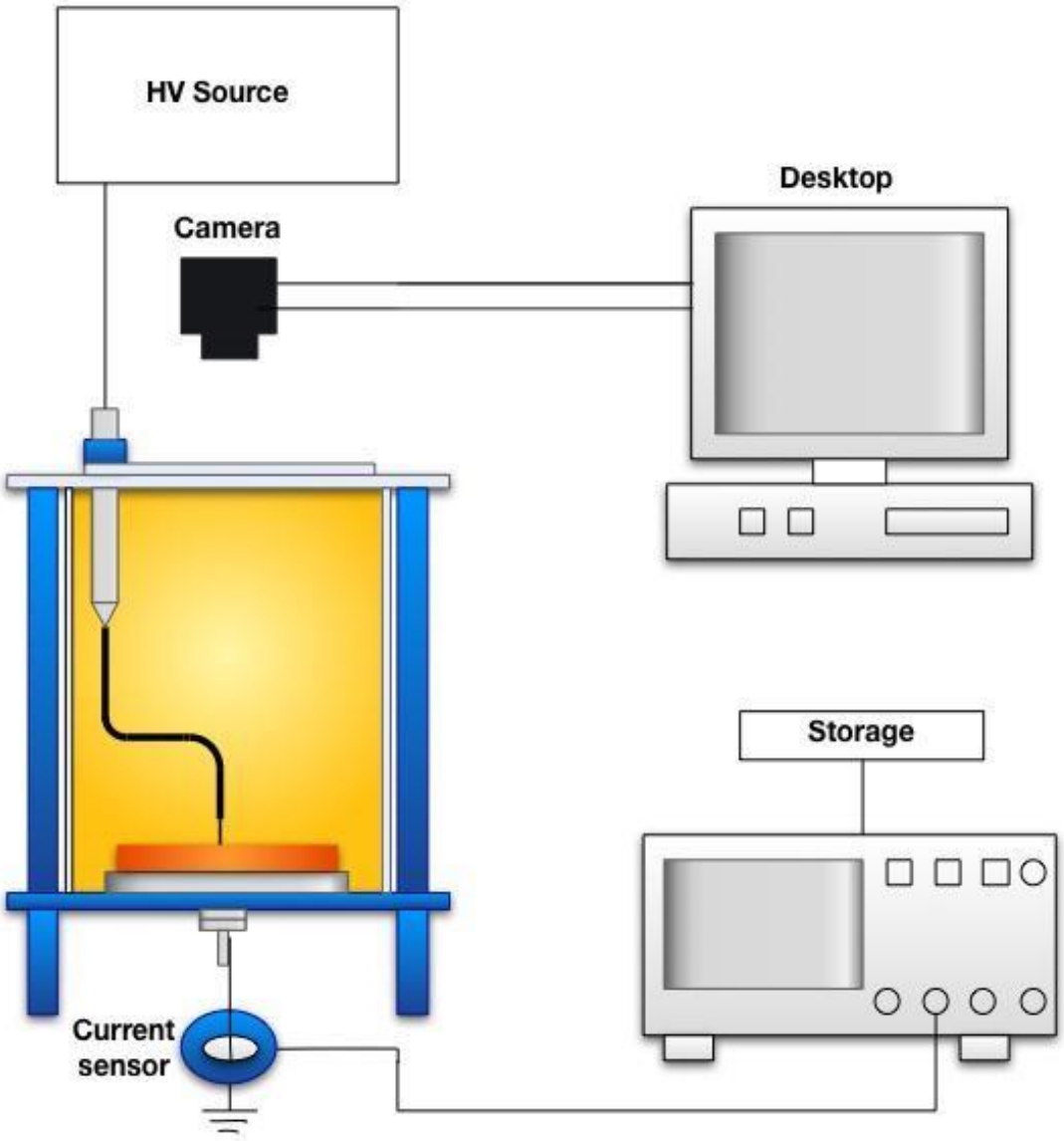

Figure 5.1 Schematic of Experiment layout

5.1 Power Supply

It was decided to examine surface discharges under AC conditions at voltages below 50 kV. Two transformer systems were used in this project. Both of the HV supply set was contained within an interlocked cage in HVT laboratory area. For monitoring the output, two voltage dividers were used to supply information on the voltage to an auto-ranged multimeter for data collecting.

The first power supply used was an Oil Test System manufactured by the Forster transformer company. This is based on a centre-tapped secondary providing ±25 kV at each terminal and 50 kV across the terminals. The maximum rating of this transformer is 75 VA; the frequency is 50 Hz. Although this transformer is useful for testing the breakdown strength for insulating materials, it was not suited for collecting the current waveform of discharges since the whole system was floating and not connected to the ground. This voltage transformer was used initially during the development of the image capture system but was not used in subsequent experiments.

Figure 5.2 Transformer set

The second power supply was made up of two transformers: one is a low voltage Variac transformer made by Forster with an output voltage range from 0 V to 275 V and a current output of 7.5 A; the other one is High voltage transformer with symmetrical winding and the transform ratio is 440/80000, rated at 8 kVA, frequency is 50 Hz. These transformers are shown in Figure 5.2. By calculation, in this project, the supply voltage range is from 0 V to 50 kV. There is a 6 A rated circuit breaker connected between two transformers for protection, in case there is short circuit in the system or unexpected breakdown of the sample.

For performing the test, it was initially assumed that the output voltage level of the HV transformer could be stably set by calibrating the percentage output on the Variac transformer to the output of the HV transformer. However, the output value of the HV

transformer was found to be inconsistent during the day time, because of the voltage drop caused by the multiple loads in the working building.

The system was tested first to check if problems existed in the HV transformer. The ratio of the input to output voltages using a Tektronix oscilloscope probe in the range of 0 to 20 kV showed no problems. The output of the Variac transformer was then monitored. It was found that at a fixed percentage position that the output varied with time during the day. A stable output was possible after 18:30 and at the weekend. This was probably due to variation in Mains supply voltage in the building caused by daytime load changes.

Initially the experimental schedule was modified so that experiments were performed in the evening and weekends. Later a procedure was adopted where the correct setting of the Variac was determined before each experimental run by monitoring the output of the Variac while the HV transformer was isolated using the circuit breaker.

5.2 Test cell

In this project, the test cell was self-designed and was manufactured by workshop in the department. The test cell is the container of the sample and oil; it has to be able to fulfil certain requirements:

1. Provide a stable environment;
2. The sample and oil are replaceable;
3. It should contain replaceable HV electrodes;
4. The surface discharge can be seen and captured by the camera;
5. The discharge pattern should not be blocked too much by the HV electrode.

5.2.1 Test cell Geometry

The electrode geometry used in the test cell is the well-known point-plane. This type of electrode design has been used previously for creeping discharge test [1][2] and allows discharge activity to be produced on the surface of the sample without obscuring much of the surface allowing it to be recorded by a camera. There were two designed

test cell used in this project. The original design of the test cell is shown in Figure 5.3. Each number in the figure represents one element of the cell.

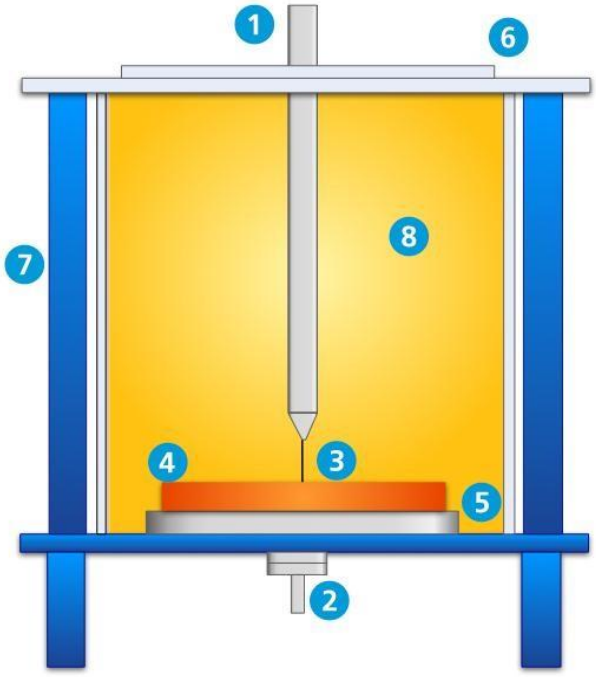

Figure 5.3 Schematic of the first test cell

1. HV Connection (copper rod 0.6 cm diameter)
2. Ground Connection
3. Gramophone needle as the needle electrode with a tip diameter of 25 µm.
4. Solid nanocomposite sample (diameter: 8.5 cm, Thickness: 0.5 cm-2 cm)
5. Ground electrode
6. Transparent upper window material (Perspex PMMA thickness: 0.9 cm)
7. PVC as the frame of the test cell
8. Mineral insulating oil

The main body of the test cell was made out of a section of PMMA tube with outer diameter of 11 cm and wall thickness 0.5 cm. A full diagram of the test cell giving all dimensions is included in Appendix A. The main body is made of two materials: PVC and Perspex PMMA; in order to maintain the necessary consistent experimental condition, it is designed to be fully disassembled for cleaning.

Work with the original test cell revealed several problems:

1. The upper HV connection and the cable between this and the HV transformer blocked the cameras view of a large section of the materials surface;
2. The HV connection itself was not mechanically fixed but could move freely in the vertical direction the whole weight of the copper rod is passed to the sample through the needle electrode and surface damage was occurring to the sample before the experiment started;
3. Surface tension caused a meniscus to form round the HV connection which distorted the view of the sample;
4. Discharge activity was also observed where the HV connection passed into the oil. It was not possible to determine whether the activity observed by the camera was occurring at the surface of the oil or on the surface of the sample;
5. The volume of oil used was relatively large. This had the advantage that minor changes in the oil due to discharges should have had little effect on the properties of the oil. Therefore it would not be necessary to change the oil in the test cell as often. However to avoid problems with possible oil contamination during sample changeover it was felt that for the consistency of the test conditions, it was better to change the oil each time the sample was changed.
   Therefore it would be better to use a chamber with a smaller volume.

Base on this experience, a second test cell was designed with modifications.

Figure 5.4 below shows the basic structure of the final version of the test cell, where:

1. HV connection (copper rod 0.6 cm diameter)
2. Ground connection
3. Brass 1 mm tube
4. Gramophone needle as the needle electrode with a tip diameter of 25 µm.
5. Solid nanocomposite sample (diameter: 8.5 cm, Thickness: 0.5 cm-2 cm)
6. Ground electrode
7. Transparent material (Perspex PMMA)
8. PVC as the frame of the test cell
9. Mineral insulating oil

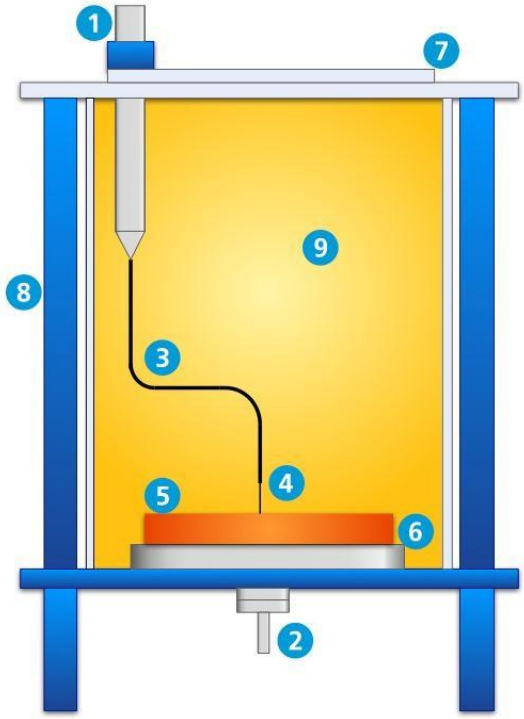

Figure 5.4 Schematic of second test cell

The HV connection to the needle electrode is now in two parts: The first section is a copper rod offset from the central axis of the test cell the length is 10 cm, diameter is 0.6 cm; the second section is a brass tube with an outer diameter of 1 mm. This was bent into two 90° bends. So that the gramophone needle mounted in the end of the tube was located on the vertical axis of the test cell. There are two reasons for using this brass tube:

1. Since the camera is located vertically above the test cell. The small diameter of the tube reduces the area of the sample which is obscured by the electrode. In first test cell, the upper electrode and HV connection will generate a relatively large shadow that blocked the actual discharge pattern;
2. Light emission due to discharges from the HV connection along the surface of

the oil has been moved away from the area of active surface discharge, the distortion due to the meniscus mentioned above has also been moved away from the active surface discharge area. To further reduce problems with light emission at the surface of the oil an insulating sleeve was placed round the HV connection.

The point of the upper electrode is a gramophone needle made of steel; it connects to the brass tube with a friction fit. The reason for choosing this type of needle is to achieve a consistent electrode profile. Figure 5.5a show 4 needles under a microscope indicating that the profiles are consistent. Figure 5.5b shows a gramophone needle next to a standard thickness block which was used to determine the tip radius.

The gramophone needle was changed each time the oil and sample was changed. Microscopic examination of needles that had been used in tests showed no significant damage to the tip after each samples test (there are 4 different voltage level and 5 tests for each sample under each voltage level.)

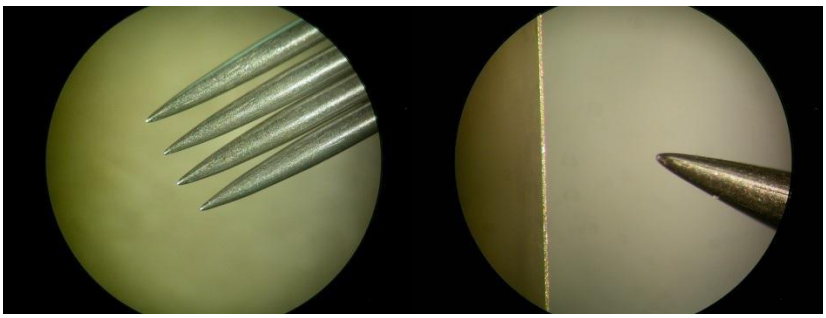

(a) (b)

Figure 5.5 (a) Four soft gramophone needle; (b) Soft gramophone needle compare with standard thickness (25 µm)

The Lower electrode (ground electrode) is a flat plate made of aluminium. The diameter of this plate is 9 cm, the thickness is 0.5 cm. The distance between upper and lower electrodes is designed to be adjustable due to the possible thickness variation of solid samples. It can be set between 0.5 cm and 2 cm, however the available distance range is from 0.1 cm to 7 cm.

5.2.2 Insulating liquid

The basic knowledge of insulating liquid has been introduced in Chapter 2. For this project, there were three different liquids under consideration for the second insulating material: synthetic ester, Reclaimed inhibited Mineral oil and Mineral oil.

For physical property, synthetic ester and mineral oil are clear liquid, reclaimed inhibited Mineral oil is yellow liquid. It was felt that the colour of the reclaimed inhibited mineral oil would affect image capture of surface discharges. The reclaimed inhibited Mineral oil is also not a pure liquid, so there were also concerns with the consistency of its properties.

Between Synthetic ester and mineral oil, Mineral oil was chosen as the other insulating material, Shell Diala D is readily available within the research group. As insulating oil, its dielectric properties has been well tested[3]–[7], the details are shown in Table 5.1, it is very stable and good insulating liquid in general conditions. The relative permittivity of mineral oil is 2.5; The breakdown voltage in cone-sphere electrode configuration (spacer 2 mm) under different voltage condition is[8]:

Table 5.1 Breakdown voltage of liquid

Voltage condition	Breakdown Voltage (kV)
AC voltage (50 Hz)	30.4±3.4
Nanoseconds Impulse Voltage	154.7±16.4

Although synthetic esters were not investigated in this project it would be interesting to examine their performance under the same experimental conditions.

5.3 Waveform collection

The waveform collected is the sensed current pulse from each discharge. It can provide the detail of discharge current over certain period, by comparing with the captured images of the discharge; more discharge behaviour can be investigated. From Figure 5.1, the discharge monitoring uses two parts: the current sensor and oscilloscope. The current sensor used in this experiment is a High frequency current transformer (HFCT) with a transfer impedance of 5 V/A, the frequency response is shown in Figure 5.6. This type of HFCT has been used before for measuring partial discharge currents [9].

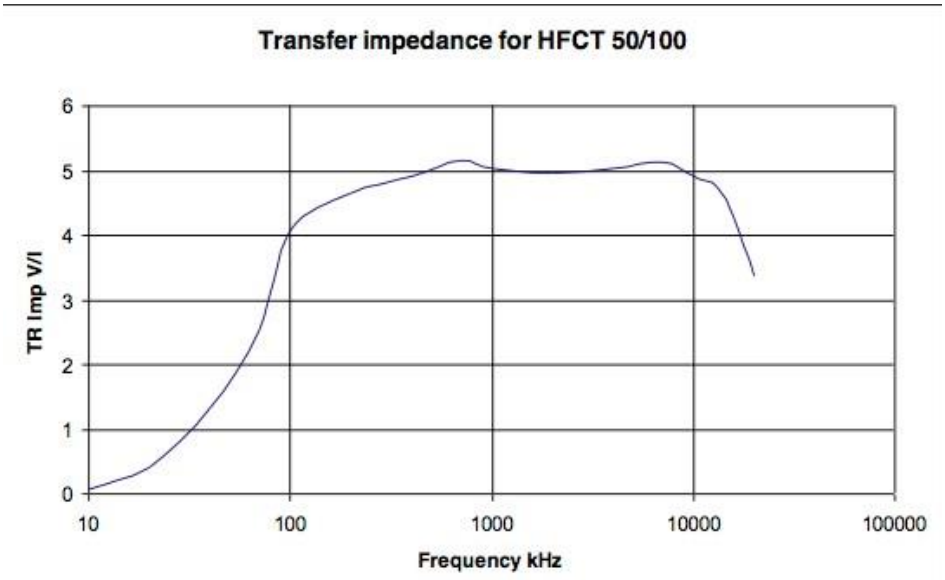

Figure 5.6 Transfer impedance for HFCT 50/100(adapted from HFCT datasheet)

Two oscilloscopes have been used. The first was a Tektronix TDS3054C, bandwidth is 500 MHz, the max sample rate is 5 GS/s and record length is 10K points. This was used initially to determine the size and shape of the discharges occurring. The second oscilloscope used was TELEDYNE LECROY WaveRunner 610Zi; bandwidth is 1 GHz, the max sample rate is 20 GHz and max recording length can be 128 Mpoint. This allowed the discharge activity over 100 cycles of the waveform to be observed and stored for future analysis.

5.4 Discharge images acquisition

A portion of results in this project's rely on images of the discharges. This section will give the details of the hardware and software used for image acquisition. There are three hardware elements:

- **Industrial camera:** Full scanning camera, uses progressive scanning rather than interlaced scanning so each frame contains more pixel information.

- **Frame Grabber**: Hardware for transferring the data between camera and desktop, such as camera setting commands from camera operating software and the image data to storage;

- **Operating desktop:** with a high speed slot for frame grabber to connect, it is also provides the hardware for storage of images.

There are three pieces of software that were used for image acquisition:

- **CLCtrl:** Driver and camera setting software from Sentech
- **MIL Library:** Frame grabber control and program software
- **MATLAB:** Frame software for MIL library, also the main program software for image processing and Fractal analysis

5.4.1 Equipment selection

In the initial tests, a PHOTRON FASTCAM 10K SERIES camera (Figure 5.7a) and a Dell Optiplex 760 Desktop were used. Although it is from 1980s, this camera is an industrial camera with 10000 full frame per second capture speed, a 512x480 display size under 250 fps which was hoped to provide a relatively good quality image for analysis.

However, after a few test runs for this experiment set, the results from PHOTRON FASTCAM 10K SERIES camera indicating that it was not a suitable camera for this project. The two reasons for making this conclusion were:

1. Although this camera has a very high frame rate, the light sensitivity was too low to capture adequate images of the surface discharges.
2. The pixel resolution was not very high. As has been mentioned, the image captured will be sent to a program to analysis the fractal dimension of each surface discharge. The accuracy of results depends on the pixel resolution of the camera. The higher, the better.

(a) **(b)**

Figure 5.7 (a) PHOTRON FASTCAM 10K SERIES; **(b)** Sentech CL33A

A new camera was then selected; it required a high light sensitivity and relatively high resolution. The new camera chose is Sentech CL33A (Figure 5.7b). It is a full scanning monochrome CCD camera with 30, 60 and 90fps frame rates. It can provide a high light sensitivity at 0.12 Lux @ F1.2, 50 IRE and the active resolution is 648×494. Figure 5.8 are the captured images from the cameras described above. As can be seen in Figure 5.8, the discharge image captured by Sectech CL33A is much better quality than the one captured by PHOTRON FASTCAM 10K SERIES.

The frame grabber used was Matrox Solios eCL which is a one base Camera Link configuration. It has 64MB acquisition buffer and fully compatible with Sentech CL33A camera. Desktop used was a Dell Optiplex 745 with one High speed PCIe slot with transferring speed at 5Gbps. These frame grabber was operated by two softwares: MATLAB and the MIL library.

(a)

(b)

Figure 5.8 (a) Image captured from PHOTRON FASTCAM 10K SERIES;

(b) Image captured by Sentech CL33A under the same conditions

5.4.2 Procedure for Capturing Images

Before image capture was started, the capture system was prepared:

1. The camera operating parameters: shutter speed (1/60s), frame rate (60fps), trigger mode (Normal) were set using the CLCtrl software.
2. In the MATLAB operating environment using the Image Acquisition Toolbox, the storage location for output files was set with the number of frames to be captured, typically 120 and the trigger mode.

Once the system has been setup, recording can begin. The practical operating procedure is as follows: The camera started to record at the same time as voltage was applied to the sample, under the control of MATLAB and MIL. The recording images will be transferred through the frame grabber to the desktop and stored in the hard drive. The stored file is actually an uncompressed video. This was then processed using

Registax 6 obtained on the internet and MATLAB programs written by the author. Figure 5.9 shows the steps of this process:

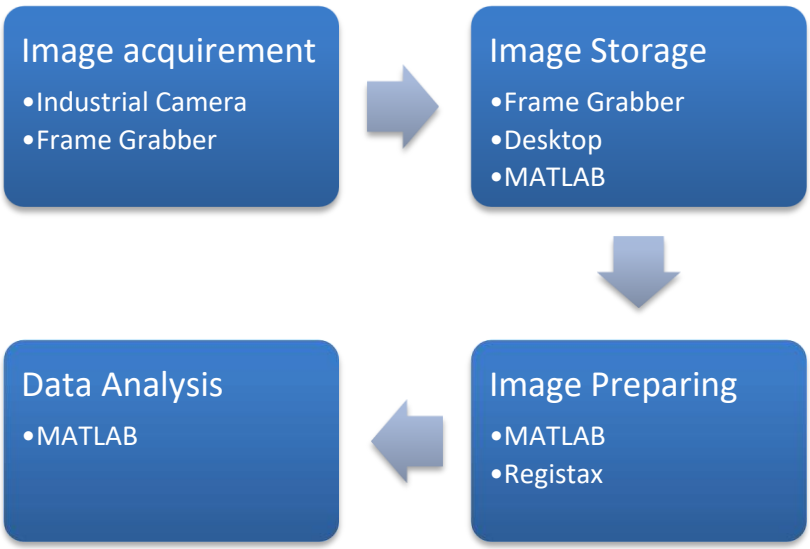

Figure 5.9 Image process steps

5.5 Image data processing and analysis

This section introduces the image data preparing detail. It will discuss the data collected from the images: why this set of data is needed, what are they representing; the process steps, the methods used and the reason for such processing.

5.5.1 Processing steps

There are 7 steps performed after discharge images were captured, these are:

Image processing

1. **Frames separation:** as mentioned in Section 5.4.1, the activities of the discharges were stored into an uncompressed video file. In order to analyse it frame by frame it was necessary to split the Video file into individual frames;
2. **Image synthesis**: to identify the regions in the images where discharges occurred, A composite image based on all the frames was synthesized for further analysis;
3. **Discharge pattern enhancement:** The composite image was then enhanced using the RegiStax6[10] image processing software to clarify the boundaries of the discharges that had occurred.

A more detailed description of Steps 1 to 3 is provided in Section 5.5.2 below

4. **Determine the background threshold:** For determination of fractal dimension and the maximum length of the discharge it was necessary to convert the image into a binary image. A threshold value needed to be found to allow background regions to be set to black (0) and light emitting regions set to white (1). The determination of this threshold is described in Section 5.5.3.
5. **Fractal analysis:** Using fractal analysis function developed in MATLAB (Appendix B) the fractal dimension of the composite image was determined.
6. **Maximum Branch Length:** Base on the binary image used for fractal analysis the max distance that the discharge branches reached was determined.
7. **Total light emission analysis:** Functions were developed in Matlab to allow the total light emission from the active discharge areas for each frame, using the binary image from Step 4 as a mask. This number should relate to the energy dissipated in the discharges in each frame.

The output of Steps 5,6 and 7 provide methods of numerically characterising the behaviour of the discharge and will allow comparisons to be made between different nanocomposites.

5.5.2 Image separation, Synthesis and enhancement

The output of image acquirement system is an uncompressed RGB Video. A combination of defined functions in MATLAB (dir(), VideoReader(), read(), imwrite() and rgb2gray())was used to separate the video into individual frames and convert them into 8 bit greyscale images. Greyscale was used as it reduced the storage requirements and no information was lost because the video camera was monochrome This individual images were then synthesized into one image which showed all recorded information of discharge in that particular capture period (60fps for 120 frames, shutter speed 1/60 sec), Figure 5.10 shows the process.

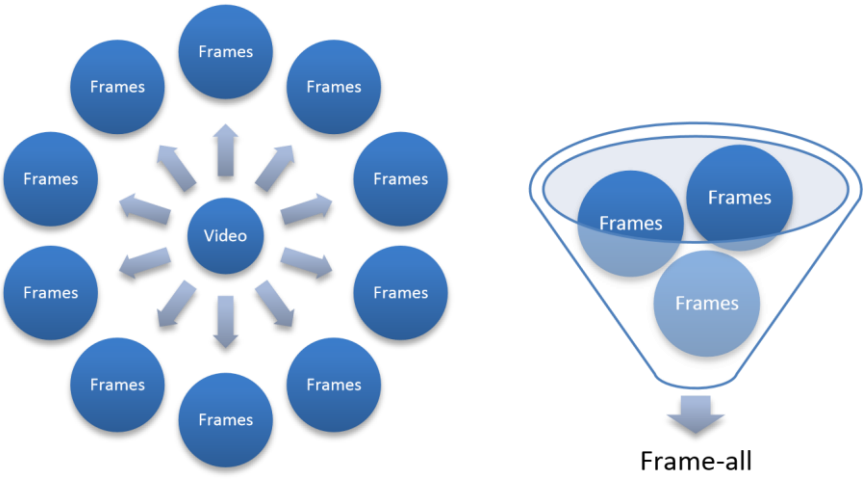

Figure 5.10 Process step diagram about separation and synthesis

Base on the principle of filming, during certain period of time, each frame will be recording the events occurred during 1/60 sec as the shutter opened and the synthesized image will be carrying all information during 2 seconds as the total filming time. Figure 5.11 shows the comparing between one frame and synthesis frame. As can be seen that Figure 5.11a is part of the Figure 5.11b.

(a)

(b)

Figure.5.11 (a) One frame separated from the capture video;

(b) Synthesis image from same video;

After synthesizing, the one image will be put in RegiStax6 for discharge enhancement. RegiStax6 is a free image processing software focusing on processing astronomy images by using wavelet. It provided the capability of enhancing the contrast of the images, particularly where the discharge activity was faint and also allowed the edges of the discharge channels to be sharpened to enhance the different between the discharge pattern and the background.

From the image comparison in Figure 5.12, it is easy to see that processed image has shown more detail than the unprocessed image. After a number of tests, the processing scheme that optimized the discharge image was found and saved, this scheme was then used for all composite images. The technical details of the scheme depend on the image captured, for different experiment setup and further research, it is better to explore the scheme in each cases and be consistent.

(a)

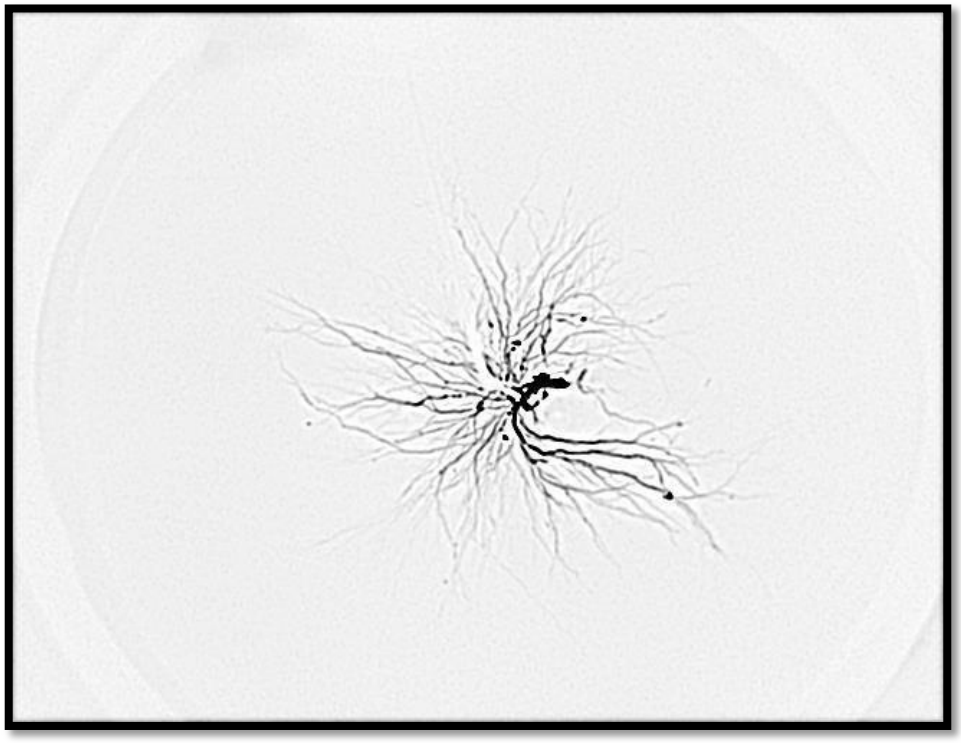

(b)

Figure.5.12 (a) Unprocessed synthesis image; (b) Processed synthesis image

5.5.3 Threshold determination

For fractal analysis and determination of discharge length, a binary image was used. This required the determination of a threshold. Any pixel with a value greater than or equal to the threshold will be set to 1 in the new image; pixels below the threshold lower number were set to 0. The MATLAB function im2bw() requires a threshold value in the range of 0 to 1, 1 corresponding to a pixel value of 255.

Figure 5.13 are grey and binary images produced by the im2bw() function with a threshold value of 0.09 which corresponds to a greyscale value of 23.

Threshold determines the binary image quality; therefore, it has a strong impact on fractal analysis result. If the threshold is set too low, points will appear in the binary image due to noise in the background of the greyscale image. In fractal analysis, these point due to noise will be considered as part of discharge leading to a false value for the fractal dimension; if the threshold is set to high, pixels which are part of the discharge would be falsely considered as background and set to 0. A method of determining an appropriate threshold value was therefore required to optimize the binary image.

The method to determine the threshold is to check the histogram of the greyscale image; in MATLAB, there is a function imhist() to display a histogram about number of value in every pixel of image. Figure 5.14 (a) is one histogram from the composite image captured under 35 kV AC condition at 60 frames per second for an epoxy sample without filler. In this diagram, it can be seen that there is a large peak in the histogram in the region of 10 to 17. Above a pixel value of 17 the number drops rapidly to a pixel value of 23. Above this value small peaks are observed in the histogram.

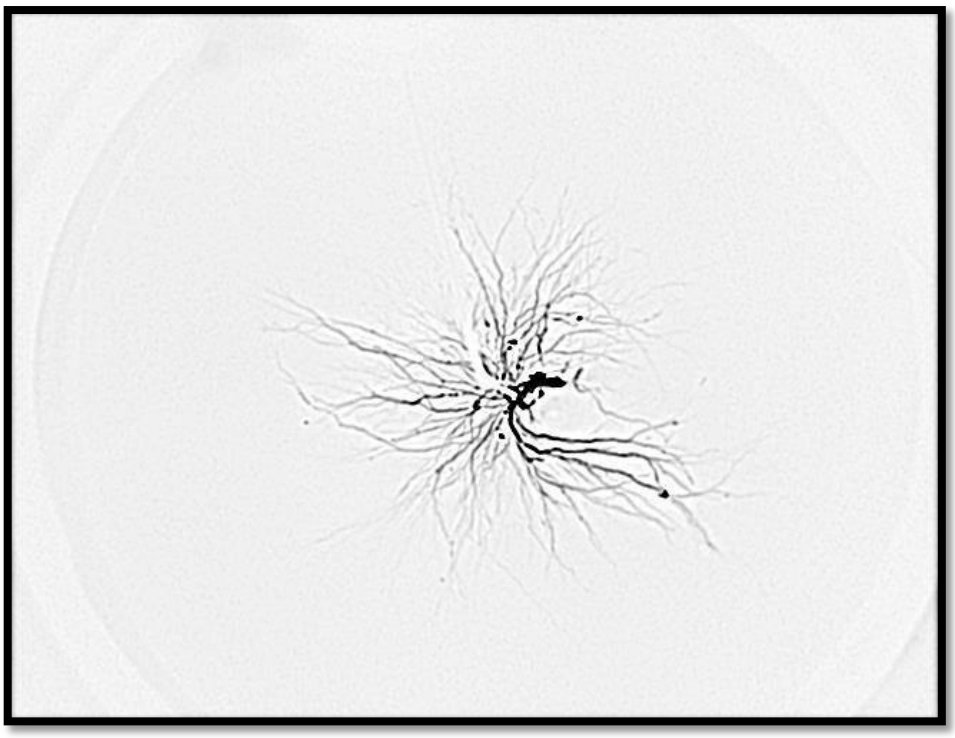

(a) Gray image

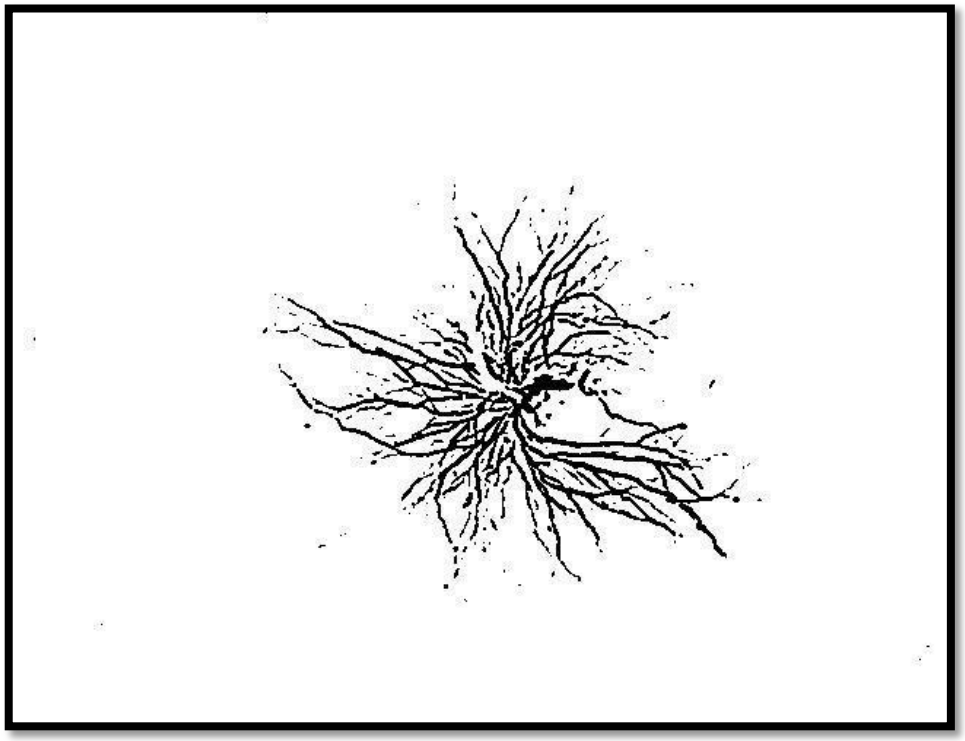

(c) Binary image

Figure 5.13 Grey to Binary image Figure 5.14 (b) is a histogram of an image which didn't show a minimum at the value of 23 but the appearance of a shoulder. However processing this type of image with a threshold value of 23, also produced suitable binary images. It was assumed therefore for all images that values below the threshold value of 23 were part of the background noise.

During data processing random composite images were tested with a range of values between 20 and 27. In these cases again the threshold value of 23 was judged to produce the optimal results, when threshold value was set to 20, part of the background was considered the discharge, when threshold was set to 27, part of the discharge pattern was missing from the results. This test was applied to 10 of the 500 composite images produced in the project.

It is important to point out that image capture was performed in as near as possible identical light conditions where the expected background light and its noise should be similar, due to the technical limitation of the equipment, complete dark environment was not acceptable. However the threshold value used is related to the environment for running these experiments and it would be necessary if the parameters were changed, to again examine histograms to determine the suitable threshold value in different cases.

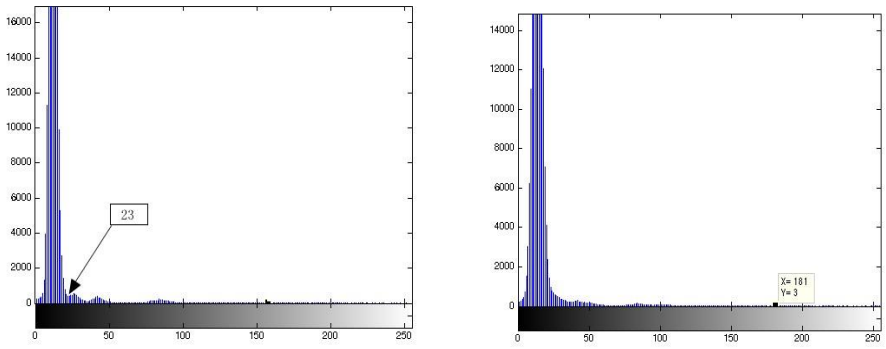

(a) (b)

Figure 5.14 Histogram of a composite image

5.5.4Image analysis Methods

After the threshold was determined, the images would be analysed with developed MATLAB functions to determine the fractal dimension, total light emission and the final length of the surface discharge pattern. These three variables would be used to describe and compare each discharge pattern over certain period (2 seconds). This section will describe the basic idea and the actual program structure of each M-file. First comes the Fractal dimension calculation.

5.5.4.1 Fractal Dimension

For fractal dimension calculation: In this project, the pixel resolution is 648*494. In order to analyze image, after it has been synthesized and transform into binary image, the following steps was then used to calculate the fractal dimension, Figure 5.15 shows the program structure:

1. Introduce the binary composite image into MATLAB. It is much easier to run the calculation if the image is a square, since the image captured is 648*494, it is better to generate a new square matrix of dimension 648*648 which contains the original image matrix and to fill the new elements with value of 0. The fractal dimension of the pattern does not depend on the size of the image.
2. Divide this matrix into smaller square sub matrices which contain k*k elements (k = 1, 2, 4…2^x). These sub matrices are selected so that each element of the main array is contained in only one sub matrix. The sub matrices are then all checked and total number of sub matrices that contain at least one element of value 1 is calculated. The number of the squares with 1 inside sees as N_k. As k is changed, N changes as well ($N_1, N_2 \ldots N_{2^x}$).
3. Create a log-log plot using $-\log k$ and $\log N_k$ as horizontal and vertical axis. There would be a line of best fit on the log-log plot; the slope of this line will be equal to the fractal dimension.

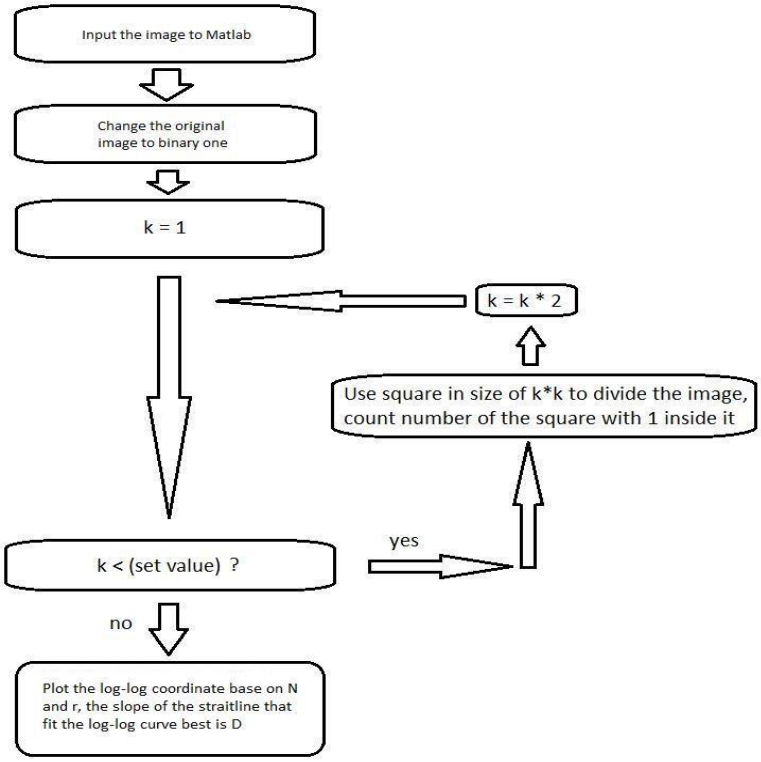

Figure 5.15 the procedures of analysis program (r represents the side length)

One example of the output of this function is showing in Figure 5.16. The red line shows the space-filling box-count for an image where every pixel is one. This would have a fractal dimension of 2.The blue line is the actual box-count results for a discharge. The fractal dimension associated with the blue line is 1.7.

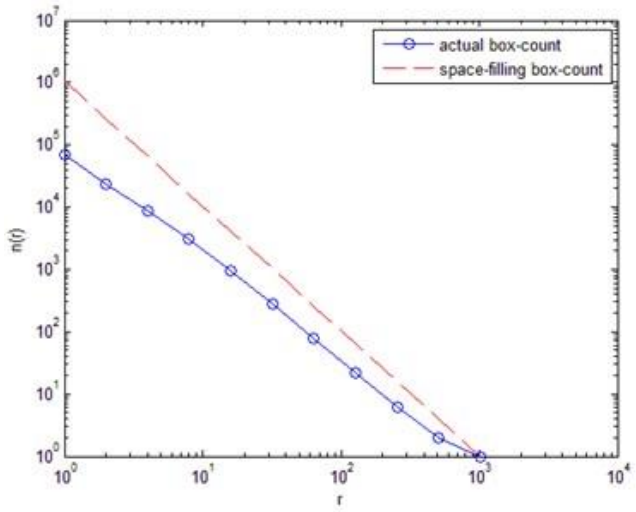

Figure 5.16 Example of an Output plot of the fractal dimension

5.5.4.2 Total light emission and final length

The fractal dimension measured for a discharge does not contain information about the intensity of the discharge process and does not describe the scale of the discharge pattern. Therefore it is necessary to also measure the Total Light Emission (TLE) and Final Length (FL) of the discharge.

The idea of the TLE is this: after the surface discharge image was transform into grey image, value of each pixel in the image is between 0 and 255. TLE is calculated by summing the pixel value from the active discharge area over all the frames captured during the two seconds measurement period. By ignoring the background regions in the images the contribution of background pixel values to TLE is eliminated. The steps are as follows:

1. The composite image before image sharpening with Registax was converted into a binary image in a similar manner to that described above. This image was used as the mask matrix;

2. The dot product of the mask matrix and each original image matrix separated from the captured video was calculated. This value corresponds to the sum of the pixel values in the active regions of the discharge during the frame.

3. These values were then summed over all of the frames to calculate the TLE.

The final length is measured manually by using the Registax 6 processed binary synthesis image. The brass tube forming the upper electrode leaves a relatively small shadow in the captured image. The tip of the shadow was assumed to be the initiating point of the discharge on the image. The functionality provided in MATLAB to measure the separation of two points on an image was then used to find the distance between the point of initiation and the end of the discharge channel that had reached the largest distance. The value obtained is expressed in units of pixel size. As the geometry of the camera, test cell and sample were fixed (Appendix A), the distance between these three elements is consistent for all of the images. Given the known dimensions of the sample, the measured length can be scaled to the actual length of the discharge. Figure 5.17 shows the standard length measurement, Figure 5.18 show an example of the measurement of the final length of a discharge pattern.

The radius of the earth electrode is 45 mm and the length unit associated within the capture image was 308, so the relationship between the measured length unit and reality length is in Equation 5.1:

$$Real\ Length(mm) = \frac{45}{308} \times Measured\ Units(pixel\ size) \quad (5.1)$$

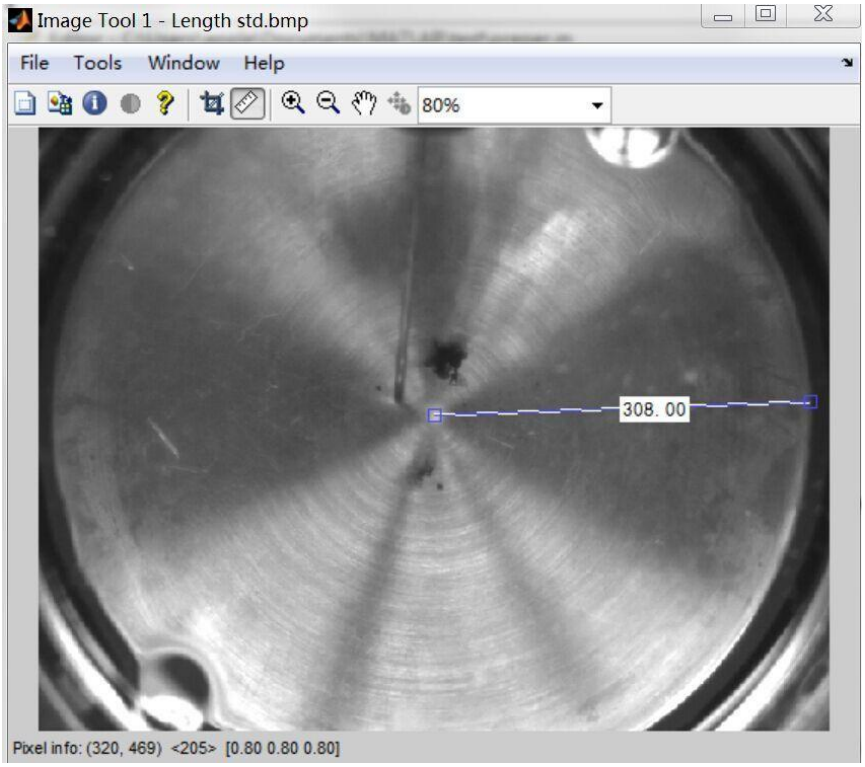

Figure 5.17 Standard length measurement

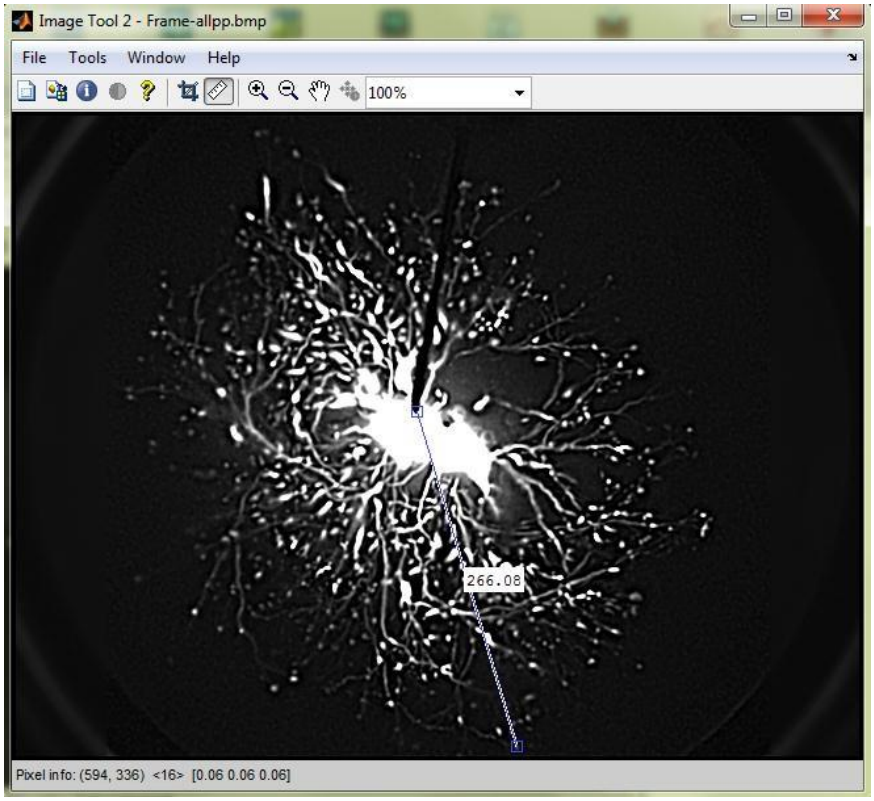

Figure 5.18 Final length measurement

5.6 Summary

This chapter described the development of the experimental setup for causing and observing surface discharges on the epoxy and nanocomposite samples. The general view of experiment setup was described along with the technical detail of equipment used. The reasons for selecting experimental equipment were discussed along with the problems for linking them together and how these problems were solved. The data processing performed on images prior to analysis was also described.

In Chapter 6, the experiment results will be listed and the further analysis will be discussed. There will also be a section about the relationship between the optical experiment results and discharge condition. The relationship between optical experiment results and current data will also be discussed.

References

[1] Y. Nakao, a. Mouri, T. Itooka, H. Tagashira, Y. Nakagami, M. Miyamoto, and Y. Sakai, "Propagation of creepage discharge on solid insulator in insulating oil," *Proc. 1999 IEEE 13th Int. Conf. Dielectr. Liq. (Cat. No.99CH36213)*, pp. 257–260, 1999.

[2] C. Ecole, C. De Lyon, and E. Cedex, "Creeping Discharge on Solid/Liquid Insulating Interface under AC and DC Voltages," in *Electrical Insulation and Dielectric Phenomena, 2000 Annual Report Conference on*, 2000, pp. 784–787.

[3] Y. Jing, I. V Timoshkin, M. P. Wilson, M. J. Given, S. J. Macgregor, T. Wang, G. Street, and J. M. Lehr, "Dielectric Properties of Natural Ester , Synthetic Ester Midel 7131 and Mineral Oil Diala D," pp. 644–652, 2013.

[4] K. Bandara, S. Member, C. Ekanayake, T. K. Saha, and S. Member, "Comparative Study for Understanding the Behaviour of Natural Ester with Mineral oil as a Transformer Insulating Liquid," pp. 792–795, 2014.

[5] P. Rain, E. Brun, C. Guillermin, and S. W. Rowe, "Experimental model of a silica/epoxy interface submitted to a hygrothermal aging: a dielectric characterization," *IEEE Trans. Dielectr. Electr. Insul.*, vol. 19, no. 1, pp. 343–351, Feb. 2012.

[6] S. Rao and R. Rao, "Cure studies on bifunctional epoxy matrices using a domestic microwave oven," *Polym. Test.*, vol. 27, no. 5, pp. 645–652, Aug. 2008.

[7] C. Y. Perkasa, N. Lelekakis, T. Czaszejko, J. Wijaya, and D. Martin, "A Comparison of the Formation of Bubbles and Water Droplets in Vegetable and Mineral Oil Impregnated Transformer Paper," *IEEE Trans. Dielectr. Electr. Insul.*, vol. 21, no. 5, pp. 2111–2118, 2014.

[8] I. V. Timoshkin, R. a. Fouracre, M. J. Given, S. J. MacGregor, P. Mason, and R. Clephan, "Dielectric properties of Diala D, MIDEL 7131 and THESO insulating liquids," *Annu. Rep. - Conf. Electr. Insul. Dielectr. Phenomena, CEIDP*, pp. 622–625, 2008.

[9] R. Sarathi, S. Aravinth, and K. Sethupathi, "Analysis of surface discharge activity in epoxy nanocomposites in liquid nitrogen under AC voltage," *IEEE Trans. Dielectr. Electr. Insul.*, vol. 21, no. 2, pp. 452–459, Apr. 2014.

[10] C. Berrevoets, "RegiStax 6," 2011. [Online]. Available: http://www.astronomie.be/registax/. [Accessed: 12-Jul-2015].

6. OPTICAL RESULTS ANALYSIS

As described in Chapter 5, there are three main optical data collected from the experiments: Fractal dimension of the discharge pattern, the total light emission from image capture period and the final length of the discharge branch reached on the sample surface. Each of them provides information on the discharge appearance. By comparing them for different nanocomposites and applied voltages, differences can be seen in these values, these differences may relate to the dielectric permittivity or condition changes. The voltage level of the experiment was set between 30 kV and 45 kV with 5 kV steps; for each sample type, there are at least 5 samples were tested; for each voltage level, there are 5 tests were made on each sample.

In this chapter, the test results will be stated and discussed. In Section 6.1, the results for fractal dimension, light emission and final length will be listed and described; in Section 6.2, there are the discussions of the permittivity changes affecting the optical results and other possible meanings that are indicated.

6.1 Optical Results

Surface discharge behavior was investigated for five samples for each nanocomposite material: Pure Epoxy, 0.1 wt% ZnO, 0.5 wt% ZnO, 1 wt% ZnO, 2 wt% ZnO, 3 wt% ZnO, 0.1 wt% Al_2O_3 and 0.5 wt% Al_2O_3.

From early experiment, the initiating voltage level for surface discharge on interface of epoxy and Shell Diala was around 24 kV. The minimum voltage level was set at 30 kV based on the absolute certainty of initiating surface discharge. The early work also showed that voltages above 45 kV could lead to a discharge propagation over the entire sample and breakdown to the earth plane would occur at the sample edge. This set the upper limit of the voltages applied to the sample. Four voltage levels were applied: 30 kV, 35 kV, 40 kV and 45 kV.

For every sample, 5 surface discharge tests were made at each voltage level, each of 2 s duration. There was a 10 minute interval between each surface discharge test to allow the liquid insulation to recover and any thermal motion of the oil to stop.

There were concerns about the surface degradation to the sample over the 20 tests performed, but the experimental results suggest that the surface discharge behavior was consistent. This was confirmed by performing the set of 20 measurements on 5 samples in a random order. No significant differences were observed in the behavior during these random tests. This is also confirmed looking at data over successive tests at 45 kV for 4 different pure epoxy samples, Figure 6.1.

In Figure 6.1, the fractal dimension (DF) calculated for 5 successive tests on 4 samples are shown. There is no evidence of a trend in the behavior of the fractal dimension with test number.

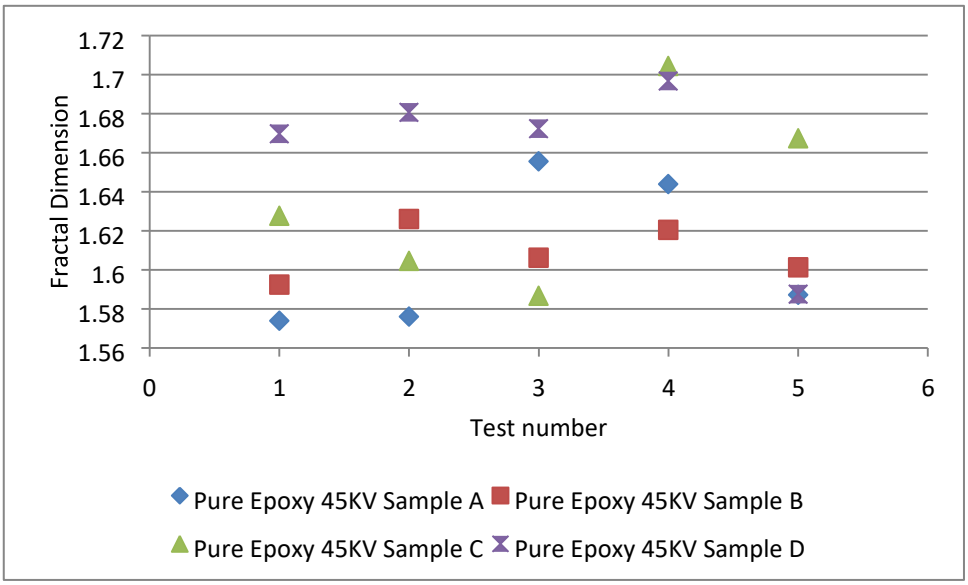

Figure 6.1 FD distribution of surface discharge on pure epoxy under 45 kV

As described in Section 5.5.4, there were three parameters used to describe the optical results: fractal dimension, total light emission and maximum length of discharge. Table 6.1, Table 6.2 and Table 6.3 shows the mean value of the three parameters different concentrations.

Tests were attempted on other nanocomposites: ZnO 4 wt%, ZnO 5 wt%, Al_2O_3 1 wt% and Al_2O_3 2 wt%. No results could be obtained from these samples as rapid bulk breakdown rather than surface breakdown occurred even at the lowest test voltages. Other samples which had been manufactured at higher concentrations (Al_2O_3 3 wt%, Al_2O_3 4 wt%, Al_2O_3 5 wt%) were therefore not tested.

Table 6.1 Mean value of Fractal dimension

FD	30 kV	35 kV	40 kV	45 kV
Pure	1.05±0.08	1.29±0.07	1.46±0.07	1.62±0.04
ZnO 0.1 wt%	1.05±0.14	1.30±0.08	1.45±0.07	1.56±0.07
ZnO 0.5 wt%	1.11±0.1	1.35±0.07	1.46±0.1	1.55±0.14
ZnO 1 wt%	1.02±0.09	1.28±0.1	1.42±0.09	1.56±0.08
ZnO 2 wt%	1.04±0.15	1.30±0.1	1.50±0.1	1.56±0.12
ZnO 3 wt%	1.07±0.13	1.39±0.09	1.50±0.11	1.62±0.09
Al_2O_3 0.1 wt%	1.06±0.11	1.26±0.09	1.45±0.06	1.59±0.04
Al_2O_3 0.5 wt%	1.05±0.15	1.25±0.1	1.47±0.09	1.59±0.05

Table 6.2 Mean value of Total light emission

LE	30 kV	35 kV	40 kV	45 kV
Pure	3147751	8687137	21553433	42006866
ZnO 0.1 wt%	615717	2435968	9611974	20491984
ZnO 0.5 wt%	297604	1569665	7310975	17467775
ZnO 1 wt%	3238841	7153490	14724208	40763567
ZnO 2 wt%	1168658	7582678	19993221	54846589
ZnO 3 wt%	605016	3085065	7539541	25790259
Al_2O_3 0.1 wt%	449059	1611173	5018558	11593026
Al_2O_3 0.5 wt%	467864	1600132	3221574	10400776

Table 6.3 Mean value of Final Length

FL (mm)	30 kV	35 kV	40 kV	45 kV
Pure	14.47±1.65	21.81±3.05	28.09±3.3	35.02±2.37
ZnO 0.1 wt%	12.45±2.19	20.52±2.34	30.16±3.23	36.93±2.83
ZnO 0.5 wt%	14.81±2.24	24.11±3.51	32.41±4.77	39.35±4.27
ZnO 1 wt%	10.69±3.33	20.62±4.94	28.06±3.19	33.65±3.3
ZnO 2 wt%	13.80±3.94	22.17±3.83	32.21±3.93	36.76±3.84
ZnO 3 wt%	16.55±2.6	26.64±3.47	33.23±3.37	39.24±3.75
Al_2O_3 0.1 wt%	15.51±1.73	22.22±1.98	29.51±1.98	36.61±2.79
Al_2O_3 0.5 wt%	14.93±1.7	22.25±2.56	28.15±2	35.44±1.84

Table 6.4 shows the standard deviation which is commonly used to indicate the range of data within a set of experimental results.

Table 6.4 Standard deviation of Total light emission

LE StD D	30 kV	35 kV	40 kV	45 kV
Pure	2030283	5110781	19143537	17947076
ZnO 0.1 wt%	508060	1848399	5621253	9025206
ZnO 0.5 wt%	324046	1483255	4303121	18134214
ZnO 1 wt%	2727819	2983254	7954660	17524246
ZnO 2 wt%	1110491	9074521	26922118	28606357
ZnO 3 wt%	804155	1676227	4406881	18274075
Al_2O_3 0.1 wt%	694817	1779506	4141936	10381681
Al_2O_3 0.5 wt%	675398	1560852	3092881	9702613

From Tables 6.2 and 6.6, it can be seen that the standard deviation for certain conditions was larger than its mean value; this suggested that the distribution of the data was not normal. The skewness, kurtosis and median of light emission data was calculated for the three parameters of DF maximum length and light emission. The comparison of median and mean values for light emission shows in Table 6.5.

Table 6.5a Comparison of median and mean for Total light emission under 30 and 35 kV

LE	30 kV		35 kV	
Type	Mean	Median	Mean	Median
Pure	3147751	2371187	8687137	7472909
ZnO 0.1 wt%	615717	432072	2435968	1843896
ZnO 0.5 wt%	297604	173238	1569665	1296899
ZnO 1 wt%	3238841	2372141	7153490	6522731
ZnO 2 wt%	1168658	859507	7582678	4418523
ZnO 3 wt%	605016	226350	3085065	2684686
Al_2O_3 0.1 wt%	449059	133820	1611173	1168566
Al_2O_3 0.5 wt%	467864	55276	1600132	834296

Table 6.5b Comparison of median and mean for Total light emission under 40 and 45 kV

LE	40 kV		45 kV	
Type	Mean	Median	Mean	Median
Pure	21553433	11554739	42006866	35875141

ZnO 0.1 wt%	9611974	9491695	20491984	19016434
ZnO 0.5 wt%	7310975	6973277	17467775	10880752
ZnO 1 wt%	14724208	12494183	40763567	34172356
ZnO 2 wt%	19993221	12868366	54846589	53786458
ZnO 3 wt%	7539541	6762685	25790259	15520686
Al_2O_3 0.1 wt%	5018558	2578056	11593026	6344390
Al_2O_3 0.5 wt%	3221574	2256716	10400776	5855053

There is clearly a difference between the mean value and the median value with the median value being lower. This indicated that the distribution of values was skew with a tail in the distribution at higher light emissions. This was confirmed by calculating the skewness of the data. It was decided to use the median value to describe the behavior of the light emission. To represent the range of a set of results, the values associated with the 0.168 and 0.832 percentiles were calculated. For a normal distribution these percentiles would correspond to +/- 1 standard deviation from the mean. However the percentile values can be calculated without knowledge of the underlying distribution. It was felt that these percentiles described the distribution more usefully than calculated standard deviations value; the calculated deviation is shown in Table 6.6.

Table 6.6a Deviation of the Total light emission under 30 and 35 kV

LE	30 kV		35 kV	
Deviation	+	-	+	-
Pure	2956480	862342	7811783	4217919
ZnO 0.1 wt%	613751	242058	1706846	877720
ZnO 0.5 wt%	319318	117132	655529	793100
ZnO 1 wt%	2182808	961146	3750102	2400671
ZnO 2 wt%	1129104	631064	4755092	2183582
ZnO 3 wt%	1149522	137221	1586915	1324795
Al_2O_3 0.1 wt%	740762	112268	889300	1029358
Al_2O_3 0.5 wt%	1078471	20590	2121490	413987

Table 6.6b Deviation of the Total light emission under 40 and 45 kV

LE	40 kV		45 kV	
Deviation	+	-	+	-
Pure	31084919	5625302	27216909	9162016
ZnO 0.1 wt%	4071434	4543324	11356469	7838588

ZnO 0.5 wt%	4405937	4502741	22112372	2002780
ZnO 1 wt%	9519621	4574003	26529006	12108810
ZnO 2 wt%	7316049	3709135	27299847	13349332
ZnO 3 wt%	3082476	3954876	7336695	4397904
Al_2O_3 0.1 wt%	7544106	1027436	13751484	8051354
Al_2O_3 0.5 wt%	5609752	1706435	13973185	10946513

The median value of Fractal dimension and maximum length of the discharge pattern was also calculated; these two sets of values are very close to each other. So for fractal dimension and maximum length, the mean value and standard deviation were used to represent the data; for Total Light Emission, the median value and percentile based deviation were chosen to represent the data.

6.1.1 Fractal Dimension

An example of fractal dimension test results with their standard deviation as error bars are shown in the Figure 6.2, To allow more detailed analysis the rest of the plots will be listed in Appendix C. In every case a linear relationship between applied voltage and fractal dimension exists. From the equations of the line of fit, the value of fractal dimension at V=0 is close to zero. The results indicated that the area of the sample surface occupied by the discharge pattern was linearly increased with voltage increased.

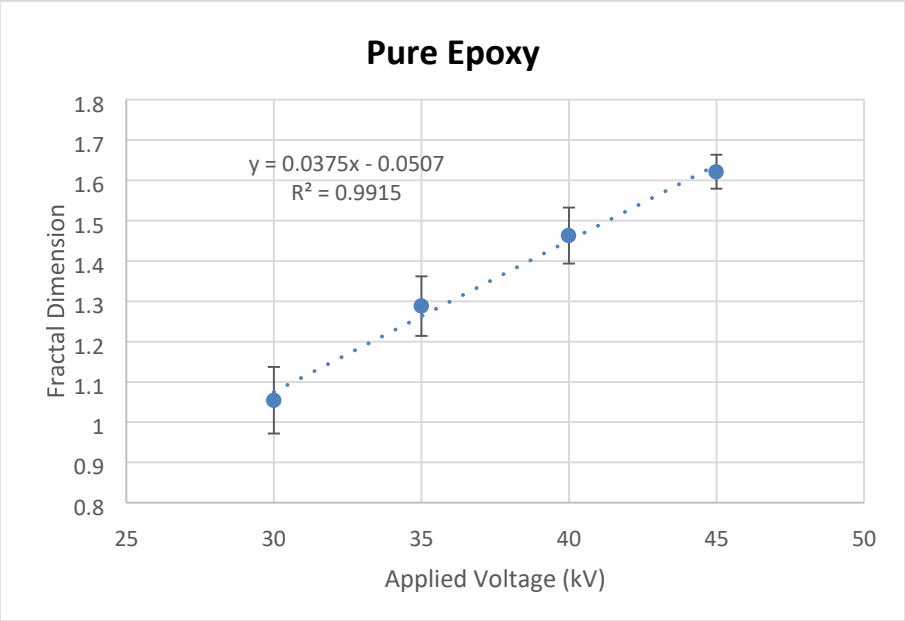

Figure 6.2 Fractal Dimension of pure epoxy

The slope of the trend line for mean value represents the increase in the surface area of the sample covered by the discharge pattern. As can be seen in Figures 6.3 to 6.5 there are no significant changes in the gradient of the lines as the composition of the nanocomposite is changed.

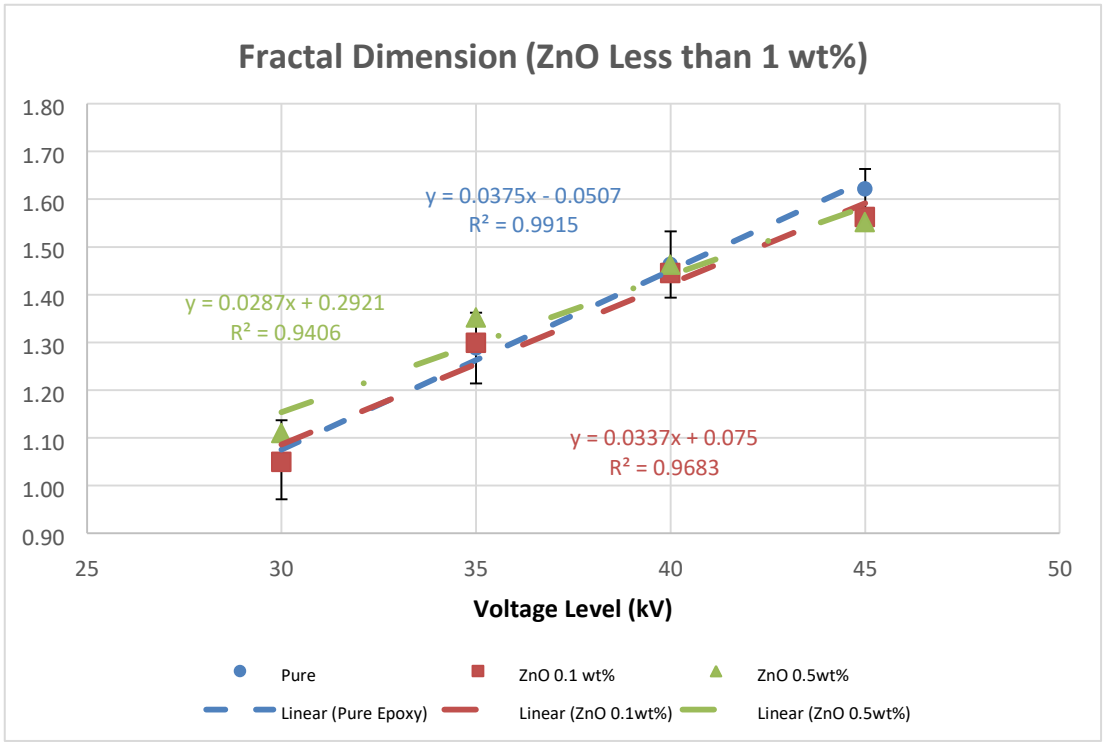

Figure 6.3 Fractal dimension of ZnO nanofiller less than 1 wt%

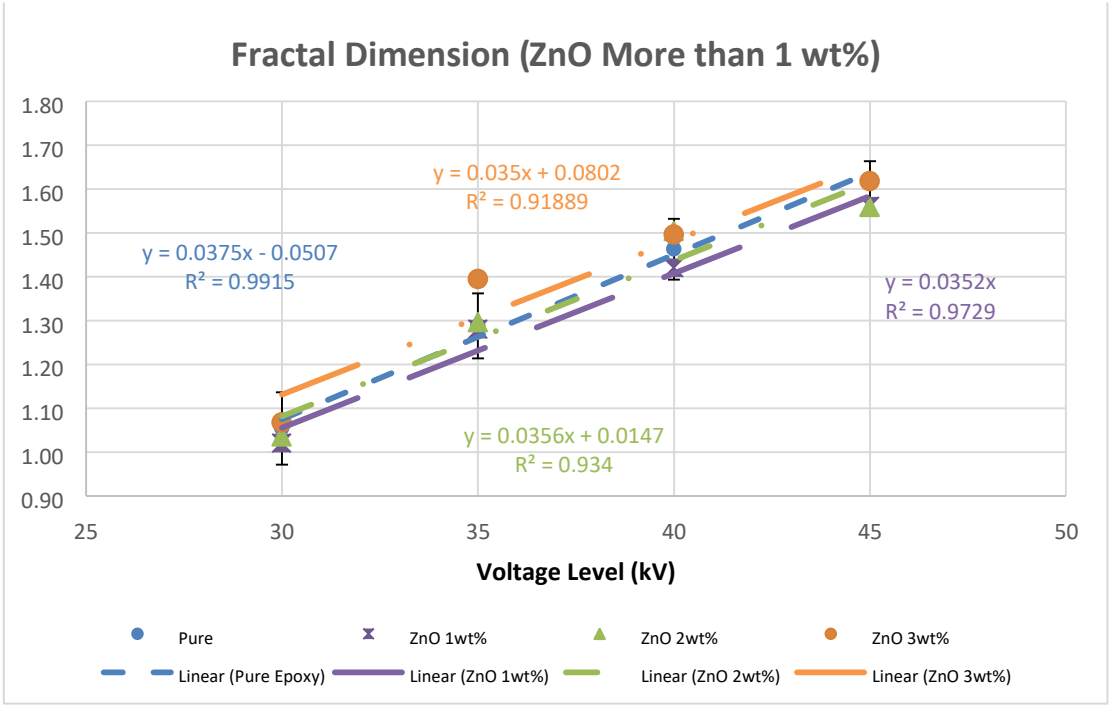

Figure 6.4 Fractal dimension of ZnO nanofiller more than 1 wt%

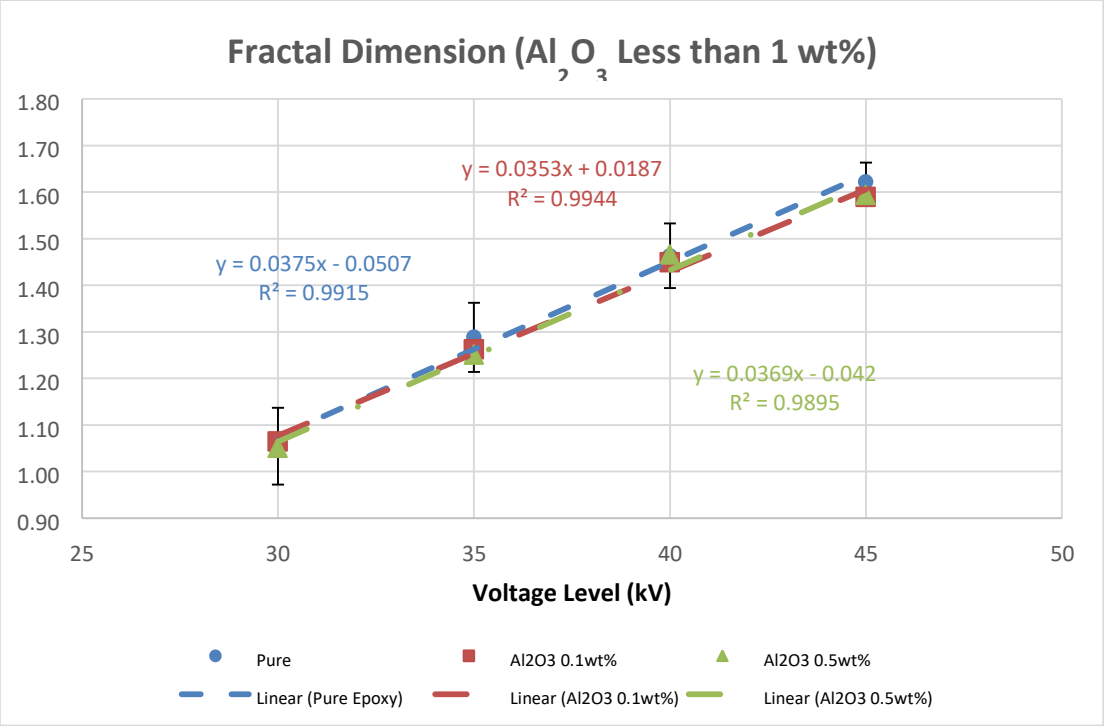

Figure 6.5 Fractal dimension of Al_2O_3 nanofiller

From the gradients and intercepts of the lines of best fit the value of applied voltage associated with a fractal dimension of 1 can be calculated. This voltage would correspond with the first observable discharge activity on the surface. These values are shown in Table 6.7. No relationship between this voltage and the composition of the nanocomposite can be seen. The average value of the voltage calculated for first observable discharge activity is 27.3 kV and the standard deviation is 1.27 kV.

Table 6.7 Analysis results of the trend line

	Gradient	Y_0	V_FD1
Pure	0.0376	-0.055	28.05851064
ZnO 0.1 wt%	0.0336	0.08	27.38095238
ZnO 0.5 wt%	0.0286	0.295	24.65034965
ZnO 1 wt%	0.0352	-2.22045E-16	28.40909091
ZnO 2 wt%	0.0352	0.03	27.55681818
ZnO 3 wt%	0.0352	0.075	26.27840909
Al_2O_3 0.1 wt%	0.0356	0.005	27.9494382
Al_2O_3 0.5 wt%	0.0368	-0.04	28.26086957

The changes on fractal dimension mean values at a given voltage of different nanocomposite do not exceed the standard deviation range of the pure epoxy results. Different nanofillers and concentration of the nanofillers seem to have no effect on the behaviour of the fractal dimension.

In Chapter 4, the dielectric property tests reveal that the permittivity was changed due to the nanofiller concentration change. Permittivity mismatch has been shown to be an important parameter for influencing the behaviour of surface discharges[1], [2]. The experiment results shows that changing the permittivity mismatch does not influence the fractal dimension of the discharge pattern.

6.1.2 Final Length of discharge branch

An example of the mean value for maximum length for discharge branches and the standard deviation is shown in Figure 6.6, the rest of the plots will be listed in Appendix C. With applied voltage increase, the max lengths of the discharge branches also increase linearly.

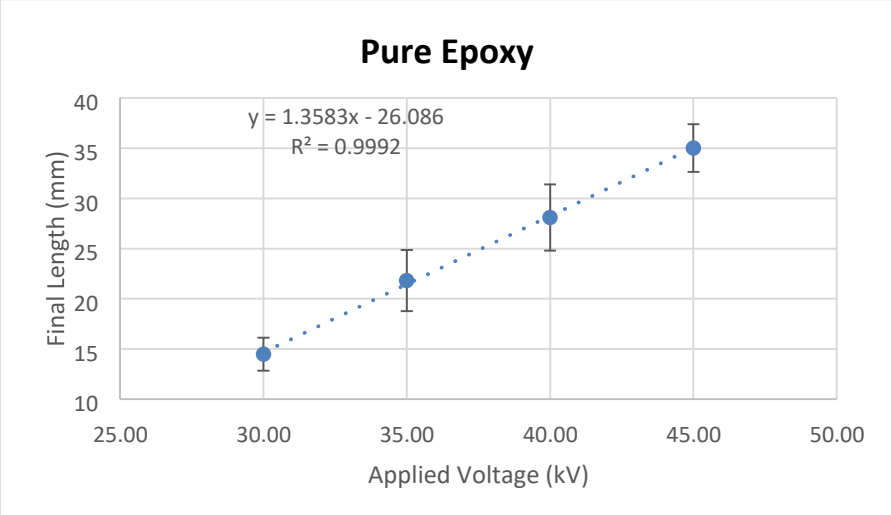

Figure 6.6 Final length of branch on pure epoxy sample

Based on the comparison of experiment results, the final length of the discharge pattern is related to the applied voltage levels. From Figure 6.7 to Figure 6.9, the final length results of different nanocomposite are all located in the standard deviation range of the pure epoxy results, which indicate that final length of discharge pattern may be not

related to the nanofiller concentration of the nanocomposite and may not relate to the solid sample property at all.

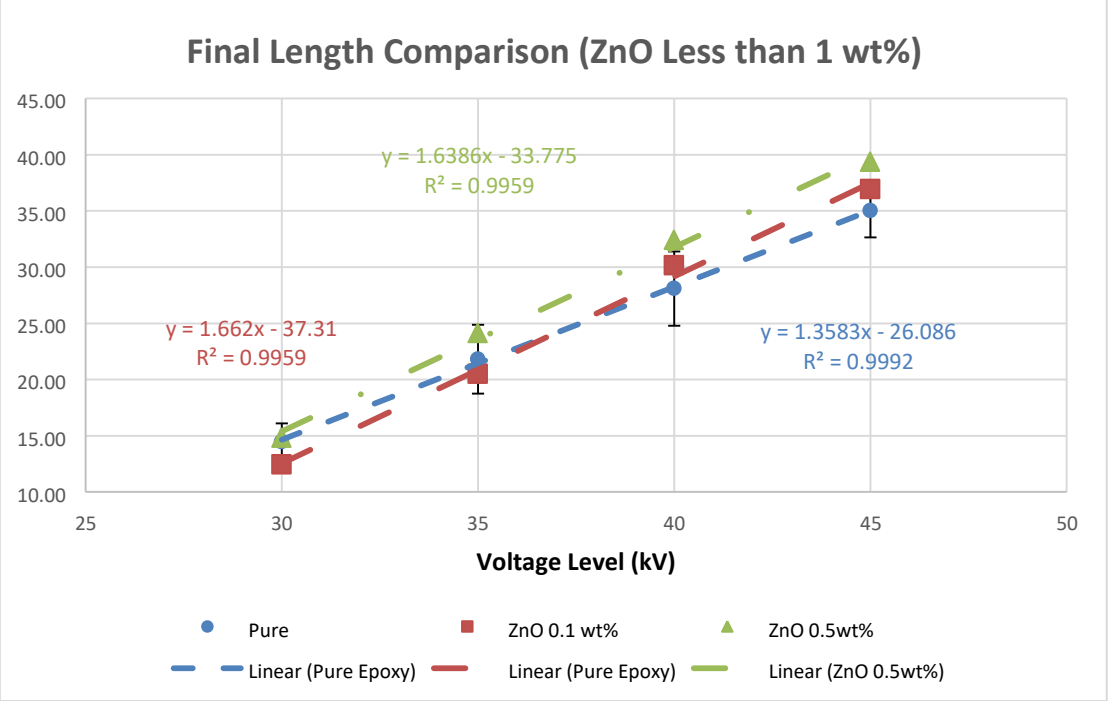

Figure 6.7 Final length comparison (ZnO less than 1 wt%)

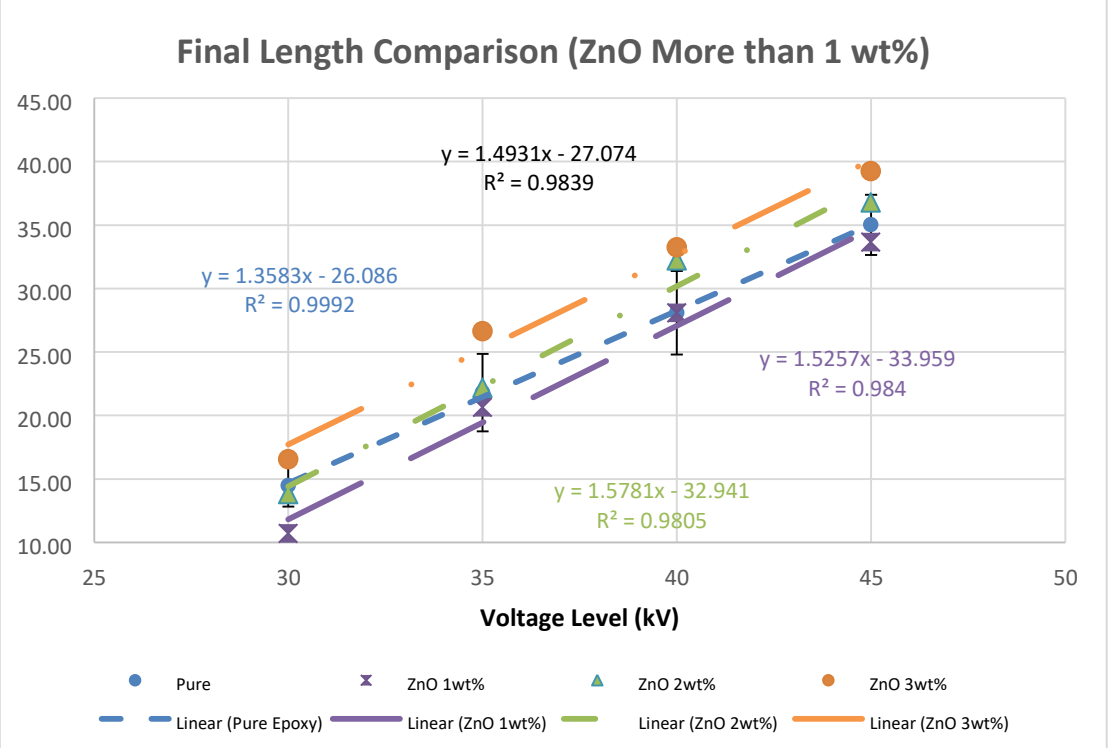

Figure 6.8 Final Length comparison (ZnO more than 1 wt%)

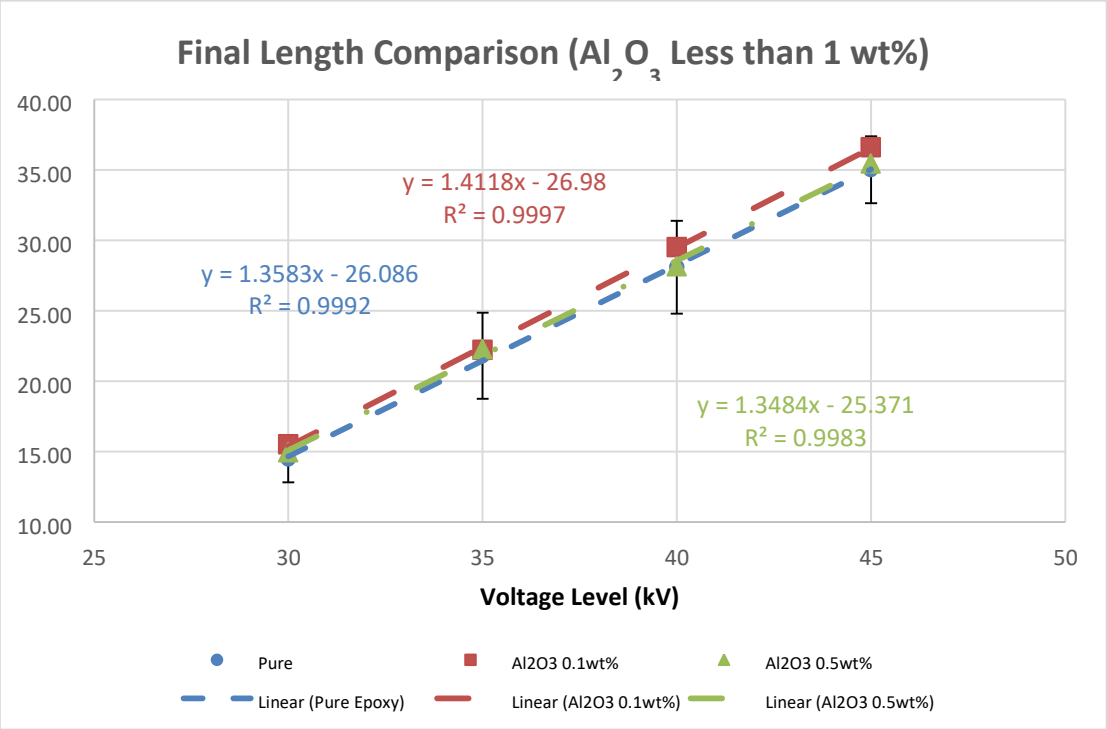

Figure 6.9 Final length comparison (Al_2O_3 less than 1 wt%)

From the gradients and intercepts of the lines of best fit the value of applied voltage associated with a final length of 0 can be calculated. This voltage would correspond with the initiation of discharge activity on the surface. These values are shown in Table 6.8. Again no relationship between this voltage and the composition of the nanocomposite can be seen. The average value of the voltage calculated for initiation of discharge activity is 20.18 kV and the standard deviation is 1.61 kV.

Table 6.8 Analysis results of the trend line

	Gradient	Y_0	V_0
Pure	1.3586	-26.1	19.21095245
ZnO 0.1 wt%	1.6616	-37.295	22.44523351
ZnO 0.5 wt%	1.6384	-33.77	20.61157227
ZnO 1 wt%	1.5264	-33.985	22.26480608
ZnO 2 wt%	1.5784	-32.955	20.87873796
ZnO 3 wt%	1.4932	-27.08	18.13554782
Al_2O_3 0.1 wt%	1.4118	-26.98	19.11035557
Al_2O_3 0.5 wt%	1.3486	-25.38	18.81951654

For the final length of the ZnO 3 wt% nanocomposite samples, the final length was over the limit of standard deviation. It will be better if the 4 wt% nanocomposite can

be tested. But as mentioned before, ZnO 4 wt% and 5 wt% nanocomposite was unsuitable for discharge pattern observation because the sample would suffer unexpected bulk breakdown.

6.1.3 Total light emission of the discharge pattern

The behaviour of the total light emission of the discharge patterns increases with increasing voltage following a power law. With the applied voltage increased, the scatter of the experimental values also increases. However unlike fractal dimension and maximum length of discharge, the behaviour of light emission was affected by the nanofiller. Initial fits to a general power law $L(V) = AV^n$ generally provided reasonable fits to the experimental data, Figures 6.10 and 6.11 are two examples. The values of the exponent n were in the range of 24 to 40 and it is not clear what this represents. Also the form of the fitting curve suggests that light should be emitted at voltages in the range of 1 to 20 kV which is in contradiction to the threshold values observed in the Fractal Analysis: 27.3 □1.27 kV or from discharge length: 20.18 □ 1.61 kV.

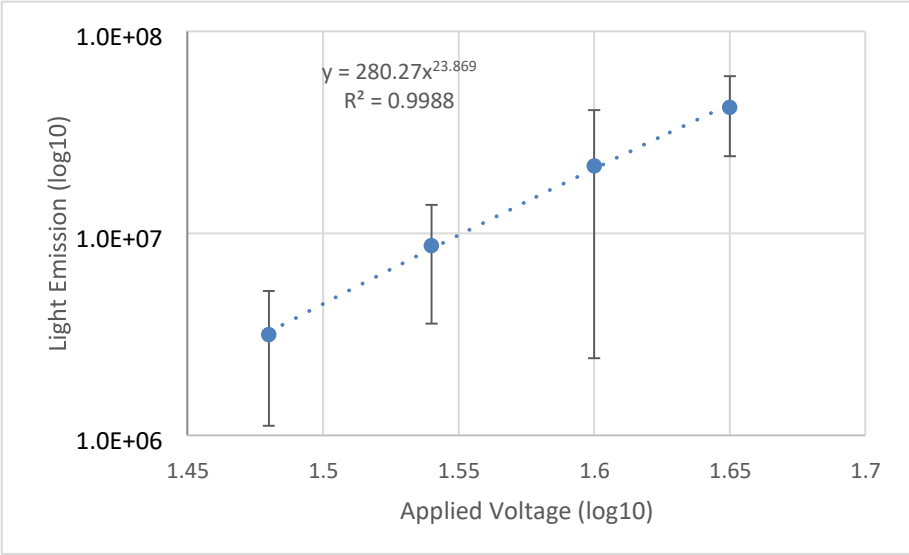

Figure 6.10 Total light emission of Pure Epoxy

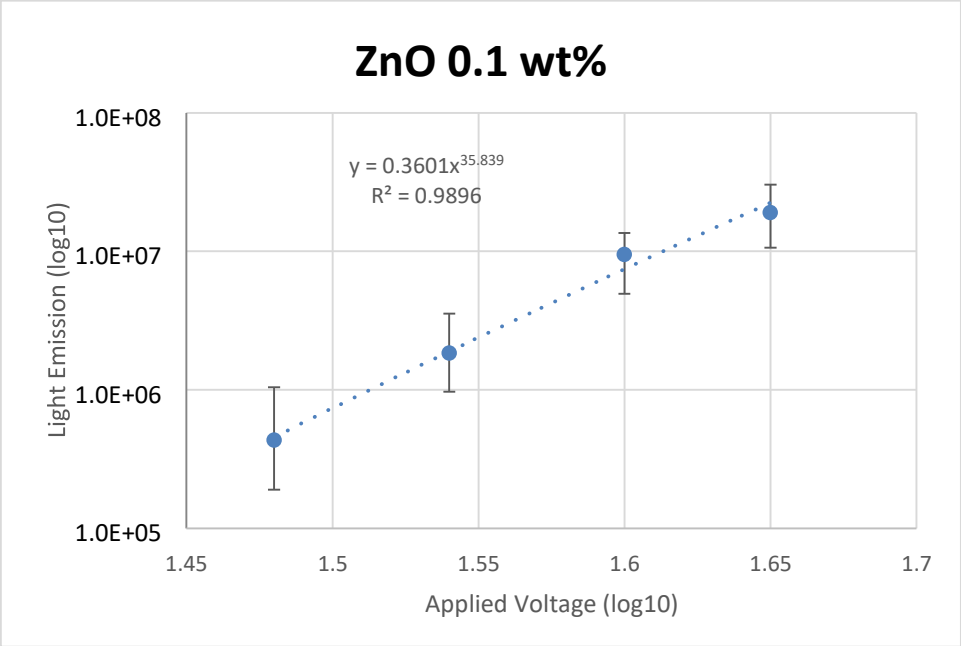

Figure 6.11 Total light emission of ZnO 0.1 wt%

It was therefore decided to try fitting the data to two possible power functions:

$$(V) = A(V - V_0)^2 \tag{6.1}$$

and

$$(V) = A(V^2 - V_0^2) \tag{6.2}$$

Equation 6.1 assumes that light emission depends on the square of a voltage difference in the system. It can be thought of as assuming that the light emission is proportional to power dissipated in a resistance. Equation 6.2 assumes that light emission is proportional to the difference of the squares of two voltages. It can be thought of as representing a change in capacitive energy storage in the system.

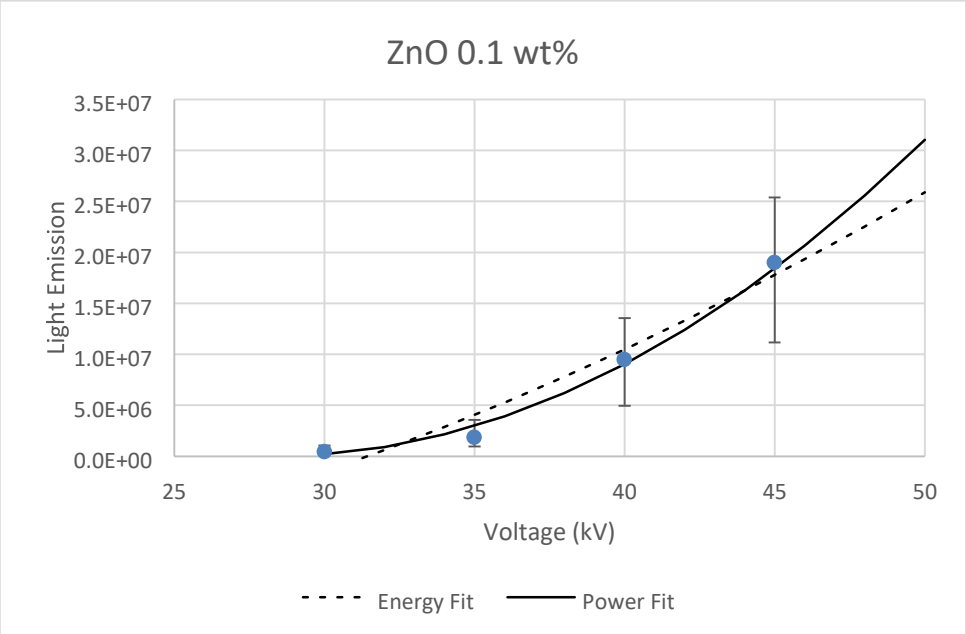

Figure 6.12 Total light emission of 0.1 wt% ZnO material fitted to power and energy plots

Table 6.9 Fit results of Equation 6.1 (power) and Equation 6.2 (energy)

	$L(V) = A(V - V_0)^2$ Power Fit			Energy Fit $L(V) = A(V^2 - {V_0}^2)$		
	A	V_0	R^2	A	V_0	R^2
Pure	7.86E+04	25.31	0.926	2.85E+04	30.57	0.864
ZnO 0.1 wt%	6.59E+04	28.29	0.977	1.71E+04	31.44	0.949
ZnO 0.5 wt%	4.12E+04	28.27	0.975	1.01E+04	31.00	0.963
ZnO 1 wt%	7.73E+04	25.38	0.949	2.76E+04	30.55	0.893
ZnO 2 wt%	1.71E+05	29.08	0.921	4.58E+04	32.32	0.828
ZnO 3 wt%	5.16E+04	27.97	0.996	1.35E+04	31.16	0.951
Al_2O_3 0.1 wt%	1.95E+04	27.53	0.989	5.42E+03	31.08	0.937
Al_2O_3 0.5 wt%	2.04E+04	28.63	0.991	5.10E+03	31.57	0.927

The parameters for the fits to the data and the quality of fit are shown in Table 6.9. From Figures 6.12 to 6.15, it looks as if the power fits are better than the energy fits. This is backed up from the higher values of Pearson correlation R^2 calculated for the power based fits. The values of V_0 obtained from fits of Equation 6.2 are also all above 30 kV which is not reasonable as discharge activity was observed in samples exposed to 30 kV. The values for V_0 obtained using the power related fit are more reasonable in

the range of 27.6 □ 1.44 kV. These values are broadly similar to those obtained from the fractal dimension analysis of 27.3 □1.27 kV.

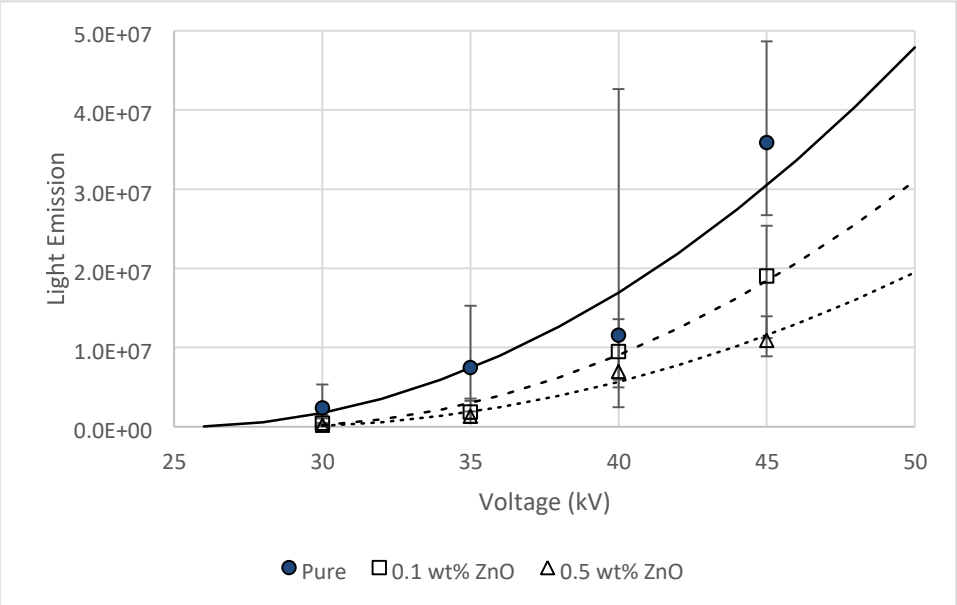

Figure 6.13 Total light emission comparison (less than ZnO 1 wt%)

Figure 6.13 shows the behaviour of light emission or ZnO nanocomposites with concentration <1 wt%. The total light emission is reduced by the addition of the nanofiller. The change in light emission is also dependant on the concentration.

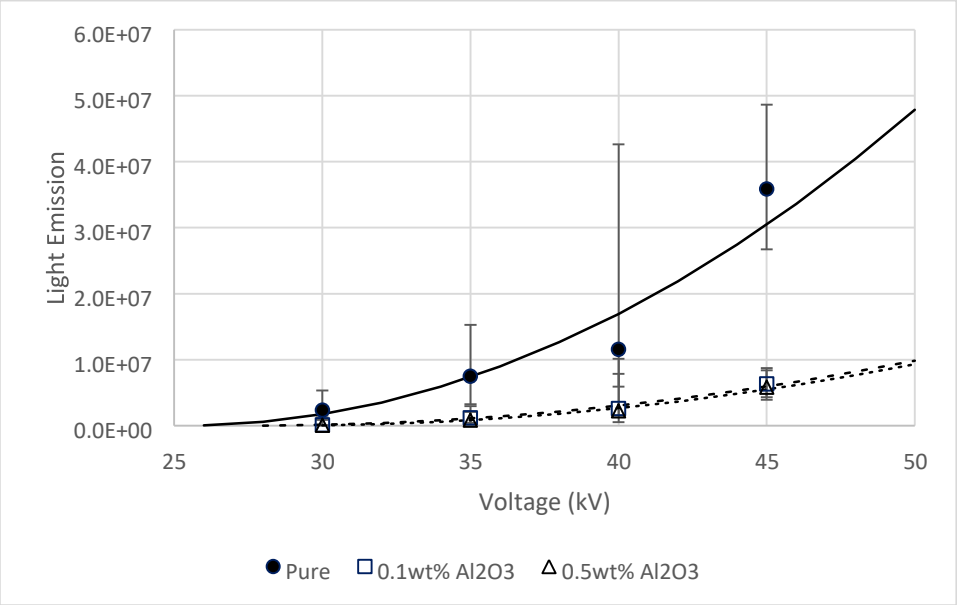

Figure 6.14 Total light emission comparison (Al_2O_3 less than 1wt %)

For Al_2O_3 nanocomposite in Figure 6.14, the total light emission of the discharges has also dropped compared to pure epoxy resin. The total light emission of the discharge across 0.1 wt% Al_2O_3 nanocomposite has little difference with 0.5 wt% Al_2O_3 nanocomposite.

The situation is unclear when looking at higher concentrations of ZnO nanofiller (Figure 6.15). There is no difference between the behaviour of the light emission as a function of voltage of the pure epoxy resin and the 1 wt% nanocomposite. For the 2 wt% nanocomposite the light emission has increased significantly. For the 3 wt% material the light emission seems to have fallen below the values measured for the pure samples.

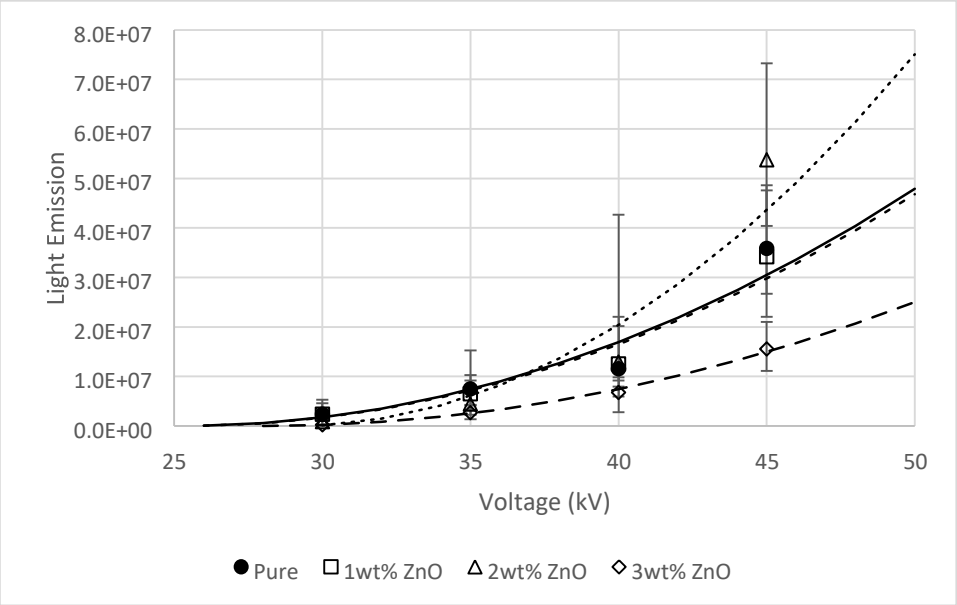

Figure 6.15 Total light emission comparison (ZnO more than 1 wt%)

6.2 Discussion

From the experiment results listed in Section 6.1, the fractal dimension and final length of the discharge pattern were linearly influenced by the applied voltage level but were not dependant on the concentration of nanofiller.

It has been reported that mismatch of the solid and liquid permittivities were able to influence the surface flashover voltage and the propagation of the discharges event [1] and [2]. The permittivity mismatch changes the field distribution on the surface which influences the initiating voltage of the discharge or flashover. A servere mismatch of permittivity will increase the probability of surface flashover occurring.

In [1] the ratio of the solid and liquid permittivities was used as a parameter to compare with the discharge behaviour, the calculating equation of μ is listed in Equation 6.3:

(6.3) $$\mu = \frac{\varepsilon' permittivity\ of\ the\ liquid\ material}{\varepsilon' permittivity\ of\ the\ Solid\ material}$$

Table 6.10 Permittivity and Fractal dimension comparison

Insulation Property				Fractal Dimension			
Liquid	Solid Type	ε’	μ	30 kV	35 kV	40 kV	45 kV
She Shell Diala D ε’=2.45	Pure Epoxy (30)	4	0.61	1.05	1.29	1.46	1.62
	Al_2O_3 0.5 wt%(25)	3.74	0.66	1.05	1.25	1.47	1.59
	ZnO 1 wt%(25)	4.65	0.53	1.02	1.28	1.42	1.56
	ZnO 2 wt%(25)	4.37	0.56	1.04	1.30	1.50	1.56

Table 6.10 shows the data for fractal dimension with values of the measured permittivity of the material at 50 Hz and the derived values of the ratio □. The number inside bracket is number of tests on this type of sample at each voltage level.The values of □ are in the range of 0.53 to 0.66. Table 6.11 shows the comparison results for permittivity and the final length of discharge pattern.

Table 6.11 Permittivity and Final length comparison

Insulation Property				Final length (mm)			
Liquid	Solid Type	ε’	μ	30 kV	35 kV	40 kV	45 kV

Shell Diala D ε'=2.45	Pure Epoxy (30)	4	0.61	14.47	21.81	28.09	35.02
	Al_2O_3 0.5 wt%(25)	3.74	0.66	14.93	22.25	28.15	35.44
	ZnO 1 wt%(25)	4.65	0.53	10.69	20.62	28.06	33.65
	ZnO 2 wt%(25)	4.37	0.56	13.8	22.17	32.21	36.76

In [1], for μ value in the range of 0.5 to 0.7 little change was observed in the surface breakdown strength. This agrees with the data on fractal dimension and breakdown length found in this project. Given that any changes occurring in the fractal dimension or length of the discharge are small it is difficult to separate any changes in the behaviour from the variation between individual measurements.

Among these three data groups, only light emission had visible changes with the variation of applied voltage and nanofiller concentrations. For nanocomposite with the nanofiller concentration lower than 1 wt%, the light emission values were lower than the pure epoxy resin. The light emission could be fitted to an equation of the form of Equation 6.1.

This suggests that the light emission is effectively linking into an expression associated with electrical power rather than energy.

Table 6.12 Permittivity and Light Emission Comparison

Insulation Property				Light Emission			
Liquid	Solid Type	ε'	μ	30 kV	35 kV	40 kV	45 kV
Shell Diala D ε'=2.45	Pure Epoxy (30)	4	0.61	2371187	7472909	11554739	35875741
	Al_2O_3 0.5 wt%(25)	3.74	0.66	55276	834296	2256716	5855053
	ZnO 1 wt%(25)	4.65	0.53	2372141	6522731	12494183	34172356
	ZnO 2 wt%(25)	4.37	0.56	859507	4418523	12868366	53786458

From the comparison results shows in Table 6.12, there is no apparent relationship between the light emission and the permittivity ratio of the polymer and the liquid insulation.

6.3 Conclusion

In this chapter, the optical results collected from the discharge pattern observation experiment have be reported and analysed. There was also a discussion about the problems of using fractal dimension as a method of defining structure in images of electrical breakdowns.

For optical results analysis, it can be confidently stated that the fractal dimension, final length of the discharge pattern reached and the total light emission of the discharge event is related to the applied voltage.

No significant changes in either fractal dimension or maximum discharge length were observed for the various nanocomposites. For the changes in permittivity mismatch this agrees with findings on surface breakdown strength

In general, changes were observed in the light emission for the nanocomposites compared to the pure material. The light emission being reduced, as the fractal dimension that corresponds to the light emitting surface area does not change and the maximum length is unchanged. This indicates that light per unit discharge area is being reduced for the nanocomposite samples with the reason unknown.

References

[1] R. J. Taylor, “Effect of permittivity matching on the flashover of solid/liquid interfaces,” *Proc. Inst. Electr. Eng.*, vol. 124, no. 10, p. 899, 1977.

[2] M. Anker, “Effect Of Test Geometry, Permittivity Matching And Metal Particles On The Flashover Voltage Of Oil/Solid Interfaces,” *IEEE Trans. Power Appar. Syst.*, vol. PAS-102, no. 12, pp. 3796–3802, Dec. 1983.

[3] K. Kudo, “Fractal analysis of electrical trees,” *IEEE Trans. Dielectr. Electr. Insul.*, vol. 5, no. 5, pp. 713–727, 1998.

[4] W. Lu, X. F. Wang, and Q. Liu, “Fractal index of streamer patterns in insulating liquids under lightning impulse voltages,” in *2014 IEEE 18th International Conference on Dielectric Liquids (ICDL)*, 2014, pp. 1–4.

[5] L. Kebbabi and a. Beroual, “Optical and electrical characterization of creeping discharges over solid/liquid interfaces under lightning impulse voltage,” *IEEE Trans. Dielectr. Electr. Insul.*, vol. 13, no. 3, pp. 565–571, Jun. 2006.

[6] L. Kebbabi and a Beroual, “Fractal analysis of creeping discharge patterns propagating at solid/liquid interfaces: influence of the nature and geometry of solid insulators,” *J. Phys. D. Appl. Phys.*, vol. 39, no. 1, pp. 177–183, Jan. 2006.

[7] G. Chen and C. Tham, “Electrical treeing characteristics in XLPE power cable insulation in frequency range between 20 and 500 Hz,” *IEEE Trans. Dielectr. Electr. Insul.*, vol. 16, no. 1, pp. 179–188, Feb. 2009.

[8] a. Beroual, “Fractal analysis of lightning impulse surface discharges propagating over pressboard immersed in mineral and vegetable oils,” *IEEE Trans. Dielectr. Electr. Insul.*, vol. 20, no. 4, pp. 1402–1408, Aug. 2013.

[9] L. Niemeyer, L. Pietronero, and H. J. Wiesmann, “Fractal Dimension of Dielectric Breakdown,” *Phys. Rev. Lett.*, vol. 52, no. 12, pp. 1033–1036, Mar. 1984.

7. ELECTRICAL DATA ANALYSIS

For a better observation and comparison of the surface discharge happened along the nanocomposite surface, the sensed current pulse were recorded at the same time as the optical data. In this chapter, the processing of the pulse data will be described and the processed results will also be presented with the discussion of the differences seen.

In Section 7.1, the detail of processing the electrical pulse data of surface discharge for each nanocomposite under different applied voltage level will be described and data for the behavior of the discharge pulse pattern with phase angle and any changes occurring per cycle during the tests will be presented.

In Section 7.2, the optical discharge images were matched with the sensed electrical pulse in 2 seconds period to reveal more information of the surface discharge for each different nanocomposite

7.1 Discharge Pulse Analysis

From the described experimental setup in Section 5.3, the sensed current pulse of the surface discharge was recorded by a HFCT which is also a common tool for testing partial discharges. From the observation of pulses conducted on a Tektronix oscilloscope, the typical behavior of the voltages observed as a result of current pulses for surface discharge is shown in Figure 7.1, the value of this pulse may different with the actual test results since it is test with a different oscilloscope in different setting. From these measurements, the duration of the pulses was around 1 µs. This agrees with the data presented in [1][2]. The quoted response frequency range of this HFCT is between 100 kHz and 10 MHz (0.1 µs – 10 µs duration)[3].

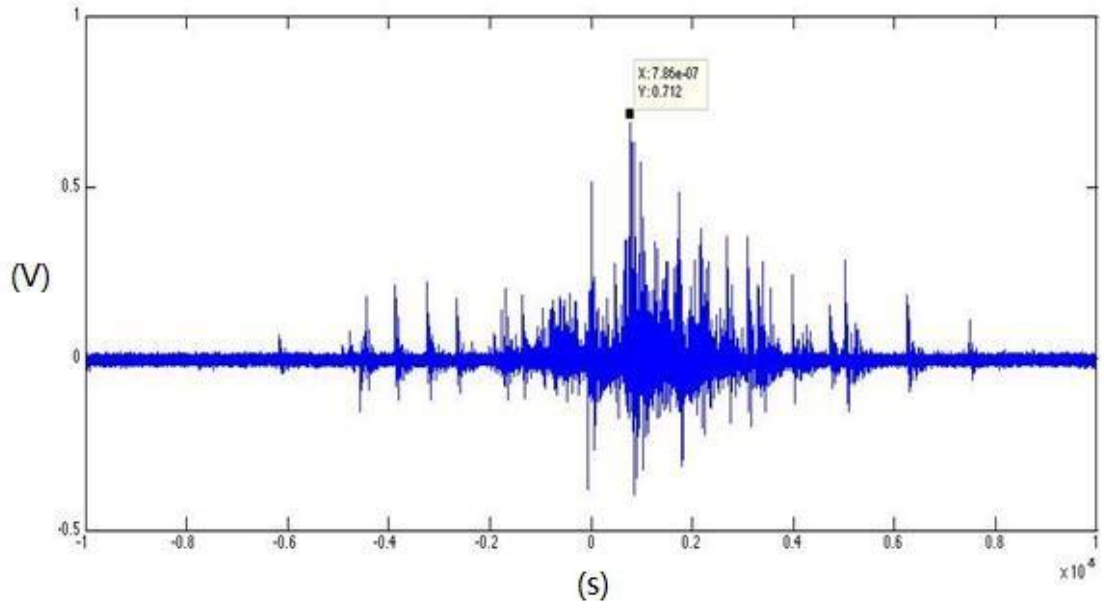

Figure 7.1 Current Pulse from primary experiment (40 kV)

As optical data was recorded during 2-second period, the current pulse was also recorded in 2 second period; this meant the oscilloscope sample rate had to be set at 10M/s. This means that each pulse was recorded a ten points.

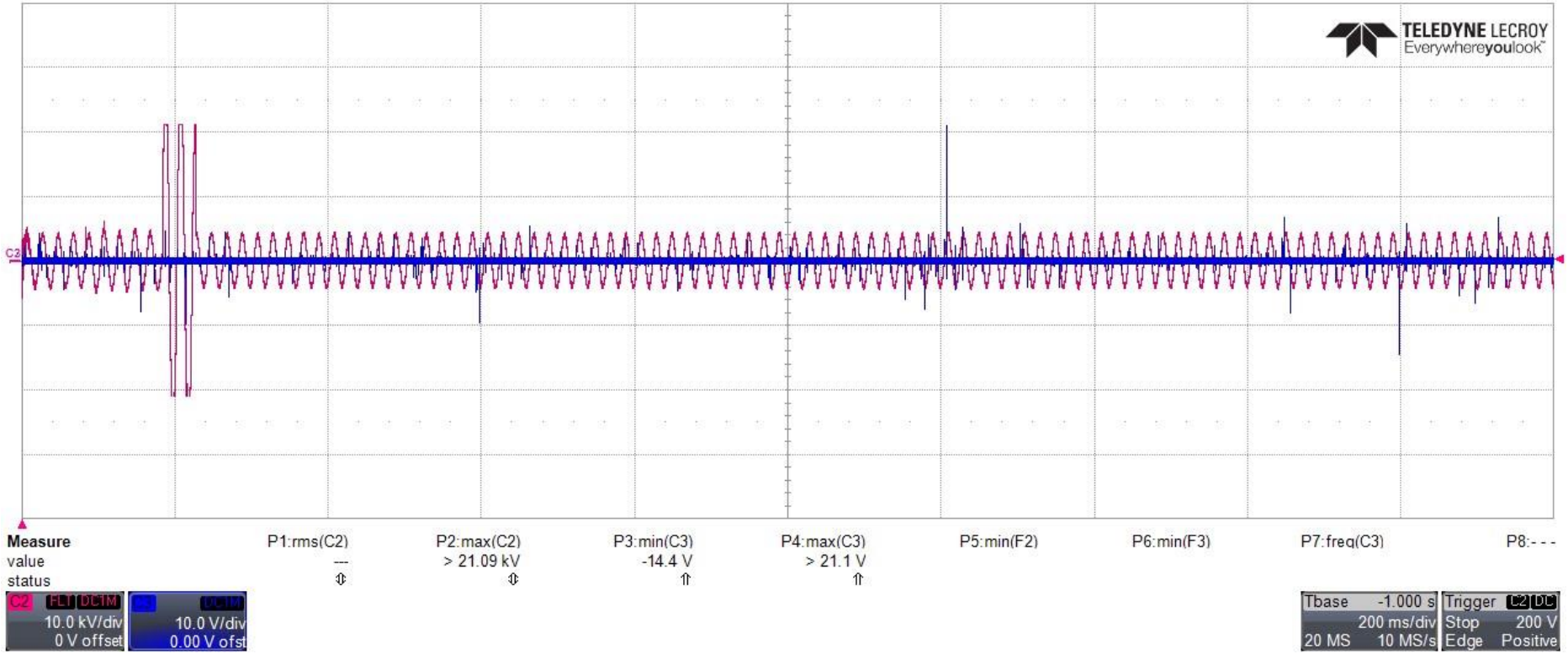

Figure 7.2 Initial Recorded Waveform and Pulse

Under 50 Hz AC condition, the 2 second recording picked up 100 cycles of data, Figure 7.2 show the results of an early trial measurement. The red trace records the applied voltage waveform measured through a divider the blue line is the output of the HFCT

There were two problems with the raw data. Because of the high voltages associated with some pulses the range settings for the oscilloscope caused two problems with data recorded. Distinct bands were observed in the data. These are due to the quantisation of the data during the analog to digital conversion and also due to the number of bits assigned to store each data point. These bands can clearly be seen in Figure 7.3 which shows part of the data of a typical waveform recorded. From noise in the system a large number of data points fell in the range of 1 to -1. This can be seen in the figure where there are 7 data bands between -1 and 1, and a single point lying outside this range which was assumed to represent a discharge event. Frequently an offset was observed in the data with the bands not appearing symmetrically about the zero level. An offset for the raw data was calculated using its mean value. This assumes that the actual discharge peaks had little effect on the mean value.

To remove the noise threshold values of 1 and -1 were used. Any points with value between the thresholds were set to 0. As for each pulse 10 data points were likely to have a value outside the thresholds it was necessary to develop a filter to represent the pulse by a single data point setting the remaining points to zero. The filter worked by examining a 10 point section of the data. The highest magnitude value in this sample was found. The 5 points before the position of the highest magnitude were set to zero. The 10 points after the largest point were also set to zero. The new search window was then moved to the position of the first point that is non zero after the position of the current maximum.

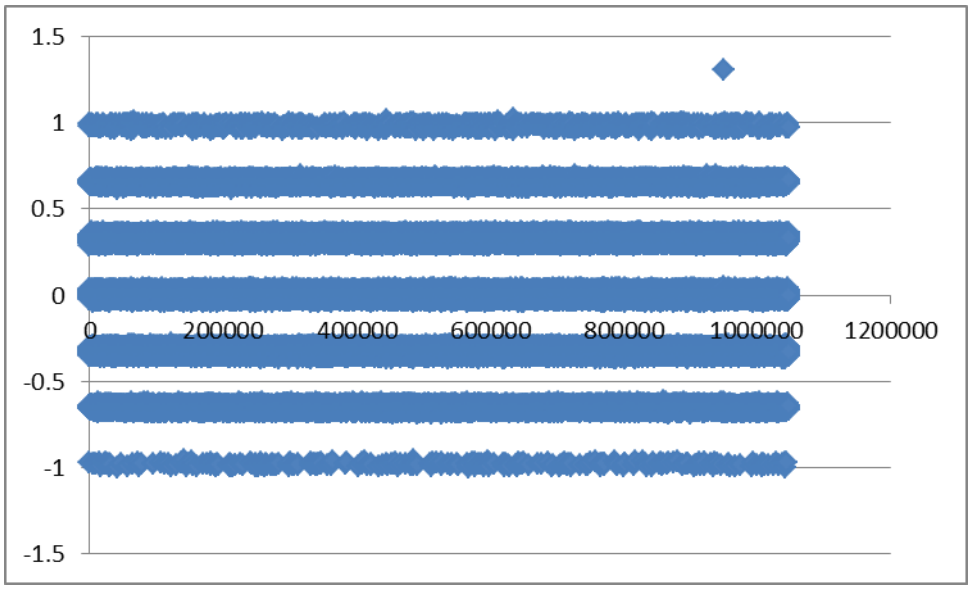

Figure 7.3 Typical data bands present in recorded data

After the data for the applied waveform and the current pulses was recorded this necessary processing was performed in MATLAB; using functions developed in this project. Based on the applied voltage data the cycle that each peak appeared in was found and the phase angle within the cycle was calculated. The details of the MATLAB programme developed are given in Appendix B.

The steps in the programme were:

- **Offset correction**: the mean value of the data set associated with the current pulses was calculated. If this was not zero it indicated that there was an offset in the data. The calculated mean value was therefore subtracted from each point in the dataset. As mentioned above this assumes that the actual discharge activity does not affect the mean value. This is reasonable as typical pulse activity lead to a maximum of 2,000 pulses occurring within the 2 second measurement period. The total number of data points associated with the pulses therefore is 20,000 the total number of points in the dataset was 20,000,000. In addition it would be expected that the values of the points associated with the discharges would be symmetrically distributed.
- **Threshold filter**: Scan through the dataset measured from the HFCT, if the magnitude of a data point is lower than 1, the value will be set to 0. From the data there were a large number of data points whose magnitudes were less than

one. It was assumed that these represented the noise, unlike the larger values which can be seen in Figure 7.2 which were assumed to represent discharges.

- **Peak determine**: To reduce the size of the dataset the peaks were located and the maximum amplitude of each peak and the time at which it occurred were stored. To prevent miscounting the highest non zero value was assumed to represent the value of the pulse. Lower values in the 5 points before the peak and the 10 points after the peak were set to zero.
- **Cycle and phase angle determination**: From the dataset for applied waveform the positive gradient zero crossing points were determined. This allowed the start and end point of each cycle to be found. The zero crossing point was determined by finding the point in the dataset where the next point was positive and the previous point was negative. With a sample rate of 10 MHz the error in determining the crossing point 0.1μ was considered to be insignificant. Phase was determined by filtering the data for the voltage waveform to recover a pure sinusoid and then using a built in MATLAB function.

At the end of this data processing a file was output containing data on the peak heights of pulses, the phase angle associated with each pulse and the cycle in which the pulse had occurred.

7.1.1 Weibull Distribution Analysis

In dealing with the large quantities of data produced in this research the statistical distribution of parameters such as the magnitude of the signals associated with discharges or the number of discharges occurring in a cycle has been examined. The Weibull distribution was used as it can describe a very wide range of single peaked probability distributions using 3 parameters. It was hoped that changes in the behaviour of the materials would lead to changes in these parameters. Normally the Weibull distribution is used to predict the probability of failure in this application it is only being used to define the form of a measured probability distribution.

The pulse data were mostly fitted using a three-parameter Weibull distribution. For this, the cumulative probability $F(V)$ of a property having a magnitude less than or equal to V is given by Equation 7.1[4]:

(7.1)
$$F(V) = 1 - e^{-(\frac{V-\gamma}{\alpha})^{\beta}}$$

The parameters of the Weibull distribution are: α is the scale parameter; β is the shape parameter; γ is the location parameter. The value of $\alpha + \gamma$ is where the probability of the event having occurred is equal to 0.632; β decides how rapidly the probability changes with the property V; γ is sometimes referred as the offset this represents the value of the parameter V below which the probability value is zero. In this project, two properties of the discharge distribution have been analysed: the magnitude measured for pulses or the number of pulses occurring in a cycle.

To determine if a distribution can be described by the Weibull distribution Equation 7.1 can be converted into linear form: $y = mx + n$. The new form converted from the function is in Equation 7.2:

$$\ln[\ln(\frac{1}{1 - F(V)})] = \beta \ln(V - \gamma) - \beta \ln \alpha \quad (7.2)$$

Therefore with data on the cumulative probability function $F(V)$ a plot of $\ln(-\ln(1 - F(V))$ against $\ln(V - \gamma)$ should produce a straight line with gradient equal to β and intercept at $-\beta \ln \alpha$. In cases where the parameter γ is equal to zero, the distribution is a two parameter Weibull distribution and a plot of $\ln(-\ln(1 - F(V))$ against $\ln(V)$ gives a straight line. The relationship between the gradient and intercept of the plot and the parameters β and α are the same as for the three- parameter Weibull plot.

7.1.2 Relationships between phase angles, cycles and Pulse number

Relationships between phase angles, cycles and pulse numbers were investigated in this section. Each analysis was aim to discover the relationship between two variables from phase angles, cycles and pulse numbers and comparisons was made for different nanocomposite type and applied voltage level. The electrical data for 30 kV were excluded from the analysis since the pulse numbers under this voltage level were too small to provide a conclusive analysis results, even for sum of results from multiple samples.

7.1.2.1 Relationship between Phase angle and Cycles

The first analysis was to discover if there was any relationship between the phase angles at which discharges were occurring and the cycle numbers. As last section mentioned there are 100 cycles in each waveform collected and each cycle is a sinusoidal wave.

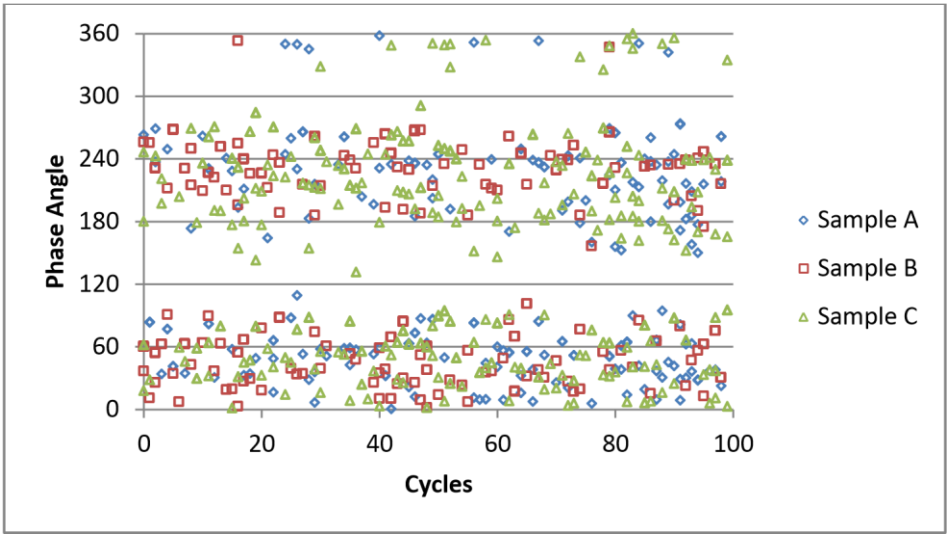

Figure 7.4 Plot of Phase Angle against Cycle for Pure Epoxy

Figure 7.4 is an example of a plot for phase angle against cycle number of pulse location; this plot uses the pulse data from three random selected samples (A to C) of pure Epoxy tested at 45 kV. As it can be seen that the phase angles of pulse occurring are mostly located in the first (0° to 90°)and third quadrant (180° to 270°), small number of pulse located in fourth quadrant. The phase angles at which pulse occur does not change with increasing cycle number. Therefore, in this two-second period, the phase angles for the pulse are not related to the time. This behaviour with the phase angle of pulse occurrence being independent of time or cycle was consistently observed for all of the sample materials examined. Plots of this data for other materials have therefore not been included.

7.1.2.2 Distribution of Pulse Number with Cycles

The second analysis is to investigate whether the pulse number is related with the cycle number. An example is shown in Figure 7.5. This plot was obtained from a sample of 0.1 wt% ZnO. These results were obtained from 5 consecutive tests performed at 45 kV. 10 minutes time gap was applied between these 5 tests for the recovery of any non-

permanent damage. Prior to this the sample had also undergone 5 tests at each of 30, 35 and 40 kV. From this plot, it is clear to see that the total discharge numbers are almost linearly increased with increase in cycle number, that is the total number of discharges are increasing with time. The lowest rate of increase is associated with the 5th test in the sequence while the highest rate is seen for the second test in the sequence. The linear behaviour suggests that the number of discharges that occur per cycle is relatively constant.

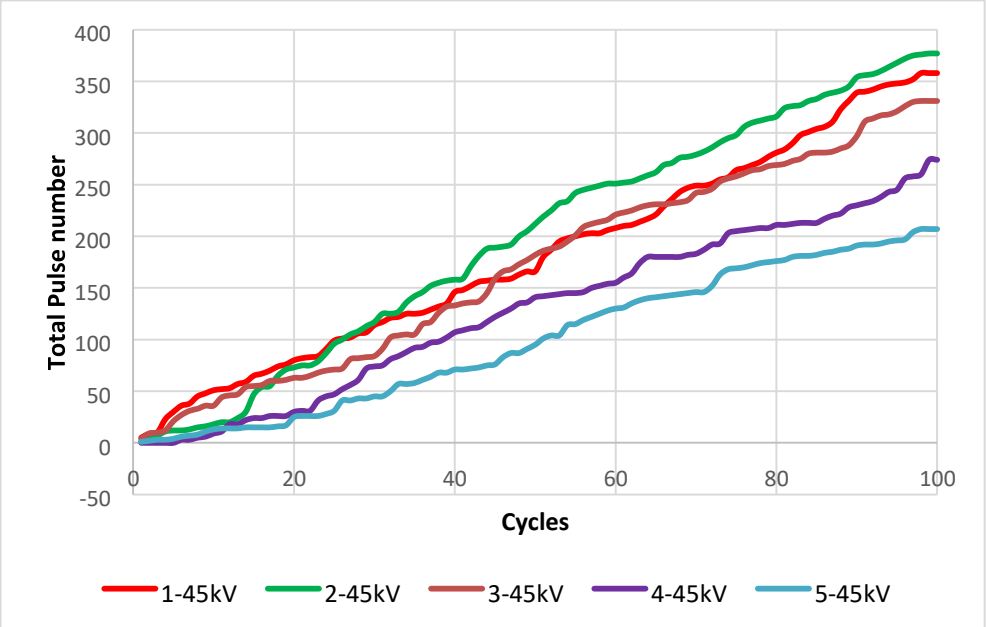

Figure 7.5 an example of the discharge number associated with cycle number

Table 7.1 is the statistical analysis of the variation in the number of pulses for each cycle for these 5 tests. Pearson correlation coefficient was calculated using the cycle number and the pulse number in each cycle for each test. As it can be seen, the coefficient is very low which indicated that there is no relationship between the two sets of data.

Table 7.1 Statistic analysis of Figure 7.5

	Correlation	Mean	Shape	Scale	Position	R_2
A	-0.022	3.58	1.14	5.76	0	0.9965
B	-0.104	3.77	1.54	6.84	0	0.9949
C	-0.037	3.31	0.82	4.18	0	0.9476
D	0.134	2.74	0.87	2.78	0	0.9842
E	0.073	2.07	0.93	4.64	0	0.9799

From the appearance of the distribution of the data on the number of pulses per cycle the data was fitted using a 2-parameter Weibull distribution. Values for the shape and scale parameters are shown in Table 7.1 and Weibull plots of the data are shown in Figure 7.6. The value of R^2 refers to the correlation of the Weibull plot. Although changes occur in the values of the shape and scale parameters, no clear pattern can be seen with respect to test order.

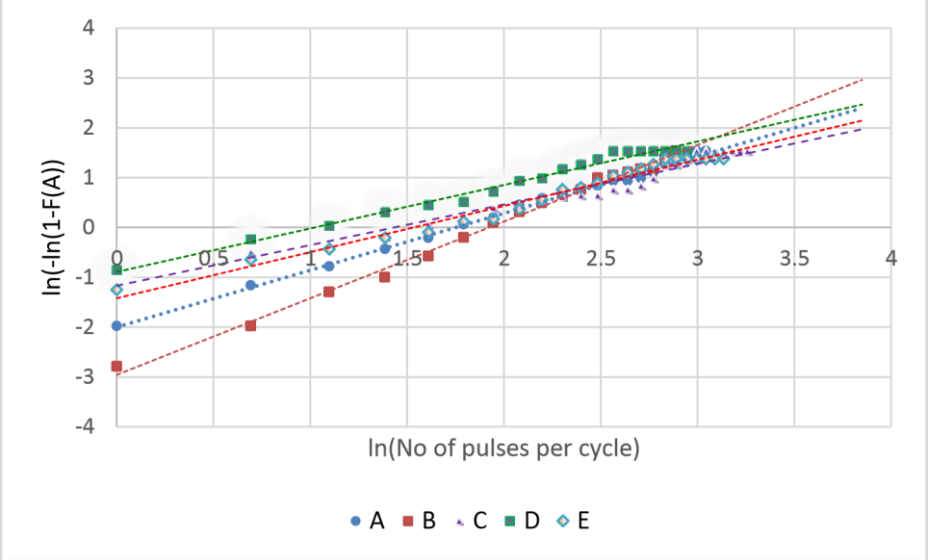

Figure 7.6 the comparison of the probability of the discharge number occurring between different tests on one sample of ZnO 0.1 wt% at 45 kV

Figure 7.7 shows the Weibull plots of the discharge rate per cycle for the same sample under three tested voltage levels. In these plots the data analysed was the combination of 5 test runs. That is the data set includes all of the data used to produce the individual data plots in Figure 7.6. The plots for 40 kV appear to deviate from that expected from a 2 parameter Weibull plot. It was therefore decided to plot the data using a 3-parameter Weibull plot.

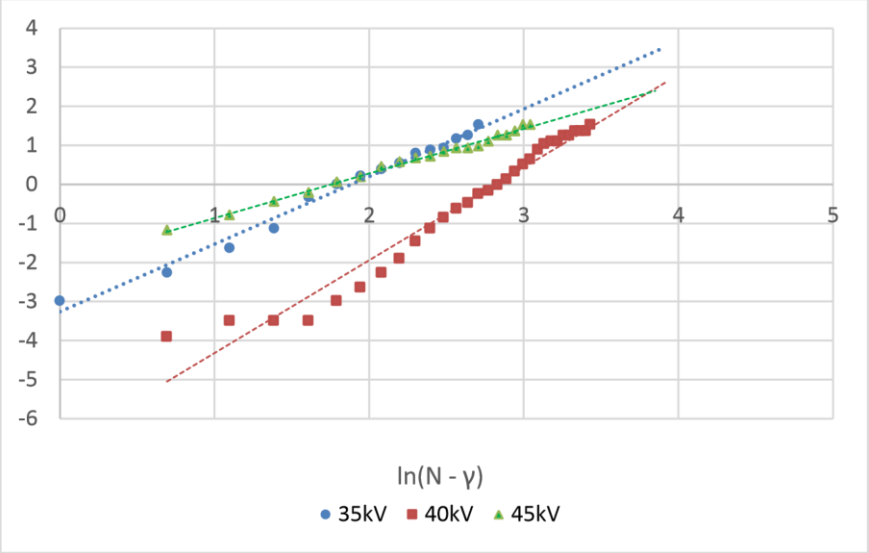

Figure 7.7 the comparison of 2-parameter Weibull plot of the discharge number occurring for same type of sample under different voltages

Table 7.2 Statistic data for 3 parameter Weibull distributions for number of pulses per cycle for all test results

Applied Voltage	Material Type	Pure	ZnO				Al_2O_3	
	Concertation	0 wt%	0.1 wt%	0.5 wt%	1 wt%	2 wt%	0.1 wt%	0.5 wt%
35 kV	Shape	1.52	1.48	1.53	1.52	1.41	1.56	1.71
	Scale	7.73	12.25	9.77	12.23	11.66	11.12	11.64
	Location	5.0	13.00	5.00	13.00	20.00	17.00	22.00
40 kV	Shape	1.69	1.23	1.10	1.04	1.19	1.51	1.42
	Scale	15.03	14.09	9.77	12.23	20.74	19.81	16.76
	Location	14.00	40.00	5.00	35.00	40.00	50.00	25.00
45 kV	Shape	1.37	0.53	1.57	1.13	0.99	1.09	0.54
	Scale	24.98	2.63	19.39	21.66	20.91	34.45	5.43
	Location	18.00	80.00	10.00	45.00	125.00	60.00	92

Table 7.2 shows the 3-parameter Weibull plot results of phase number per cycle for all test results. As the voltage is increased in general across all of the samples the shape parameter is tending to decrease. This means that the skewness of the distribution is becoming larger. The scale parameter is generally increasing as we increase the voltage indicating that the width of the probability distribution function is increasing. The combination of the decreasing shape and increasing scale indicates that the distribution of probabilities is being shifted to larger numbers of pulses occurring in a cycle comparing to pure samples. The location parameter also generally increases with

voltage. This indicates that the minimum number of pulses occurring in a cycle is increasing with voltage.

At 35 kV the shape parameter seems to show little change when the behavior of nanocomposites are compared with the pure material. At 40 and 45 kV the shape parameter seems to be smaller for the nanocomposites but there is considerable variation between different nanocomposites. At 35 kV the scale parameter increases for the nanocomposites but no obvious pattern of change can be seen at 40 and 45 kV. The location parameter is observed to be generally larger for the nanocomposite materials compared to the pure material over all of the voltage levels.

The shape of the distribution of number of discharges per cycle is affected by the nanocomposite materials as shown by the change in shape at 35 kV and the changes of scale at 40 and 45 kV. No pattern in terms of the nanocomposite concentration can be seen in the changes for ZnO. The location parameter is generally increased for ZnO nanocomposites though the results for the 0.5 wt% samples appear to be lower. Again no trend can be observed in the value of the location parameter due to nanofiller concentration. A similar increase in the value of the location parameter is observed for Al_2O_3 nanocomposites. However with only 3 data points at each voltage it is not possible to determine if there are any trends due to concentration. The increase in the value of the location parameter indicates that the nanocomposites have a higher minimum discharge per cycle number than the pure samples.

7.1.2.3 Distribution of Pulse Number with Phase Angles

The plots of the pulse numbers as a function of phase angle for each type of nanocomposite under different applied voltages are shown in Figure 7.8 and Figure 7.9. For each material and voltage level the figures are based on the data from 5 tests from three random samples. The total number of discharges for 36 10° windows were calculated for each test run and then summed. The total discharge number therefore reflects average discharge behaviour based on 15 test runs each containing data for 100 cycles.

In all the figures the discharge numbers increase with increased voltage. The general shape of the distribution of discharge number with phase angle is similar for each type of

sample. One obvious feature is that there are clear regions where discharge activity is large and other regions where discharge activity is consistently lower. As observed in Figure 7.4, the majority of the discharge activity is occurring in the first and third quadrants. This indicates that the voltage and the rate of change of voltage must have the same sign for discharge activity to occur. Within these quadrants there is a peak (Peak 1) occurring approximately 10° before the peak voltage value (~80° and ~260°).

There is also evidence of a second peak (Peak 2) occurring at phase angles ~60° and 240° and a third peak (Peak3) at 20° and 190°. There is a region with a consistently low value of discharges at 30° which have been observed in all samples. At the corresponding angle in the third quadrant 210° the number of discharges is lower but not zero.

With increasing voltage for each type of sample the number of discharges associated with each peak position increases, but there does not seem to be any shifts in the distribution of the peaks shown in Figure 7.8.

Looking at the ZnO nanocomposites (Figure 7.10) in general the number of discharges in each peak has increased compared with the pure epoxy samples. For 35 kV and 40 kV, the largest number of discharges occurs with the 0.1 wt% samples. The number of discharges falls for the 0.5 wt% sample and then remains reasonable constant for the 1 and 2 wt% samples. The behaviour for 2 wt% samples is different with an initial fall in discharge numbers for the 0.5 wt% samples but an increase is then observed for the 1 and 2 wt% samples. The position of peak 1 also appears to shift from 80°-90° to 70°-80° for the 0.1 wt % and 0.5 wt% samples. A corresponding shift is also observed in the third quadrant. This shift is not observed in the 1 and 2 wt% samples.

For the Al_2O_3 nanocomposites results (Figure 7.11), the discharge activity for the 0.1 wt% samples is higher than those observed in the pure samples. In general there is little difference between the behaviour of the 0.1 and 0.5 wt% samples. However a broad peak is observed for the 0.1 wt% sample under 40 kV voltages between 140° and 220°. The positions of peaks 1 and 2 in the first and third quadrants seem to again shift to lower values by 10°.

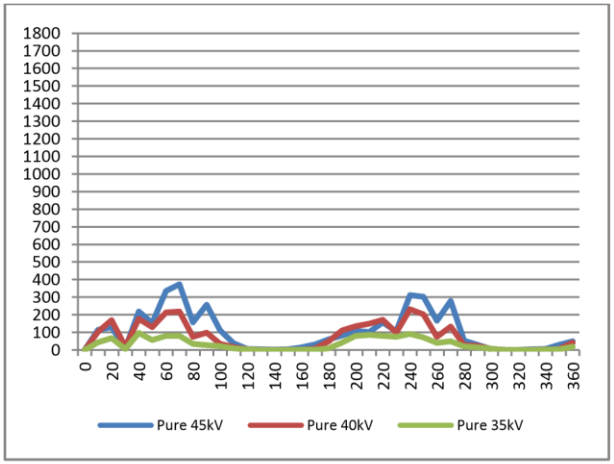

(a) Pure Epoxy Resin

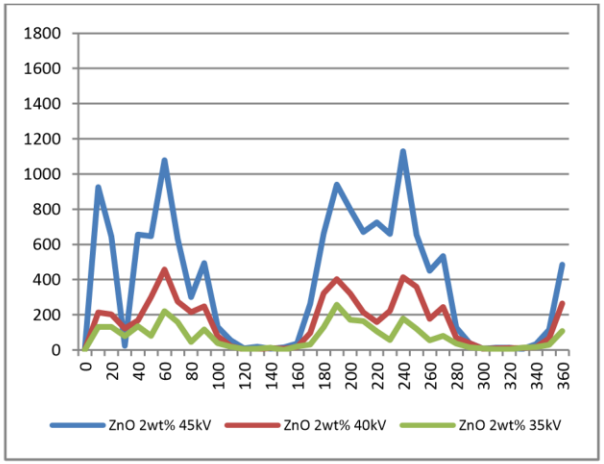

(b) ZnO 2 wt% nanocomposite

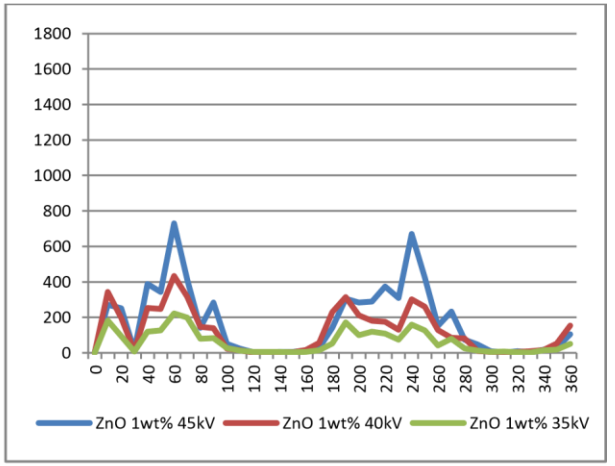

(c) ZnO 1 wt% nanocomposite

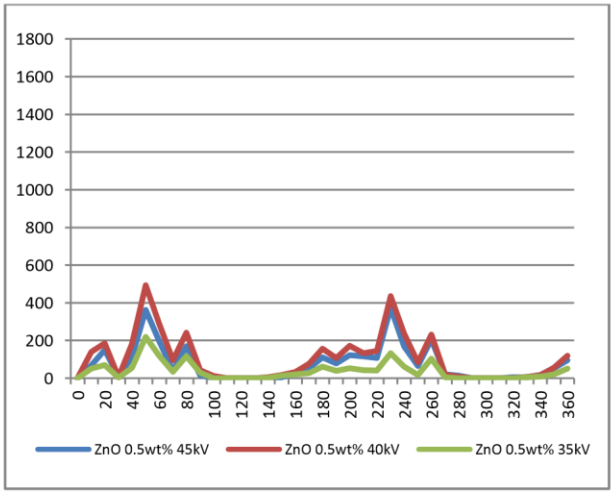

(d) ZnO 0.5 wt% nanocomposite

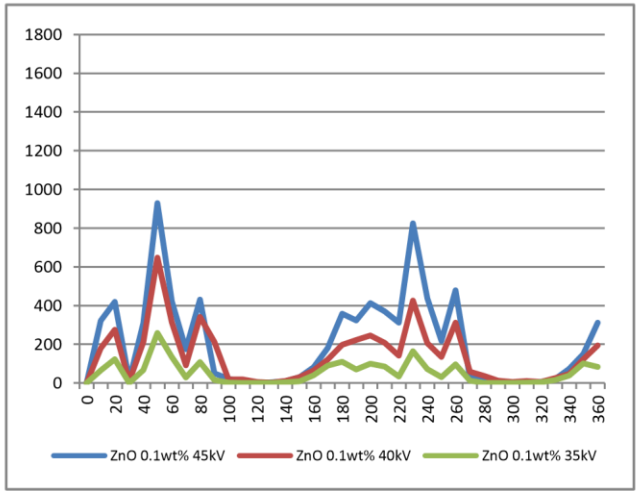

(e) ZnO 0.1 wt% nanocomposite **Figure**

7.8 Relationship between Discharge number and degree in ZnO nanocomposite

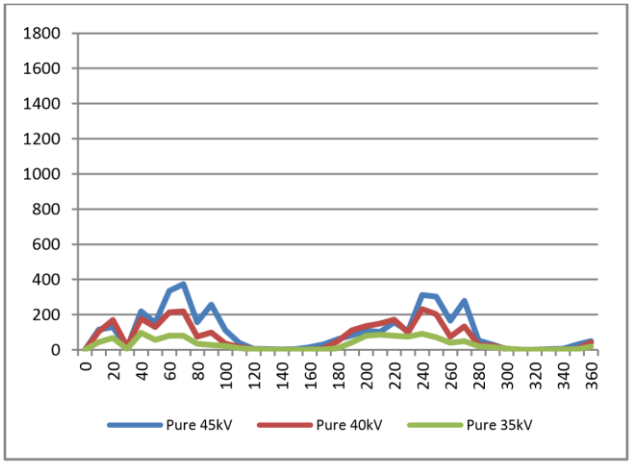

(a) Pure Epoxy Resin

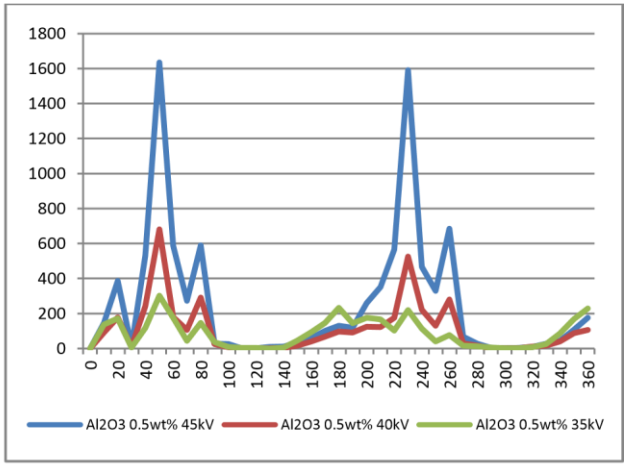

(b) Al_2O_3 0.5 wt% nanocomposite

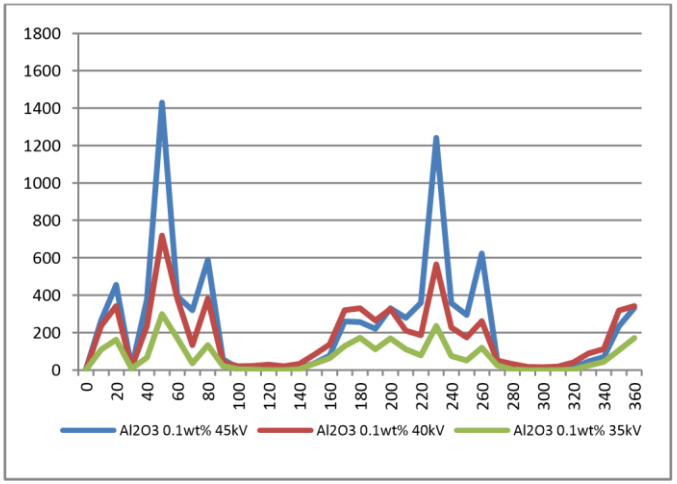

(c) Al_2O_3 0.1 wt% nanocomposite

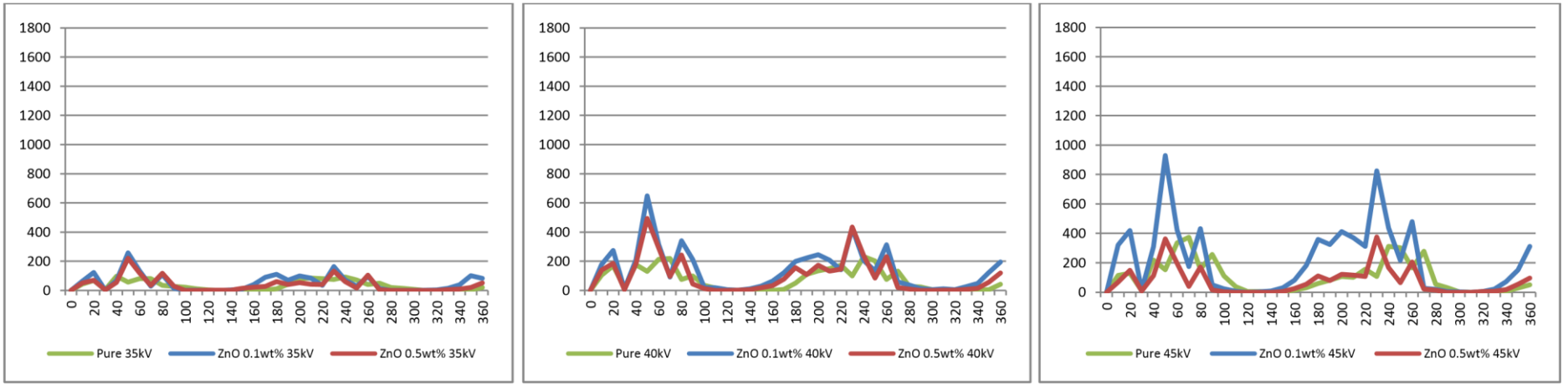

Figure 7.9 Relationship between Discharge number and degree in Al_2O_3 nanocomposite (a)ZnO 0.1 wt% 0.5 wt% 35 kV (b) ZnO 0.1 wt% 0.5 wt% 40 kV (c) ZnO 0.1 wt% 0.5 wt% 45 kV

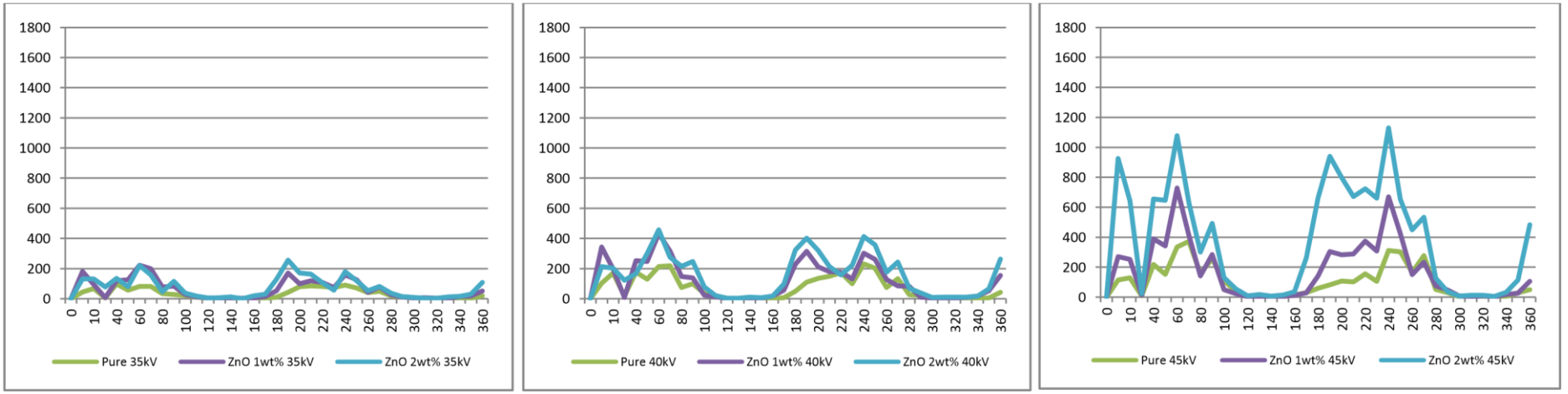

(a) ZnO 1 wt% 2 wt% 35 kV (b) ZnO 1 wt% 2 wt% 40 kV (c) ZnO 1 wt% 2 wt% 45 kV

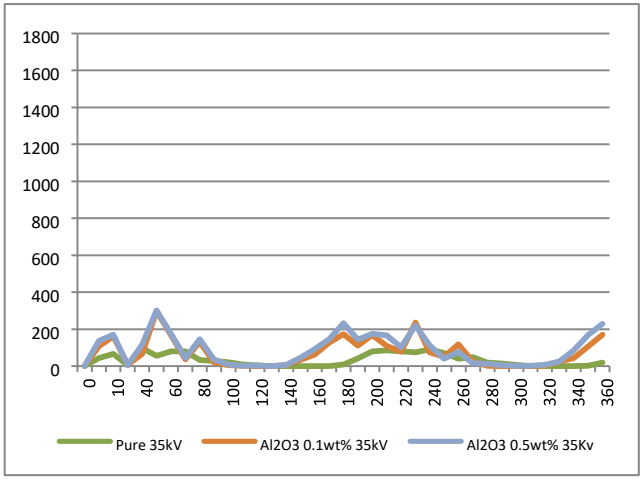

Figure 7.10 Distribution comparison for ZnO nanocomposite under same voltage

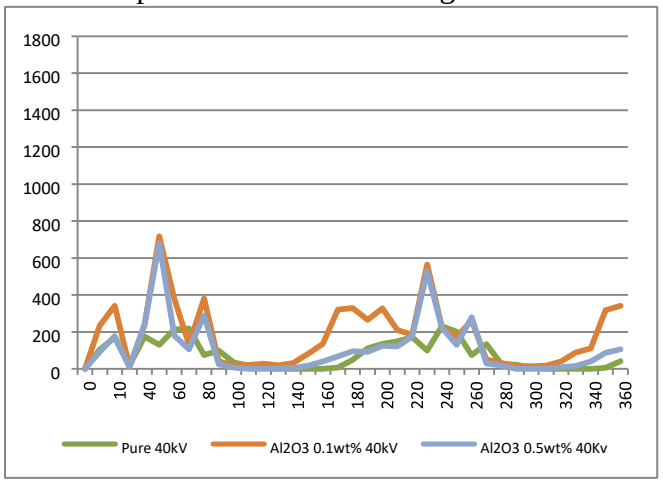

(a) Al_2O_3 0.1 wt% 0.5 wt% 35 kV

(b) Al_2O_3 0.1 wt% 0.5 wt% 40 kV

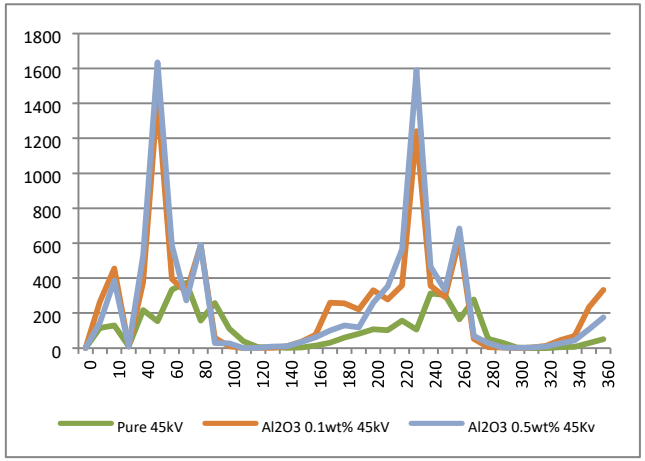

(c) Al_2O_3 0.1 wt% 0.5 wt% 45 kV

Figure 7.11 Distribution comparison for ZnO nanocomposite under same voltage

7.1.3 Analysis of Pulse value

Originally, the data for the magnitude of the measured electrical pulse and its phase angle were plotted in the form shown in Figure 7.12, which shows the data for 5 successive runs at 40 kV for a single 0.1 wt% ZnO sample. It was difficult to see if any changes in the discharge activity were occurring as a result of differing nanocomposite material from the 76 plots obtained.

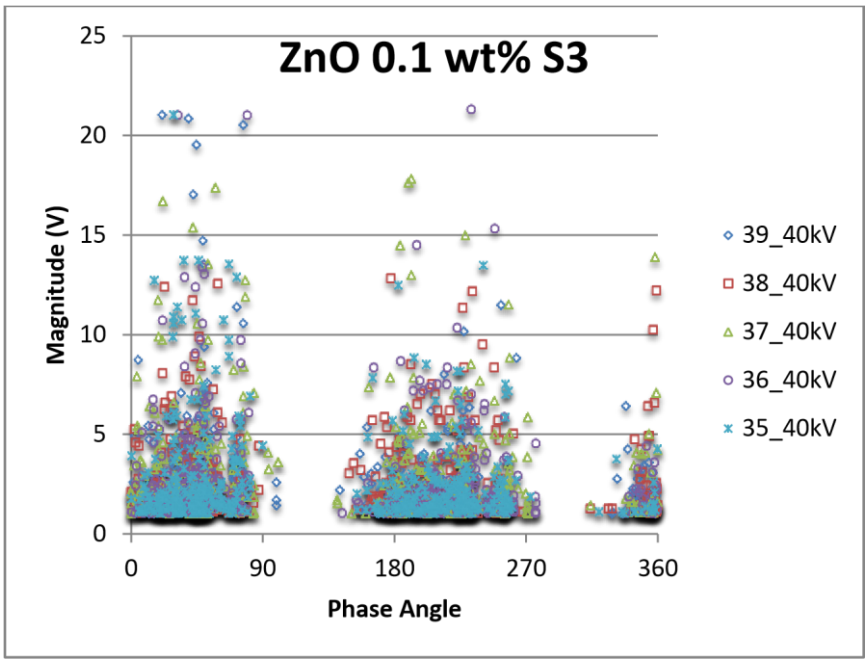

Figure 7.12 an example of pulse data

As an alternative it was decided to see if the statistical distribution of the measured voltages associated with discharges was changing, as this would describe the peak data using a small number of parameters. Again the Weibull distribution was used, Figure 7.13 shows the Weibull distribution plot for Al_2O_3 nanocomposite with 0.1 wt% nanofiller under 35 kV applied voltage. The Pearson correlation coefficient R^2 is equal to 0.9934 which indicate that the data fits a straight line when plotted as the Weibull distribution. The range of R^2 calculated from Weibull plots of the data from all types of samples are from 0.9981 to 0.9507 which indicates that the 2 parameter Weibull distribution can describe the experimental data.

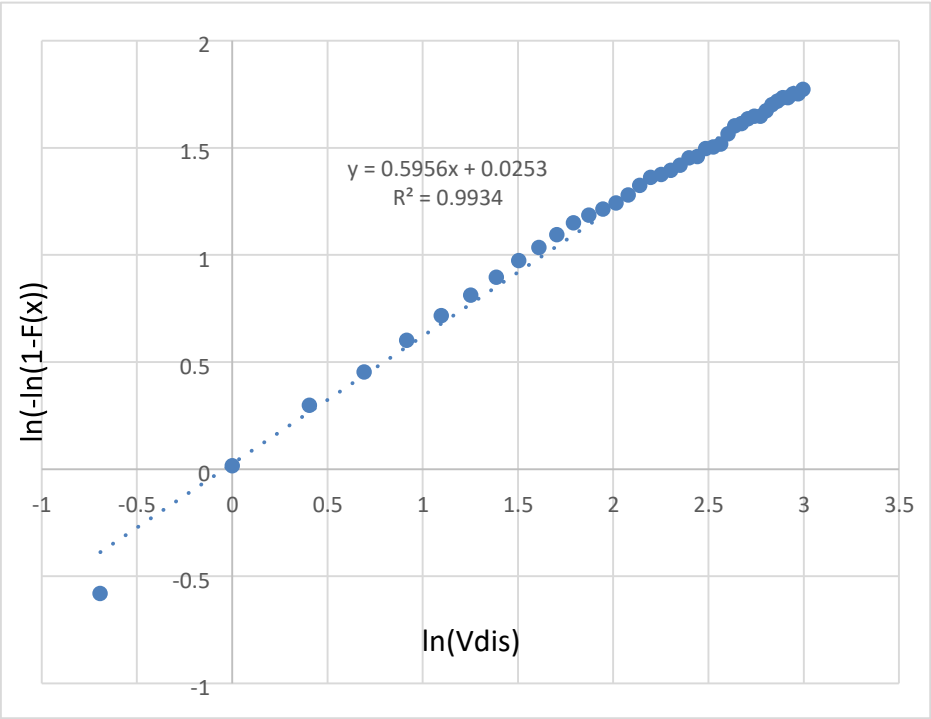

Figure 7.13 An example for Weibull Distribution plot Al_2O_3 nanocomposite at 35 kV

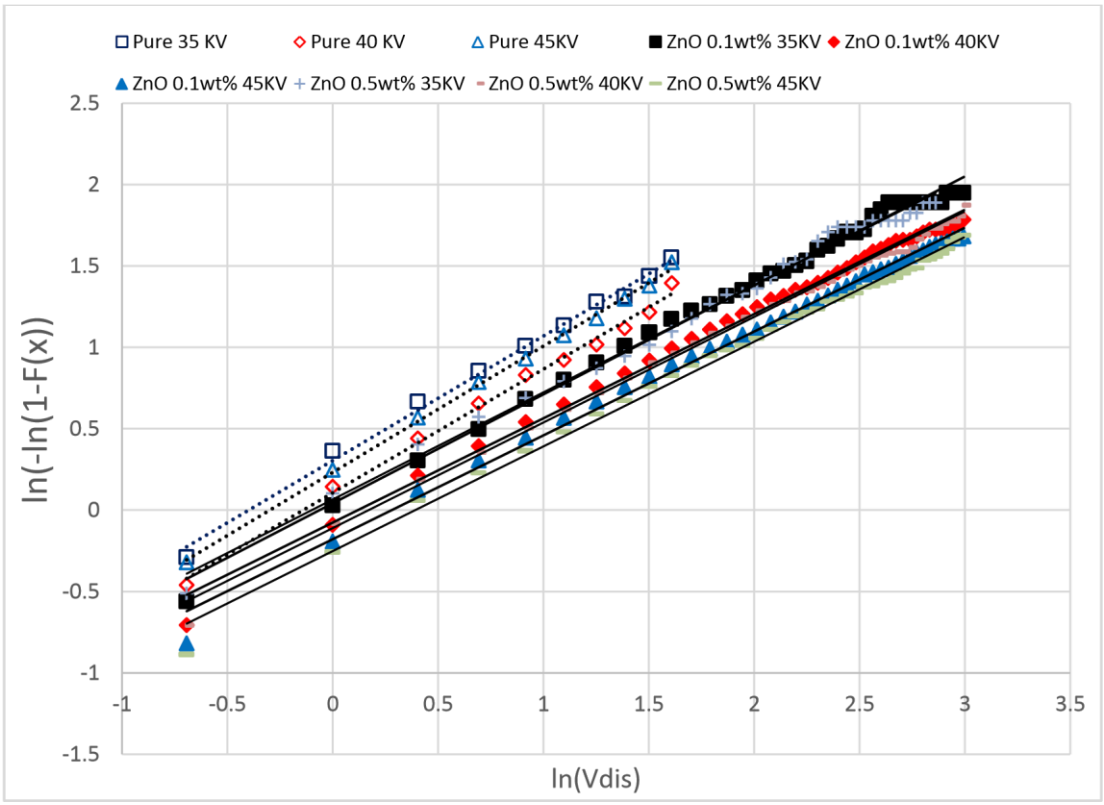

Figure 7.14 Weibull distribution of pure epoxy resin, ZnO 0.1 wt% and ZnO 0.5 wt%

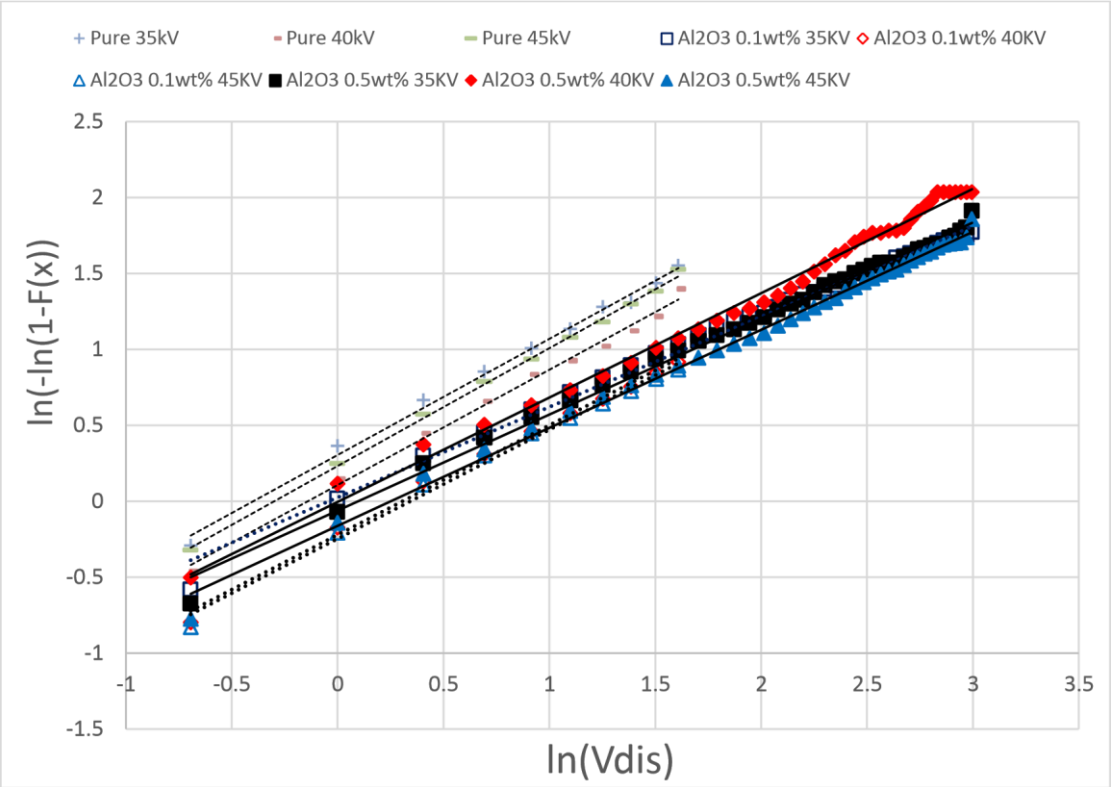

Figure 7.15 Weibull distribution of Al_2O_3 0.1 wt% and Al_2O_3 0.5 wt%

From Figure 7.14 it can be seen that the pure material contains no discharges of a value greater than 5V, The ZnO nanocomposite in this figure contains discharges up to a value of 20V a similar behaviour is observed for the Al_2O_3 data in Figure 7.15. It should be noted that these larger magnitude discharges make up less than 1% of the total discharge activity observed in the nanocomposite materials.

The values for the shape and scale parameters extracted from the Weibull plots are shown in Table 7.3 it is clear to see that all shape parameter β are less than 1. This implies that the probability density will have its maximum value at 0 and decreases for higher values of discharge peak magnitude.

As the voltage is increased the scale parameter for the distribution seems not to change significantly with voltage. The scale parameter in general decreases with voltage. This implies that the probability of discharges with a lower measured voltage increases as the voltage increases.

The value of the scale parameter tends to be smaller for the nanocomposite materials then for the pure material at all of the voltage levels. This change would reduce the probability of discharges with values close to zero from occurring while increasing the probability of larger value discharges occurring. There is little change in the value of the shape parameter for differing concentrations of nanocomposites and between nanocomposites based on ZnO and Al_2O_3.

Table 7.3 Value of α and β

Applied Voltage	Material Type	Pure	ZnO				Al_2O_3	
	Concertation	0 wt%	0.1 wt%	0.5 wt%	1 wt%	2 wt%	0.1 wt%	0.5 wt%
35 kV	Shape	0.76	0.67	0.66	0.68	0.68	0.60	0.63
	Scale	1.49	1.06	1.11	0.97	0.93	1.04	0.91
40 kV	Shape	0.76	0.64	0.65	0.68	0.70	0.69	0.69
	Scale	1.11	0.89	0.84	0.79	0.76	0.75	0.99
45 kV	Shape	0.88	0.64	0.64	0.73	0.66	0.67	0.65
	Scale	1.25	0.76	0.68	0.62	0.62	0.73	0.78

The scale parameter is also reduced for the nanocomposites when compared with the pure material this suggests that the nanocomposites have an increased probability for discharges with a lower measured magnitude occurring.

7.1.4 Discussion

Based on the results for discharge activity, the number of discharges observed in the nanocomposite materials is larger than those observed in the pure epoxy resin samples. As would be expected the number of discharges increased with increasing voltage. There is no observed dependence on the number of discharges and the type or concentration of the nanofiller used. Weibull analysis of the distribution of pulse number per cycle suggests that as well as the increase in pulse number that the distributions of the pulses per cycle were different for the nanocomposite materials when compared with the pure materials.

The majority of the discharges occurred in the first and third quadrants of the applied waveform. Interestingly, there were regions in the first quadrant were no discharges were observed. For certain concentrations of nanofiller the phase distribution of discharge activity appeared to change with discharges occurring at a lower phase angle.

No significant changes in the phase distribution were observed in the course of individual 100 cycle test runs.

The magnitude distribution of the observed pulses is also affected by the nanocomposite. Larger discharges are observed in the nanocomposite material in the range of 5 to 20 volts but these make less than 1% of the total discharge activity. From the Weibull plots of the discharge behaviour the nanocomposite materials have an increase in the probability of discharges producing low voltages which is more significant than the small number of high magnitude pulses. Again no influence of the nanocomposite concentration or material was observed.

There is little information available on the behaviour of breakdown along the surface of a nanocomposite and a liquid. In [5], which reported surface breakdown between epoxy resin based nanocomposite and liquid, discharges occurred in the first and third quadrant of the cycle as has been seen here. Higher magnitude discharges occurred in the first quadrant which was not observed in this project. However this work was performed using liquid nitrogen as the insulating liquid rather than mineral oil, so comparisons are difficult. In [6], the surface discharge behaviours along the interface of polymeric material and air were investigated. It states that the discharges are predominant in the positive half cycle due to the remained positive charge on the surface. It also said that the surface discharges are mainly related to the material permittivity, surface conditions and the thickness of the sample. It is not clear how this would relate to the experimental system considered here.

There are more suggestions as to how nanocomposite materials may effect bulk breakdown mechanisms involving partial discharge activity[7][8], where four effects caused by nanofiller were confirmed to have impact on the PD resistance:

- **Nanoscale segmentation effect:** introducing the nanoparticles to the matrix material will divide the materials into an aggregation of small segments, the finer distribution of the nanofillers, the finer segmentation it is. The finer segmentation provides higher PD resistance due to the suppression of PD erosion.
- **Coupling agent effect**: the band between the matrix material and the nanofiller can influence the PD resistance of nanocomposite, if the bond is

tighter, the PD resistance is stronger; the best way to enhance the bond is bring in coupling agent between nanofiller and matrix

- **Nanofiller pile-up effect**: nanofiller tend to pile-up on the surface where the PD is happened, this could suppress any further damage of PD erosion.
- **Permittivity difference effect:** For nanocomposite, the electric fields were higher around the nanofiller. Since generally, the nanofiller have higher permittivity than the matrix material and different permittivity can alter the electric field. This could change the behaviour of partial discharge events

Partial discharge activity in the bulk of the material may be different from surface discharge activity. The first three effects are not relevant to the results obtained, as no evidence of material degradation that affected the behaviour of surface discharges was observed during our tests. However the fourth effect may be relevant with local scale changes, in electric field, due to the presence of nanoparticles near the surface, producing a larger number of discharges with smaller amplitude on the surface of the material.

7.2 Optical and Electrical Data Matching

The optical and electrical data has all been analysed separately. In optical data analysis, there are no significant changes in the fractal dimension and length observed which indicated that the optical discharge pattern was not strongly influenced by the different type of nanofiller and concentrations. Changes were observed in the total light emission. In electrical data analysis, the discharge pulse patterns were analysed in terms of discharge number and phase, the number of discharges per cycle and the distribution of discharge pulse magnitudes. The discharge numbers were increased for nanocomposite materials and the distribution of pulse magnitudes was also changed. Nanocomposite material had a small percentage of high magnitude pulses which were not observed in the pure material. The change in pulse number for nanocomposites was due not to the presence of these larger pulses but an increase in the number of low energy pulses.

When the number of pulses is compared to the total optical emission it can be seen that the number of discharges for nanocomposite materials increases for samples with both ZnO and Al_2O_3 while the total light emitted from the discharge area decreases.

This suggests that discharges are occurring in the system that are not contributing to the light emission.

One of the original plans in this project was to observe the optical and electrical events simultaneously. Due to the limitations of the equipment and software it was not possible to use the camera to trigger the start of the oscilloscopes recording cycle. This made the synchronization of the electrical and optical data during experimental measurements impossible. It was then decided to see if the electrical data could be correlated with the optical data through data analysis.

The main difficulty for synchronizing the optical and electrical data is finding the common time between these two sets of data. Decisions needed to be made on the parameters of the data sets that would be used to correlate the data. For electrical data, there was only the pulse value to compare, but for optical data, it needed more consideration. As mentioned in Chapter 5 and Chapter 6, there are three groups of the optical data were recorded:

- **Fractal dimensions**
- **Final length**
- **Light Emission**

Among these three type of data, Fractal dimension and final length were certainly linked to applied voltage level, whether they are linked to other parameters were unable to prove. The light emission was the only one that linked to the type and the concentration of the nanofiller; it did also have an obvious link with the expected power dissipated in the discharges. Light emission was therefore decided to be the parameter for matching with the pulse heights in the electrical data.

The match process was programmed and conducted in MATLAB.

7.2.1 Function Geometry

After decided the parameters to use for the match process, these two groups of data would need to be brought to same dimension. Electrical data had been divided into cycles for analysis; each waveform representing each test was cut into 100 cycles according to the frequency. In the same time interval (2 seconds), where there were 100 cycles of electrical data recorded, 120 frames of optical data was recorded. Since each frame is indivisible, the electrical data would needs to be divided into correspond sections. There are 20 million points in each waveform; each section would therefore contain 166666 points. The actual matching was between the light emission of one actual frame and the summation value of 166666 points. However the correct point in time to start dividing the voltage data into sections for a time interval corresponding with a frame was not known.

Therefore to try to correlate the data many different starting points for the division of the electrical data needed to be considered. This lead to the introduction of:

- **Offset Point(OP):** actual points on the collected waveform, set range from 1 to 160000 with 1000 as a step

Even with the correct setting for the Offset Point a displacement in frame number may also be occurring. This lead to the introduction of:

- **Hypothetic Frames Numbers (HFN):** hypothetical frames, each of these frames contain 166666 points.

The basic idea of the Matlab program is this: for each OP considered the cross correlation of the optical and electrical data was performed using the HFN values. This gives the position where the HFN best matches the optical frame numbers and also gives a value indicating the quality of this match. By comparing the match quality for all the possible Offset Points the optimal Offset Point and the relationship between the HFN and optical frame number can be found.

The basic operation steps for this function are:

1. Importing the electrical data and went through the basic filter mentioned in Section 7.1;
2. Loading the optical data frame by frame and calculating the light emission for each frame, record the calculated value in a array, the match sample size was set to be 41 frames;

3. Matching started, for each OP and HFN value, calculating the cross correlation then finding out the highest value and OP/HFN associated with this value.
4. Use this value to cut the electrical data and store into required form

The correlation method used was cross-correlation. Originally, this method was used in digital signal processing to identify a signal in a noisy environment. Since the data set for a digital signal is merely a set of numbers the technique can be applied to any data set assuming that the data points are evenly spaced along a single dimension

Cross-correlation method used a pre-programmed function in MATLAB and would produce the information on quality of fit and HFN match automatically However 160 Offset points were being considered in each matching cycle. To reduce the processing time, the electrical data set was optimised. Originally, the electrical data was directly introduced as it was collected by oscilloscope. The number of the data is still 2×10^8, for processing this amount of data, the program would take 10 minutes. A new form of the data was created; the data was recorded in cumulative form using the sum of the peak magnitudes. By using this new form, the processing time was reduced to 2 minutes. The light emitted from a hypothetical frame could be calculated using the difference in values of cumulative light emission at the end and start of a Hypothetical Frame.

As mentioned in Section 7.1, there was a data band present in the electrical waveform collected in oscilloscope. In Section 7.1, a threshold value of 1 was introduced to limit this band by setting any point with value lower than 1 to 0. In the matching process, there is also necessary to limit this band. The method used is the same as used in Section 7.1, but the threshold value was set to 0.8. This value was shown to improve the accuracy of the matching process.

7.2.2 Matching Results

By using the program, the optical data and electrical data were synchronized. The value range of offset point was between 8891 and 132801, the value range of hypothetical frames is between 19 and 60. This corresponds to an average offset between the start of the two measurements of 0.3 seconds. Human reaction time is normally higher than 0.19 seconds[9], so the delays observed are in the expected range. Two examples of matched optical and electrical output are shown in Figure 7.16 and Figure 7.17.

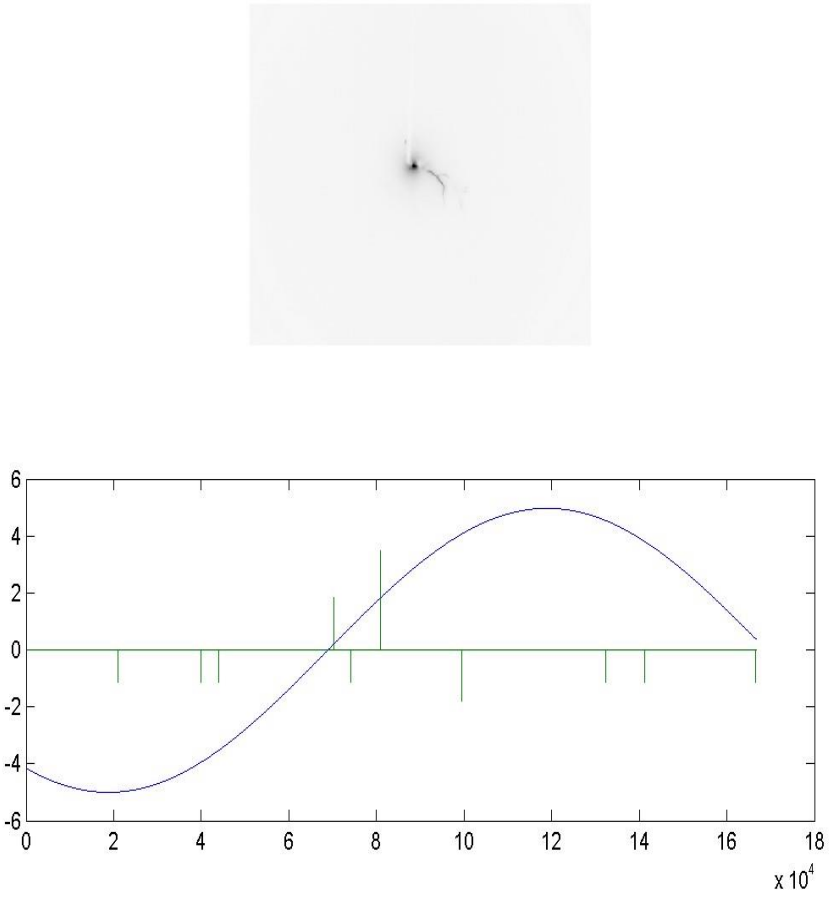

Figure 7.16 An example of an image of less severe discharges synchronized with electrical data

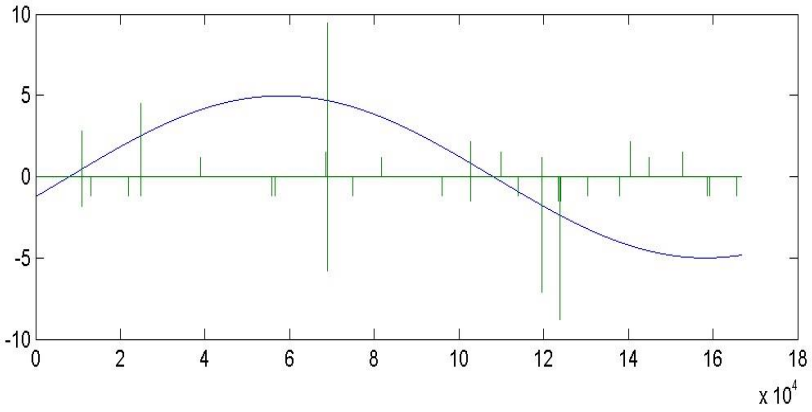

Figure 7.17 An example of an image of severe discharges synchronized with electrical data

In Figure 7.16, the discharge events captured in the image is not severe. There are only one clear discharge branch in the image; there are also some small branches surrounding the high voltage electrode (the needle), but the track is less clear compare to the large branch. In the waveform synchronized for this image, the largest pulse value was 4 mV which could be representing the large branch; there are also 9 small pulses recorded in the waveform.

In Figure 7.17, the discharge events captured is much severe than the ones in Figure 7.16. There are five main branches and several sub-branch extended from the main branches. There are more small branches around the needle. The waveform supports the observation on the image, there are several large pulses recorded in the waveform and the largest pulse value is nearly 10 mV. Apparently the largest pulse was in the

second quadrant, this is different from the general observation in Section 7.1.1, where the majority of the discharges occurred in the first and third quadrants.

A problem in this approach is the influence of the parameter chosen to correlate the data sets. For simplicity the sum of the absolute magnitudes of the peaks in a hypothetical frame was correlated with the optical emission in a frame. It would have also been possible to correlate the data using the sums of the squares of the discharge peaks that would relate to energy. The behaviour of the correlation process would not necessarily be the same using this approach. It is difficult then to be confident in the validity of the correlations. Because of this and as the total number of data sets recorded is nearly 1000 (one optical data and electrical data is consider a data set), the synchronized results are not presented in this thesis.

7.3 Conclusion

In this chapter, the collected electrical pulse data were analyzed using several different methods and several differences of discharge properties were discovered between pure epoxy resin and different types of nanocomposite.

In Section 7.1.2, it was noticed that the cycle number does not have an impact on the pulse distribution and does not have a relationship with phase angle. This suggests that the test time is too short for permanent changes in the system to interfere with the discharge behavior.

For the relationship phase number plot with phase angle, in all of the plot figures, the discharge numbers increase with increased voltage. The general shape of the distribution of discharge number with phase angle is similar for each type of sample. There are clear regions where discharge activity is large and other regions where discharge activity is consistently lower. The majority of the discharge activity is occurring in the first and third quadrants. This indicates that the voltage and the rate of change of voltage must have the same sign for discharge activity to occur. With increasing voltage for each type of sample, the number of discharges increases, but there does not seem to be any shifts in the distribution of the discharges.

For the ZnO nanocomposites in general, the number of discharges in each peak has increased compared with the pure epoxy samples. There is no clear relationship between the changes in the discharge patterns and the concentration of nanofiller. For the Al_2O_3 nanocomposites, the discharge activity for the 0.1 wt% samples is higher than those observed in the pure samples. In general, there is little difference between the behaviour of the 0.1 wt% and 0.5 wt% samples.

In Section 7.1.3, for the discharge value comparison results, there are several features found regarding different type of materials:

1. For pure epoxy resin, the maximum value of the current pulses does not increase with the applied voltage.

2. For nanocomposites higher valued pulses occur compared to the for pure epoxy resin, but the number of these large value pulses are no more than 1% of the total pulse number observed.

3. The magnitude of the current pulses for nanocomposites does depend on the value of the applied voltage; increasing as the voltage level increases.

4. In Weibull Statistic analysis of the pulse magnitude, the shape parameter β of pure epoxy resin is larger than the shape parameter β of nanocomposite. The values of β indicate that the probability density will have its maximum value at 0 and decreases for higher values of discharge peak magnitude. The shape parameter β of nanocomposite materials is not changed with concentration.

5. In Weibull Statistic analysis, of the pulse magnitude, scale parameter α for the nanocomposites is smaller than those found for pure epoxy. The decrease in the shape parameter indicates that pulses with a lower magnitude are more likely to occur in the nanocomposite materials. There is little change in the value of the shape parameter for differing concentrations of nanocomposites and between nanocomposites based on ZnO and Al_2O_3.

In Section 7.2, the method for synchronizing the electrical data and optical images were described. The synchronized results were presented. The information of discharges which this synchronization and comparison process brought were limited, but the fact

that it can work provides a new way of observe the discharges. Further research is needed to discover more information regarding relations between the electrical pulse waveform and the appearance of surface discharges in images.

References

[1] H. Zainuddin, P. L. Lewin, and P. M. Mitchinson, "Characteristics of leakage current during surface disharge at the oil-pressboard interface," *Annu. Rep. - Conf. Electr. Insul. Dielectr. Phenomena, CEIDP*, pp. 483–486, 2012.

[2] a. Beroual, L. Kebbabi, E. a. Al-Ammar, and M. I. Qureshi, "Analysis of creeping discharges activity at solid/liquid interfaces subjected to ac voltage," *IET Gener. Transm. Distrib.*, vol. 5, no. 9, p. 973, 2011.

[3] IPEC, "HFCT 100-50 Product Specification sheet." [Online]. Available: HFCT 100-50 Product Specification sheet. [Accessed: 01-Jan-2015].

[4] M. P. Wilson, "IMPULSE BREAKDOWN OF LIQUID-SOLID," 2011.

[5] R. Sarathi, S. Aravinth, and K. Sethupathi, "Analysis of surface discharge activity in epoxy nanocomposites in liquid nitrogen under AC voltage," *IEEE Trans. Dielectr. Electr. Insul.*, vol. 21, no. 2, pp. 452–459, Apr. 2014.

[6] Y. Komiyama, S. Suzuki, H. Miyake, Y. Tanaka, and T. Takada, "Investigation of surface discharges on different polymeric materials under HVAC in atmospheric air," *IEEE Trans. Dielectr. Electr. Insul.*, vol. 18, no. 2, pp. 485–494, Apr. 2011.

[7] T. Tanaka, "Similarity between treeing lifetime and PD resistance in aging mechanisms for epoxy nanocomposites," in *2009 IEEE 9th International Conference on the Properties and Applications of Dielectric Materials*, 2009, pp. 741–744.

[8] T. Tanaka and T. Iizuka, "Generic PD resistance characteristics of polymer nanocomposites," in *2010 Annual Report Conference on Electrical Insulation and Dielectic Phenomena*, 2010, pp. 1–4.

[9] C. R. Metzgar, "A Literature Review on Reaction Time," *Prof. Saf.*, Jan. 2008.

8. CONCLUSIONS AND FURTHER WORK

8.1 Conclusions

Surface breakdown along the interface of two insulating materials is the weakest link of combine insulation system. This project was aimed to investigate the surface

discharge behaviour along the interface of mineral oil and nanocomposite under AC condition by observing the optical figure and the electrical data of the discharge. For performing this experiment, the manufacture method, test cell and data processing method were designed or programmed.

The first area researched for this project is the manufacture of nanocomposite. The processes investigated to successfully manufacture samples suitable for surface breakdown testing have been described in Chapter 3. The investigation was drawn out and tedious and many different attempts were needed before developing the successful procedures which has been described in detail. The development of the moulding technique has been described and the geometries of the moulds are also given to ensure that this work can be repeated if needed in any further research. For both nanoparticles ZnO and Al_2O_3, there are seven concentrations made for each type: 0.1 wt%, 0.5 wt%, 1 wt%, 2 wt%, 3 wt%, 4 wt% and 5 wt%. For each concentration, there are 6 to 10 sample made, depend on the material stock and the sample condition.

After developing the method for the making of nanocomposites and making the samples, the exploration of its dielectric properties becomes the next step. By using different methods, some nanocomposite manufactured in this project were tested to investigate the property changes among them. The permittivity and loss tangent of Both ZnO and 1 wt% Al_2O_3 nanocomposite were increased comparing to pure epoxy; the permittivity and loss tangent of 0.5 wt% Al_2O_3 nanocomposite has no significant changes comparing to pure epoxy. There are also increases on the conductivity of all the nanocomposite comparing to pure epoxy. At present it is not possible to fully explain the observed behaviour of the dielectric properties of the material. There is a possible explanation: the balancing between increase effect in permittivity due to the presence of the nanoparticles and the decrease effect caused by the reduced polarizability of the epoxy material in the regions close to the nanoparticles.

These results are different to results reported by other workers. The differences are probably caused by: the different manufacture methods of the nanoparticles with the possibility of introducing impurities; different surface modifications being made to the nanoparticles, and different methods of mixing the nanoparticles into the polymer matrix which may affect the distribution of the nanoparticle after they had been added

into the matrix material. There is also the effect of the matrix material; as the properties of nanocomposite can be impact by both the nanoparticle and the matrix materials. A problem with investigations of nanocomposites is the difficulty caused by these factors in comparing data in the literature.

The surface discharge observation system along with the test cell were then designed and built. There are two types of data collected from this system: the optical data which collected by the CCD camera and the electrical data which collected by the HFCT and oscilloscope. The original desire was to record the optical data and electrical data simultaneously, but it was not possible to achieve this. During measurements, the camera was manually synchronized with the electrical data.

In the experimental programme, the samples were not all tested. For ZnO nanocomposite, 4 wt% and 5 wt% were unsuitable for surface breakdown tests since they rapidly failed through bulk breakdown. The same occurred with Al_2O_3 nanocomposite with the concentration over 1 wt%. At the end, the test sample types are as follow: pure epoxy, ZnO 0.1 wt%, 0.5 wt%, 1 wt%, 2 wt%, 3 wt% and Al_2O_3 0.1 wt%, 0.5 wt%. There were a total of over 1000 tests performed on samples in the course of this work.

From analyzing the optical data, several conclusions about the optical behavior of surface discharge can be made:

- The fractal dimension of the images based on 100 cycles of AC stressing has been calculated. It is found that the fractal dimension values are linearly dependent on the applied voltage and no significant changes observed in fractal dimension as a result of changing nanofiller or concentration. Based on the trend line which best fits the data distribution, an initiating voltage for the discharge was calculated (27.3 kV) which is close to the observed initiating voltage (24 kV) found in preliminary tests.

- The maximum or final length associated with the surface discharge pattern has been measured. The final length of the surface discharge is also linearly depending on the applied voltage and no significant changes observed in final length as a result of changing nanofiller or concentration. From fitted trend line of the data, a

value of initiation voltage for discharges on the surface was calculated. This value was lower than that found from the fractal dimension analysis. The difference is possibly due to resolution/sensitivity of the camera system or due to actual relationship between applied voltage and length not being linear but approximating to a linear behaviour over voltage range considered.

- The total light emission from the surface discharge of each type of sample were measured and calculated by the programed MATLAB function. The total light emissions were dependent on the voltage, but not linearly. It can be related to the applied voltage in term of an expression reflecting electrical power: $L(V) = A(V - V_0)^2$. The value for parameter V_0 is similar to that found through fractal analysis. The behavior of total light emission was related to the nanofiller in general, the total light emission of surface discharge over Al_2O_3 and ZnO nanocomposite with concentration lower than 1 wt% is significantly lower than pure epoxy and 1 wt% ZnO nanocomposite, the total light emission of 2 wt% ZnO nanocomposite shows the largest total light emission value.

For analyzing the electrical data, a program was developed in MATLAB to recognize and store the pulse data (cycles, phase angles and values). From analyzing the electrical data from nearly 1000 files, several conclusions about the power behavior of surface discharge can be made:

- The number of current pulses were increased if the measurement was performed on a nanocomposite material but no trend with the filler or concentration could be seen.

- The cycle number does not have an impact on the pulse distribution and does not have a relationship with phase angle where the pulse located. This suggests that the test time is too short for permanent changes in the system to interfere with the discharge behavior.

- For the relationship phase number plot with phase angle, in all of the plot figures, the discharge numbers increase with increased voltage. The general shape of the distribution of discharge number with phase angle is similar for each type of sample. There are clear regions where discharge activity is large and other regions

where discharge activity is consistently lower. The majority of the discharge activity is occurring in the first and third quadrants. There are three peak regions present in these quadrants. For nanocomposite tested with a lower concentration than 1 wt%, the first peak shifts ahead for 10°, there is rarely any pulse occurring at 30°.

- For the discharge value analysis results, several features were found regarding different type of materials: For pure epoxy resin, the pulse value of discharge is not affected by the applied voltage in the two seconds period. Higher value pulses were observed in nanocomposites but the number of these pulses is no more than 1% of the total pulse number. The pulse value of discharge for nanocomposites can be affected by the applied voltage; with voltage level increased, the size of pulses increased. From Weibull Statistical analysis, its suggests that the increase in pulse number is dominated by smaller pulses rather than the high magnitude pulses There is little change in the probability distribution for differing concentrations of nanocomposites and between nanocomposites based on ZnO and Al_2O_3.

After analyzing the optical and electrical data separately, an attempt was made to match these two sets of data. Through MATLAB programming, this method was developed base on the method of cross-correlation, the results were briefly presented in Chapter 7 due to concerns with the correlation process being self-fulfilling.

Overall, in this project, the lab method for manufacturing large nanocomposite with different concentration was developed and the samples were successfully made. The broad data for understanding the behavior of surface discharge across ZnO and Al_2O_3 nanocomposite and liquid interface were collected. From general observation, it is not possible to see significant changes in the behavior of surface discharge along the nanocomposites surface compare to pure epoxy. There was a suggestion for the change of permittivity would affect the surface discharge behavior. However, the changes in permittivity mismatch between nanocomposite and pure epoxy may have been insufficient to affect the behavior of surface discharge. Regarding the usage of fractal dimension, there have been questions about how meaningful this method can be on the surface discharge pattern analysis. The matching method for these two types of data was developed, but further optimization was needed for better performance.

8.2 Further work

There is a large quantity of data collected in this project and additional analysis of the discharge activity could be possible using other techniques such as pulse sequence analysis. Especially the results regarding the reduced light emission with nanocomposite while the rest of the discharge activities remain the same.

Based on the data collected in this project, the dielectric properties and surface discharge behavior of the nanocomposites was complex with concentration. It could be a result of the manufacturing process. The experiments could be repeated using a different mixing process but identical nanofillers and epoxy resin to see if similar behaviors are observed.

If the differences between the dielectric behaviors observed in the nanocomposites were real, more measurements over a larger number of different concentrations would be useful to gain a clearer understanding of the behavior of nanocomposites. It would also be useful to determine the behavior for both light emission and discharge pulse activity for a larger number of concentrations in the range of 0 to 1 wt%.

Although the optical data and electrical data were matched in data process stage, the method itself was not desirable. In further research, it may be possible to develop a system where the optical output is automatically coordinated with the measurement of electrical output during the experiment.

Further analysis of the significance of fractal analysis of discharge patterns is needed. This method has been used to classify the behavior of many electrical breakdown phenomena. The relationship, if any, between the fractal dimensions associated with a 3 dimensional structure, such as an electrical tree, which should be in the range of 2 to 3 and the values obtained from a 2 dimensional image of a 3 dimensional structure which would be in the range of 1 to 2 of the structure, needs to be defined.

It would also be useful to examine the behavior of surface discharges along a liquid nanocomposite interface under different waveforms including a step DC, impulse and a bipolar pulse.

APPENDIX A: Mould and Test Cell Design

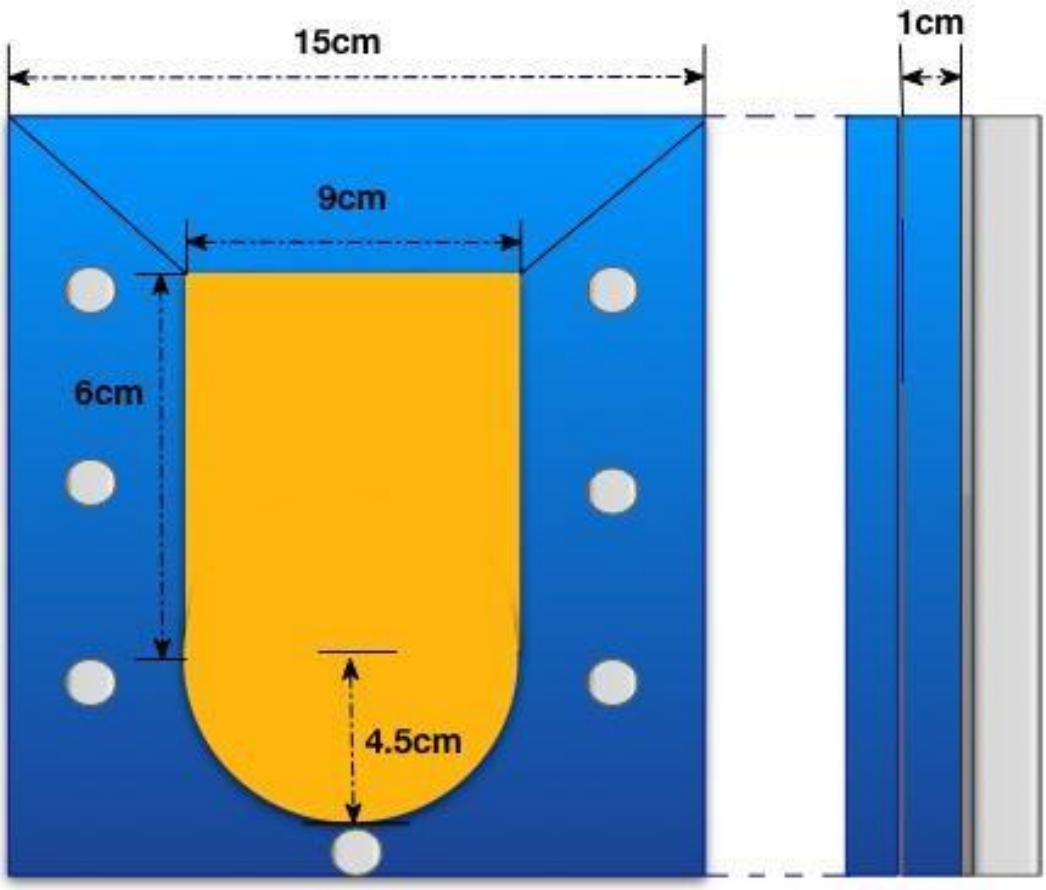

Figure A.1 Mould geometry

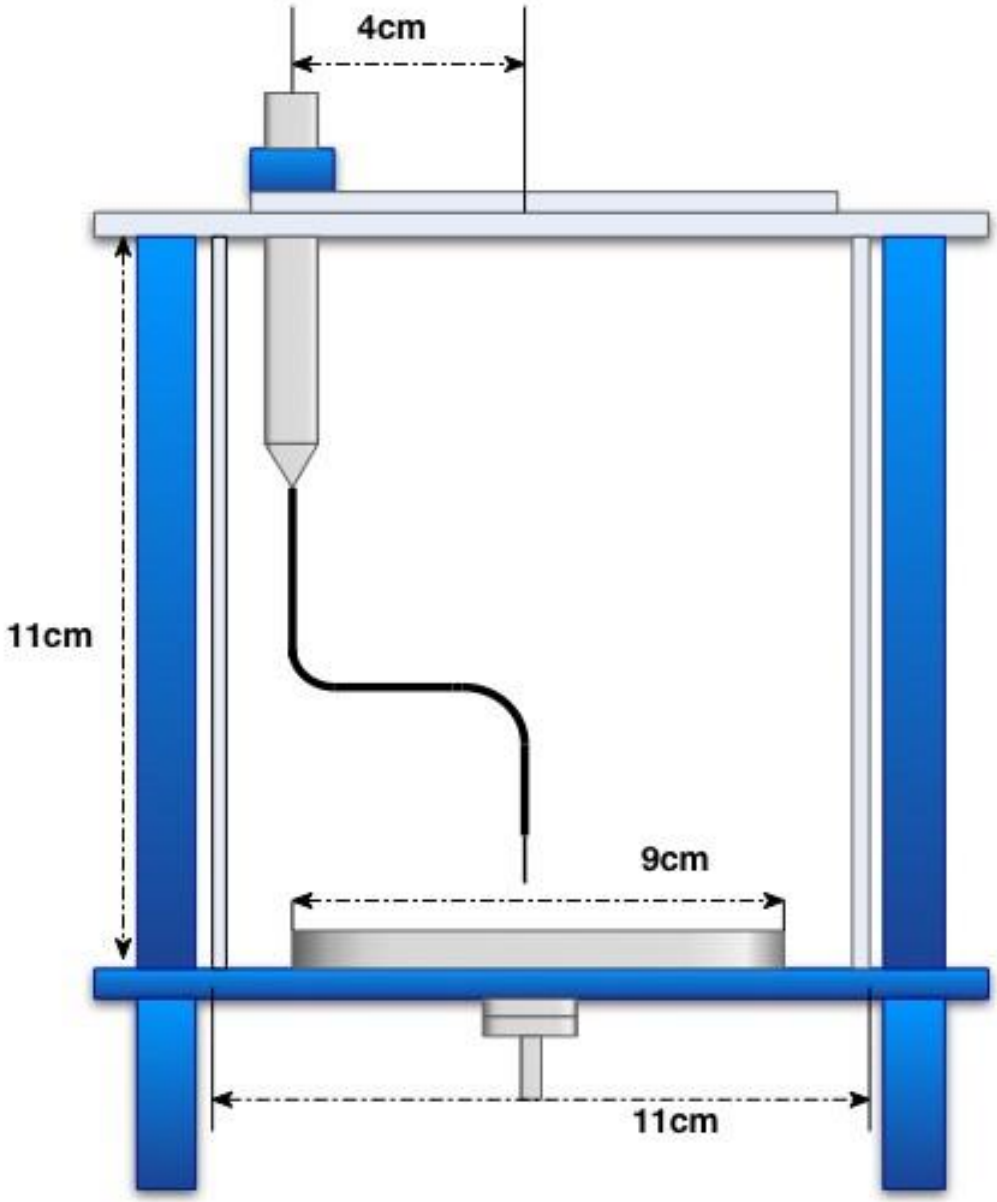

Figure A.2 Test cell

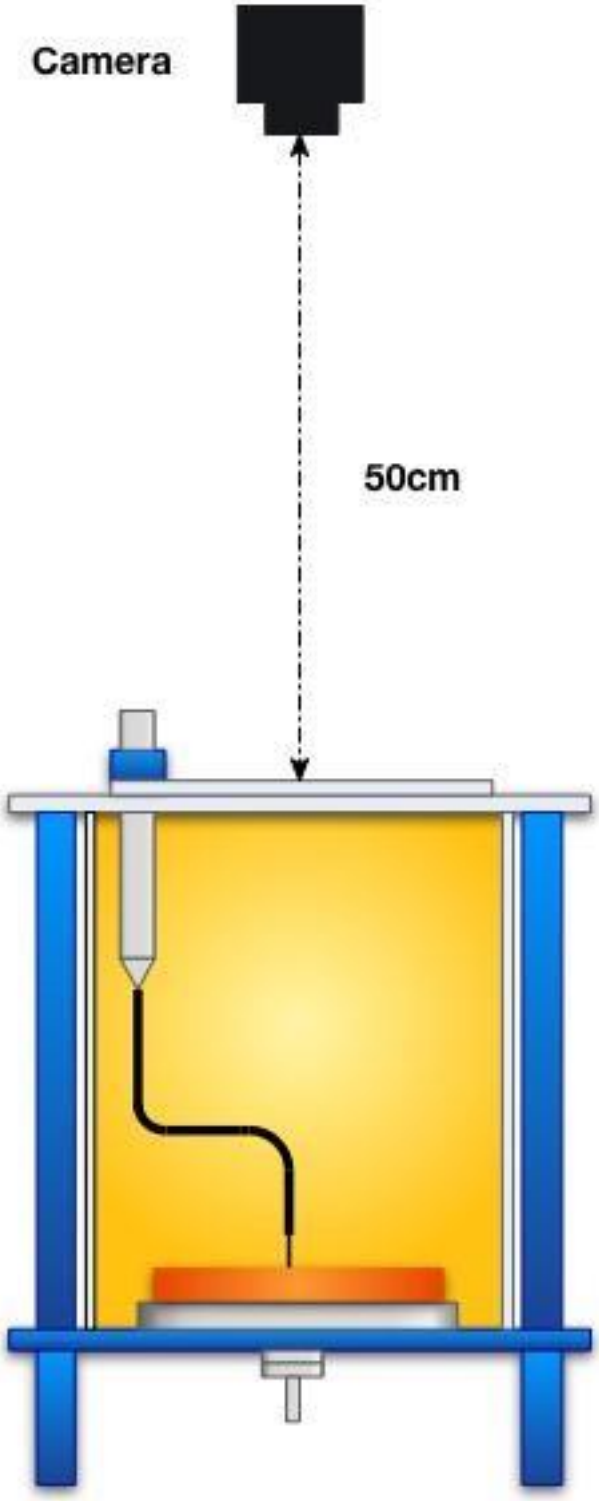

Figure A.3 Camera distance

APPENDIX B: MATLAB Code

Video separation:

```
di=dir('*.avi') obj = VideoReader(['',di.name]); vid =
read(obj); frames = obj.NumberOfFrames; for x = 1 :
frames     imwrite(vid(:,:,:,x),strcat('frame-
',num2str(x),'.bmp')); end
 clear all
```

BATCHING images:

```
function[output_image]= batching(noi)
image_3D=zeros(494,648,noi);
fileName = 'frame-'; for
build3dmatrix=1:noi
    ImgName = [fileName,num2str(build3dmatrix),'.bmp'];
q=imread(ImgName);     image_3D(:,:,build3dmatrix)=q;
end
output_image=max(image_3D,[],3); imwrite(
uint8(output_image),'Frame-all.bmp','bmp') EDGE
```

PROCESSING OF THE REGTIX OUTPUT:

```
function areg(p) t=imread('Frame-
allp.bmp'); t1=rgb2gray(t); for
i=[1,2,3,492,493,494]     for j=1:648
t1(i,j)=p;     end end for m=1:494     for
n=[1,2,3,646,647,648]         t1(m,n)=p;
end end     imwrite( uint8(t1),'Frame-
allpp.bmp','bmp')
```

FRACTAL DIMENSION CALCULATION MAIN FILE:

```
function df = do(level)
a=imread('Frame-allpp.bmp');
```

```
x=level/255; a2=im2bw(a,x);
[n,r]=BCs(a2);
df = -diff(log(n))./diff(log(r));
disp(['Fractal dimension, Df = ' num2str(mean(df(4:8))) ' +/- ' num2str(std(df(4:8)))]);
clear all
```

FRACTAL DIMENSION SUBFUNCTION FILE:

```
function[n,r]= BCs(c) width = max(size(c)); p=log(width)/log(2);
if p~=round(p)||any(size(c)~=width)  p=ceil(p);  width=2^p;
mz=zeros(width,width);  mz(1:size(c,1),1:size(c,2)) =c;
c=mz; end n=zeros(1,p+1); n(p+1) = sum(c(:)); for g=(p-1):-1:0
siz = 2^(p-g);  siz2 = round(siz/2);  for i=1:siz:(width-siz+1)
for j=1:siz:(width-siz+1)  c(i,j) = ( c(i,j) || c(i+siz2,j) ||
c(i,j+siz2) || c(i+siz2,j+siz2) );  end  end
   n(g+1) = sum(sum(c(1:siz:(width-siz+1),1:siz:(width-siz+1))));
end n = n(end:-1:1); r = 2.^(0:p);
```

TOTAL LIGHT EMISSION CALCULATION:

```
function[output]= lighte(level,noi)
x=level/255; p=imread('Frame-
all.bmp'); p1=im2bw(p,x);
image_3D=zeros(494,648,noi);
fileName = 'frame-'; for
build3dmatrix=1:noi
   ImgName = [fileName,num2str(build3dmatrix),'.bmp'];
OriImg = imread(ImgName);  y=OriImg;  for
a=1:494  for b=1:648  if (OriImg(a,b)<level);
y(a,b)=0;  end  end  end
image_3D(:,:,build3dmatrix)=double(y).*p1; end output
= sum(image_3D(:));
```

PHASE ANGLE, CYCLE, LOCATION AND VALUE:

```
function[points_phs,points_cyc,points_loc,points_val]=pciv(wave_num,vol_num,thr
e shold)
%%%%%%%%%%%%%%%% INPUT %%%%%%%%%%%%%%%%
di=dir('*.txt'); c2=dlmread([di(1).name],',',5,1); c3=dlmread([di(2).name],',',5,1);
%%%%%%%%%%%%%%%% WAVELOAD & CONVERTION
&FILTERING %%%%%%%%%%%%
% PHASE DETERMINE
Hd=filter09;
phase1=flipud(filter(Hd,flipud(filter(Hd,c2))));
phase2=hilbert(phase1); angle1=angle(phase2);
% OFFSET DETERMINE
offset= mean(c3); z=c3-offset;
phase3=(abs(z))>threshold;
p=phase3.*z;
% THRESHOLD & PEAK FILTERING
for r=10:(length(z)-10)
        if
        abs(p(r))>abs(p(r+1))&&abs(p(r))>abs(p(r+2))&&abs(p(r))>abs(p(r+3))&&a
        bs(p(r))>abs(p(r+4))&&abs(p(r))>abs(p(r+5))&&abs(p(r))>abs(p(r+6))&&ab
        s(p(r))>abs(p(r+7))&&abs(p(r))>abs(p(r+8))&&abs(p(r))>abs(p(r+9))&&abs
        (p(r))>abs(p(r+10))&&abs(p(r))>abs(p(r-
        10))&&abs(p(r))>abs(p(r9))&&abs(p(r))>abs(p(r-8))&&abs(p(r))>abs(p(r-
        7))&&abs(p(r))>abs(p(r-
        6))&&abs(p(r))>abs(p(r-5))&&abs(p(r))>abs(p(r-4))&&abs(p(r))>abs(p(r-
        3))&&abs(p(r))>abs(p(r-2))&&abs(p(r))>abs(p(r-1))
p(r+1)=0;       p(r+2)=0;       p(r+3)=0;       p(r+4)=0;
p(r+5)=0;       p(r+6)=0;       p(r+7)=0;       p(r+8)=0;
p(r+9)=0;
```

```
        p(r+10)=0;
p(r-1)=0;
p(r-2)=0;
p(r-3)=0;
p(r-4)=0;
p(r-5)=0;
p(r-6)=0;
p(r-7)=0;
p(r-8)=0;
p(r-9)=0;
p(r-10)=0;
end end
 % SELECTING THE POINTS
psp=1; for tp=1:length(c2)
if abs(p(tp))>0;
points_val(psp)=p(tp);
points_loc(psp)=tp;
points_phs(psp)=angle1(tp);
psp=psp+1;     end end
%%%%%%%%%%%%%%%%%%%%%  FIND THE CYCLES &
CUTTING %%%%%%%%%%%%%%%%%%%%%%%%%% k=1;
for n=2:length(phase1)      if phase1(n)>=0&&phase1(n-1)<0
index_a(k)=n;         k=k+1;     end end
points_cyc=zeros(1,length(points_loc)); for wel=2:length(index_a)
for t2=1:length(points_loc)
        if points_loc(t2)>index_a(wel-1)&& points_loc(t2)<=index_a(wel)
points_cyc(t2)=wel-1;         end     end end
comb_al=[points_phs',points_cyc',points_loc',points_val'];
csvwrite(strcat(num2str(wave_num),'_',num2str(vol_num),'KV_threshold_',num2str(
t hreshold),'.csv'),comb_al);
```

IMAGE AND PULSE MATCHING POINTS DETERMINENATION:

```
%%%%%%%%%%%%IMAGE LOAD%%%%%%%%%%%%%%
LE_single=zeros(40+1,2);
t=23/255;
mask=imread('Frame-all.bmp');
%p1=im2bw(p,t); fileName =
'frame-';
for k=1:40+1%%%%%%%%%%%%
   ImgName = [fileName,num2str(k),'.bmp'];
a=imread(ImgName);     a2=im2bw(a,t);
b=double(mask).*a2;     LE_single(k,1)=k;
LE_single(k,2)=sum(b(:)); end
%%%%%%%%%%%%Pulse value Integration%%%%%%%%%%%%
pp=size(c3); pulse_points=c3(:,2);
num_pul=abs(pulse_points)>1; sum_qq=0; psp=1;
for tp=1:pp(1)        if abs(pulse_points(tp))>1;
points_val(psp)=abs(pulse_points(tp))+sum_qq;
points_loc(psp)=tp;
sum_qq=abs(points_val(psp));        psp=psp+1;
end end
%%%%%%%%%%%% Compare and Match %%%%%%%%%%%%%
tt=size(points_val);
location_matrix=zeros(20000,90);
comatrix=zeros(100,1); for offset=1:20000
for sett=1:119        Last_value=0;        for
```

```
tel=1:tt(2)            if

points_loc(tel)<=(offset+sett*166666);

comatrix(tel)=points_val(tel);            end

end

      corr_matrix(sett)=max(comatrix)-Last_value;

Last_value=corr_matrix(sett);        clear

Last_value;       end     for sel_image_pulse=1:90


          location_matrix(offset,sel_image_pulse)=abs(corr2(corr_matrix(sel_image_p
          ulse:(sel_image_pulse+20)),LE_single(:,2)'));

   end end

value=ma

x(max(loc

ation_mat

rix));


 [rows,cols]=find(location_matrix==max(max(location_matrix)));
```

WAVECUT FILE:

```
%%%%%%%%%%%%%% INPUT %%%%%%%%%%%%%%%%%%%%

dif=; offset=;

noi=119-dif;

threshold=;

%%%%%%%% SHOW IMAGE%%%%%%%%%%%%%%%%

fileName = 'frame-'; Hd=filter09;

phase1=flipud(filter(Hd,flipud(filter(Hd,c2(:,2)))));

u=c3(:,2); offs= mean(u); sampl=u-offs;

num_pul=abs(sampl)>threshold;

samp2=sampl.*num_pul; for bd=1:noi

    ImgName = [fileName,num2str(bd),'.bmp'];

    OF                  =                  imread(ImgName);

 OOF=imcomplement(OF);

    subplot(2,1,1);

 imshow(OOF);

    subplot(2,1,2);                                          pulse_s(:,2)=samp2((offset+(bd-

 1+dif)*166666):(offset+(bd+dif)*166666));


          pulse_s(:,1)=phase1((offset+(bd-
       1+dif)*166666):(offset+(bd+dif)*166666))*0.0001;

    plot(pulse_s);

newname=strcat('E:\im_ele_match\0000\',num2str(bd+dif));

saveas(gcf,newname,'png'); end
```

APPENDIX C: DF, FL and TLE Plots

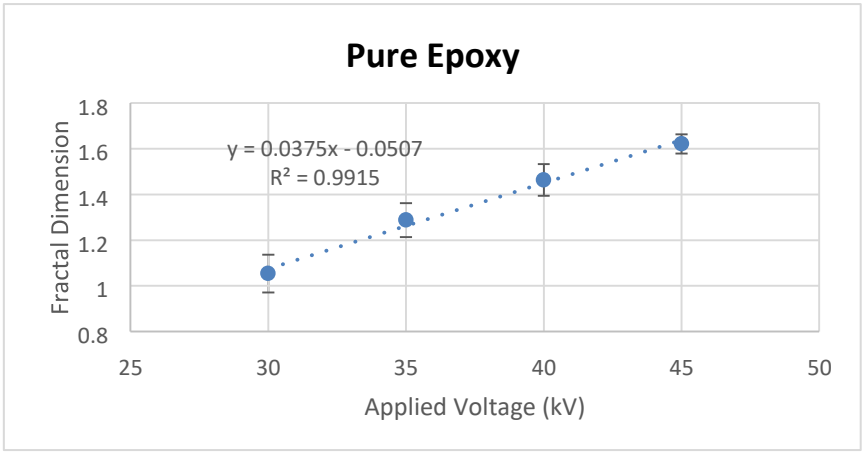

Figure C.1 Fractal Dimension of pure epoxy

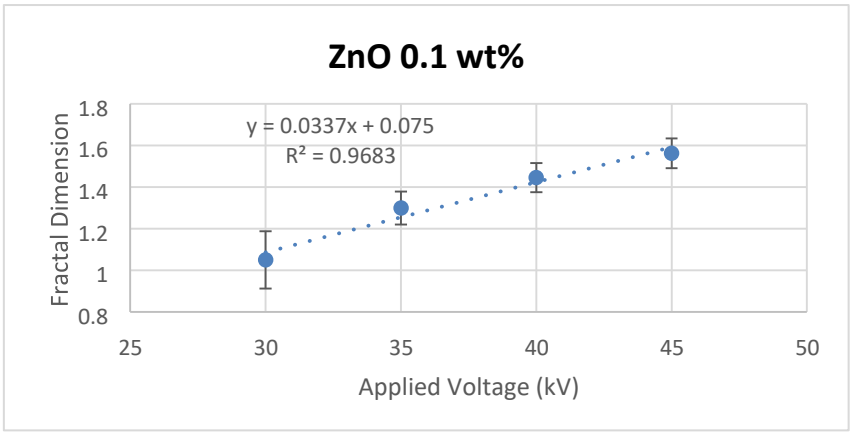

Figure C.2 Dimension of ZnO 0.1 wt% nanocomposite

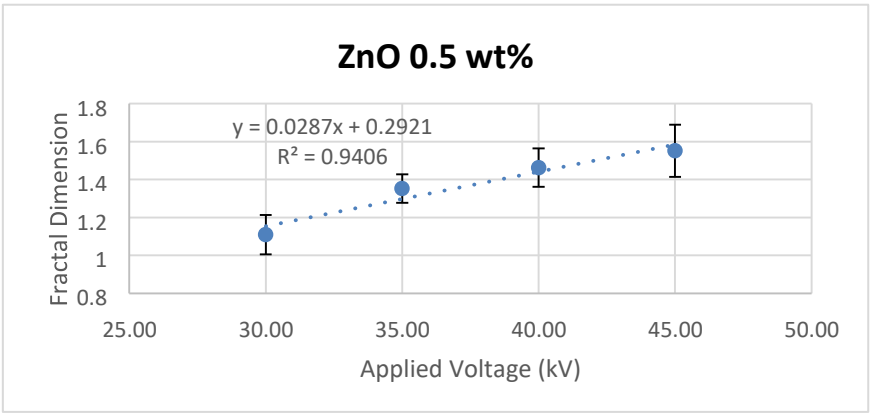

Figure C.3 Fractal Dimension of ZnO 0.5 wt% nanocomposite
Figure C.4 Fractal Dimension of ZnO 1 wt% nanocomposite

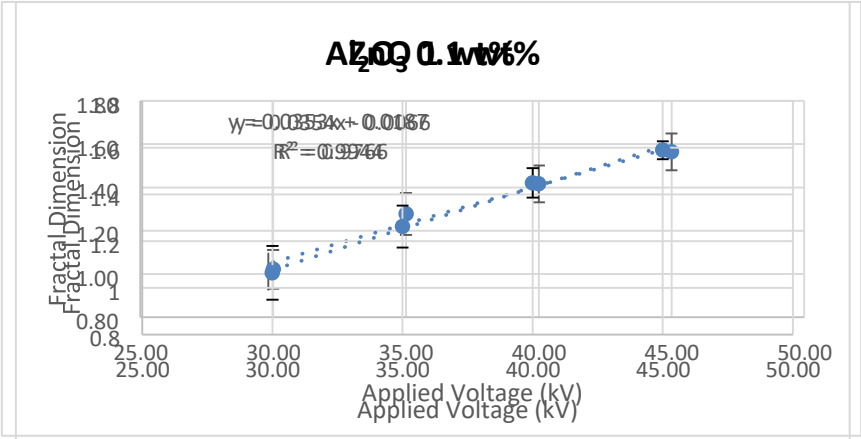

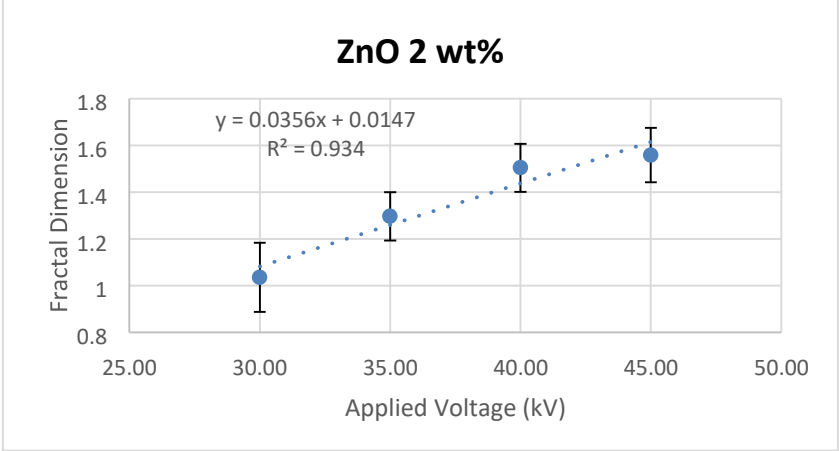

Figure C.5 Fractal dimension of ZnO 2 wt% nanocomposite

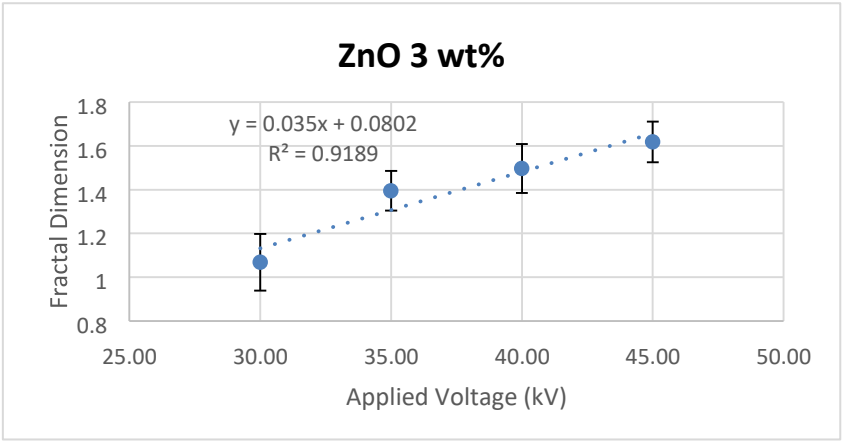

Figure C.6 Fractal dimension of ZnO 3 wt% nanocomposite
Figure C.7 Fractal dimension of Al_2O_3 0.1 wt% nanocomposite

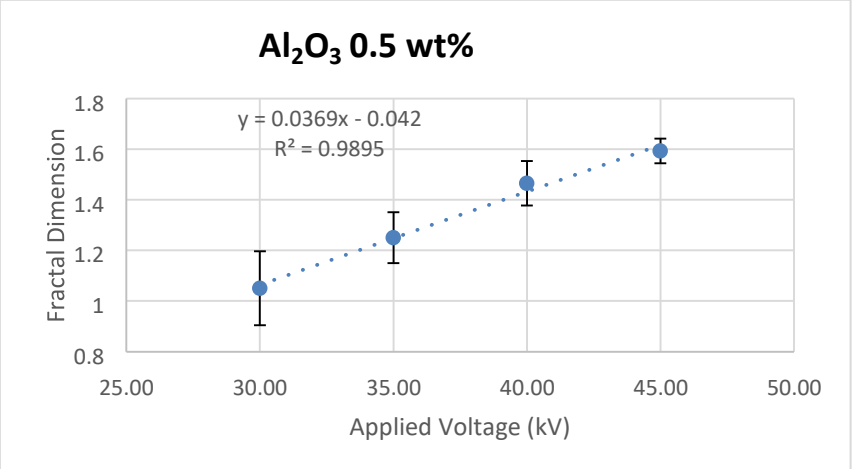

Figure C.8 Fractal dimension of Al_2O_3 0.5 wt% nanocomposite

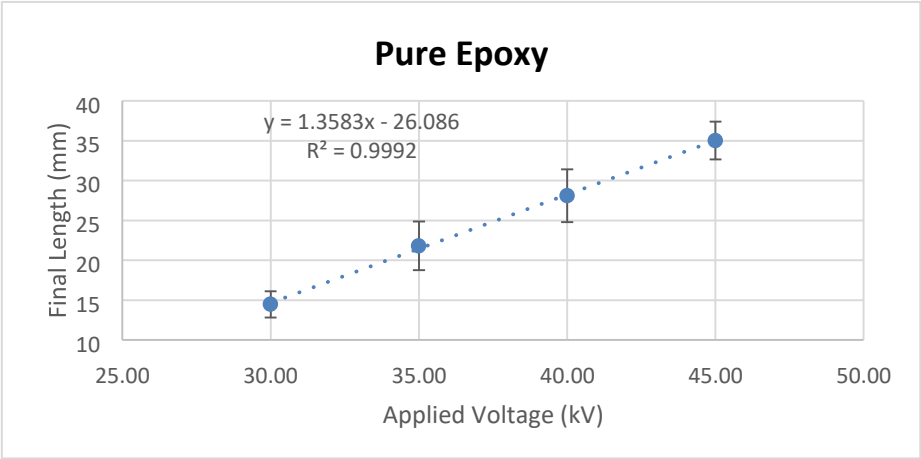

Figure C.9 Final length of branch on pure epoxy sample

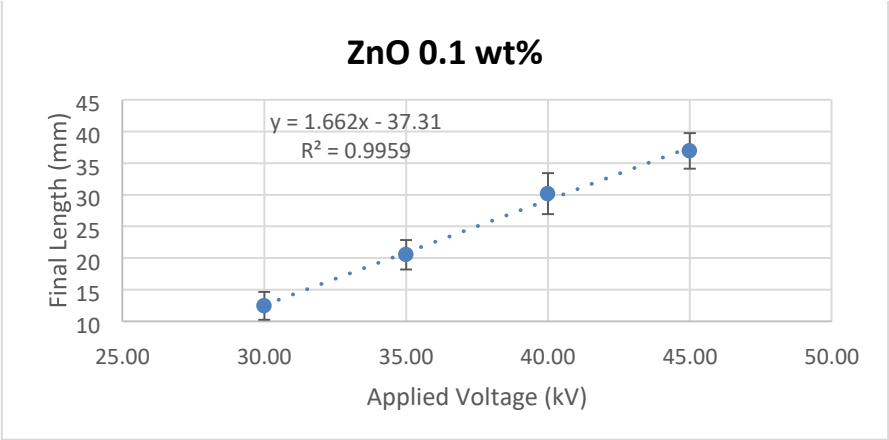

Figure C.10 Final length of branch on ZnO 0.1 wt%

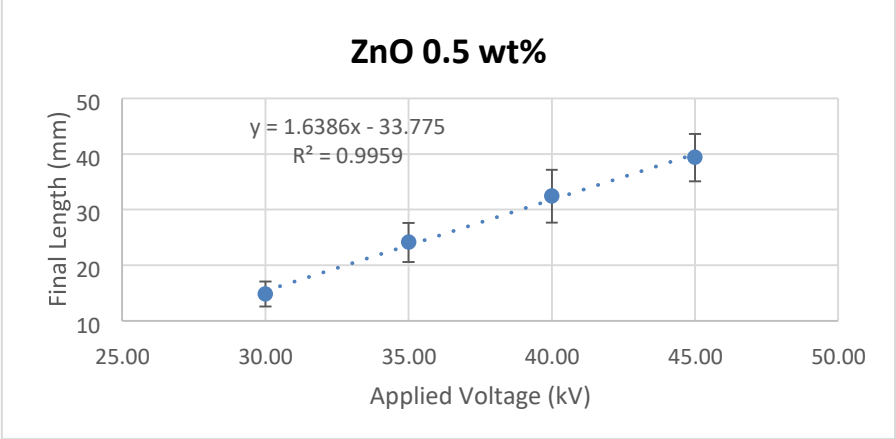

Figure C.11 Final length of branch on ZnO 0.5 wt% **Figure C.12** Final length of branch on ZnO 1 wt%

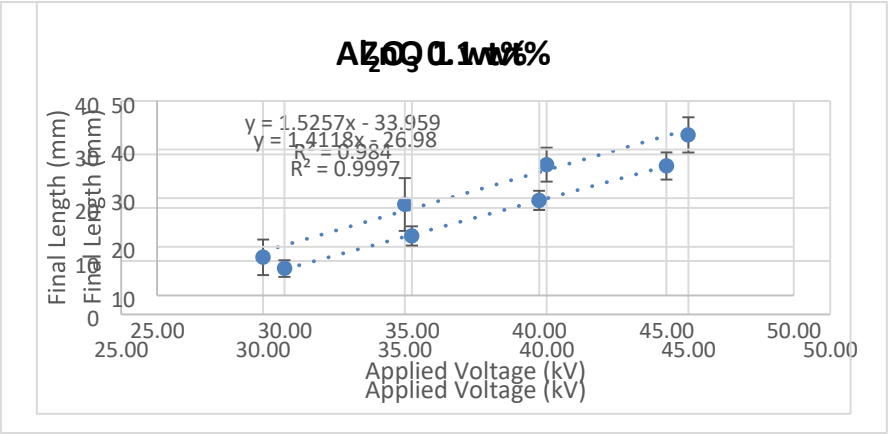

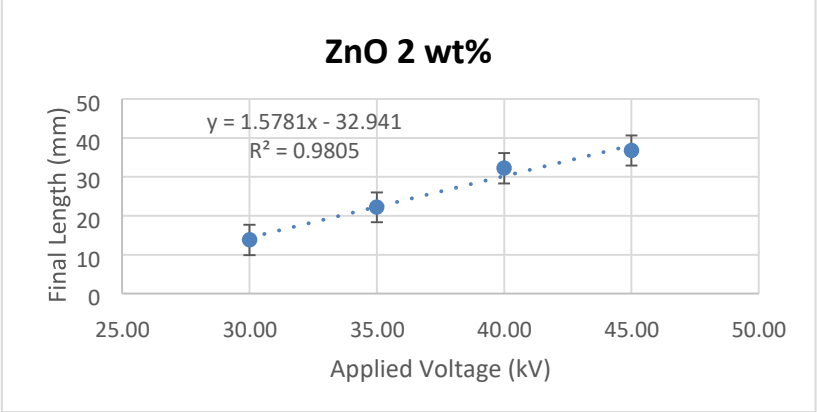

Figure C.13 Final length of branch on ZnO 2 wt%

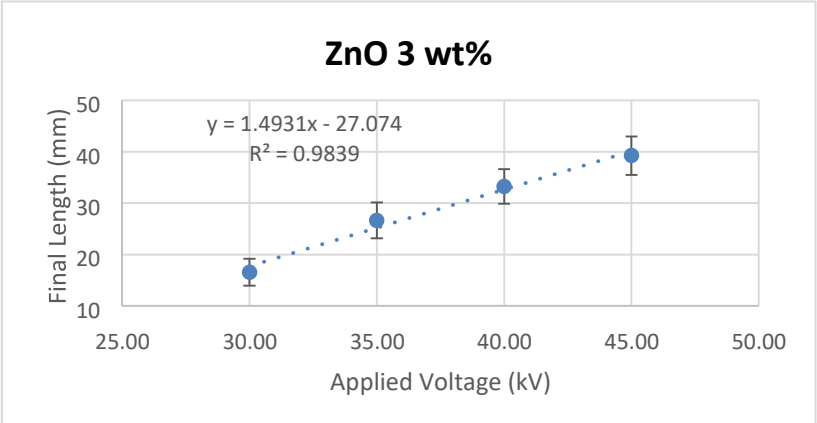

Figure C.14 Final length of branch on ZnO 3 wt% **Figure C.15** Final length of branch on Al_2O_3 0.1 wt%

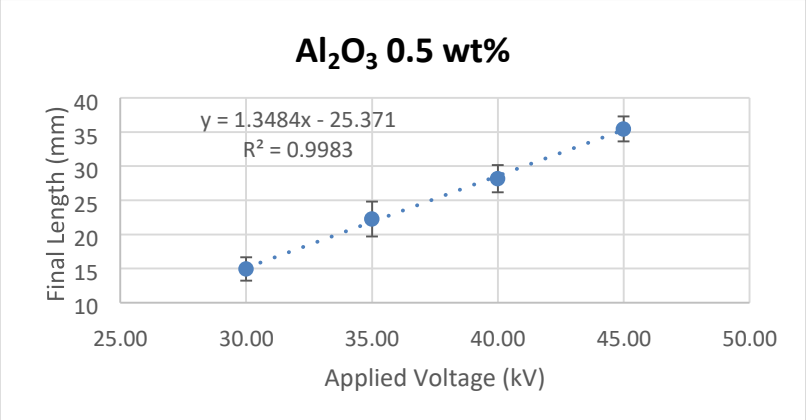

Figure C.16 Final length of branch on Al_2O_3 0.5 wt%

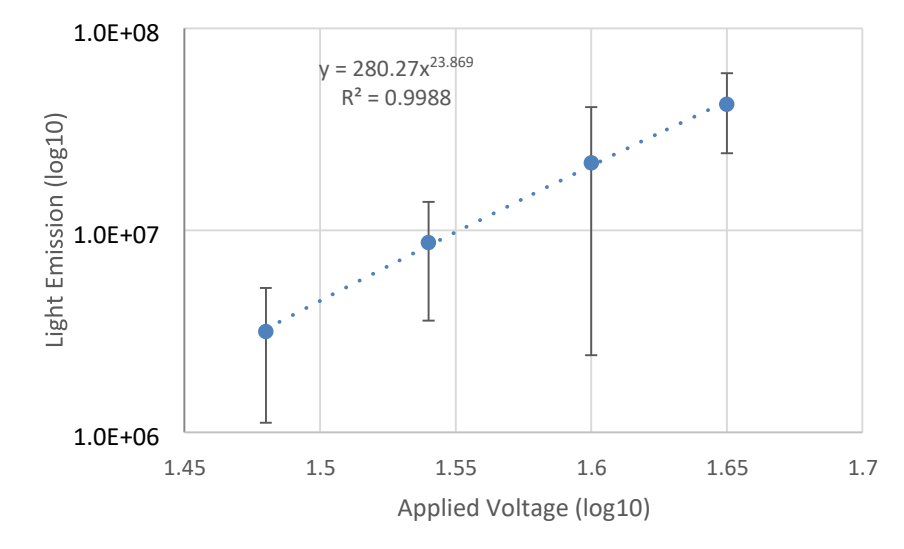

Figure C.17 Total light emission of Pure Epoxy

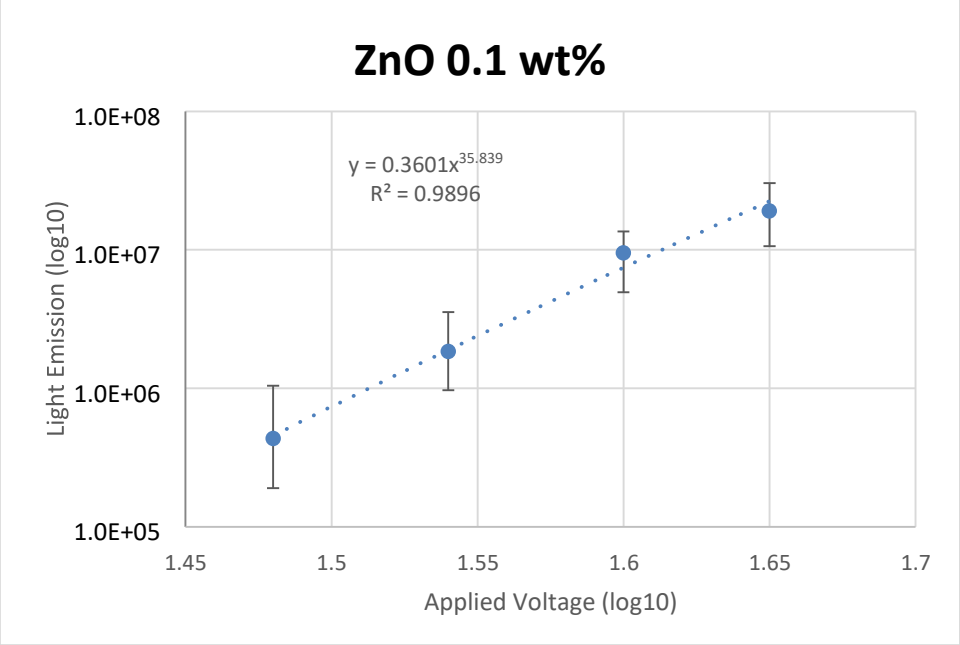

Figure C.18 Total light emission of ZnO 0.1 wt%

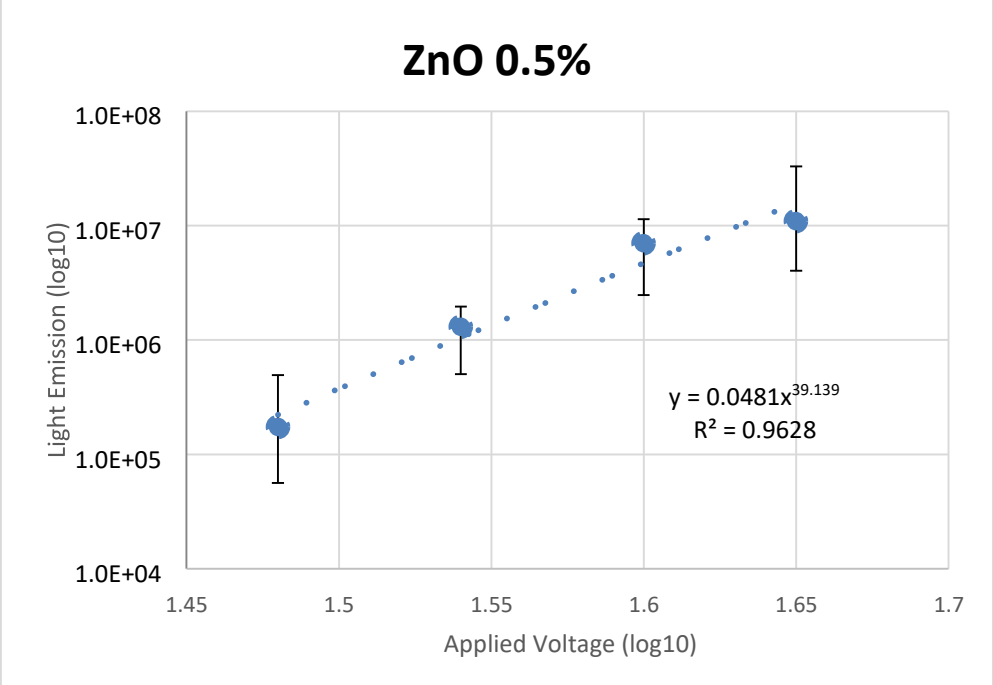

Figure C.19 Total light emission of ZnO 0.5 wt%

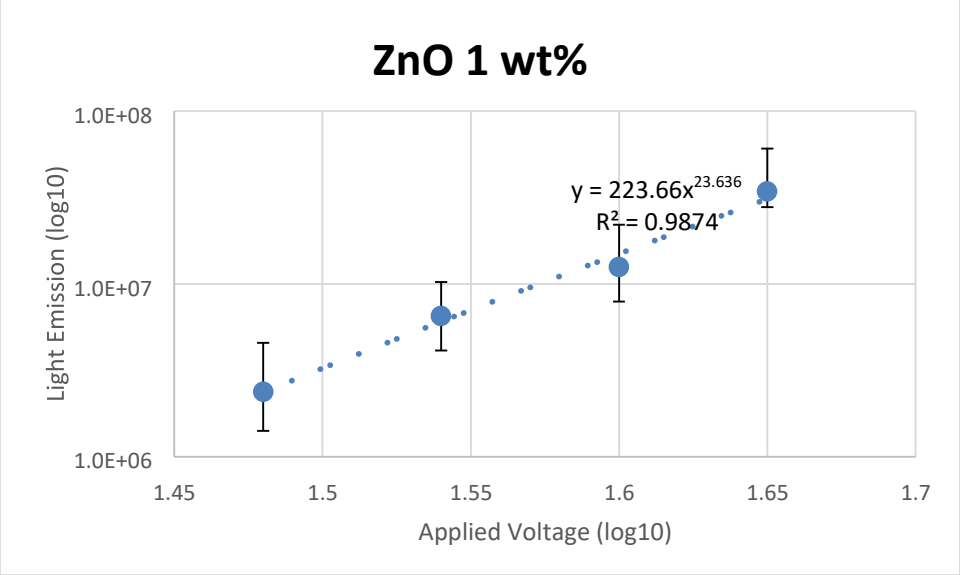

Figure C.20 Total light emission of ZnO 1 wt%

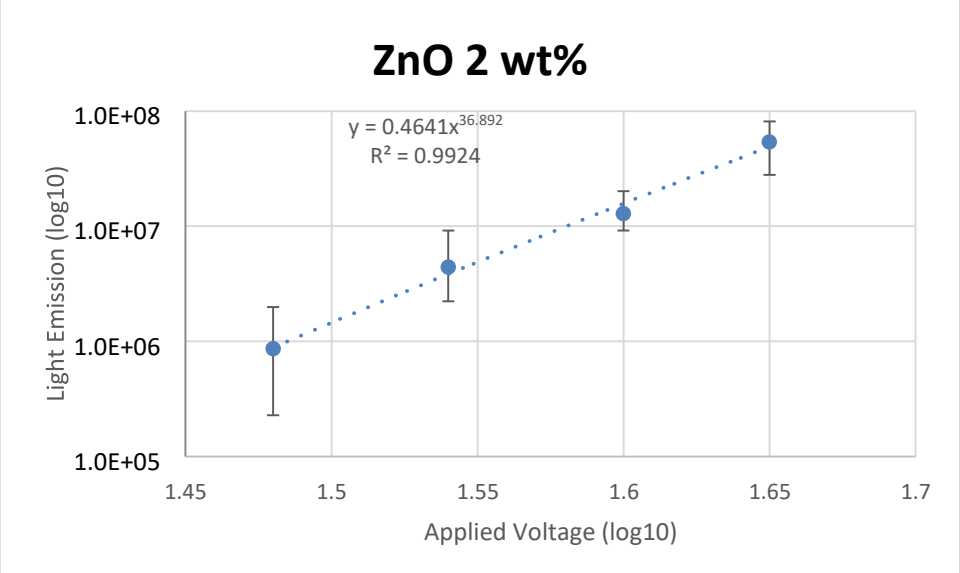

Figure C.21 Total light emission of ZnO 2 wt%

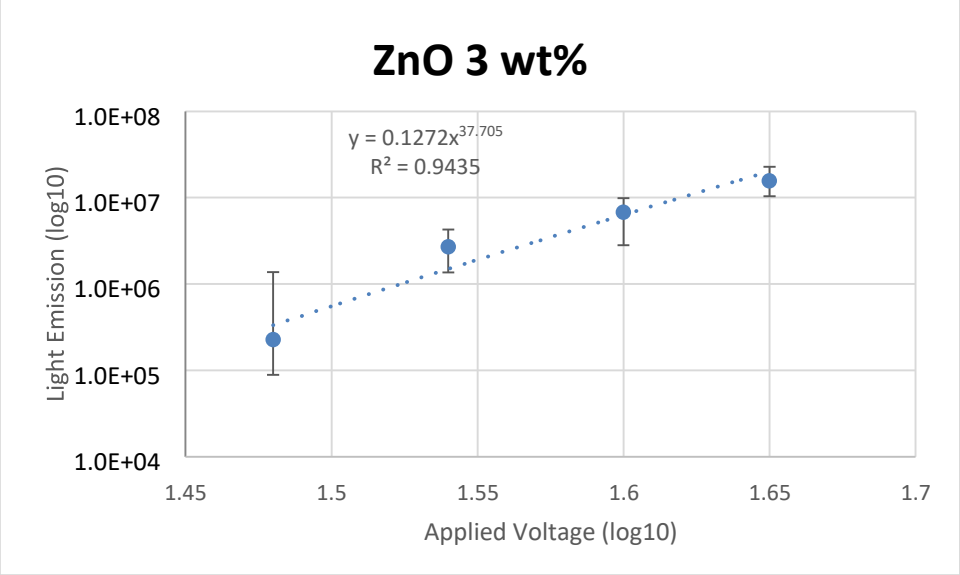

Figure C.22 Total light emission of ZnO 3 wt%

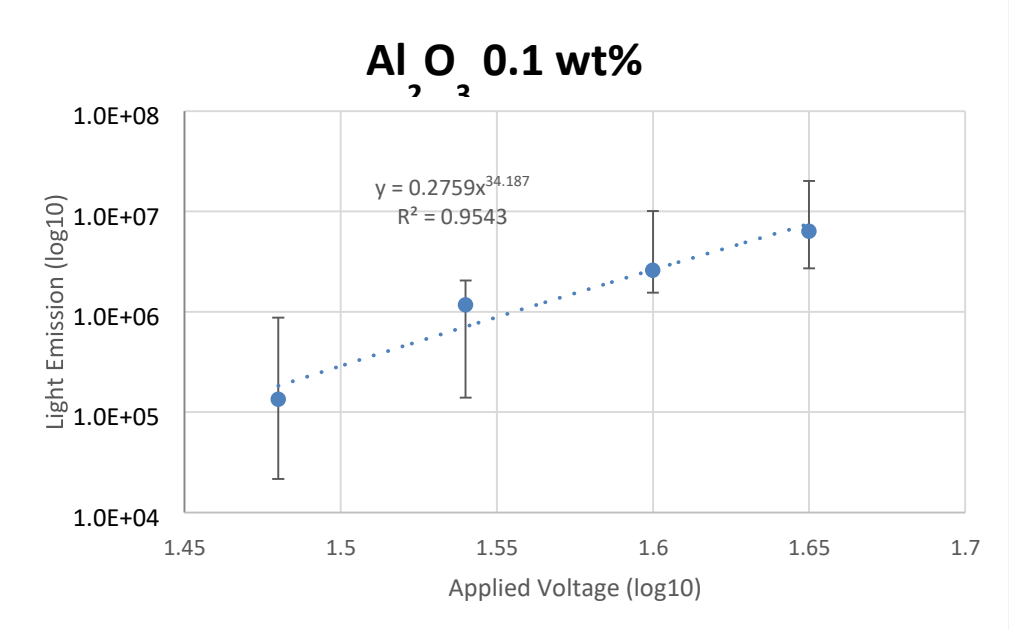

Figure C.23 Total light emission of Al_2O_3 0.1 wt%

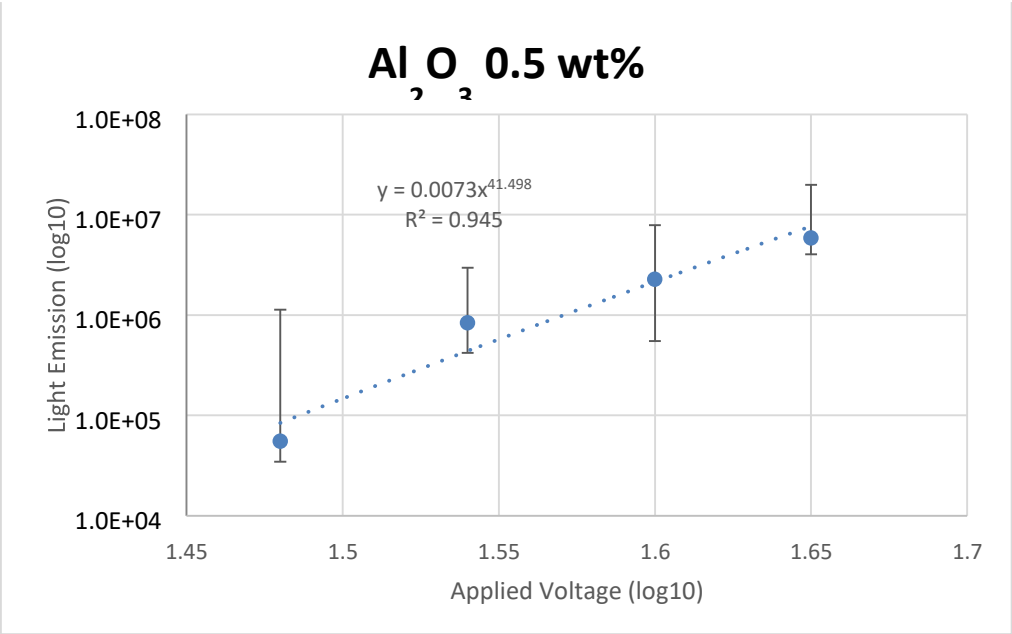

Figure C.24 Total light emission of Al_2O_3 0.5 wt%

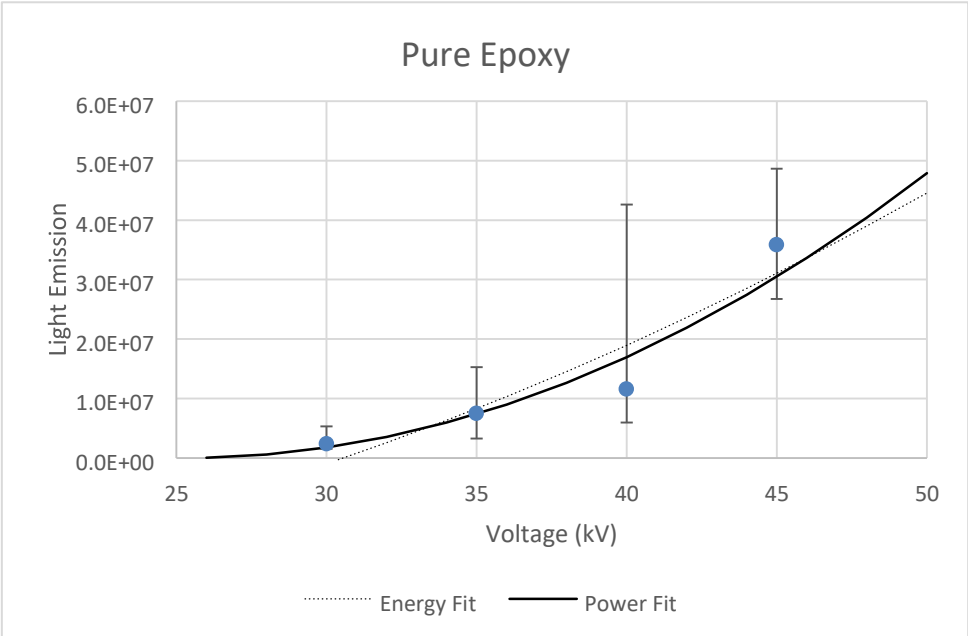

Figure C.25 Total light emission of pure material fitted to power and energy plots

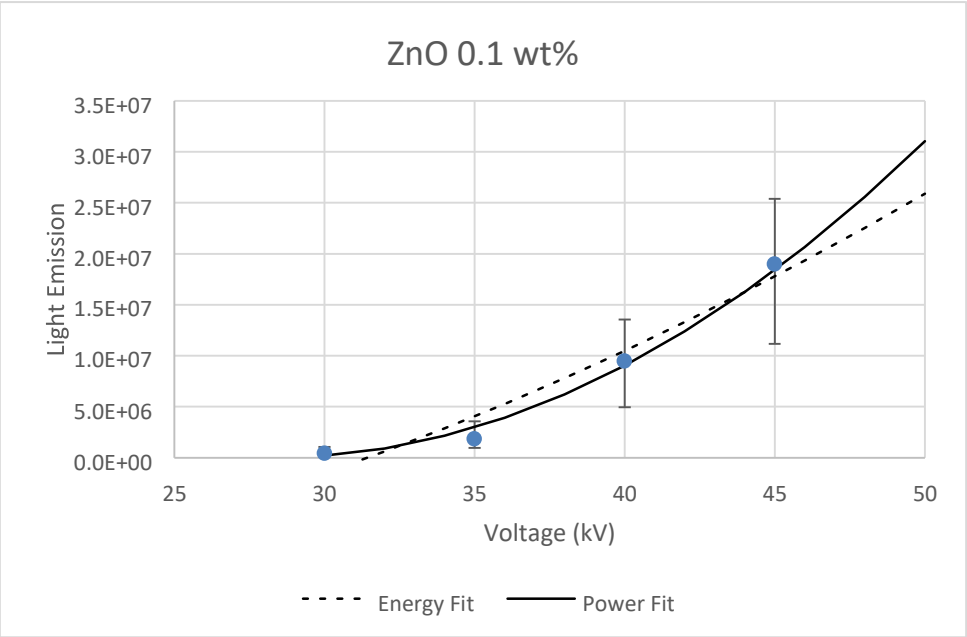

Figure C.26 Total light emission of 0.1 wt% ZnO material fitted to power and energy plots

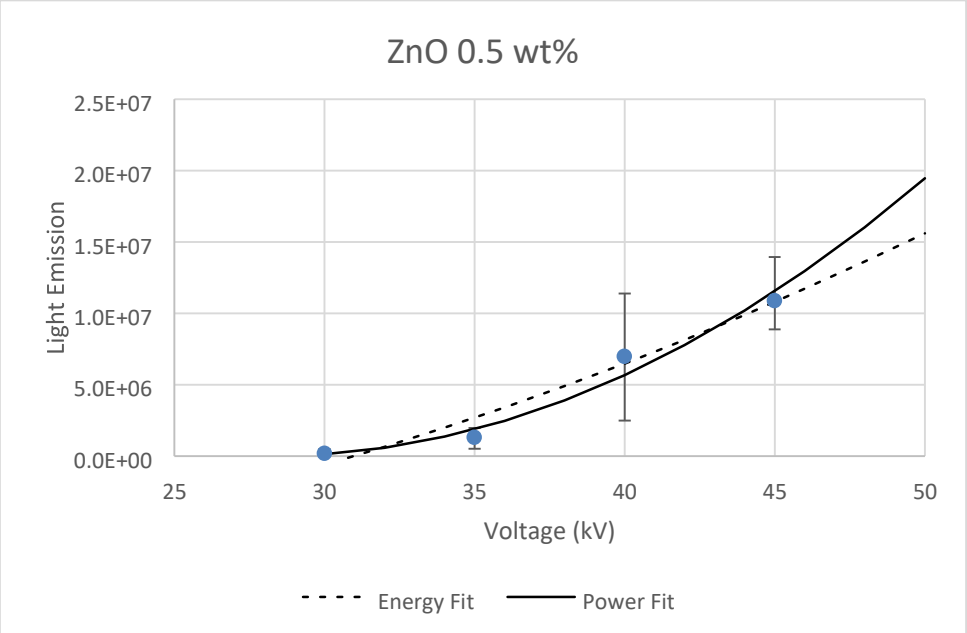

Figure C.27 Total light emission of 0.5 wt% ZnO material fitted to power and energy plots

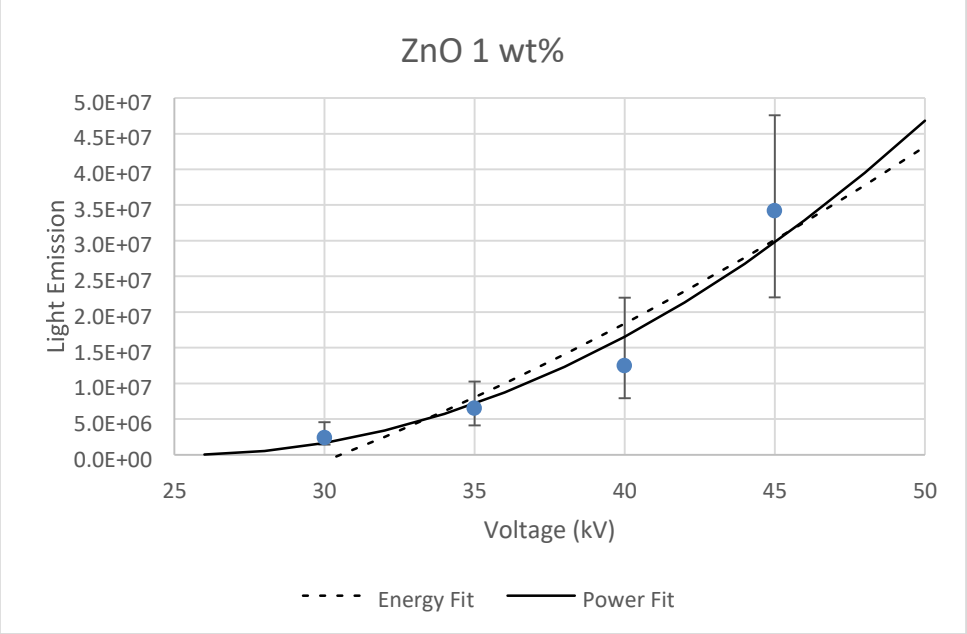

Figure C.28 Total light emission of 1 wt% ZnO material fitted to power and energy plots

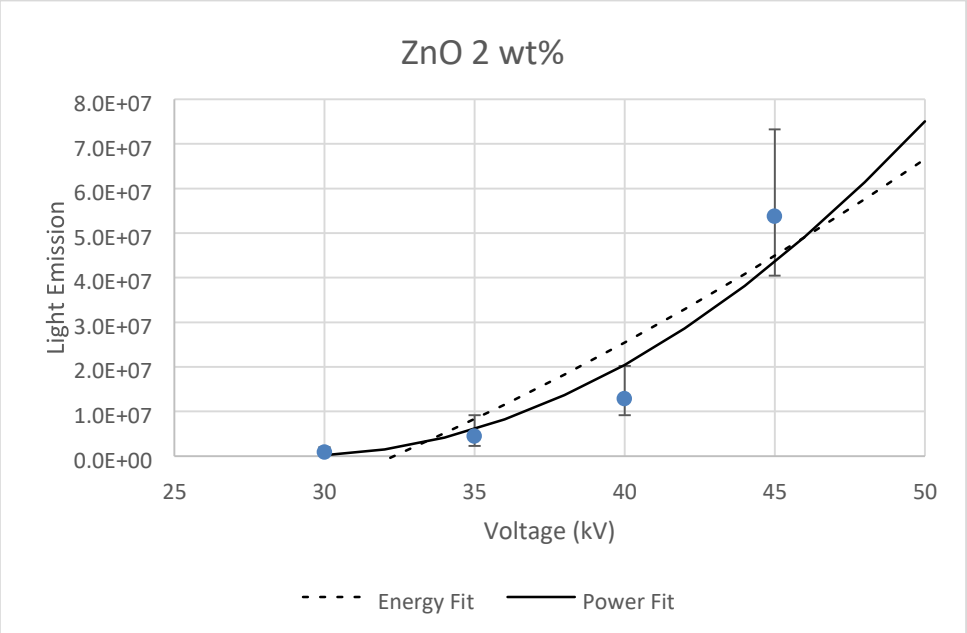

Figure C.29 Total light emission of 2 wt% ZnO material fitted to power and energy plots

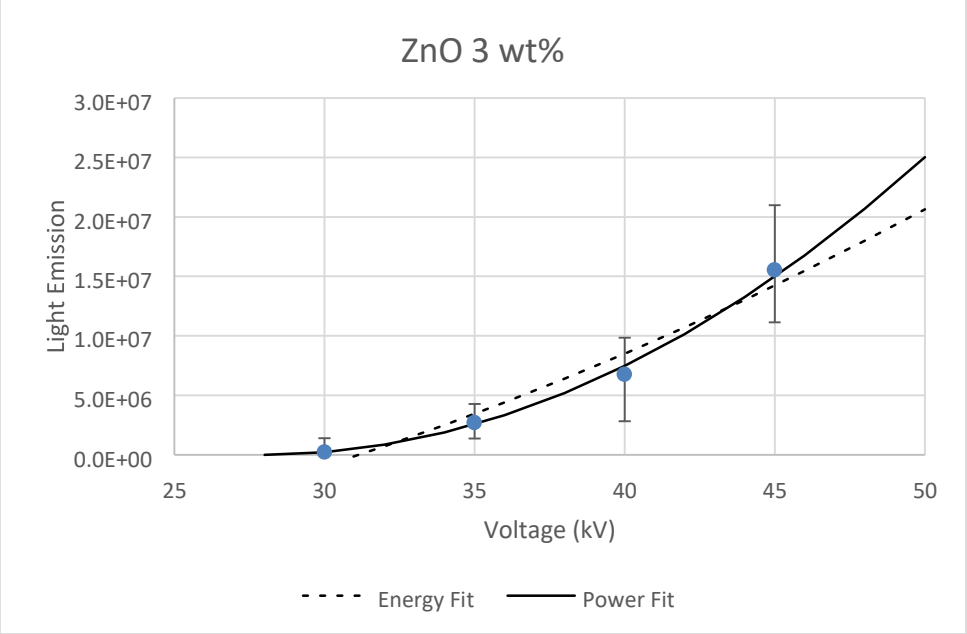

Figure C.30 Total light emission of 3 wt% ZnO material fitted to power and energy plots

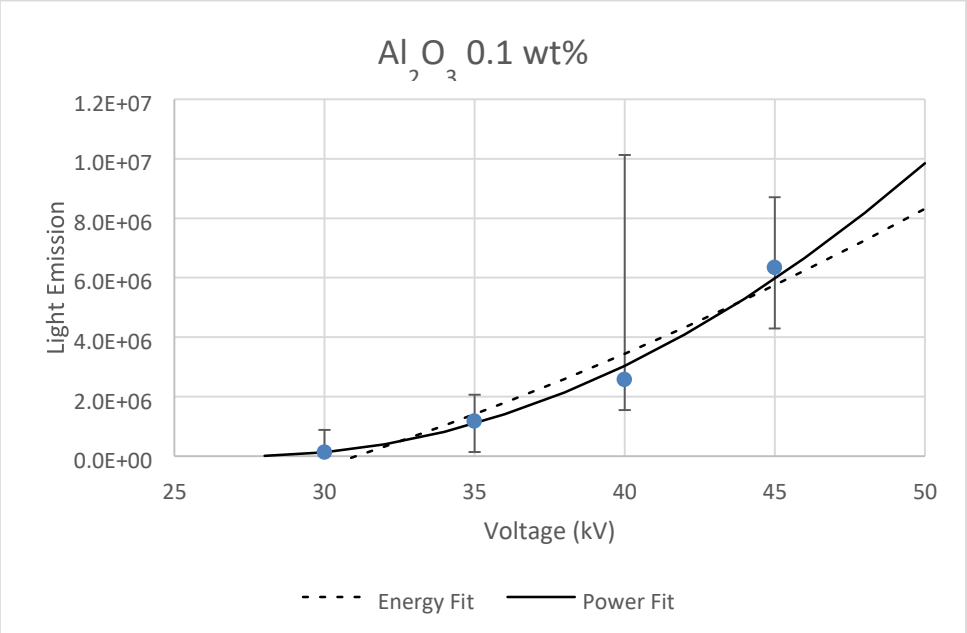

Figure C.31 Total light emission of Al_2O_3 0.1 wt% fitted to power and energy plots

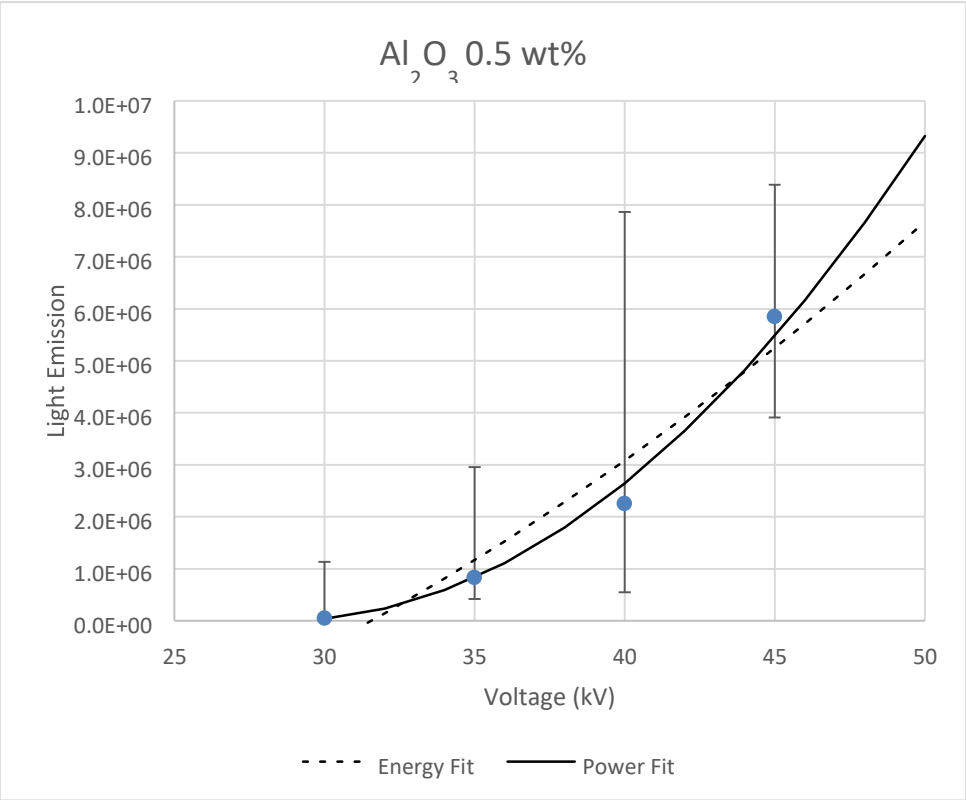

Figure C.32 Total light emission of Al_2O_3 0.5 wt% fitted to power and energy plots